

**APPLIED  
COMPUTATIONAL  
ELECTROMAGNETICS  
SOCIETY  
JOURNAL**

October 2015  
Vol. 30 No. 10  
ISSN 1054-4887

**The ACES Journal is abstracted in INSPEC, in Engineering Index, DTIC, Science Citation Index Expanded, the Research Alert, and to Current Contents/Engineering, Computing & Technology.**

The illustrations on the front cover have been obtained from the research groups at the Department of Electrical Engineering, The University of Mississippi.

# THE APPLIED COMPUTATIONAL ELECTROMAGNETICS SOCIETY

<http://aces-society.org>

## EDITOR-IN-CHIEF

**Atef Elsherbeni**

Colorado School of Mines, EECS Dept.  
Golden, CO 80401, USA

## ASSOCIATE EDITORS-IN-CHIEF

**Sami Barmada**

University of Pisa, EE Dept.  
Pisa, Italy, 56126

**Mohammed Hadi**

Kuwait University, EE Dept.  
Safat, Kuwait

**Paolo Mezzanotte**

University of Perugia  
I-06125 Perugia, Italy

**Yasushi Kanai**

Niigata Inst. of Technology  
Kashiwazaki, Japan

**Alistair Duffy**

De Montfort University  
Leicester, UK

**Antonio Musolino**

University of Pisa  
56126 Pisa, Italy

**Ozlem Kilic**

Catholic University of America  
Washington DC, 20064, USA

**Mohamed Bakr**

McMaster University, ECE Dept.  
Hamilton, ON, L8S 4K1, Canada

**Marco Arjona López**

La Laguna Institute of Technology  
Coahuila 27266, Mexico

**Fan Yang**

Tsinghua University, EE Dept.  
Beijing 100084, China

**Abdul Arkadan**

Rafik Hariri University  
Chouf 2010, Lebanon

## EDITORIAL ASSISTANTS

**Matthew J. Inman**

University of Mississippi, EE Dept.  
University, MS 38677, USA

**Shanell Lopez**

Colorado School of Mines, EECS Dept.  
Golden, CO 80401, USA

## EMERITUS EDITORS-IN-CHIEF

**Duncan C. Baker**

EE Dept. U. of Pretoria  
0002 Pretoria, South Africa

**Ahmed Kishk**

University of Mississippi, EE Dept.  
University, MS 38677, USA

**Allen Glisson**

University of Mississippi, EE Dept.  
University, MS 38677, USA

**Robert M. Bevensee**

Box 812  
Alamo, CA 94507-0516, USA

**David E. Stein**

USAF Scientific Advisory Board  
Washington, DC 20330, USA

## EMERITUS ASSOCIATE EDITORS-IN-CHIEF

**Mohamed Abouzahra**

MIT Lincoln Laboratory  
Lexington, MA, USA

**Erdem Topsakal**

Mississippi State University, EE Dept.  
Mississippi State, MS 39762, USA

**Levent Gurel**

Bilkent University  
Ankara, Turkey

**Alexander Yakovlev**

University of Mississippi, EE Dept.  
University, MS 38677, USA

## EMERITUS EDITORIAL ASSISTANTS

**Khaled ElMaghoub**

University of Mississippi, EE Dept.  
University, MS 38677, USA

**Christina Bonnington**

University of Mississippi, EE Dept.  
University, MS 38677, USA

**Anne Graham**

University of Mississippi, EE Dept.  
University, MS 38677, USA

**Mohamed Al Sharkawy**

Arab Academy for Science and Technology, ECE Dept.  
Alexandria, Egypt

## OCTOBER 2015 REVIEWERS

**Mohammad Alibakhshi Kenari**

**Abdulrahman Alqadami**

**Gulam Alsath**

**Rodolfo Araneo**

**Abdul-Rahman Arkadan**

**Mohamed Bakr**

**Sami Barmada**

**Toni Björninen**

**Sultan Can**

**Zhipeng Cao**

**Ying Cao**

**Deb Chatterjee**

**Giuseppina Dallarmistoks**

**Vinh Dang**

**Carlos Delgado**

**Satya Dubey**

**Noha El-Shalaby**

**Francisco Falcone**

**Ali Foudazi**

**Alfredo Gomes Neto**

**Ahmad Hosseinbeig**

**Mohammad Khalil**

**Mohsen Khalily**

**Ali Lotfi**

**Lester Low**

**Ricardo Matias**

**Zahéra Mekkioui**

**Antonio Moreira**

**Enrique Moreno**

**Ivor Morrow**

**Andrew Peterson**

**Brian Woods**

**Qi Wu**

**John Young**



**THE APPLIED COMPUTATIONAL ELECTROMAGNETICS SOCIETY**  
**JOURNAL**

Vol. 30 No. 10

October 2015

**TABLE OF CONTENTS**

“FEKO Simulation of Multi-Resonant Low-Profile PIFA” Christian W. Hearn and William A. Davis .....	1041
“Sensitivity Analysis of the Orthorhombic Design Parameters in the Artificially Biaxially Dielectric Crystal” Jason Brand and Michael A. Saville .....	1046
“A Novel Wedge Diffraction Modeling Using Method of Moments (MoM)” Gokhan Apaydin and Levent Sevgi .....	1053
“Scattering Analysis of Periodic Composite Metallic and Dielectric Structures with Synthetic Basis Functions” Xu Yanlin, Yang Hu, and Yu Weikang .....	1059
“An Efficient FDTD Algorithm to Analyze Skewed Periodic Structures Impinged by Obliquely Incident Wave” Ming Bai, Bin Liang, and Hui Ma .....	1068
“Modal Analysis of Frequency Selective Surface Containing Ring Loops” Mehran Shamaei-Samani, Reza Sarraf-Shirazi, and Gholamreza Moradi .....	1074
“Multi-Band Frequency Selective Surface Design Based on Idea of Clusters in Cellular Communication Systems” Mehran Shamaei-Samani, Reza Sarraf-Shirazi, and Gholamreza Moradi .....	1079
“Design Investigation of an X-Band SIW H-Plane Band Pass Filter with Improved Stop Band Using Neural Network Optimization” Zahra S. Tabatabaeian and Mohammad H. Neshati .....	1083
“A Circular Slot UWB Antenna with Independently Tunable Quad-Band Filtering Characteristics” Yingsong Li, Wen Zhang, and Wenhua Yu.....	1089
“Dual Band Bandpass Filter Using Multilayer Structure” Sohrab Majidifar and Seyed-Vahab Makki .....	1096

“Nonlinear Analysis of Active Aperture Coupled Reflectarray Antenna Containing Varactor Diode” Iman Aryanian, Abdolali Abdipour, and Gholamreza Moradi .....	1102
“Design and Fabrication of Aperture Coupled Microstrip Increased Bandwidth Antenna” Mohsen J. Chashmi, Hadi Ghobadi, and Mahdi Oliaei .....	1109
“Full-Wave Fast Solver for Circuit Devices Modeling” Yuteng Zheng, Yanwen Zhao, Zaiping Nie, and Qiangming Cai .....	1115
“Firefly Algorithm for Failure Correction of Linear Array of Dipole Antennas in Presence of Ground Plane with Mutual Coupling Effects” Ramalingam Muralidharan, Athinarayanan Vallavaraj, and Gautam K. Mahanti .....	1122
“Lattice Boltzmann Model for Simulation of Avalanche Formation and Streamer Discharge in Breakdown of Gaseous Dielectrics” Nan Wang and Qingquan Lei .....	1129

# FEKO Simulation of Multi-Resonant Low-Profile PIFA

Christian W. Hearn<sup>1</sup> and William A. Davis<sup>2</sup>

<sup>1</sup>Department of Engineering Technology  
Weber State University, Ogden, UT 84408-1802, U.S.A.  
christianhearn@weber.edu

<sup>2</sup>Department of Electrical and Computer Engineering  
Virginia Tech, Blacksburg, VA 24061-0111, U.S.A.  
WADavis@vt.edu

**Abstract** – A passive, low-profile multi-resonant planar-inverted-F antenna (PIFA) element well-suited for portable communications is presented. The antenna combines the optimal low-profile geometry of a planar inverted-F antenna with a double-tuned structure to create a multi-resonant element with monopole-class radiation properties. The form factor and overall dimensions are held constant for comparisons to a similar single-resonant antenna in different near-field environments.

**Index Terms** – Bandwidth enhancement, double-resonant, low-profile, near-field detuning, PIFA.

## I. INTRODUCTION

The planar inverted-F antenna (PIFA) is a popular, small and relatively low-profile, vertically-polarized communications antenna characterized by an omnidirectional radiation pattern in the azimuth (XY) plane. Single-resonant, low-profile configurations of PIFAs suffer from an impedance-bandwidth limitation primarily established by the antenna's effective height. [1].

Double-tuning the PIFA maintains the optimal low-profile characteristic with a potential for increasing impedance bandwidth. The non-volumetric form factor precludes the PIFA from a select class of electrically-small antennas that approach the fundamental limit [2].

However, double-tuning is a useful mechanism to enhance impedance bandwidth in a single frequency band. Comparisons of far-field radiation patterns and mode distributions indicate the radiation properties of the single-resonant and double-tuned PIFAs are nearly equivalent.

One significant fabrication advantage from double-tuning bandwidth enhancement is an effective reduction

to near-field detuning prevalent in the integration of small antennas in portable devices.

## II. ANTENNA GEOMETRY

The antenna geometry is shown in Fig. 1. The overall height of the antenna is less than one centimeter, which corresponds to an electric height of  $h \approx \lambda/35$ . The dimensions for the double-tuned PIFA are presented in Table 1. Some miniaturization is achieved with capacitive-loading. Additional miniaturization may be obtained with the introduction of a dielectric. Air-backed dielectrics and perfectly conducting metal are utilized for this example to create a lossless antenna model utilizing FEKO.

The coupling of the driven element to the parasitic element is highly sensitive to both the width and depth of the slot. The vertical shorting bar is common at the base of the PIFA and increases the coupling to the parasitic element. Figure 2 illustrates VSWR impedance responses for the multi-resonant (solid) and single-resonant (dashed) planar inverted-F antennas with similar form-factors. FEKO simulation results shown were with infinite PEC ground planes for matching boundary conditions. Reference impedance for VSWR was  $50 \Omega$ . Similar comparisons of VSWR responses for different near-field environments will be presented.

The half-power bandwidths observed from the VSWR responses shown in Fig. 1 are  $82 \text{ MHz}$  and  $54 \text{ MHz}$  for the multi-resonant and single-resonant elements respectively. The integration of the parasitic element within the same structural form results in a greater than  $50\%$  increase in half-power bandwidth. Differences observed in the radiation pattern and percent power modal distributions are negligible between the multi-resonant and single-resonant models mounted on square ground planes.

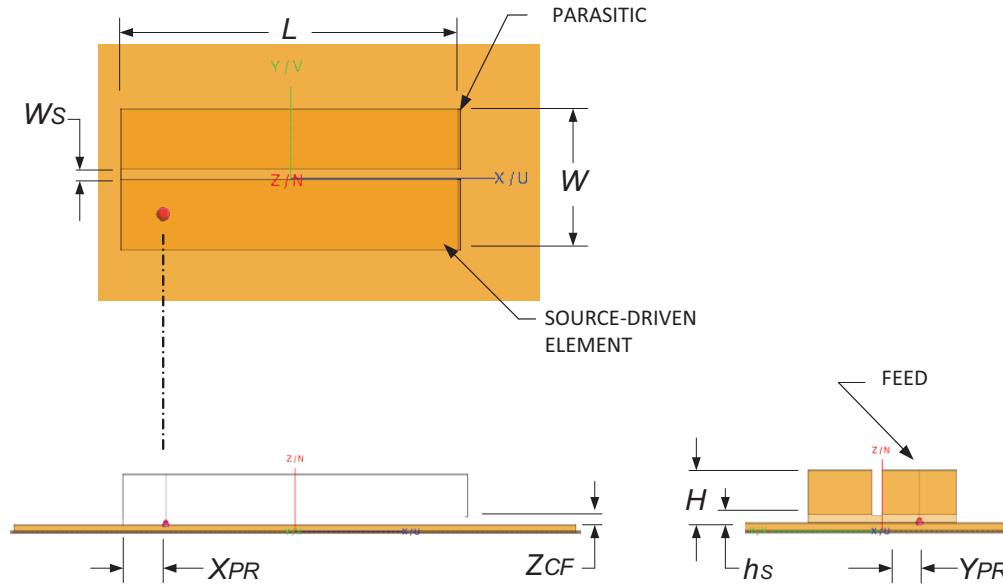


Fig. 1. Engineering perspective of multi-resonant planar inverted-F antenna.

Table 1: Dimensions of the CADFEKO geometry of the multi-resonant PIFA. A capacitive point load of  $C=1.65$  pF is applied at the feed for matching

$L$ [cm]	$W$ [cm]	$H$ [cm]	$W_S$ [mm]	$h_S$ [mm]	$X_{PR}$ [mm]	$Y_{PR}$ [mm]	$Z_{CF}$ [mm]
5.52	2.29	0.83	1.65	1.10	7.0	5.7	1.4

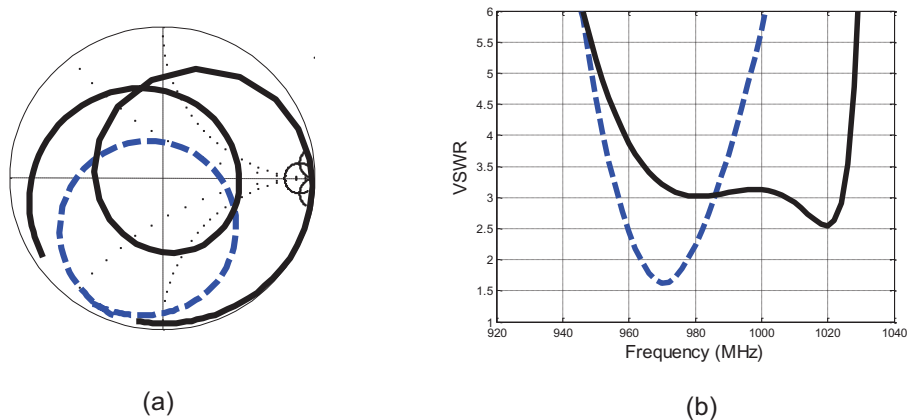


Fig. 2. (a) Normalized impedance and (b) VSWR responses for multi-resonant (solid) and single-resonant (dashed) planar inverted-F antennas with similar form-factors. The boundary condition for both simulations shown was a perfect-electrically-conducting (PEC) infinite ground plane.

### III. ANTENNA GEOMETRY

The multi-resonant PIFA was mounted on a PEC model of a handheld chassis to assess the antenna sensitivity to a typical near-field environment. Single-resonant monopole-class antennas are typically less sensitive to antenna placement/structure interaction, where multi-resonant low-profile antennas may suffer significant detuning with a similar change in boundary conditions.

The purpose of the step is to determine if the multi-resonant PIFA maintains the double-tuning impedance characteristic and omnidirectional radiation in azimuth when subjected to a different boundary condition and near-field environment.

Figure 3 illustrates the integration of the double-resonant PIFA to a handheld device platform. The dimensions of the lossless chassis are approximately  $H=10$  cm,  $W=6.5$  cm and  $D=4.0$  cm.

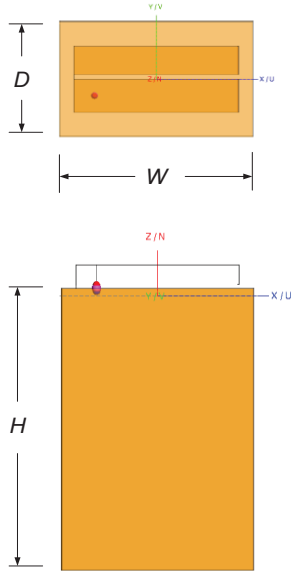


Fig. 3. CADFEKO rendering of double-resonant PIFA integrated to handheld device platform. The dimensions of the lossless chassis are approximately  $H=10\text{ cm}$ ,  $W=6.5\text{ cm}$  and  $D=4.0\text{ cm}$ .

Tuning of the multi-resonant PIFA on the handheld chassis can be improved with adjustments to the coupling factors (slot width,  $W_s$ , and the depth of the slot on the shorting bar,  $h_s$ ). Table 2 indicates changes to the two coupling parameters. The PIFA form factor and probe position are held constant. The same capacitive point load ( $C=1.65\text{ pF}$ ) is applied at the feed for matching.

Table 2: Tuning parameters for integration of double-resonant PIFA to the portable structure (shown in Fig. 3). PIFA geometry and probe position are held constant. The same capacitive point load ( $C=1.65\text{ pF}$ ) is applied at the feed for matching

Double-Resonant PIFA	$W_s$ [mm]	$h_s$ [mm]
Un-tuned	1.65	1.1
Tuned	0.70	4.4

Figure 4 compares the VSWR responses of the un-tuned and tuned double-resonant PIFAs integrated to a handheld device. The infinite ground plane model (described in Fig. 1 and Table 1) was directly applied to the handheld device. No adjustments to coupling factors and/or probe position were made for the dashed trace. The double-tuning characteristic was maintained from a change in boundary conditions without tuning.

The solid trace incorporates the slot parameter adjustments shown in Table 2. The observed result is an increase in 2:1 impedance bandwidth of  $\Delta B \approx 25\%$ .

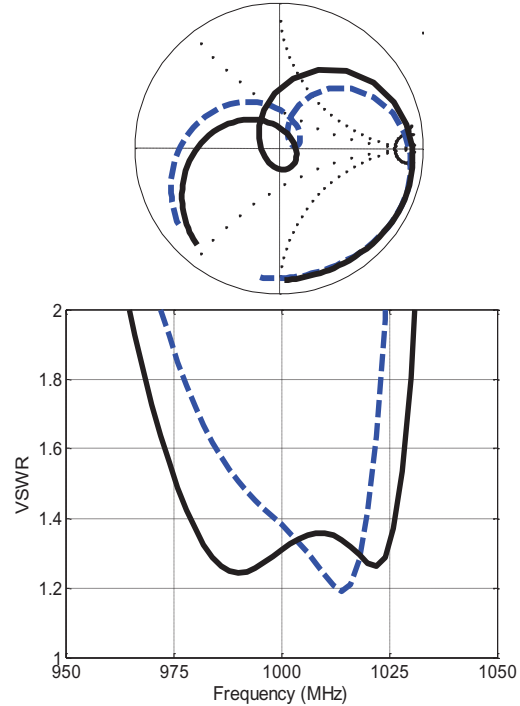


Fig. 4. Impedance responses for ‘untuned’ (dashed) and ‘tuned’ (solid) double-resonant PIFAs integrated to a handheld device (shown in Fig. 3). The observed results are the double-tuning is maintained but with adjustments to the parameters of the coupling slot, an increase in 2:1 VSWR impedance bandwidth of  $\Delta B \approx 25\%$  may be obtained.

Figure 5 (a) presents the normalized impedance and (b) VSWR responses for the single resonant (dashed) double-resonant (solid) inverted-F antennas mounted on the handheld chassis. The 2:1 VSWR bandwidths for the single-resonant and tuned double-resonant antennas are  $46\text{ MHz}$  and  $65\text{ MHz}$  respectively. The double-tuning seen clearly in Fig. 5 (a) results in a 2:1 VSWR impedance bandwidth improvement of greater than  $\Delta B > 40\%$ .

Figure 6 (a) presents the  $E_\theta$  and (b)  $E_\phi$  radiation patterns for the multi-resonant PIFA mounted on a handheld chassis. The significant coupling between the source-driven element and the parasitic creates nearly symmetric patterns with negligible differences in comparison to the single resonant PIFA mounted to the same chassis.

Figure 7 (a-d) are post-processed renderings of the surface current distributions of the multi-resonant PIFA mounted on the handheld chassis. The magnitudes of the surface current densities for both the driven and parasitic elements are comparable. Some phasing is observed at  $\omega t = [0^\circ, 180^\circ]$  where the currents on the parasitic element are lagging the driven element currents.

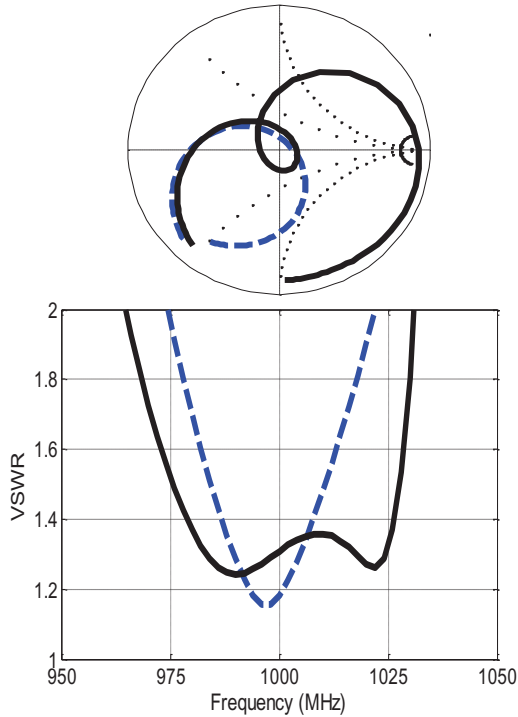


Fig. 5. (a) Normalized impedance and (b) VSWR for the double resonant (solid) and single-resonant (dashed) PIFA integrated to handheld device (shown in Fig. 3).

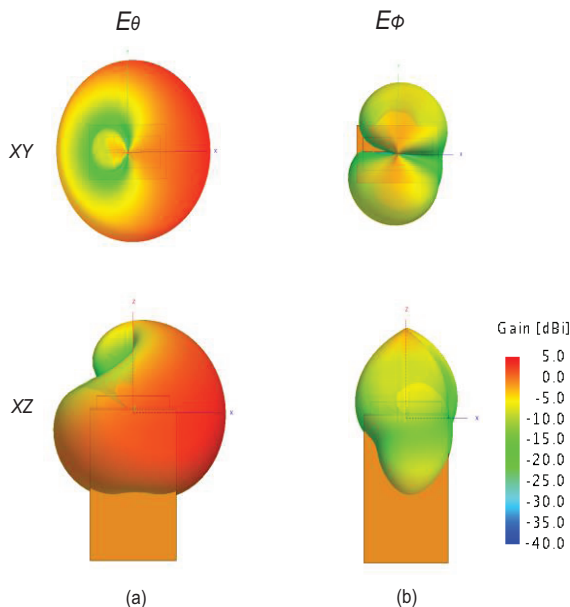


Fig. 6. POSTFEKO renderings of: (a)  $E_\theta$  and (b)  $E_\phi$  radiation patterns for the multi-resonant PIFA mounted on a handheld chassis.

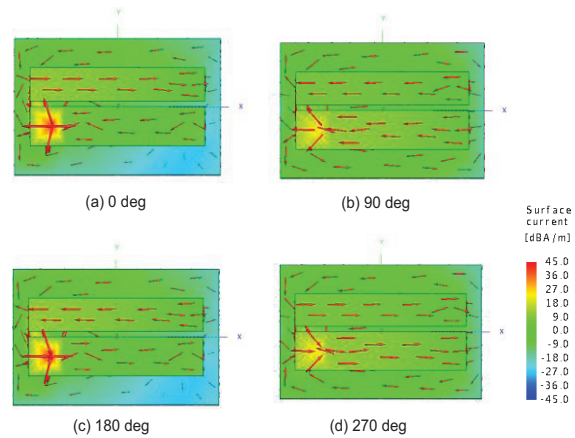


Fig. 7. Surface current distributions on handheld PIFA geometry for  $\omega t = [0^\circ, 90^\circ, 180^\circ, 270^\circ]$ .

#### IV. DISCUSSION

The double-tuned PIFA shown in Fig. 3 enhanced the impedance bandwidth in a single frequency band. Figure 4 illustrates an effective reduction to near-field detuning prevalent in the integration of small antennas in portable devices. The position of the probe and parameters of the slot were unchanged from the finite ground plane example shown earlier. The result indicates the double-tuning characteristic is maintained with the change in finite ground plane/near-field environment of the radiating structure.

Both the source-driven and parasitic elements share part of the shorting bar to increase coupling. The increased coupling balances the surface current distributions and minimizes asymmetries in the far-field radiation patterns.

Bandwidth performance beyond double-tuning and multi-resonant techniques for antenna designs can be improved with the reduction of sharp edges, mechanically in the structural design of the antenna [3], and electrically, in terms of reducing the slope discontinuities in the surface current distributions [4].

#### V. CONCLUSION

A passive, low-profile multi-resonant antenna element with monopole radiation characteristics has been introduced. The structure is an extension of the planar inverted-F antenna with a double-tuned structure to enhance reliable operation in unknown environments. The overall height of the antenna is less than one centimeter, which corresponds to an electric height of  $h \approx \lambda/35$ .

Comparisons to a similar low-profile single-resonant antenna in both the finite ground plane and

handheld geometries were shown. The source-driven element and parasitic are joined at the base of the shorting bar to improve the capacitive coupling. The result is a balanced element in terms of radiation and modal performance with a double-tuned impedance response and 2:1 VSWR bandwidth improvement of over forty percent.

### REFERENCES

- [1] L. M. Feldner, et. al., "Electrically-small frequency-agile PIFA-as-a-package for portable wireless devices," *IEEE Trans. Antennas Propagat.*, vol. 55, no. 11, pp. 3310-3319, Nov. 2007.
- [2] L. J. Chu, "Physical limitations of omnidirectional antennas," *J. Appl. Phys.*, vol. 19, pp. 1163-1175, Dec. 1948.
- [3] D. F. Sevenpiper, et. al., "Experimental validation of performance limits and design guidelines for small antennas," *IEEE Trans. Antennas Propagat.*, vol. 60, no. 1, pp. 8-19, Jan. 2012.
- [4] T. Yang, et. al., "Cellular-phone and hearing-aid. Interaction: an antenna solution," *IEEE Antennas and Propagation Magazine*, vol. 50, no. 3, pp. 51-64, June 2008.

**Christian Hearn** received the Ph.D. degree from Virginia Polytechnic Institute and State University in 2012. He was a Member of the Virginia Tech Antenna Group and a Research Engineer for Applied EM during his Ph.D. plan-of-study. He was originally a Mechanical Engineer for NSWC-UERD and earned a professional engineering license before returning to graduate school in Electrical Engineering. Hearn is currently an Assistant Professor at Weber State University, College of Applied Science and Technology. His interests are design and validation of multi-resonant electrically-small antennas, in addition to communications and signal processing.

**William A. Davis** received the Ph.D. degree from the University of Illinois, Urbana in 1974. He has held academic positions at both the Air Force Institute of Technology and Virginia Polytechnic Institute and State University, Blacksburg where he is a Professor Emeritus and Director of the Virginia Tech Antenna Group. His primary interests are antennas, measurements, scattering theory and material characterization with an emphasis on numerical method, electromagnetic theory and microwave measurements.

# Sensitivity Analysis of the Orthorhombic Design Parameters in the Artificially Biaxially Dielectric Crystal

Jason Brand and Michael A. Saville

Department of Electrical Engineering  
Wright State University, Fairborn, Ohio 45435, USA  
jbrand16@wright.edu, michael.saville@wright.edu

**Abstract** — A full-wave modeling and simulation analysis method is presented for performing sensitivity analysis of artificial uniaxial and biaxial crystals previously reported for study with waveguide measurement systems. Small occlusions were machined into bulk dielectric material to impose effectively biaxial material properties. Here, the primary design parameters for orthorhombic occlusions are presented. Using multivariate parameter estimation, the effective material properties are characterized in a way that is equivalent to waveguide measurement methods. The advantage in using full-wave simulation allows investigation beyond measurement and fabrication capabilities, but is still limited because of the mesh size needed to model the fine geometric sizes of the occlusions in the crystal. The analysis shows that the effects of the primary design parameters on anisotropy can achieve 2-3 dB of axial difference for the biaxially dielectric crystal. Although, only the dielectric case is presented, the multivariate estimation method used to estimate the material parameters is applicable for characterizing lossy and magnetic materials.

**Index Terms** — Biaxial material, permeability, permittivity, sensitivity analysis, waveguide.

## I. INTRODUCTION

Design of electromagnetic metamaterials for antenna substrates, guiding structures, and controlled scattering is challenging because the performance requirements often demand inhomogeneous and anisotropic material properties [1], [2]. Although, analysis methods using Green's functions [3] and transformational optics [4] have produced theoretical profiles for the relative permittivity and permeability, fabrications of such designs have been very limited.

Recent experimental approaches for characterizing the electromagnetic properties of bulk materials [5], [6] using rectangular waveguide measurements enable a way to systematically design biaxial materials. By placing a cubic sample in the waveguide system at four different orientations and measuring ( $S_{11}$ ,  $S_{21}$ ), a Newton

method solution is used to estimate the material tensors from a mode-matching model of the scattering parameters.

Building upon the waveguide methods, Knisely et al. proposed a 3D printing method for making uniaxial and biaxial materials from machined bulk isotropic dielectric materials [7]. Referring to Fig. 1, the design concept is based on symmetry of the occlusions in the bulk material with respect to the primary axes of the material. A detailed summary of the underlying crystallographic theory and mathematics is nicely provided in [8]. Using an ultra-violet cured polymer material for 3D printing, [8] prints axially symmetric cubic samples that have unidirectionally air-filled vias as shown in Fig. 1. Following the mode-matching and Newton method approaches in [5], [9], Knisely et al. perform similar material characterization using waveguide measurements and full-wave simulation to validate the measurement. As the empirical approach includes measurement uncertainty, physical constraints on manufacturing, and machining uncertainty, use of full-wave modeling and simulation as a surrogate for measurement offers a way to limit the uncertainty so that the design parameters can be optimized. The simulation approach allows nearly unconstrained study of how the crystal's design parameters influence effective relative permittivity and permeability. The dominant simulation uncertainty is caused by the specific numerical method and mesh definition because of the frequency sweep.

Here, we build upon the works in [5] and [7] and present sensitivity analyses of the primary design parameters used to impose anisotropic behavior in bulk dielectric material, e.g., uniaxial ( $\bar{\epsilon} = \text{diag}[\tau_A, \tau_A, \tau_C]$ ) and biaxial ( $\bar{\epsilon} = \text{diag}[\tau_A, \tau_B, \tau_C]$ ). The approach is suitable for both measurement- and simulation-based methodologies where the designer might choose the method based on available resources or associated error sources. We demonstrate a simulation-based approach by analyzing the Knisely crystal [7] and showing how the dimensions, electric density, and pose of the vias impact the effective relative permittivity and permeability. Section II summarizes the analytic mode-matching model from [5],

[9] and how we use finite element simulation as a substitute for the measurement system in [5]. Section III presents the detailed cost function and practical considerations of the search method. Section IV presents sensitivity analysis of the artificial biaxial sample in [7], and Sections V and VI present results and conclusions.

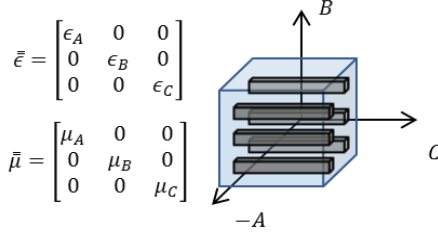


Fig. 1. Illustration of principal axes for artificial biaxial dielectric crystal of [7]. Shaded boxes denote machined vias in bulk isotropic dielectric cubic sample.

## II. MODE MATCHING MODEL

Rectangular waveguide systems are convenient for biaxial material characterization because the TE<sub>10</sub> mode excites only one sample axis and the biaxial region only supports odd-numbered TE<sub>n0</sub> modes. Although higher-order waves are excited at the waveguide junctions, those modes evanesce and do not significantly contribute to ( $S_{11}$ ,  $S_{21}$ ) measurements. Hence, ( $S_{11}$ ,  $S_{21}$ ) are TE<sub>n0</sub> (for  $n = 1, 3, \dots$ ).

Using  $e^{j\omega t}$  time convention and the reduced aperture waveguide system in [5], the total electric field at the guide-sample interface nearest to measurement port 1 must satisfy:

$$A_1^+ \mathbf{e}_1^{\text{wg}}(x, y) e^{-jk_{z,1}^{\text{wg}} z} + \sum_{n=1}^{\infty} A_n^- \mathbf{e}_n^{\text{wg}}(x, y) e^{+jk_{z,n}^{\text{wg}} z} = \sum_{n=1}^{\infty} (B_n^- \mathbf{e}_n^{\text{sa}}(x, y) e^{+jk_{z,n}^{\text{sa}} z} + B_n^+ \mathbf{e}_n^{\text{sa}}(x, y) e^{-jk_{z,n}^{\text{sa}} z}), \quad (1)$$

and the total electric field at the sample-guide interface closest to measurement port 2 must satisfy:

$$\sum_{n=1}^{\infty} (B_n^- \mathbf{e}_n^{\text{sa}}(x, y) e^{+jk_{z,n}^{\text{sa}} z} + B_n^+ \mathbf{e}_n^{\text{sa}}(x, y) e^{-jk_{z,n}^{\text{sa}} z}) = \sum_{n=1}^{\infty} C_n^+ \mathbf{e}_n^{\text{wg}}(x, y) e^{-jk_{z,n}^{\text{wg}} z}, \quad (2)$$

where superscripts + and - in the amplitude coefficients  $A_n, B_n, C_n$  denote forward and backward propagation. The vector basis functions ( $\mathbf{e}_n^{\text{wg}}, \mathbf{e}_n^{\text{sa}}$ ) are in general determined by two subscript indices. However, following [10], in the case of the symmetric dielectric crystal under study, only TE<sub>n0</sub> modes are excited in the sample region for TE<sub>10</sub> excitation. The amplitude coefficients are determined in straightforward fashion by testing each boundary equation with the electric or magnetic field basis function and solving the complete set of equations to compute  $S_{11} = A_1^-/A_1^+$  and  $S_{21} = C_1^+/A_1^+$ .

The complete description of the mode matching

equations including magnetic field boundary conditions has been presented in [5], [9] and for brevity, we refer the reader to [5] for the complete descriptions of the four boundary equations, electric field basis functions ( $\mathbf{e}_n^{\text{wg}}, \mathbf{e}_n^{\text{sa}}$ ), magnetic field basis functions ( $\mathbf{h}_n^{\text{wg}}, \mathbf{h}_n^{\text{sa}}$ ), propagation constants ( $k_{z,n}^{\text{wg}}, k_{z,n}^{\text{sa}}$ ), and matrix algebra formulation.

The  $S$ -parameters' dependencies on  $\bar{\epsilon}_r$  and  $\bar{\mu}_r$  are utilized in a numerical search algorithm as:

$$\hat{\bar{\epsilon}}_r, \hat{\bar{\mu}}_r = \arg \min_{\bar{\epsilon}_r, \bar{\mu}_r} \|\mathbf{S}(f) - \mathbf{S}^{\text{MM}}(f; \bar{\epsilon}_r, \bar{\mu}_r)\|_{\ell}, \quad (3)$$

where the specific type of  $\ell$ -norm  $\|\cdot\|_{\ell}$  depends on the search algorithm. As described in [5], six measurements are needed to estimate the biaxial material properties from the mode matching ( $\mathbf{S}^{\text{MM}}$ ) solutions. However, only four orientations of the sample are required when both  $S_{11}$  and  $S_{21}$  are available. Here, we use finite-element-method simulation of the physical measurement system and assemble the simulated and theoretical (mode matching) solutions as:

$$\mathbf{S} = [S_{11,A}, S_{21,A}, S_{11,B}, S_{11,B'}, S_{21,B'}, S_{21,C}]^T, \quad (4)$$

$$\mathbf{S}^{\text{MM}} = [S_{11,A}^{\text{MM}}, S_{21,A}^{\text{MM}}, S_{11,B}^{\text{MM}}, S_{11,B'}^{\text{MM}}, S_{21,B'}^{\text{MM}}, S_{21,C}^{\text{MM}}]^T, \quad (5)$$

where subscripts  $A, B, B', C$  refer to the excitation of the sample axes as shown in Fig. 2. Clearly, measured or simulated values of  $\mathbf{S}$  suffice.

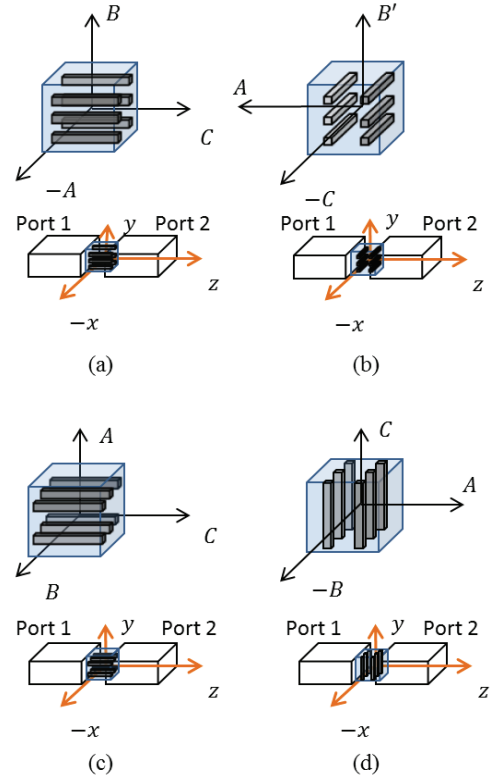


Fig. 2. Illustration of four measurement configurations needed to estimate: (a)  $\epsilon_B, \mu_A, \mu_C$ , (b)  $\epsilon_B, \mu_A, \mu_C$ , (c)  $\epsilon_A, \mu_B, \mu_C$ , and (d)  $\epsilon_C, \mu_A, \mu_B$  using reduced aperture waveguide system [5].

### III. MATERIAL PROPERTY CHARACTERIZATION

The solution to Equation (3) can be determined directly, but is computationally expensive. Alternatively, we use the iterative approach in [5] where,

$$\hat{\epsilon}_B, \hat{\mu}_A, \hat{\mu}_C = \arg \min \left\| \begin{bmatrix} S_{11,B} \\ S_{21,B} \\ S_{21,B'} \end{bmatrix} - \begin{bmatrix} S_{11,B}^{MM}(\epsilon_B, \mu_C, \mu_A) \\ S_{21,B}^{MM}(\epsilon_B, \mu_C, \mu_A) \\ S_{21,B'}^{MM}(\epsilon_B, \mu_C, \mu_A) \end{bmatrix} \right\|_{\ell} \quad (6)$$

$$\hat{\epsilon}_A, \hat{\mu}_B = \arg \min \left\| \begin{bmatrix} S_{11,A} \\ S_{21,A} \end{bmatrix} - \begin{bmatrix} S_{11,A}^{MM}(\epsilon_A, \mu_B, \hat{\mu}_C) \\ S_{21,A}^{MM}(\epsilon_A, \mu_B, \hat{\mu}_C) \end{bmatrix} \right\|_{\ell} \quad (7)$$

$$\hat{\epsilon}_C = \arg \min \left\| [S_{21,C}] - [S_{21,A}^{MM}(\epsilon_C, \hat{\mu}_A, \hat{\mu}_B)] \right\|_{\ell} \quad (8)$$

Equations (6) to (8) are solved using non-linear optimization [11, chap. 4], [12], e.g., Newton method uses the  $\ell_1$  norm and gradient descent uses the  $\ell_2$  norm. We observed a more stable solution using the  $\ell_1$  norm. Also, in each case, the cost function is often decomposed into real and imaginary components.

For example, the cost function in Equation (8), which uses the sample orientation of Fig. 2 (d) and estimates of permeability from Equations (6) and (7), would typically be expressed explicitly in terms of real and imaginary parts as:

$$\hat{\epsilon}_{C,re}, \hat{\epsilon}_{C,im} = \arg \min \left\| \begin{bmatrix} \text{real } S_{11,A} \\ \text{imag } S_{21,A} \end{bmatrix} - \begin{bmatrix} \text{real } S_{11,A}^{MM}(\epsilon_C, \hat{\mu}_A, \hat{\mu}_B) \\ \text{imag } S_{21,A}^{MM}(\epsilon_C, \hat{\mu}_A, \hat{\mu}_B) \end{bmatrix} \right\|_{\ell} \quad (9)$$

However, these search methods are sensitive to the initial search point. The cost functions represented by Equations (6) to (8) are highly oscillatory and have many local minima and maxima. As the contrast between the air-filled waveguide and sample-filled test regions increases, the search volume increases and the iterative search algorithms can take a very long time.

Hence, we have found it best to constrain the search according to physical reasoning. For the material models  $\epsilon_{re} - j\epsilon_{im}$ ,  $\mu_{re} - j\mu_{im}$  with dielectric, non-magnetic, and lossless conditions  $\epsilon_{re} \geq 1.0$ ,  $\mu_{re} = 1.0$ , and  $\epsilon_{im}, \mu_{re} = 0.0$ .

Therefore, Equations (6), (7), (8) represent six, four and two simultaneous equations, respectively. We use non-linear constrained least squares because it is very fast and straightforward to implement. In this study, the specific constraints are:

$$1.0 \geq \epsilon_{re} \geq \epsilon_r \in [2.8, 5.6], \quad (10)$$

$$0.0 \leq \epsilon_{im} \leq 0.1, \quad (11)$$

$$1.0 \leq \mu_{re} \leq 1.1, \quad (12)$$

$$0.0 \geq \mu_{im} \leq 0.1. \quad (13)$$

The parameter estimation process is still supervised because there are many local minima. Table 1 lists the algorithm used to extract all 6 complex-valued material

properties. In addition, the tolerance (TOL) determines when the result has not changed significantly and when the residual of the cost function is sufficiently small. However, when using a single mesh to simulate the  $S$ -parameters, the numerical error increases with frequency. Therefore, the supervised process allows the supervisor to accept a larger residual error. We observed residuals of the order of 0.01 for the upper range of frequencies.

Table 1: Supervised search algorithm

Input	$\mathbf{S}, \mathbf{S}^{MM}$ from Eqs. (4), (5), TOL=0.001, Constraint Equations (10) to (13)
Output	$\bar{\epsilon}_r, \bar{\mu}_r$ for all frequencies
FOR	$q$ -th frequency, $f_q$
<i>Step 1</i>	Estimate $\epsilon_B(f_q), \mu_A(f_q), \mu_C(f_q)$
	initialize $\hat{\epsilon}_B(f_q), \hat{\mu}_A(f_q), \hat{\mu}_C(f_q)$ in Eqs. (10) to (13)
	IF $q > 1$ , initialize with $(q - 1)$ estimates
	WHILE Equations (10) to (13) are unsatisfied
	$[\hat{\epsilon}_B(f_q), \hat{\mu}_A(f_q), \hat{\mu}_C(f_q)]$ from Equation (6)
	$r = \ \mathbf{S}(f_q) - \mathbf{S}^{MM}(f_q; \hat{\epsilon}_r(f_q), \hat{\mu}_r(f_q))\ _1$
	IF $r < \text{TOL}$ GOTO <i>Step 2</i> , ELSE repeat <i>Step 1</i>
<i>Step 2</i>	Estimate $\epsilon_A(f_q), \mu_B(f_q)$
	initialize $\hat{\mu}_C(f_q)$ from <i>Step 1</i>
	initialize $\hat{\epsilon}_B(f_q), \hat{\mu}_A(f_q)$ in Equations (10) to (11)
	IF $q > 1$ , initialize with $(q - 1)$ estimates
	WHILE Equations (10) to (13) are unsatisfied
	$[\hat{\epsilon}_A(f_q), \hat{\mu}_B(f_q)]$ from Equation (7)
	$r = \ \mathbf{S}(f_q) - \mathbf{S}^{MM}(f_q; \hat{\epsilon}_r(f_q), \hat{\mu}_r(f_q))\ _1$
	IF $r < \text{TOL}$ GOTO <i>Step 3</i> , ELSE repeat <i>Step 2</i>
<i>Step 3</i>	Estimate $\epsilon_C(f_q)$
	initialize $\hat{\mu}_A(f_q), \hat{\mu}_B(f_q)$ from <i>Step 1</i> and <i>Step 2</i>
	initialize $\hat{\epsilon}_C(f_q)$ in Equations (10) to (11)
	IF $q > 1$ , initialize with $(q - 1)$ estimates
	WHILE Equations (10) to (13) are unsatisfied
	$[\hat{\epsilon}_C(f_q)]$ from Equation (8)
	$r = \ \mathbf{S}(f_q) - \mathbf{S}^{MM}(f_q; \hat{\epsilon}_r(f_q), \hat{\mu}_r(f_q))\ _1$
	IF $r < \text{TOL}$ next frequency, ELSE repeat <i>Step 3</i>

### IV. BIAXIAL MATERIAL FROM MACHINED BULK ISOTROPIC MATERIAL

We perform the analysis by analyzing simulated biaxial properties of the artificial material proposed by [7], where rectangular vias are unidirectional along the  $C$ -axis (Fig. 3 (a)). Figure 3 (b) illustrates the cross-sectional dimensions of a via ( $\delta_A, \delta_B$ ) and its pose angle ( $\psi$ ). Additionally, Fig. 3 (c) depicts the uniform array of vias with  $N_A = 4$  along the  $A$  axis and  $N_B = 8$  along the  $B$  axis and sized to fit within the short dimension of WR90 waveguide.

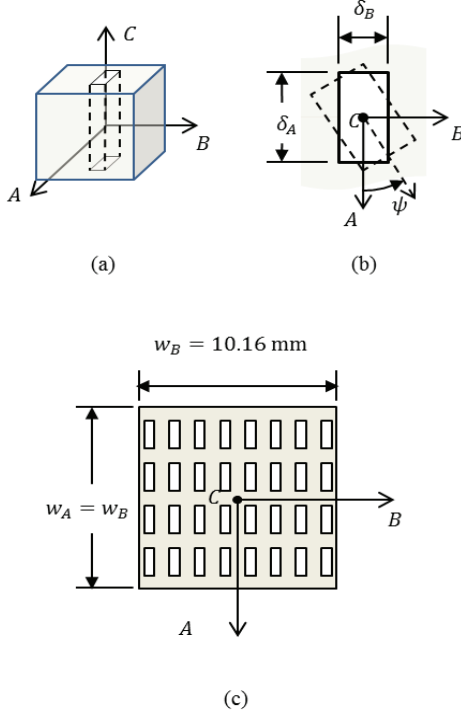


Fig. 3. Illustration of symmetric crystal design [7]. (a) Cubic sample showing single via (dashed lines) relative to principal axes. (b) Cross-sectional view of orthorhombic via showing dimensions along  $A$  and  $B$  axes and pose angle. (c) Biaxial design similar to [7] with  $N_A = 4, N_B = 8, \delta_A = 1.53$  mm,  $\delta_B = 0.51$  mm, and  $\psi = 0$  deg.

### A. Simulation parameters

Then, we simulate the  $S$ -parameters for the variety of design variables listed in Table 2 and observe how the particular combination of via pose, dimension and number affect the relative material properties. The vias are air-filled, and although we could consider vias filled with other materials, we elect a pragmatic set of material properties which are easily fabricated with 3D printing and typical of printing materials. To assist in comparing to other works, we define the air ratio as the ratio of the cross-section of air (via) to the cross-section of dielectric material with respect to each axis as:

$$\rho_A = \delta_B N_B / (L - \delta_B N_B), \quad (14)$$

$$\rho_B = \delta_A N_A / (L - \delta_A N_A), \quad (15)$$

$$\rho_C = \delta_A N_A \delta_B N_B / (L^2 - \delta_A N_A \delta_B N_B), \quad (16)$$

where the edge length  $L$  of the cubic sample is sized to fit inside the cubic waveguide section of the reduced-aperture system (Fig. 2) [5]. We chose that system rather than the transition guide in [7] because it is smaller in size and poses a lower computational burden. It also has an exact mode-matching solution needed for root finding in Equations (6) to (8). The bulk material is assumed to be lossless, homogeneous and the guide walls are perfectly electrically conducting waveguide walls. We

simulate  $S_{11}$  and  $S_{21}$  for each orientation in Fig. 2 and deburred to the sample planes for comparison with the mode matching solution. Then, we follow the procedure described in Section III where we use non-linear least squares with the constraints in Equations (10) to (13).

In summary, each configuration of Table 2 required four simulations at nine frequencies for a total of 864 simulations for the uniaxial case without via rotation, and another 864 simulations for the biaxial case without via rotation. Simulations were completed on a Unix server hosting dual, 3.3 GHz, six-core Xeon X5680 processors and 15GB RAM. In the cases of non-zero pose angle, only 144 simulations were needed.

Table 2: Study parameters for artificial uni/biaxial material Design Constraints

Type	Uniaxial
Bulk permittivity	$\epsilon_r \in [2.8, 5.6]$
Bulk permeability	$\mu_r = 1.0$
Via size	$\delta \in [1.0 : 0.5 : 5.0]$ mm
Lattice size	$N = 2, 3, \dots, 7$
Pose angle	$(\delta = 1.0$ mm, $N = 6)$ , $\psi = 0, 15, \dots, 45$ deg
Air ratio	$0.04 < \rho_C < 31.00$
Type	Biaxial
Bulk permittivity	$\epsilon_r = 2.86$
Bulk permeability	$\mu_r = 1.0$
Via size	$\delta_A = 1.53$ mm, $\delta_B = 0.51$ mm,
Lattice size	$N_A \in [2, 3, \dots, 6]$ , $N_B \in [2, 4, \dots, 10]$
Pose angle	$\psi = 0$ deg
Air ratio $A$ axis	$0.11 < \rho_A < 1.00$
Air ratio $B$ axis	$0.33 < \rho_B < 1.29$
Air ratio $C$ axis	$0.03 < \rho_C < 0.83$

### B. Comments on finite-element modeling

In this work, simulations are performed using the finite element method as implemented in COMSOL version 4.4 [13]. To increase efficiency, the mesh was sized according to the middle frequency of the nine-point sweep (i.e., 8.0 to 10.0 GHz in 0.50 GHz steps). Typical mesh density is of the order of 10 samples per guided wavelength ( $\lambda_g$ ). However, from Table 2, the sizes of the vias are much smaller than  $\lambda_g/50$  which could cause numerical instability and unacceptable numerical error.

Hence, we first meshed the sample region exactly the same as the most densely occluded configuration of Table 2. The mesh in the sample region was of the order of  $\lambda_g/100$ , while the meshes in the WR90 waveguide sections were of the order of  $\lambda_g/8$  using a tetrahedral mesh. Then, we verified that the numerical error of the

$S$ -parameters did not exceed 0.01 using an air-filled sample region. In other words, we followed the procedure outlined in Section III for an isotropic air-filled sample and verified that the extracted relative material tensors were identity tensors.

We also considered the length of the WR90 waveguide sections. Under the premise that only  $TE_{10}$  modes will propagate back to Port 1 and forward to Port 2 because the high-order modes will evanesce, we studied lengths of WR90 ranging from  $0.33 \lambda_g$  to  $1.00 \lambda_g$ . The  $S$ -parameters had a larger error for the shorter length, but the relative error of the  $S$ -parameter magnitude was of the order of 0.01. The increased error suggests weakly evanescent modes still affect the  $S$ -parameter calculation which is based on a pure  $TE_{10}$  mode. Hence, we continued to use waveguide sections with lengths of the order of  $1.0 \lambda_g$ .

Lastly, should one choose to check how the effective material property compares to a bulk material that exhibits the same biaxial properties, it is necessary to simulate the anisotropic bulk material. Clearly, the bulk material eliminates the need for a finely detailed mesh in the sample region. However, the different discretization approaches can cause numerical differences. Hence, the mesh for the anisotropic bulk material can be the same as the mesh for the machined isotropic bulk material. There are different ways to define the anisotropy. First, the material can be defined for the sample region which requires the modeler to carefully select all of the subdomain elements. This approach can be tedious. An alternative approach is to redefine the constitutive relations in the sample region and assume a completely air-filled region. We elected the latter approach which significantly reduced the time needed to build the dozens of geometric models listed in Table 2 and eliminated accidental exclusion of a tetrahedron in the sample region.

## V. RESULTS

### A. Effects on uniaxial design

Referring to Table 2, we modeled 23 combinations of square via size and number to provide air ratio values ranging from 0.04 to 31. Additionally, vias were placed symmetrically and uniformly in the  $A$ - $B$  plane. Estimated material parameter values had imaginary components of  $0.00 \pm 0.05$  and  $\mu_{re}$  equaled  $1.00 \pm 0.05$  and agreed with the lossless and non-magnetic constraints. For this reason, we only show the results of  $\text{real}(\bar{\epsilon})$ .

Figure 3 shows the effective relative permittivity versus frequency for both bulk dielectrics and three levels of air ratio along the  $C$  axis ( $\rho_{C,1} = 0.03$ ,  $\rho_{C,2} = 0.93$ ,  $\rho_{C,3} = 31.00$ ). As expected, the effective relative permittivities tend toward 1.0 for large air-to-dielectric ratios, toward the bulk dielectric value for small ratios and toward  $(\epsilon_r + 1)/2$  when the air and

dielectric cross-sections are nearly equal.

We define the normalized effective relative permittivity as  $\tilde{\epsilon} = (\hat{\epsilon} - 1)/(\epsilon_r - 1)$  to compare effects of different design parameters and present results for the square vias at 10.0 GHz. Figure 4 only shows curves of  $\tilde{\epsilon}_C$  because the curves for  $\tilde{\epsilon}_A$  have similar trends. We also show  $\tilde{\epsilon}_C$  as calculated from the dimensions used in [7] (Fig. 4 dashed lines with  $\otimes$ ).

To determine the range of  $\rho_C$  that results in the maximum axial difference, we graph the normalized axial difference  $|\epsilon_A - \epsilon_C|/(\epsilon_r - 1)$  in Fig. 5. As there are multiple design combinations that result in the same value of  $\rho_C$ , dark solid and dashed lines denote the averages. The results show that the square via design can achieve 2-3 dB axial difference for values of  $\rho$  that span 1 to 2 orders of magnitude.

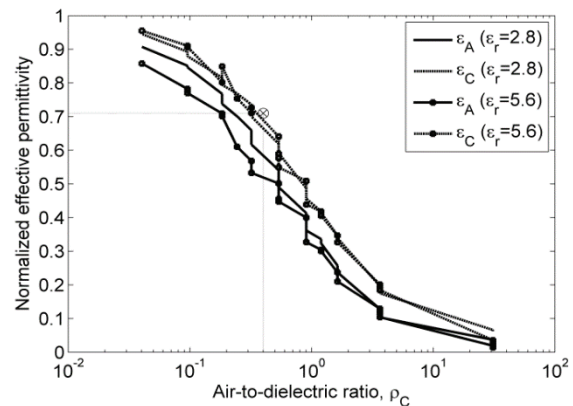


Fig. 4. Uniaxial normalized effective relative permittivity versus air-to-dielectric ratio along  $C$  axis. Dashed line and marker highlight  $\tilde{\epsilon}_C$  from [7].

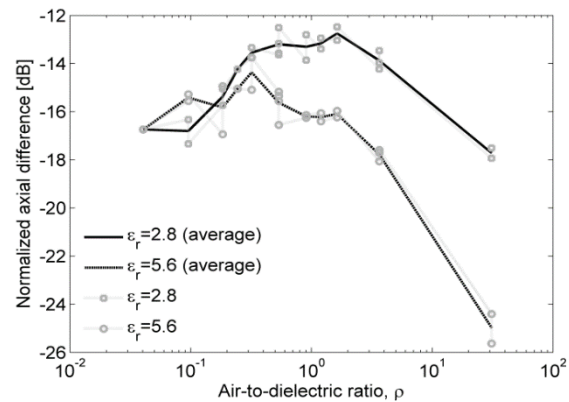


Fig. 5. Uniaxial, axial difference of effective relative permittivity versus air-to-dielectric ratio along the  $C$  axis at 10.0GHz.

### B. Effects on biaxial design

Figure 6 shows the effective relative permittivity versus frequency for the biaxial design parameters in

Table 2 and shows distinct anisotropy for  $\rho = 0.83$ . The normalized axial differences  $\tilde{\epsilon}_A$  and  $\tilde{\epsilon}_B$  are shown in Fig. 7. The trend for  $\tilde{\epsilon}_A$  is similar to the uniaxial behavior seen in Fig. 5, achieving 2-3 dB axial difference, but  $\tilde{\epsilon}_B$  appears to be more sensitive to increasing air-to-dielectric ratio.

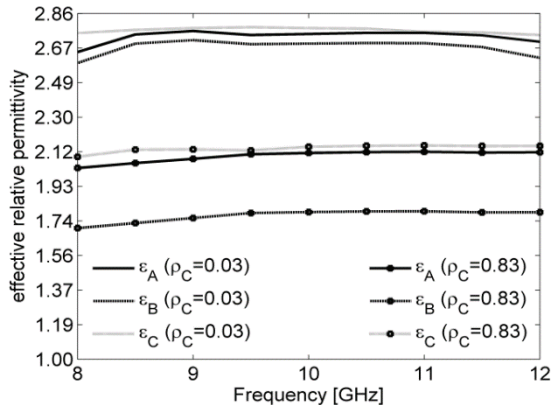


Fig. 6. Biaxial effective relative permittivity versus frequency for two different levels of air ratio ( $\rho_C = 0.03$  and  $\rho_C = 0.83$ ).

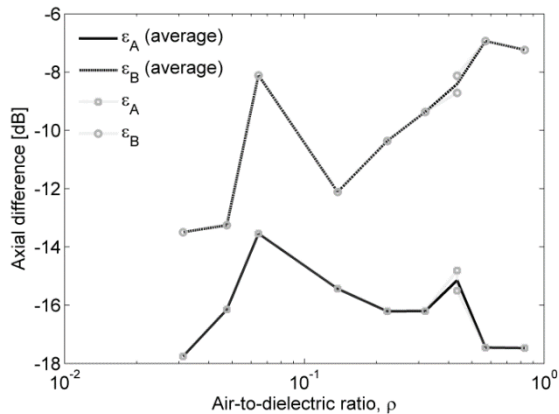


Fig. 7. Biaxial, axial difference versus air-to-dielectric ratio along C axis at 10.0 GHz.

## VI. CONCLUSION

A detailed analysis method is presented for studying the sensitivity of the effective biaxial dielectric material properties as imposed by the primary design parameters of a recently reported orthorhombic dielectric crystal design. Using a well-known mode-matching model for characterizing the effective relative permittivity and permeability tensors, we demonstrate the process and show how the air-filled orthorhombic occlusions in bulk dielectric material can achieve a 3-dB axial difference. The analysis method is suitable for both measurement- and simulated-based methodologies and for lossy and magnetic materials.

## ACKNOWLEDGMENT

The authors thank Dr. Jeffrey Allen and Dr. Monica Allen of the Air Force Research Laboratory, and Ms. Karen Bocko of S4, Inc. for supporting this work.

## REFERENCES

- [1] J. B. Pendry, D. Schurig, and D. R. Smith, "Controlling electromagnetic fields," *Science*, vol. 312, no. 5781, pp. 1780-1782, 2006.
- [2] H. Tao, J. J. Amsden, A. C. Strikwerda, K. Fan, D. L. Kaplan, X. Zhang, R. D. Averitt, and F. G. Omenetto, "Metamaterial silk composites at terahertz frequencies," *Advanced Materials*, vol. 22, no. 32, pp. 3527-3531, Feb. 2010.
- [3] M. Havrilla, "Scalar potential formulation for a uniaxial inhomogeneous medium," in *Radio Science Meeting (USNC-URSI NRSM), 2014 United States National Committee of URSI*, pp. 1-1, Jan. 2014.
- [4] N. Kundtz, D. Smith, and J. Pendry, "Electromagnetic design with transformation optics," *Proceedings of the IEEE*, vol. 99, no. 10, pp. 1622-1633, Oct. 2011.
- [5] B. Crowgey, O. Tuncer, J. Tang, E. Rothwell, B. Shanker, L. Kempel, and M. Havrilla, "Characterization of biaxial anisotropic material using a reduced aperture waveguide," *Instrumentation and Measurement, IEEE Transactions on*, vol. 62, no. 10, pp. 2739-2750, Oct. 2013.
- [6] N. G. Rogers, M. J. Havrilla, M. W. Hyde, and A. E. Bogle, "Nondestructive electromagnetic material characterization of uniaxial media using a two-flanged rectangular-waveguide technique," *Radio Science Meeting (Joint with AP-S Symposium), 2014 USNC-URSI*, pp. 20, July 6-11, 2014.
- [7] A. Knisely, M. Havrilla, P. Collins, M. Hyde, A. Bogle, J. Allen, and E. Rothwell, "Biaxial anisotropic material characterization using rectangular to square waveguide," in *36th Annual Antenna Measurement & Techniques Association Symposium*, Oct. 2014.
- [8] A. Knisely, *Biaxial Anisotropic Material Development and Characterization Using Rectangular to Square Waveguide*, M.S. Thesis, Air Force Institute of Technology, Mar. 2015.
- [9] J. Tang, J. B. Crowgey, O. Tuncer, E. Rothwell, B. Shanker, L. Kempel, and M. Havrilla, "Characterization of biaxial materials using a partially-filled rectangular waveguide," *Applied Computational Electromagnetics Society Journal*, vol. 28, no. 12, pp. 1134-1144, Dec. 2013.
- [10] V. Dmitriev, "Tables of the second rank constitutive tensors for linear homogeneous media described by the point magnetic groups of symmetry," *Progress in Electromagnetics Research*, vol. 28, pp. 43-95, 2000.
- [11] J. K. Au, *An Ab Initio Approach to the Inverse*

*Problem Based Design of Photonic Bandgap Devices*, Ph.D. dissertation, California Institute of Technology, 2007. [Online]. Available: <http://resolver.caltech.edu/CaltechETD:etd-05242007-160527>.

- [12] L. Sorber, M. V. Barel, and L. D. Lathauwer, "Unconstrained optimization of real functions in complex variables," *Optimization, SIAM Journal on*, vol. 22, no. 3, pp. 879-898, 2012.
- [13] COMSOL Multiphysics 4.4. url: [www.comsol.com](http://www.comsol.com).
- [14] A. Knisely, M. Havrilla, and M. Hyde, "Material characterization uncertainty analysis for rectangular to square waveguide," in *2015 IEEE AP-S Symposium on Antennas and Propagation and URSI CNC/USNC Joint Meeting*, July 2015.

**Jason Brand** completed the B.S.E.E. and M.S.E.E. degrees at Wright State University in 2013 and 2015, respectively. He is a veteran of the United States Air Force and is currently with Northrup Grumman.

**Michael A. Saville** received the B.S.E.E., M.S.E.E. and Ph.D. degrees from Texas A&M University in 1997, the Air Force Institute of Technology in 2000, and the University of Illinois at Urbana-Champaign in 2006, respectively. He is currently an Assistant Professor at Wright State University.

# A Novel Wedge Diffraction Modeling Using Method of Moments (MoM)

Gokhan Apaydin<sup>1</sup> and Levent Sevgi<sup>2</sup>

<sup>1</sup>Department of Electrical-Electronics Engineering  
Zirve University, Gaziantep, 27260, Turkey  
gokhan.apaydin@zirve.edu.tr

<sup>2</sup>Department of Electrical and Electronics Engineering  
Okan University, Istanbul, 34959, Turkey  
levent.sevgi@okan.edu.tr

**Abstract** — Scattering from edges and/or tips (i.e., diffraction) has long been modeled using different approaches. Initially, it was handled analytically using high frequency asymptotics (HFA). Parallel to the development in computer technology diffraction has begun to be modeled using numerical approaches also. Here, method of moments (MoM) is used to model the canonical wedge scattering problem and a novel, generally applicable procedure is introduced to extract diffracted fields and diffraction coefficients.

**Index Terms** — Diffraction, high frequency asymptotics, Method of Moments (MoM), wedge.

## I. INTRODUCTION

The word *scattering* is used to represent all wave components produced from the interaction of electromagnetic (EM) waves with objects and include *incidence*, *reflection*, *refraction*, and *diffraction*. Mathematical (analytical) methods are used when frequency is high (i.e., when electromagnetic signal wavelength is quite low compared with the interacted object size) and these are geometric optics (GO), physical optics (PO), geometric theory of diffraction (GTD), uniform theory of diffraction (UTD), and physical theory of diffraction (PTD) [1-10]. GO is a ray-based approach which models incident, reflected, and refracted fields between source and receiver. PO, on the other hand, is an induced-surface-current based approach and models wave scattering caused by the induced-currents on the illuminated side of the object. Both GO and PO models are incapable of modeling edge and/or tip diffracted fields. These deficiencies were removed with the introduction of diffraction models GTD, UTD, and PTD. GTD takes into account diffraction everywhere except near critical angles and caustics. UTD can handle diffraction near critical angles but still suffers from caustics. Original PTD is general and can handle diffraction everywhere except near grazing

incidence (this deficiency is then removed, see [2], Sec. 7.9). A very useful MatLab wedge diffraction package has been introduced for the illustration and visualization of all these HFA approaches [11].

Finite difference time domain (FDTD) method [12] is an effective approach in diffraction modeling [13-14]. A novel multi-step FDTD modeling has been introduced for the extraction of diffracted fields and diffraction coefficient [15]. A useful MatLab-based FDTD package was also introduced for the visualization of diffracted fields and for comparisons with several HFA models [16].

There have been several attempts in diffraction modeling using method of moments (MoM) in hybrid form [14-21]. The idea was to focus on and around the tip of the wedge and use MoM there; then combine the solution with one of the HFA approaches elsewhere. For example, MoM is combined with PO in [17] and then modified in [18] to overcome the failure of the hybrid approach in some cases. A similar hybridization example may be [19] where MoM was combined with the GTD. MoM solutions of wedge problems are well known and - in particular - adequate modeling by suitable basis-functions incorporating appropriate edge conditions well discussed in [20].

A novel two-step MoM [22] approach is introduced here for the extraction and visualization of diffracted fields on the canonical wedge scattering problem.

## II. TWO DIMENSIONAL (2D) WEDGE SCATTERING AND DIFFRACTION MODELING

The non-penetrable wedge diffraction problem is canonical and plays a fundamental role in understanding and construction of HFA techniques as well as for the numerical tests. The exact solution to this scattering problem was first found by Sommerfeld [23] in the particular case of a half-plane. For the wedge with an arbitrary angle between its faces, the solution was

obtained by Macdonald and later on by Sommerfeld who developed the method of branched wave functions.

Figure 1 shows the 2D geometry of the semi-infinite wedge with PEC boundaries and exterior angle  $\alpha$ . Wedge is located in a homogenous medium and illuminated by a cylindrical wave diverging from the line source  $S(r_0, \varphi_0)$  and receiver point is given by  $R(r, \varphi)$ , where  $r, \varphi, z$  are the polar coordinates. The  $z$ -axis is aligned along the edge of the wedge. The angle  $\varphi$  is measured from the top face of the wedge. The time dependence  $\exp(-i\omega t)$  is accepted in the paper.

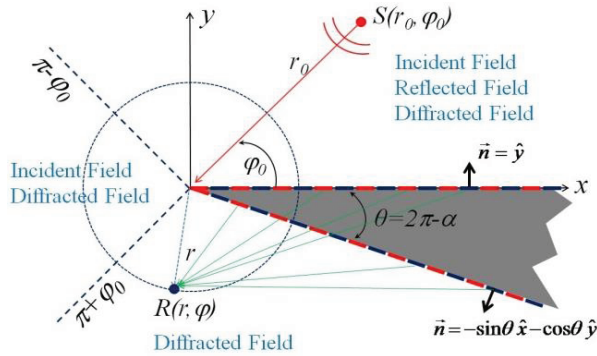


Fig. 1. 2D wedge geometry, line source and critical angles separating incident, reflected, diffracted fields.

The scenario in Fig. 1 ( $0 < \varphi_0 < \alpha - \pi$ ) belongs to the single side illumination (SSI) where the top face is illuminated. In this case, the 2D scattering plane around the wedge may be divided into three regions in terms of critical wave phenomena occurring there. The region ( $0 < \varphi < \pi - \varphi_0$ ) includes all the field components - incident, reflected, and diffracted fields. The critical angle  $\varphi = \pi - \varphi_0$  is called *Reflection Shadow Boundary (RSB)*. The region ( $\pi - \varphi_0 < \varphi < \pi + \varphi_0$ ) contains only incident and diffracted fields. The critical angle  $\varphi = \pi + \varphi_0$  is the limiting boundary of the incident field and called *Incident Shadow Boundary (ISB)*. The third region ( $\pi + \varphi_0 < \varphi < \alpha$ ) is the shadow region where only diffracted fields exist.

The scenario with ( $\alpha - \pi < \varphi_0 < \pi$ ) belongs to the Double Side Illumination (DSI) where both faces are always illuminated. In this case, the 2D scattering plane around the wedge may also be divided into three regions. The regions ( $0 < \varphi < \pi - \varphi_0$ ) and ( $2\alpha - \pi - \varphi_0 < \varphi < \alpha$ ) contain all the field components. The region between these two (i.e.,  $\pi - \varphi_0 < \varphi < 2\alpha - \pi - \varphi_0$ ) contains no reflected fields and only incident and diffracted fields exist.

The field outside the wedge satisfies the Helmholtz's equation [1]:

$$\left( \frac{\partial^2}{\partial r^2} + \frac{1}{r} \frac{\partial}{\partial r} + \frac{1}{r^2} \frac{\partial^2}{\partial \varphi^2} + k^2 \right) u = \frac{I_0}{r} \delta(r - r_0) \delta(\varphi - \varphi_0), \quad (1)$$

where  $k$  is the free-space wave number,  $I_0$  is the line current amplitude,  $\delta(\cdot)$  is the Dirac delta functions, the boundary conditions (BC) on  $\varphi = 0$  and  $\varphi = \alpha$  are:

$$(TM/SBC) u_s = 0 \text{ or } (TE/HBC) \partial u_h / \partial n = 0, \quad (2)$$

and the Sommerfeld's radiation condition (SRC) at infinity is:

$$\lim_{r \rightarrow \infty} \sqrt{kr} \left( \frac{du}{dr} - iku \right) = 0. \quad (3)$$

In the case of acoustic waves, either the field or its normal derivative is zero on the surface and these conditions refer to acoustically soft (SBC) and hard (HBC) wedges, respectively. In the case of EM waves, SBC and HBC correspond to the  $z$ -component of electric field intensity  $E_z$  (TM) and the  $z$ -component of magnetic field intensity  $H_z$  (TE), respectively. Non penetrable wedge corresponds to perfectly electrical/magnetic conductors for Dirichlet/Neumann (soft/hard or TM/TE) type BCs.

The total field solutions of the Helmholtz's equation with SBC and HBC for both SSI and DSI are [2]:

$$u_s^{tot} = \begin{cases} \frac{\pi I_0}{i\alpha} \sum_{l=1}^{\infty} J_{\nu_l}(kr) H_{\nu_l}^{(1)}(kr_0) \sin(\nu_l \varphi_0) \sin(\nu_l \varphi), & r \leq r_0 \\ \frac{\pi I_0}{i\alpha} \sum_{l=1}^{\infty} J_{\nu_l}(kr_0) H_{\nu_l}^{(1)}(kr) \sin(\nu_l \varphi_0) \sin(\nu_l \varphi), & r \geq r_0 \end{cases}, \quad (4)$$

$$u_h^{tot} = \begin{cases} \frac{\pi I_0}{i\alpha} \sum_{l=0}^{\infty} \varepsilon_l J_{\nu_l}(kr) H_{\nu_l}^{(1)}(kr_0) \cos(\nu_l \varphi_0) \cos(\nu_l \varphi), & r \leq r_0 \\ \frac{\pi I_0}{i\alpha} \sum_{l=0}^{\infty} \varepsilon_l J_{\nu_l}(kr_0) H_{\nu_l}^{(1)}(kr) \cos(\nu_l \varphi_0) \cos(\nu_l \varphi), & r \geq r_0 \end{cases}. \quad (5)$$

Here,  $J_{\nu_l}(\cdot)$  and  $H_{\nu_l}^{(1)}(\cdot)$  are Bessel and Hankel functions, respectively;  $\nu_l = l\pi / \alpha$ , and  $\varepsilon_0 = 0.5$ ,  $\varepsilon_1 = \varepsilon_2 = \varepsilon_3 = \dots = 1$ .

The diffracted fields  $u_{s,h}^{diff}$  can be calculated by subtracting the GO fields from (4) and (5) in different regions as:

$$u_{s,h}^{diff} = u_{s,h}^{tot} - \frac{I_0}{4i} u_{s,h}^{GO}, \quad (6)$$

where, for SSI ( $0 < \varphi_0 < \alpha - \pi$ ):

$$u_{s,h}^{GO} = \begin{cases} H_0^{(1)}(kR_1) \pm H_0^{(1)}(kR_2) & 0 < \varphi < \pi - \varphi_0 \\ H_0^{(1)}(kR_1) & \pi - \varphi_0 < \varphi < \pi + \varphi_0, \\ 0 & \pi + \varphi_0 < \varphi < \alpha \end{cases}, \quad (7)$$

and for DSI ( $\alpha - \pi < \varphi_0 < \pi$ ):

$$u_{s,h}^{GO} = \begin{cases} H_0^{(1)}(kR_1) \pm H_0^{(1)}(kR_2) & 0 < \varphi < \pi - \varphi_0 \\ H_0^{(1)}(kR_1) & \pi - \varphi_0 < \varphi < 2\alpha - \pi - \varphi_0, \\ H_0^{(1)}(kR_1) \pm H_0^{(1)}(kR_3) & 2\alpha - \pi - \varphi_0 < \varphi < \alpha \end{cases}, \quad (8)$$

where (-) and (+) are for SBC and HBC, respectively, and

$$R_1 = \sqrt{r^2 + r_0^2 - 2rr_0 \cos(\varphi - \varphi_0)}, \quad (9a)$$

$$R_2 = \sqrt{r^2 + r_0^2 - 2rr_0 \cos(\varphi + \varphi_0)}, \quad (9b)$$

$$R_3 = \sqrt{r^2 + r_0^2 - 2rr_0 \cos(2\alpha - \varphi - \varphi_0)}. \quad (9c)$$

This model is based on the series summation in (4)-(5) and represents reference solution if computed accurately where the critical issue is the specification of the number of terms included which increases with frequency and/or distance.

### III. MOM MODELING OF WEDGE SCATTERING

Method of moments (MoM) is a general procedure and frequency domain approach for solving linear equations. Many problems that cannot be solved *exactly* can be solved *approximately* by this method. The MoM owes its name to the process of taking moments by multiplying with appropriate *weighting* functions and integrating. It has been applied to a broad range of EM problems since the publication of the book by Harrington [22]. A comprehensive bibliography is too vast to be given here. A useful tutorial has just been published [24].

The MoM-based scattering model requires first analytical derivation of the 2D Green's function. Then, both surfaces of the wedge are discretized and replaced with a number of neighboring segments. The segment lengths are specified according to the wave frequency. As a rough criterion, the length of each segment should be equal to or less than one-tenth of the wavelength for discretization in almost all frequency and time domain models. At least ten segments per wavelength is a rough discretization; depending on the problem at hand as many as several dozen segments may be required. The number of segments on both surfaces are  $N$ , therefore the total number of segments is  $2N$ . Note that, infinite distances, lengths, etc. can be truncated after several wavelengths (usually 10 to 100) with acceptable errors. Although it is an infinite wedge a rough truncation with ten to hundred wavelengths from the tip may be enough for the numerical simulations, depending on the polarization as well as other parameters.

Assuming that a line source illuminates the wedge, and currents induced on constant-length segments when illuminated by the source are constant, one can apply MoM technique and obtain the closed form matrix equation:

$$\bar{\bar{V}} = \bar{\bar{Z}}\bar{I}, \quad (10)$$

where  $\bar{I}$  contains the unknown segment currents,  $\bar{V}$  denotes the incident field evaluated at the segment centers, and  $\bar{\bar{Z}}$  is the  $2N \times 2N$  impedance matrix [25].

The unknown segment currents are obtained by solving the system in (10). Finally, direct wave from the

source to the receiver and scattered waves from all segments to the receiver are added and total wave at the observer is obtained.

Note that, each segment acts as a line source with omnidirectional radiation pattern on  $xz$ -plane for the TM polarization. Therefore all segment currents are in parallel (and are perpendicular to the paper). Their mutual coupling (i.e., the impedance matrix) and scattered fields depend on only the distance. On the other hand, each segment acts as a short dipole for the TE polarization. Both their coupling and scattered fields are orientation (angle)-dependent.

### IV. A NOVEL MOM PROCEDURE FOR THE EXTRACTION OF WEDGE DIFFRACTED FIELDS

Incident fields in MoM modeling are injected analytically using the Green's function solution of the problem at hand therefore the scattered fields accumulated from individual source-induced segment currents contain only reflected and diffracted fields. The critical angle  $\varphi = \pi - \varphi_0$  (RSB) divides the whole scattering region into two; with and without reflected fields. As shown in Fig. 1, diffracted fields exist everywhere and reflected plus diffracted fields exist only in the region ( $0 < \varphi < \pi - \varphi_0$ ). The MoM procedure of the wedge scattering is implemented as follows:

- i. First, incident fields upon segments are calculated using the Green's function of the problem.
- ii. The impedance matrix is formed.
- iii. Then,  $2N$  by  $2N$  matrix system is solved and source-induced segment currents are obtained.
- iv. Finally, scattered fields on the chosen observation points are calculated from the superposition of segment radiations using the Green's function.

The diffracted-only fields can be obtained using the MoM procedure if reflected fields in region ( $0 < \varphi < \pi - \varphi_0$ ) are subtracted. The reflected fields in region ( $0 < \varphi < \pi - \varphi_0$ ) can be extracted as follows:

- First, infinite-plane geometry shown in Fig. 2 is taken into account and standard 4-step MoM procedure explained above is applied. The MoM-computed scattered fields contain only reflected fields since there is no edge discontinuity.
- The scattered fields obtained with this geometry are subtracted from the scattered fields of the wedge geometry in region ( $0 < \varphi < \pi - \varphi_0$ ) and reflected fields are all eliminated. The result yields diffracted-only fields.

Note that, reflected field regions are different for the DSI, therefore this procedure is repeated for  $\varphi = \alpha$  plane and bottom-face-reflected fields are also extracted.

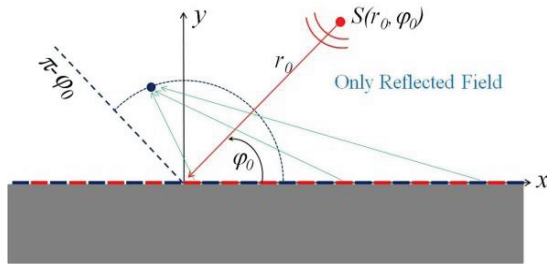


Fig. 2. Infinite-plane geometry and MoM modeling of scattered fields for the line source illumination. MoM-computed scattered fields contain only reflected fields.

Examples using this novel MoM procedure are shown in Figs. 3-7, where MoM-extracted diffracted fields for both polarizations are compared against the analytical reference solution as well as the uniform theory of diffraction (UTD) model. The total and diffracted fields are obtained.

A non-penetrable wedge with  $60^\circ$  interior angle is taken into account in Fig. 3. SBC ( $TM_z$  case) is assumed. Total and diffracted fields vs. angle around the tip of the wedge on a circle with  $5\lambda$ -radius are plotted. The wedge is illuminated by a line source located  $10\lambda$ -distance with  $\varphi_0=90^\circ$ . Infinite wedge faces are truncated in  $10\lambda$  and segment lengths are chosen  $\lambda/10$ . Total field vs. angle plots on the left show the three regions clearly. As observed, very good agreement is obtained with MoM modeling even with these rough discretization parameters.

A non-penetrable wedge with  $90^\circ$  interior angle is used in Fig. 4. All the parameters are kept the same as in Fig. 3 except the illumination angle ( $\varphi_0=60^\circ$ ). Again, total and diffracted fields vs. angle around the tip of the wedge are plotted and very good agreement is obtained among different models.

The next two examples belong to the other polarization (HBC/TE). In Fig. 5, a non-penetrable wedge with  $60^\circ$  interior angle is taken into account. Infinite wedge faces are truncated in  $100\lambda$  in this case and segment lengths are chosen  $\lambda/20$ . Source and receiver distances from the tip of the wedge are kept the same. The illumination angle is  $50^\circ$ . Total and diffracted fields vs. angle around the tip of the wedge on a circle are plotted. MoM results are compared with exact series representation.

Figure 6 belongs to a non-penetrable wedge with  $120^\circ$  interior angle. HBC is used. The illumination angle is  $30^\circ$ . Total and diffracted fields vs. angle around the tip of the wedge are plotted using three different models.

The last example shows DSI case. Figure 7 belongs to a non-penetrable wedge with  $90^\circ$  interior angle for SBC case. The illumination angle is  $120^\circ$ . As observed, the agreement among the models is very good.

Note that, different discretizations are required for the TM (SBC) and TE (HBC) polarizations. Approximately,  $10\lambda$ -long wedge sides are enough for the TM polarization and the results are in 200 by 200 matrix system. On the other hand, up to  $100\lambda$ -long wedge sides (even more) may be required for the TE polarization where 2000 by 2000 matrix system is of interest. Nevertheless, both discrete systems can be solved within a minute with a regular student computer.

In addition, the frequency is fixed to 30 MHz in all the examples. It may be any value; there is no restriction as long as wavelength – distance relation is mentioned.

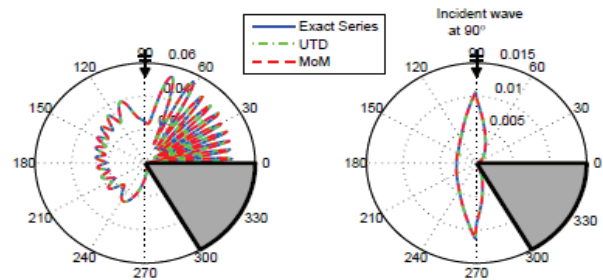


Fig. 3. Wedge scattering for TM/SBC:  $\alpha=300^\circ$ ,  $r=50$  m,  $r_0=100$  m,  $\varphi_0=90^\circ$ , and  $f=30$  MHz; (left) total fields vs. angle, (right) diffracted fields vs. angle.

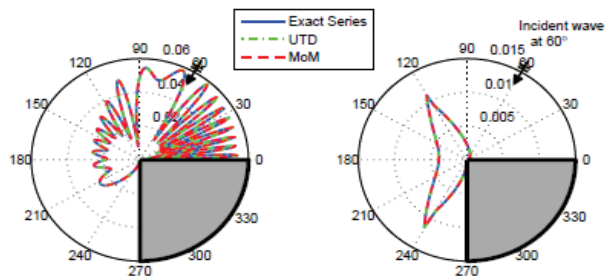


Fig. 4. Wedge scattering for TM/SBC:  $\alpha=270^\circ$ ,  $r=50$  m,  $r_0=100$  m,  $\varphi_0=60^\circ$ , and  $f=30$  MHz; (left) total fields vs. angle, (right) diffracted fields vs. angle.

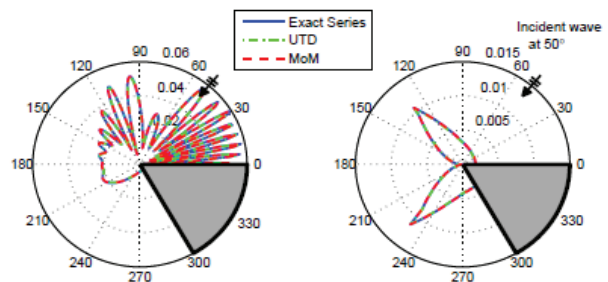


Fig. 5. Wedge scattering for TE/HBC:  $\alpha=300^\circ$ ,  $r=50$  m,  $r_0=100$  m,  $\varphi_0=50^\circ$ , and  $f=30$  MHz; (left) total fields vs. angle, (right) diffracted fields vs. angle.

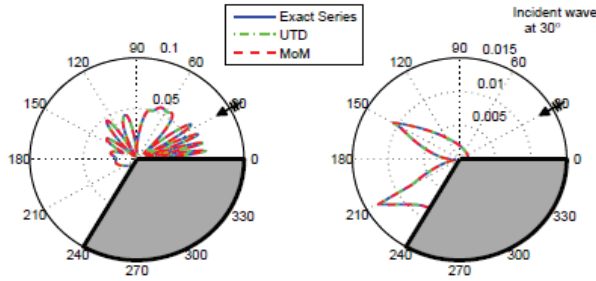


Fig. 6. Wedge scattering for TE/HBC:  $\alpha=240^\circ$ ,  $r=50$  m,  $r_0=100$  m,  $\varphi_0=30^\circ$ , and  $f=30$  MHz; (left) total fields vs. angle, (right) diffracted fields vs. angle.

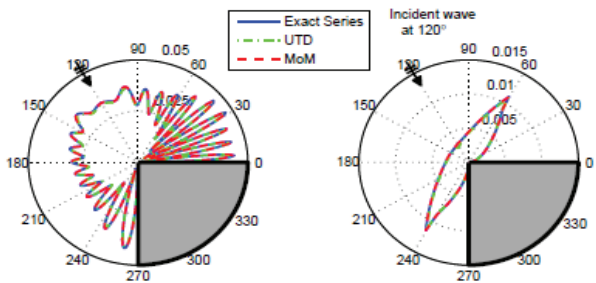


Fig. 7. Wedge scattering for TM/SBC:  $\alpha=270^\circ$ ,  $r=50$  m,  $r_0=100$  m,  $\varphi_0=120^\circ$ , and  $f=30$  MHz; (left) total fields vs. angle, (right) diffracted fields vs. angle.

## V. CONCLUSIONS

A novel Method of Moment (MoM) modeling is introduced for the calculation of diffracted fields in the frequency domain. Electromagnetic wave scattering from a non-penetrable wedge is taken into account and the edge-diffracted fields are extracted numerically. The results are validated against analytical reference solutions as well as the uniform theory of diffraction (UTD). This two-step MoM approach can be used to obtain the diffraction coefficients of scatterers with arbitrary shape and decomposition (e.g., loss-free and lossy dielectrics, metamaterials, etc.) [26]. Higher order diffraction effects can also be modeled, and, for example, double diffraction coefficients of multiple tips can be obtained.

Note that, the *diffraction coefficient* has a *physical meaning* only for high frequency fields and far away from the wedge when  $kr_0 \gg 1$ ,  $kr \gg 1$ , and  $r \gg \lambda$  [15]. This term is a high frequency asymptotic (HFA) notion. One needs to reach at least  $r=10\lambda-20\lambda$  in order to obtain some reasonable values for diffraction coefficients. For an object of a size of several wavelengths, the size of MoM space reaches to hundreds by hundreds even in 2D which necessitates several thousand segments with a rough segment discretization of  $\lambda/10$ . This is within the range of applicability with a regular student computer with 2-4 GB RAM memory

and a few GHz speed. Much larger memories are essential in 3D MoM modeling. Fortunately, there are alternatives and hybridization approaches to overcome these problems which are beyond the scope of this paper.

## REFERENCES

- [1] C. A. Balanis, *Advanced Engineering Electromagnetics*, Wiley, 2012.
- [2] P. Ya. Ufimtsev, *Fundamentals of the Physical Theory of Diffraction*, Wiley, Hoboken, 2007.
- [3] C. Balanis, L. Sevgi, and P. Ya Ufimtsev, "Fifty years of high frequency diffraction," *Int. J. RF Microw. Comput.-Aided Engrg.*, vol. 23, no. 4, pp. 394-402, July 2013.
- [4] G. Pelosi, Y. Rahmat-Samii, and J. L. Volakis, "High frequency techniques in diffraction theory: 50 years of achievements in GTD, PTD, and related approaches," *IEEE Antennas Propag. Mag.*, vol. 55, no. 3, pp. 16-17, June 2013.
- [5] P. Ya. Ufimtsev, "The 50-year anniversary of the PTD: comments on the PTD's origin and development," *IEEE Antennas Propag. Mag.*, vol. 55, no. 3, pp. 18-28, June 2013.
- [6] Y. Rahmat-Samii, "GTD, UTD, UAT, STD: a historical revisit and personal observations," *IEEE Antennas Propag. Mag.*, vol. 55, no. 3, pp. 29-40, June 2013.
- [7] G. Pelosi and S. Selleri, "The wedge-type problem: the building brick in high-frequency scattering from complex objects," *IEEE Antennas Propag. Mag.*, vol. 55, no. 3, pp. 41-58, June 2013.
- [8] F. Hacivelioglu, L. Sevgi, and P. Ya. Ufimtsev, "Wedge diffracted waves excited by a line source: exact and asymptotic forms of fringe waves," *IEEE Trans. Antennas Propagat.*, vol. AP-61, pp. 4705-4712, Sep. 2013.
- [9] A. K. Gantesen, "Diffraction of plane waves by a wedge with impedance boundary conditions," *Wave Motion*, vol. 41, pp. 239-246, 2005.
- [10] N. R. T. Biggs, "A new family of embedding formulae for diffraction by wedges and polygons," *Wave Motion*, vol. 43, pp. 517-528, 2006.
- [11] F. Hacivelioglu, M. A. Uslu, and L. Sevgi, "A matlab-based virtual tool for the electromagnetic wave scattering from a perfectly reflecting wedge," *IEEE Antennas Propag. Mag.*, vol. 53, no. 6, pp. 234-243, Dec. 2011.
- [12] K. S. Yee, "Numerical solution of initial boundary value problems involving Maxwell's equations in isotropic media," *IEEE Trans. Antennas Propagat.*, AP-14, pp. 302-307, 1966.
- [13] V. Anantha and A. Taflove, "Efficient modeling of infinite scatterers using a generalized total-field/scattered field FDTD boundary partially embedded within PML," *IEEE Trans. Antennas Propagat.*, AP-50, pp. 1337-1349, Oct. 2002.

- [14] J.-H. Chang and A. Taflove, "Three-dimensional diffraction by infinite conducting and dielectric wedges using a generalized total-field/scattered-field FDTD formulation," *IEEE Trans. Antennas Propagat.*, AP-53, pp. 1444-1454, Apr. 2005.
- [15] G. Cakir, L. Sevgi, and P. Ya. Ufimtsev, "FDTD modeling of electromagnetic wave scattering from a wedge with perfectly reflecting boundaries: comparisons against analytical models and calibration," *IEEE Trans. Antennas Propagat.*, AP-60, pp. 3336-3342, July 2012.
- [16] M. A. Uslu and L. Sevgi, "Matlab-based virtual wedge scattering tool for the comparison of high frequency asymptotics and FDTD method," *Int. J. Appl. Comput. Electromagnet.*, vol. 27, no. 9, pp. 697-705, Sep. 2012.
- [17] H. J. Bilow, "Scattering by an infinite wedge with tensor impedance boundary conditions-a moment method/physical optics solution for the currents," *IEEE Trans. Antennas Propagat.*, AP-39, pp. 767-773, June 1991.
- [18] Z. Gong, B. Xiao, G. Zhu, and H. Ke, "Improvements to the hybrid MoM-PO technique for scattering of plane wave by an infinite wedge," *IEEE Trans. Antennas Propagat.*, AP- 54, pp. 251-255, Jan. 2006.
- [19] W. D. Burnside, C. L. Yu, and R. J. Marhefka, "A technique to combine the geometrical theory of diffraction and the moment method," *IEEE Trans. Antennas Propagat.*, AP-23, pp. 551-558, July 1975.
- [20] R. D. Graglia and G. Lombardi, "Singular higher-order divergence-conforming bases of additive kind and moments method applications to 3D sharp wedge structures," *IEEE Trans. Antennas Propagat.*, AP-56, pp. 3768-3788, Dec. 2008.
- [21] U. Jakobus and F. M. Landstorefer, "Improvement of the PO-MoM hybrid method by accounting for effects of perfectly conducting wedges," *IEEE Trans. Antennas Propagat.*, AP-43, pp. 1123-1129, Oct. 1995.
- [22] R. F. Harrington, *Field Computation by Moment Method*, New York: IEEE Press, 1993.
- [23] A. Sommerfeld, "Mathematische theorie der diffraction," *Mathematische Annalen*, vol. 16, pp. 317-374, 1896.
- [24] E. Arvas and L. Sevgi, "A tutorial on the method of moments," *IEEE Antennas Propag. Mag.*, vol. 54, no. 3, pp. 260-275, June 2012.
- [25] G. Apaydin and L. Sevgi, "Method of moment (MoM) modeling for resonating structures:

propagation inside a parallel plate waveguide," *Int. J. Appl. Comput. Electromagnet.*, vol. 27, no. 10, pp. 842-849, Oct. 2012.

- [26] M. A. Uslu, G. Apaydin, and L. Sevgi, "Double tip diffraction modeling: finite difference time domain vs. method of moments," *IEEE Trans. Antennas Propagat.*, AP-62, pp. 6337-6343, Dec. 2014.



**Gökhan Apaydin** received the B.S., M.S., and Ph.D. degrees in Electrical & Electronics Engineering from Bogazici University, Istanbul, Turkey, in 2001, 2003, and 2007 respectively. He was a Teaching and Research Assistant with Bogazici University from 2001 to 2005; he was a Project and Research Engineer with University of Technology Zurich, Zurich, Switzerland from 2005 to 2010; and he was a Visiting Associate Professor with the Department of ECE, University of Illinois at Urbana-Champaign, IL, USA in 2015. Since 2010, he has been with Zirve University, Gaziantep, Turkey. He has been involved with complex electromagnetic problems and systems. His research study has focused on analytical and numerical methods in electromagnetics (especially on electromagnetic computation of wave propagation, diffraction modeling, and related areas).



**Levent Sevgi** received the Ph.D. degree from Istanbul Technical University (ITU), Turkey, and Polytechnic Institute of New York University, Brooklyn, in 1990. Prof. Leo Felsen was his advisor. He was with ITU (1991-1998); the Scientific and Technological Council of Turkey–Marmara Research Institute, Gebze/Kocaeli (1999-2000); Weber Research Institute/Polytechnic University in New York (1988-1990); the Scientific Research Group of Raytheon Systems, Canada (1998-1999); the Center for Defense Studies, ITUVSAM (1993-1998) and (2000-2002); the Department of ECE, UMASS Lowell, MA, USA (2012-2013) for his sabbatical term; and Dogus University (2001-2014). Since 2014, he has been with Okan University, Istanbul. He has been involved with complex electromagnetic problems and systems for nearly 30 years.

# Scattering Analysis of Periodic Composite Metallic and Dielectric Structures with Synthetic Basis Functions

Xu Yanlin, Yang Hu, and Yu Weikang

School of Electronic Science and Engineering  
National University of Defense Technology, Changsha, 410073, China  
xyldzx@sina.cn, yanghu90@163.com, 769280669@qq.com

**Abstract** — Synthetic basis functions method (SBFM) is used in this paper to analyze scattering properties of periodic arrays composed of composite metallic and dielectric structures based on EFIE-PMCHW equation. Compared to traditional method of moment (MoM) based on volume integral equations (VIE) or surface integral equations (SIE), SBFM uses fewer synthetic basis functions to approximate scattering properties of a target which decreases the number of unknowns as well as memory cost significantly. Auxiliary sources are introduced to imitate the mutual coupling effects between different blocks. By solving targets' responses to these auxiliary sources, scattering solution space will be determined. Then, singular value decomposition (SVD) is adopted to extract synthetic basis functions' coefficients matrix from scattering solution space. For periodic structures, synthetic basis functions of each block are exactly the same which means previously computed coefficients matrix can be recycled; therefore, SBFM is of great advantages in analyzing large scale periodic mixed problems.

**Index Terms** — Periodic structures, PMCHW formulation, scattering properties, singular value decomposition.

## I. INTRODUCTION

Surface integral equation solvers based on MoM are often adopted in the field of scattering analysis. However, standard MoM implemented with low order basis functions (e.g., RWG [1]) is hardly applied to electrically large targets for the rapid increase of computational complexity and memory cost. To solve this problem, fast multi-pole method (FMM) [2,3] and its extension (multilevel fast multi-pole method, MLFMM [4,5]) made great progresses. These algorithms are based on the sub-domain basis functions, aiming to accelerate the computational efficiency of evaluating interactions among blocks. Another approach dealing with electrically large problems is reducing the number of unknowns (e.g., characteristic basis function method, CBFM [6] and synthetic basis function method, SBFM [7-9]). These approaches

firstly divide the target into several blocks according to its physical and geometrical features. Then, high order functions, which are usually linear combinations of low order functions, are adopted to describe the target's electromagnetic properties.

SBFM was first put forward by Matekovits in 2001 [7]. Not until its systematical representation was published in 2007 [9], this approach caught much more attention. Based on sub-domain decomposition, SBFM introduces the concept of degree of freedom (DOF) in its solution space to control the generation of each block's synthetic basis functions. More importantly, synthetic basis functions can be recycled in periodic system which can improve the computational efficiency significantly. There had been many applications of SBFM both in radiating and scattering analysis since 2007 [10-14].

Although SBFM has been put forward for more than ten years, researches on this approach are mainly laid on two kinds of applications: perfectly electric conducting (PEC) and dielectric structures. For example, paper [9] utilized EFIE and SBFM to analyze large complex conducting structures, while paper [14] applied SBFM to the scattering analysis of inhomogeneous dielectric bodies based on generalized surface integral equations (GSIE) [13,14]. However, in this paper, emphasis is laid on the third application: mixed problems. SBFM is used to analyze scattering properties of large scale periodic structures composed of different kinds of mediums based on EFIE-PMCHW formulation. Compared to the GSIE used in paper [14], PMCHW formulation is adopted in the process of addressing dielectric problems in this paper, which lowers the computational accuracy to some extent but decreases the number of unknowns drastically, and thus, improves the computational efficiency. What's more, the paper also explores principles on how to get synthetic basis functions' solution space for mixed problems based on equivalence theorem. Compared to traditional analysis of mixed problems based on MoM and VIE or SIE, this approach not only reduces the number of unknowns as well as computational time

sharply, but also can make a compromise between complexity and accuracy.

## II. THEORY OF SBFM

SBFM is an improved algorithm on the basis of MoM which uses synthetic basis functions to replace traditional low order basis functions.

$$f(\mathbf{X}) = g. \quad (1)$$

Assume Equation (1) as a linear integral formula and  $\mathbf{X}$  as the unknowns defined on the surface of a target. In traditional MoM, RWG functions are usually used to discretize  $\mathbf{X}$  and to make inner product which leads to the following matrix equations:

$$\mathbf{X} = \sum_{n=1}^N x_n \mathbf{f}_n(\mathbf{r}'), \quad (2)$$

$$\begin{aligned} & \left[ \langle \mathbf{f}_m(\mathbf{r}), f(\mathbf{f}_n(\mathbf{r}')) \rangle \right]_{N \times N} \left[ x_n \right]_{N \times 1} \\ & = \left[ \langle \mathbf{f}_m(\mathbf{r}), g \rangle \right]_{N \times 1}, \end{aligned} \quad (3)$$

where  $\mathbf{f}_n(\mathbf{r})$  stands for the RWG functions and  $\langle \mathbf{A}, \mathbf{B} \rangle$  represents the inner product of  $\mathbf{A}$  and  $\mathbf{B}$ .

However, in SBFM, synthetic functions are employed in place of RWG functions which can sharply decrease the number of unknowns. There are three main steps in SBFM [9,15].

### A. Domain decomposition

To reduce the number of unknowns, the first step is breaking the target into several geometrically small and simple sub-blocks. Compared to dealing with the whole target, it will be much easier to analyze these sub-blocks. Notably, each sub-block should share the same geometrical shape for the sake of making each block's synthetic basis functions the same. For periodic structures, a single element of the structure is usually defined as a sub-block.

Suppose a target is divided into  $N_{SB}$  blocks, as is shown in Fig. 1, and label each block's surface as S block for the sake of simplicity. Considering the fact that there may be public edges between different S blocks, L block needs to be introduced on behalf of these public edges. Denote the number of L blocks is  $N_{LB}$ .

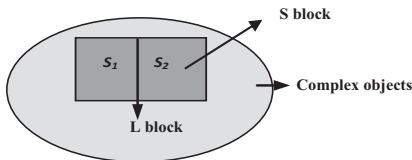


Fig. 1. Sketch map of domain decomposition.

### B. Construct synthetic basis functions

Traditionally, low order functions (e.g., RWG) are used to discretize the unknowns defined on blocks.

However, this kind of discretization usually needs quantities of basis functions which will greatly increase computational complexity and memory cost. Thus, in SBFM, we try to approximate the unknowns with less high order functions. High order functions, also called synthetic basis functions, vary with the geometrical features of blocks.

For S blocks, synthetic basis functions are set as linear combinations of a series of RWG functions:

$$\mathbf{F}_m^b(\mathbf{r}) = \sum_{k=1}^{N_b} P_{k,m}^b \mathbf{f}_k(\mathbf{r}), m=1, \dots, M_b; b=1, \dots, N_{SB}, \quad (4)$$

where  $N_b$  is the number of RWG functions defined on block  $b$  and  $M_b$  refers to the number of synthetic basis functions defined on the block. As for  $N_{SB}$ , it represents the number of S-blocks.

Obviously,  $N_b$  is determined by the triangulation carried on block  $b$  while  $M_b$  is determined by SBFM's truncation error which will be discussed in Section IV. To reach the purpose of reducing the number of unknowns, we want  $M_b \ll N_b$ .

For L blocks, define synthetic basis functions as RWG functions since RWG functions already meet the current continuity conditions on public edges:

$$\mathbf{F}_m^b(\mathbf{r}) = \mathbf{f}_m(\mathbf{r}), m=1, \dots, N_b; b=1, \dots, N_{LB}, \quad (5)$$

where  $N_b$  represents the number of RWG basis functions defined on block  $b$ .

### C. Establish synthetic matrix equation

Having got synthetic basis functions, Equations (2) and (3) can be re-written as:

$$\begin{cases} \mathbf{X} = \sum_{b=1}^{N_{SB}+N_{LB}} \sum_{n=1}^{M_b} x_n \mathbf{F}_n(\mathbf{r}') = \sum_{u=1}^{N_{SBF}} y_u \mathbf{F}_u(\mathbf{r}') \\ N_{SBF} = \sum_{b=1}^{N_{SB}+N_{LB}} M_b \end{cases}, \quad (6)$$

$$\begin{aligned} & \left[ \langle \mathbf{F}_m(\mathbf{r}), f(\mathbf{F}_n(\mathbf{r}')) \rangle \right]_{N_{SBF} \times N_{SBF}} \left[ y_u \right]_{N_{SBF} \times 1} \\ & = \left[ \langle \mathbf{F}_m(\mathbf{r}), g \rangle \right]_{N_{SBF} \times 1}, \end{aligned} \quad (7)$$

where  $N_{SBF}$  is the total number of unknowns in Equation (7), which depend on the number of synthetic basis functions defined on each block. While in traditional MoM, the total number of unknowns  $N_{MoM}$  is calculated in the following equation:

$$N_{MoM} = \sum_{b=1}^{N_{SB}+N_{LB}} N_b. \quad (8)$$

For each block, the number of synthetic basis functions is less than that of RWG functions:  $M_b \ll N_b$ . Thus, the total number of unknowns of MoM and SBFM meet the condition:  $N_{SBF} \ll N_{MoM}$ , which means memory cost of SBFM will be much smaller than that of MoM.

Further, in MoM, computational complexity and memory cost are  $O(N^3)$  and  $O(N^2)$  respectively, where

$N$  represents the number of unknowns. Since the main difference between MoM and SBFM is the selection of basal functions, the method of evaluating SBFM's computational complexity and memory cost is the same to that of MoM. Therefore, compared to MoM, SBFM has great advantages both in computational complexity and memory cost for  $N_{SBFM} \ll N_{MoM}$ .

Compared to Equation (3), Equation (7) replaces all the RWG functions with the synthetic basis functions got in B and is called synthetic matrix equation.

Taking block  $b_1$  and  $b_2$  into consideration, elements in Equation (7) can be calculated from that in Equation (3):

$$\left[ \langle \mathbf{F}_m(\mathbf{r}), f(\mathbf{F}_n(\mathbf{r}')) \rangle \right]_{b_1 b_2} = \left[ \mathbf{F}^{b_1} \right]^T \left[ \langle \mathbf{f}_m(\mathbf{r}), f(\mathbf{f}_n(\mathbf{r}')) \rangle \right]_{b_1 b_2} \mathbf{F}^{b_2}, \quad (9)$$

$$\left[ \langle \mathbf{F}_m(\mathbf{r}), \mathbf{g} \rangle \right]_{b_1 b_2} = \left[ \mathbf{F}^{b_1} \right]^T \left[ \langle \mathbf{f}_m(\mathbf{r}), \mathbf{g} \rangle \right]_{b_1 b_2}, \quad (10)$$

where  $\mathbf{F}^b$  represents the matrix of synthetic basis functions' coefficients defined on block  $b$ :

$$\begin{cases} \mathbf{F}^b = [\mathbf{F}_1^b, \mathbf{F}_2^b, \dots, \mathbf{F}_{M_b}^b] \\ \mathbf{F}_m^b = [P_{1,m}^b, P_{2,m}^b, \dots, P_{N_b,m}^b]^T \end{cases} \quad (11)$$

Obviously, synthetic basis functions' solution space influences accuracy and complexity. Thus, how to determine the solution space is of vital importance and this will be discussed in Section IV.

### III. SURFACE INTEGRAL EQUATION

For scattering problems, SIE (e.g., EFIE and MFIE) are often used when it comes to PEC structures, with RWG functions being its basis functions. As for dielectric structures, VIE and volume basis functions (e.g., SWG [16]) are usually adopted. However, volume meshing usually means a large amount of unknowns which is unbearable for a personal computer. Compared to VIE, SIE can also be used to analyze homogeneous dielectric structures with its results being less accurate but much more efficient. In this paper, EFIE and PMCHW formulation are used to analyze PEC and homogenous dielectric structures respectively. Finally, mixed problems are also explored in the method of EFIE+PMCHW.

For PEC targets, EFIE is usually expressed as [17]:

$$\hat{\mathbf{n}} \times Z^{(i)} L^{(i)}(\mathbf{J}_{si}) = \hat{\mathbf{n}} \times \mathbf{E}_{inc}^{(i)}, \quad (12)$$

where  $L$  is the electric integral operator and defined as:

$$L(\mathbf{X}) = jk \int_{\mathbf{v}'} \left[ \mathbf{X}(\mathbf{r}') G(\mathbf{r} - \mathbf{r}') + \frac{1}{k^2} \nabla' \cdot \mathbf{X}(\mathbf{r}') \nabla G(\mathbf{r} - \mathbf{r}') \right] d\mathbf{v}'. \quad (13)$$

For homogenous dielectric targets, PMCHW formulation is compactly written as [18]:

$$\begin{cases} \hat{\mathbf{n}} \times \left\{ Z^{(i)} L^{(i)}(\mathbf{J}) - K^{(i)}(\mathbf{M}) + Z^{(j)} L^{(j)}(\mathbf{J}) - K^{(j)}(\mathbf{M}) \right\} = \hat{\mathbf{n}} \times \mathbf{E}_{inc}^{(i)} \\ \hat{\mathbf{n}} \times \left\{ K^{(i)}(\mathbf{J}) + Y^{(i)} L^{(i)}(\mathbf{M}) + K^{(j)}(\mathbf{J}) + Y^{(j)} L^{(j)}(\mathbf{M}) \right\} = \hat{\mathbf{n}} \times \mathbf{H}_{inc}^{(i)} \end{cases}, \quad (14)$$

where  $K$  is the magnetic integral operator and defined as:

$$K(\mathbf{X}) = \int_{\mathbf{v}'} [\mathbf{X}(\mathbf{r}') \times \nabla G(\mathbf{r} - \mathbf{r}')] d\mathbf{v}'. \quad (15)$$

For composite metallic and dielectric targets, SIE is described as [18]:

$$\begin{cases} \hat{\mathbf{n}}_{ij} \times \left\{ \begin{aligned} & \sum_{k=0, k \neq i}^n \left[ Z^{(i)} L^{(i)}(\mathbf{J}_{sik}) - K^{(i)}(\mathbf{M}_{sik}) \right] + \\ & \sum_{k=0, k \neq j}^n \left[ Z^{(j)} L^{(j)}(\mathbf{J}_{sjk}) - K^{(j)}(\mathbf{M}_{sjk}) \right] \end{aligned} \right\}_{S_{ij}} \\ = \hat{\mathbf{n}}_{ij} \times (\mathbf{E}_{inc}^{(i)} - \mathbf{E}_{inc}^{(j)})|_{S_{ij}}, \\ \hat{\mathbf{n}}_{ij} \times \left\{ \begin{aligned} & \sum_{k=0, k \neq i}^n \left[ K^{(i)}(\mathbf{J}_{sik}) + Y^{(i)} L^{(i)}(\mathbf{M}_{sik}) \right] + \\ & \sum_{k=0, k \neq j}^n \left[ K^{(j)}(\mathbf{J}_{sjk}) + Y^{(j)} L^{(j)}(\mathbf{M}_{sjk}) \right] \end{aligned} \right\}_{S_{ij}} \\ = \hat{\mathbf{n}}_{ij} \times (\mathbf{H}_{inc}^{(i)} - \mathbf{H}_{inc}^{(j)})|_{S_{ij}} \end{cases}, \quad (16)$$

where  $S_{ij}$  refers to the interface of medium  $i$  and  $j$ ,  $\mathbf{J}$  and  $\mathbf{M}$  represent electric and magnetic currents on the interface respectively.

Specifically, magnetic currents  $\mathbf{M}$  and incident magnetic field  $\mathbf{H}_{inc}$  tend to be zero when medium  $j$  is PEC bodies. Then, Equation (16) can be re-written as:

$$\begin{aligned} \hat{\mathbf{n}}_{ij} \times \left\{ \sum_{k=0, k \neq i, j}^n \left[ Z^{(i)} L^{(i)}(\mathbf{J}_{sik}) - K^{(i)}(\mathbf{M}_{sik}) \right] + Z^{(i)} L^{(i)}(\mathbf{J}_{sij}) \right\}_{S_{ij}} \\ = \hat{\mathbf{n}}_{ij} \times \mathbf{E}_{inc}^{(i)}|_{S_{ij}} \end{aligned} \quad (17)$$

Equations (16) and (17) is called EFIE-PMCHW equation for composite metallic and dielectric targets.

To solve these SIEs listed above,  $\mathbf{J}$  and  $\mathbf{M}$  need to be discretized by basis functions firstly:

$$\mathbf{J}(\mathbf{r}') = \sum_{n=1}^N \alpha_n \mathbf{f}_n(\mathbf{r}'), \mathbf{M}(\mathbf{r}') = \sum_{n=1}^N \beta_n \mathbf{f}_n(\mathbf{r}'). \quad (18)$$

Then, according to MoM and Galerkin principle, these SIEs can be transformed into the following linear matrix equations.

• PEC Targets

$$Z\mathbf{I} = \mathbf{V}, \quad (19)$$

where  $Z$  is the impedance matrix and  $\mathbf{V}$  is the exciting matrix:

$$\begin{cases} Z_{nm} = \langle \mathbf{f}_m(\mathbf{r}), Z_0 L(\mathbf{f}_n(\mathbf{r}')) \rangle \\ V_m = \langle \mathbf{f}_m(\mathbf{r}), \mathbf{E}_{inc}(\mathbf{r}) \rangle \end{cases}, \quad (20)$$

where  $Z_0$  is the wave impedance of free space.

- Dielectric Targets

$$\begin{bmatrix} z^{EJ} & z^{EM} \\ z^{HJ} & z^{HM} \end{bmatrix} \begin{bmatrix} I^J \\ I^M \end{bmatrix} = \begin{bmatrix} V^E \\ V^H \end{bmatrix}. \quad (21)$$

The impedance matrix and exciting matrix will be obtained through Equations (22) and (23):

$$\begin{cases} z_{mn}^{EJ} = \langle \mathbf{f}_m(\mathbf{r}), [Z^{(i)}L^{(i)}(\mathbf{f}_n(\mathbf{r}')) + Z^{(j)}L^{(j)}(\mathbf{f}_n(\mathbf{r}'))] \rangle \\ z_{mn}^{EM} = \langle \mathbf{f}_m(\mathbf{r}), -[K^{(i)}(\mathbf{f}_n(\mathbf{r}')) + K^{(j)}(\mathbf{f}_n(\mathbf{r}'))] \rangle \\ z_{mn}^{HJ} = \langle \mathbf{f}_m(\mathbf{r}), [K^{(i)}(\mathbf{f}_n(\mathbf{r}')) + K^{(j)}(\mathbf{f}_n(\mathbf{r}'))] \rangle \\ z_{mn}^{HM} = \langle \mathbf{f}_m(\mathbf{r}), [Y^{(i)}L^{(i)}(\mathbf{f}_n(\mathbf{r}')) + Y^{(j)}L^{(j)}(\mathbf{f}_n(\mathbf{r}'))] \rangle \end{cases}, \quad (22)$$

$$\begin{cases} V_m^E = \langle \mathbf{f}_m(\mathbf{r}), \mathbf{E}_{inc}(\mathbf{r}) \rangle \\ V_m^H = \langle \mathbf{f}_m(\mathbf{r}), \mathbf{H}_{inc}(\mathbf{r}) \rangle \end{cases}. \quad (23)$$

- Composite Metallic and Dielectric Targets

$$\begin{bmatrix} Z^{CC} & Z^{CD} & Z^{CM} \\ Z^{DC} & Z^{DD} & Z^{DM} \\ Z^{MC} & Z^{MD} & Z^{MM} \end{bmatrix} \begin{bmatrix} I^C \\ I^D \\ I^M \end{bmatrix} = \begin{bmatrix} V^C \\ V^D \\ V^M \end{bmatrix}, \quad (24)$$

where  $V^C$  is the exciting matrix of PEC bodies and  $V^D$  and  $V^M$  represent the exciting matrixes of dielectric bodies:

$$\begin{cases} V_m^C = \langle \mathbf{f}_m(\mathbf{r}), \mathbf{E}_{inc}(\mathbf{r}) \rangle, m = 1, \dots, N^C \\ V_m^D = \langle \mathbf{f}_m(\mathbf{r}), \mathbf{E}_{inc}(\mathbf{r}) \rangle, m = 1, \dots, N^D \\ V_m^M = \langle \mathbf{f}_m(\mathbf{r}), \mathbf{H}_{inc}(\mathbf{r}) \rangle, m = 1, \dots, N^D \end{cases}. \quad (25)$$

As for impedance matrix, it is calculated similar to that in PEC and dielectric targets. For the sake of simplicity, formulas of each element are not listed here but can be found in paper [18]:

$$\begin{cases} \mathbf{J}(\mathbf{r}') = \sum_{b=1}^{N_B} \sum_{m=1}^{M_b^J} j_m^b \mathbf{F}_m^b(\mathbf{r}') \\ \mathbf{M}(\mathbf{r}') = \sum_{b=1}^{N_B} \sum_{m=1}^{M_b^M} m_m^b \mathbf{F}_m^b(\mathbf{r}') \end{cases}. \quad (26)$$

In MoM, electric and magnetic currents are discretized by RWG functions, as is shown in Equation (18), while in SBFM, currents are discretized by synthetic basis functions, as is shown in Equation (26).

Then, all the matrix Equations (19), (21) and (24) can be transformed into synthetic matrix equations in the following method:

$$\begin{cases} [Z_{SBF}][j] = [V_{SBF}] \\ [Z_{SBF}]_{b_1 b_2} = [\mathbf{F}^{b_1}]^T [Z]_{b_1 b_2} \mathbf{F}^{b_2}, \\ [V_{SBF}]_{b_1} = [\mathbf{F}^{b_1}]^T [V]_{b_1} \end{cases}, \quad (27)$$

where  $[Z]_{b_1 b_2}$  is the impedance matrix of block  $b_1$  and  $b_2$  calculated by RWG functions. Since Equation (27)

tackles the target block by block, the scale of equation is much smaller than that in traditional MoM.

Solving Equation (27), currents coefficients matrix corresponding to synthetic basis functions  $[j]$  will be available. Then, according to Equation (26), the original currents coefficients matrix corresponding to RWG functions  $[I]$  can be transformed from  $[j]$  and synthetic basis functions' coefficients matrix  $[P]$ :

$$I_k^b = \sum_{m=1}^{M_b} P_{k,m}^b j_m^b, \quad b = 1, 2, \dots, N_B. \quad (28)$$

Having got the coefficients of initial RWG functions, it is easy to do some further processing (radiating field, scattering properties, etc.).

Overall, Equation (28) shows that the key of SBFM is determining the number of synthetic basis functions  $M_b$  and their coefficients matrix  $[P]$ . This will be discussed in Section IV.

#### IV. GENERATION OF SYNTHETIC BASIS FUNCTIONS

Paper [19] claims that DOF of a certain scatterer's scattering field is restricted to  $[D_\infty, D_1]$ , where  $D_1$  donates the total number of RWG functions defined on the surface of the scatterer. Thus, it is possible to approximate the scattering fields' solution space with fewer synthetic functions [14]. To find proper synthetic functions, there are two main steps: setting auxiliary sources and SVD.

Taking an isolated block into consideration, exciting voltage not only comes from the incident plane wave but also comes from mutual coupling effects of other blocks. Paper [14] points out mutual coupling effects can be imitated by a series of auxiliary sources based on equivalence theorem. Figure 2 demonstrates that a block is surrounded by an enclosed stereoscopic space, and a series of auxiliary sources (RWG functions) are defined on the surface of the space. By evaluating the block's responses to these auxiliary sources, solution space will be available. Synthetic basis functions' coefficients are these independent columns of the solution space. To extract independent elements, SVD will be adopted.

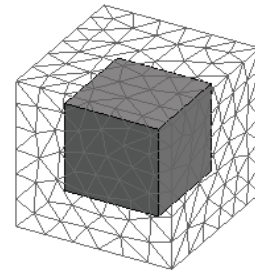


Fig. 2. An isolated block is surrounded by auxiliary sources.

- PEC Targets

Paper [9] shows the method of determining PEC's solution space. Referring to this method, re-write it as:

$$\begin{cases} [I^1] = [Z^1]^{-1} (V^1 - V^{1e}) \\ V^{1e} = \langle \mathbf{f}_m(\mathbf{r}), Z_0 L(\mathbf{f}_\alpha(\mathbf{s})) \rangle \end{cases}, \quad (29)$$

where  $V^{1e}$  represents exciting voltage caused by mutual coupling effects.

It should be noticed that Equation (29) is slightly different with that in paper [9], but corresponds to Equation (12).

Similarly, for dielectric and composite structures, solution space can also be obtained through PMCHW formulation. However, in comparison to PEC bodies, both auxiliary electric and magnetic sources are needed for dielectric bodies.

- Dielectric Targets

$$\begin{bmatrix} Z^{EJ} & Z^{EM} \\ Z^{HJ} & Z^{HM} \end{bmatrix}^{-1} \begin{bmatrix} I^J \\ I^M \end{bmatrix} = \begin{bmatrix} V^E - V^{E1e} \\ V^H - V^{H1e} \end{bmatrix}, \quad (30)$$

where  $V^{E1e}$  and  $V^{H1e}$  represent exciting voltage caused by auxiliary electric and magnetic sources:

$$\begin{cases} V^{E1e} = \begin{bmatrix} \langle \mathbf{f}_m(\mathbf{r}), [Z^{(i)} L^{(i)}(\mathbf{f}_\alpha(\mathbf{s})) + Z^{(j)} L^{(j)}(\mathbf{f}_\alpha(\mathbf{s}))] \rangle \\ \langle \mathbf{f}_m(\mathbf{r}), -[K^{(i)}(\mathbf{f}_\alpha(\mathbf{s})) + K^{(j)}(\mathbf{f}_\alpha(\mathbf{s}))] \rangle \end{bmatrix} \\ V^{H1e} = \begin{bmatrix} \langle \mathbf{f}_m(\mathbf{r}), [K^{(i)}(\mathbf{f}_\alpha(\mathbf{s})) + K^{(j)}(\mathbf{f}_\alpha(\mathbf{s}))] \rangle + \\ \langle \mathbf{f}_m(\mathbf{r}), [Y^{(i)} L^{(i)}(\mathbf{f}_\alpha(\mathbf{s})) + Y^{(j)} L^{(j)}(\mathbf{f}_\alpha(\mathbf{s}))] \rangle \end{bmatrix} \end{cases}. \quad (31)$$

- Composite Metallic and Dielectric Targets

$$\begin{bmatrix} Z^{CC} & Z^{CD} & Z^{CM} \\ Z^{DC} & Z^{DD} & Z^{DM} \\ Z^{MC} & Z^{MD} & Z^{MM} \end{bmatrix}^{-1} \begin{bmatrix} I^C \\ I^D \\ I^M \end{bmatrix} = \begin{bmatrix} V^C - V^{C1e} \\ V^D - V^{D1e} \\ V^M - V^{M1e} \end{bmatrix}, \quad (32)$$

where  $V^{C1e}$  is exciting voltage caused by auxiliary electric sources around PEC bodies,  $V^{D1e}$  and  $V^{M1e}$  represent exciting voltage caused by auxiliary electric and magnetic sources around dielectric bodies:

$$\begin{cases} V^{C1e} = [Z^{CC}]^{1e} + [Z^{CD}]^{1e} + [Z^{CM}]^{1e} \\ V^{D1e} = [Z^{DC}]^{1e} + [Z^{DD}]^{1e} + [Z^{DM}]^{1e} \\ V^{M1e} = [Z^{MC}]^{1e} + [Z^{MD}]^{1e} + [Z^{MM}]^{1e} \end{cases}. \quad (33)$$

Once the solution space is got, coefficients of synthetic basis functions defined in Equation (4) will be obtained by SVD. Denote the solution space as  $R$ , then:

$$R = U \rho V^H, \rho = \text{diag}(\rho_1, \rho_2, \dots, \rho_N), \quad (34)$$

where  $\rho_i (i=1,2,\dots,N)$  represent singular values of  $R$  and  $\rho_1 > \rho_2 > \dots > \rho_N$ .

Coefficients  $[P]$  of synthetic basis functions are elements of column vectors of  $U$ . Set truncation error as  $\rho_{\text{SBF}}$  and take the top  $M_1$  columns of  $U$  as effective independent coefficients, where  $\rho_{M_1}/\rho_1 < \rho_{\text{SBF}}$ . Thus, the number of synthetic basis functions is  $M_1$  and their coefficients:

$$[P] = \{[U_1], [U_2], \dots, [U_{M_1}]\}. \quad (35)$$

For periodic structures, coefficient space of each block is exactly the same since all the blocks share the same geometrical features. Thus, computational efficiency will be greatly improved.

## V. NUMERICAL RESULTS AND VALIDATION

As a part of scattering analysis, bistatic RCS is calculated by SBFM in this section and three examples are given to validate the accuracy of SBFM. Besides, results of commercial software Feko and MoM are also given here for comparison. Before presenting the examples, it is noteworthy that all the arrays listed in examples are placed in the plane  $xoy$ , with the incident wave coming from  $+z$  and polarizing  $+x$ . Observing plane is set as  $xoz$  and  $yoz$ . What's more, to fully validate the accuracy of SBFM, frequency of incident wave and truncation error are set differently.

Example 1 shows a  $5 \times 5$  array composed of PEC paraboloids, as is shown in Fig. 3. Row and column gap between elements are  $2\lambda$  and focal distance and radius of the paraboloid are both set as  $0.5\lambda$ . Frequency of incident wave is 3 GHz. Surface of the target is discretized into 5875 triangles and 8375 edges by setting the maximum size of meshing as  $0.1\lambda$ . In SBFM, 525 synthetic basis functions are used to analyze the target with truncation error  $\rho_{\text{SBF}}=0.1$ . Results of the example are shown in Fig. 4 and Table 1.

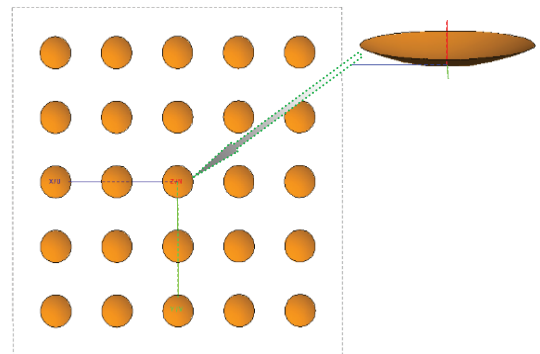


Fig. 3.  $5 \times 5$  PEC array of paraboloids.

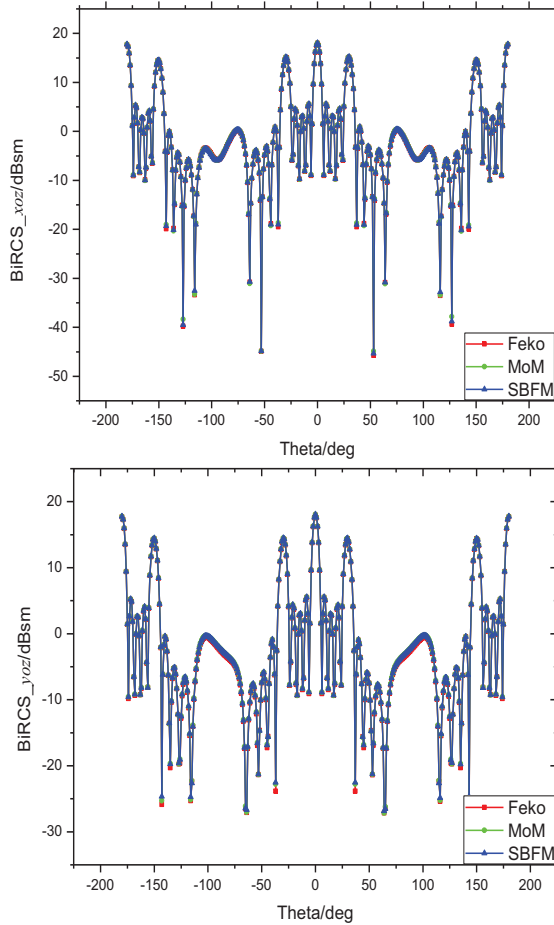


Fig. 4. Bi-RCS of 5×5 PEC array.

Table 1: Properties of MoM and SBFM in example 1

	Number of Unknowns	RAM Cost of Impedance Matrix	Time of Solving Matrix Equation	Total Elapsed Time
SBFM	525	7.69 MB	0.06s	168.53s
MoM	8375	1.79 GB	260.22s	431.86s

Example 2 is a 3×3 array consisting of 9 dielectric rectangular grooves with relative permittivity  $\epsilon_r=3.6$ , as is shown in Fig. 5. Size of the outer rectangle is  $0.4\lambda \times 0.4\lambda \times 0.3\lambda$  while size of the inner slot is  $0.25\lambda \times 0.25\lambda \times 0.2\lambda$ . Row and column gap are set as  $0.9\lambda$ . Frequency of incident wave is 1 GHz. There are 3582 triangles and 5373 edges defined on the surface. Since both electric and magnetic currents are there on the surface, 10746 RWG functions in total are needed in MoM. By setting truncation error  $\rho_{SBFM}=0.2$ , only 9 synthetic basis function for each block and 81 for total are used in SBFM. Results of this example will be displayed in Fig. 6 and Table 2.

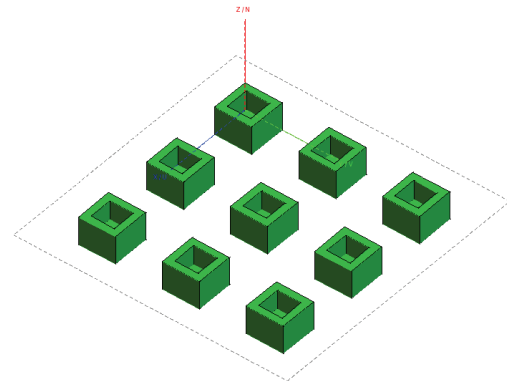


Fig. 5. 3×3 dielectric array of grooves.

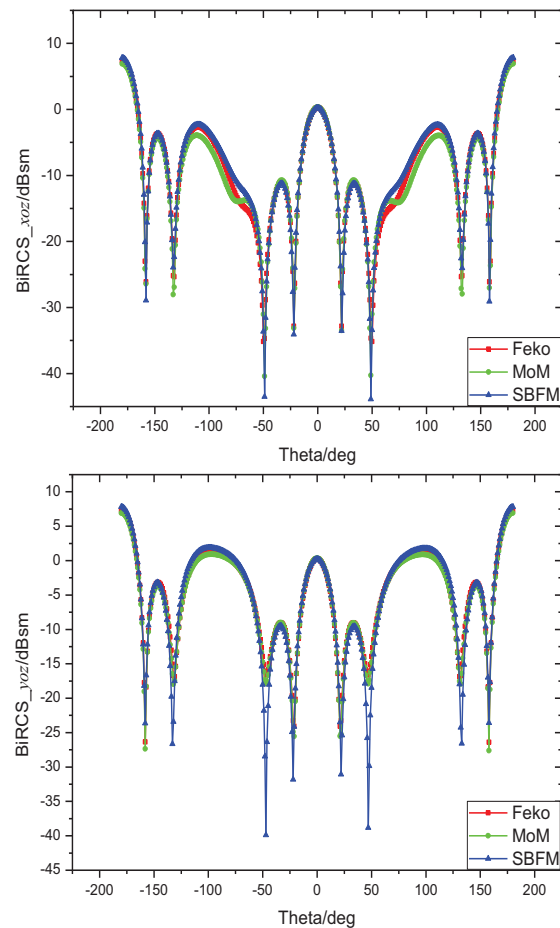


Fig. 6. Bi-RCS of 3×3 dielectric array.

Table 2: Properties of MoM and SBFM in example 2

	Number of Unknowns	RAM Cost of Impedance Matrix	Time of Solving Matrix Equation	Total Elapsed Time
SBFM	81	0.19 MB	0.001 s	571.99s
MoM	10746	3.19 GB	596.61 s	1240.96s

Example 3 is a  $3 \times 3$  composite array of monopole antennas. 9 blocks are included in the array with its row and column gap being  $0.9\lambda$ , as is shown in Fig. 7. For each block, a PEC monopole ( $0.5\lambda$  in length) is placed on a dielectric rectangular base ( $0.4\lambda \times 0.4\lambda \times 0.3\lambda$ ). Relative permittivity of the base is 2.6 and incident plane wave's frequency is 1 GHz. Since both PEC and dielectric structures are there in the system, the process of meshing needs to be carried on independently. For PEC structures, the surface is discretized into 720 triangles and 1080 edges while for dielectric structures, 2574 triangles and 3861 edges are obtained. Thus, 8802 RWG functions are needed totally in MoM. When it comes to SBFM, three kinds of auxiliary sources need to be set independently in this system: electric sources around PEC structures, electric and magnetic sources around dielectric structures. By solving the solution space and SVD, 44 synthetic basis functions are adopted for each block, where truncation error  $\rho_{\text{SBFM}}=0.15$ . Results of this example are demonstrated in Fig. 8 and Table 3.

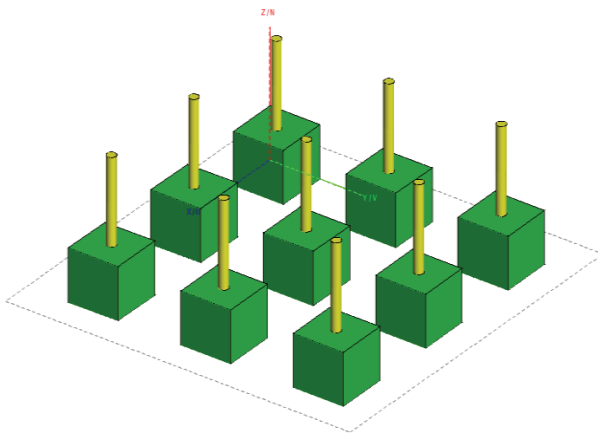


Fig. 7.  $3 \times 3$  composite array of monopole antennas.

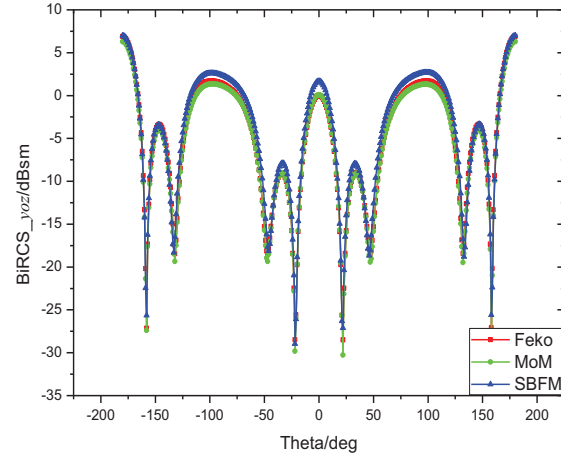
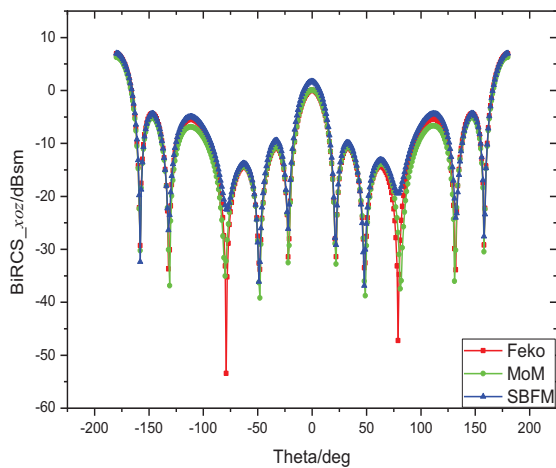


Fig. 8. Bi-RCS of  $3 \times 3$  composite array.

Table 3: Properties of MoM and SBFM in example 3

	Number of Unknowns	RAM Cost of Impedance Matrix	Time of Solving Matrix Equation	Total Elapsed Time
SBFM	396	4.41 MB	0.03 s	398.63s
MoM	8802	2.14 GB	308.63 s	575.68s

Among these Bi-RCS pictures,  $\theta=0^\circ$  and  $\theta=180^\circ$  represent backward and forward scattering respectively. These examples exhibit that results of SBFM yield well to that of Feko and MoM except for slight differences in lateral scattering. Table 1-3 give computational properties of MoM and SBFM. In MoM, the number of unknowns is depend on the triangulation carried on the surface of the target, while in SBFM, it depends on the value of truncation error and auxiliary sources. Generally, higher truncation error means less synthetic basis functions and thus less memory cost. As for computing time, elapsed time of filling impedance matrix and solving matrix equation are the two main parts in MoM while in SBFM, except for the two parts listed above, elapsed time of SVD is the third part. Since the scale of matrix equation in SBFM is much smaller than that in MoM, the solving process will be much faster.

Obviously, SBFM has great advantages over MoM in memory cost as well as computing time especially for periodic targets. More importantly, it is noteworthy that the scale of periodic array which SBFM can address is not restricted to what listed in the paper. To get the results of MoM for comparison, examples in the paper are relatively small scale problems since computational complexity and memory cost of larger scale problems are unbearable for a personal computer. Thus, compared to traditional MoM, SBFM makes it

possible to analyze large scale problems in personal computer.

## VI. CONCLUSION

SBFM is used in this paper to analyze scattering properties of periodic structures based on EFIE-PMCHW formulation. Three kinds of applications are introduced here: PEC, dielectric and composite metallic and dielectric structures. Results verify the accuracy and efficiency of the algorithm. Compared to traditional MoM, SBFM not only reduces quantities of unknowns and memory but also enables us to make a balance between accuracy and efficiency through truncation error. Besides, SBFM can also be combined with other fast approaches such as MLFMA and adaptive integral method (AIM) to further improve its properties. Thus, SBFM makes it possible to analyze large scale targets on a personal computer.

## REFERENCES

- [1] S. M. Rao, D. R. Wilton, and A. W. Glisson, "Electromagnetic scattering by surfaces of arbitrary shape," *IEEE Trans. Antennas Propag.*, vol. AP-30, no. 3, pp. 409-418, May 1982.
- [2] R. Coifman, V. Rokhlin, and S. Wandzura, "The fast multipole method for the wave equation: a pedestrian prescription," *IEEE Antennas Propag. Mag.*, vol. 35, no. 3, pp. 7-12, Jun. 1993.
- [3] N. Engheta, W. D. Murphy, V. Rokhlin, and M. S. Vassilion, "The fast multipole method (FMM) for electromagnetic scattering problems," *IEEE Trans. Antennas Propag.*, vol. 40, no. 6, pp. 634-644, Jun. 1992.
- [4] J. M. Song and W. C. Chew, "Multilevel fast multipole algorithm for solving combined field integral equations of electromagnetic scattering," *Microwave Opt. Tech. Lett.*, vol. 10, no. 1, pp. 14-19, Sep. 1995.
- [5] J. M. Song, C. C. Lu, and W. C. Chew, "MLFMA for electromagnetic scattering from large complex objects," *IEEE Trans. Antennas Propag.*, vol. 45, pp. 1488-1493, Oct. 1997.
- [6] V. V. S. Prakash and R. Mittra, "Characteristic basis function method: a new technique for efficient solution of method of moments matrix equations," *Microwave Opt. Technol. Lett.*, vol. 36, pp. 95-100, Jan. 2003.
- [7] L. Matekovits, G. Vecchi, G. Dassano, and M. Orefice, "Synthetic function analysis of large printed structures: the solution space sampling approach," in *Proc. IEEE AP-S Int. Symp.*, Boston, MA, pp. 568-571, Jul. 2001.
- [8] P. Focardi, A. Freni, S. Maci, and G. Vecchi, "Efficient analysis of arrays of rectangular corrugated horns: the synthetic aperture function approach," *IEEE Trans. Antennas Propag.*, vol. AP-53, no. 2, pp. 601-607, Feb. 2005.
- [9] L. Matekovits, V. A. Laza, and G. Vecchi, "Analysis of large complex structures with the synthetic-functions approach," *IEEE Trans. Antennas Propag.*, vol. 55, pp. 2509-2521, Sep. 2007.
- [10] L. Matekovits, G. Vecchi, M. Bercigli, and M. Bandinelli, "Synthetic-functions analysis of large aperture-coupled antennas," *IEEE Trans. Antennas Propag.*, vol. 57, no. 7, pp. 1936-1943, Jul. 2009.
- [11] W. C. Chen, G. B. Xiao, S. Xiang, and J. F. Mao, "A note on the construction of synthetic basis functions for antenna arrays," *IEEE Trans. Antennas Propag.*, vol. 60, no. 7, pp. 3509-3512, Jul. 2012.
- [12] S. Xiang, G. B. Xiao, X. Z. Tian, and J. F. Mao, "Analysis of large-scale phased antenna array with generalized transition matrix," *IEEE Trans. Antennas Propag.*, vol. 61, no. 11, pp. 5453-5464, Sep. 2013.
- [13] G. B. Xiao, J. F. Mao, and B. Yuan, "A generalized surface integral equation formulation for analysis of complex electromagnetic systems," *IEEE Trans. Antennas Propag.*, vol. 57, no. 3, pp. 701-710, Mar. 2009.
- [14] B. Zhang, G. B. Xiao, J. F. Mao, and Y. Wang, "Analyzing large-scale non-periodic arrays with synthetic basis functions," *IEEE Trans. Antennas Propag.*, vol. 58, no. 11, pp. 3576-3584, Nov. 2010.
- [15] Y. L. Xu, X. J. Tang, G. Gao, Z. L. Guo, and H. Yang, "The characteristical analysis of the synthetic basis function method," *3<sup>rd</sup> Asia-Pacific Conference on Antennas and Propag.*, pp. 995-997, 2014.
- [16] D. H. Schaubert, D. R. Wilton, and A. W. Glisson, "A tetrahedral modeling method for electromagnetic scattering by arbitrarily shaped inhomogeneous dielectric bodies," *IEEE Trans. Antennas Propag.*, vol. AP-32, pp. 77-85, Jan. 1984.
- [17] R. F. Harrington, *Field Computation by Moment Method* [M], New York: Macmillan, 1968.
- [18] J. Dong, S. L. Chai, and J. J. Mao, "On the modeling of arbitrary composite metallic and dielectric structures based on surface integral equation," *3<sup>rd</sup> International Conference on Computational Electromagnetics and Its Applications*, pp. 256-259, 2004.
- [19] O. M. Bucci and G. Franceschetti, "On the degrees of freedom of scattered fields," *IEEE Trans. Antennas Propag.*, vol. AP-37, no. 7, pp. 918-926, Jul. 1989.



**Xu Yanlin** was born in Anhui, China, in 1990. He received the B.S. degree in Electronic Engineering from National University of Defense Technology, Changsha, China, in 2013, and is currently pursuing the M.S. degree in Electronic Science and Technology at National University of Defense Technology, Changsha, China.

His research interests include computational electromagnetic and its applications in scattering analysis.



**Yu Weikang** was born in Anhui, China, in 1994. He received the B.S. degree in Electronic Engineering from National University of Defense Technology, Changsha, China, in 2013, and is prepared to pursue the M.S. degree in Electronic Science and Technology at National

University of Defense Technology, Changsha, China. His research interests include computational electromagnetic and microstrip antennas.



**Yang Hu** was born in Anhui, China, in 1973. He received the Ph.D. degree in Electronic Science and Technology at National University of Defense Technology, Changsha, China, in 2007, and is currently a Professor of National University of Defense Technology.

Yang has been researching on time domain algorithm and its applications, waveguide slot array antenna, UWB antenna, microstrip antenna etc.

# An Efficient FDTD Algorithm to Analyze Skewed Periodic Structures Impinged by Obliquely Incident Wave

M. Bai, B. Liang, and H. Ma

School of Electronic and Information Engineering  
Beihang University, Beijing, 100191, China  
mbai@buaa.edu.cn, girder21@ee.buaa.edu.cn, yoyo@ee.buaa.edu.cn

**Abstract** — An efficient wideband finite-difference time-domain (FDTD) method is proposed to analyze arbitrarily skewed periodic structures at oblique incidence. The method is free of complex step-by-step phase processing caused by the oblique incident plane wave and the stagger unit cells, and the provided periodic boundary condition (PBC) is as simple to implement as in the normal incidence case. A numerical example is simulated respectively by our method in one-time calculation over a wideband and the previous dual plane wave method requiring multiple repeated runs, which verifies the validity and efficiency of the proposed method.

**Index Terms** — Finite difference time domain (FDTD), oblique incidence, periodic structures, skewed grids, wideband.

## I. INTRODUCTION

In the field of electromagnetism, periodic structures have been drawing great attentions for tens of years, in a wide range of applications in frequency selective surfaces (FSS) [1-3], electromagnetic band gap (EBG) devices [4] and phased antenna arrays [5], etc. To analyze periodic structures, finite-difference time-domain (FDTD) algorithm [6] has been extensively utilized, and in general only one unit cell needs to be modeled and simulated according to the Floquet theory [5]. A lot of work has been done on FDTD algorithm by incorporating periodic boundary conditions (PBC) to deal with periodic structures, at both normal and oblique incidence [7-11]. When the object is illuminated by a normally incident plane wave, the electromagnetic fields on the boundary of one side of the rectangular unit cell are identical to those on the other side, so that a wideband response can be conveniently obtained by stimulating a transient pulse [8]. However, for the oblique incidence case, the time delay in the time domain caused by the phase shift between corresponding boundaries in the frequency domain leads to difficulties in using the PBCs. By proposing the dual plane wave method, [7] tackled the obstacle at oblique incidence,

but only a single frequency is fixed in each calculation. Afterwards, the split-FDTD method [6,8], some implicit-FDTD methods [9-11] and the material independent FDTD method [12] were proposed respectively, successfully realizing the ability of wideband calculation at oblique incidence.

It is worthwhile pointing out that the aforementioned implementations of the PBCs are developed to deal with regular rectangular periodic structures, as shown in Fig. 1 (a). Nonetheless, a number of applications with arbitrarily skewed adjacent rows in periodic structures as shown in Fig. 1 (b) are frequently encountered. For example, in order to obtain superior bandwidth and stability to different incident angles and polarizations, the FSS needs to be designed with a specific skewed angle [1]. Therefore, the analysis of skewed periodic structures is necessary and important. In terms of the FDTD method treating skewed periodic structures, the dual plane wave method to analyze the periodic phased array with skewed grids was adopted in [13], but each calculation is only fixed on one single frequency at the specific incident angle. Reference [14] presented another method to deal with the issue, employing the constant horizontal wavenumber approach. Although in each calculation the frequencies in a wideband are involved, the corresponding incident angle of each frequency is different from each other, because of the horizontal wavenumber being fixed. Therefore, it can be seen that for a specific incident angle, this method still fails to retain the wideband capacity of the FDTD.

In this paper, the field transformation [15] is employed in the FDTD algorithm, to analyze periodic structures with arbitrary skewed grids impinged by the obliquely incident plane wave at specific angles. We prove that the field transformation, which is the basic treatment to realize wideband FDTD analysis at oblique incidence in [8-12], is capable of dealing with the skewed periodic structures as well. The split-FDTD method is extended into the PBCs for skewed grids, and the updating equations are presented. The validity of the method is verified by a numerical example, which provides the results calculated by the dual plane wave

FDTD method as a comparison.

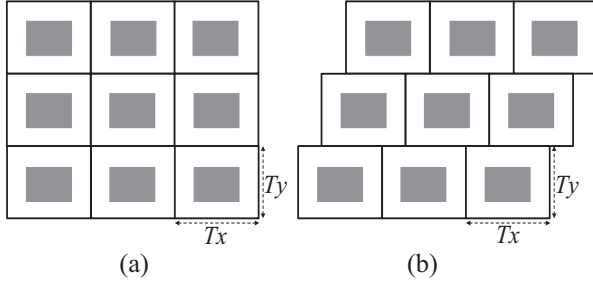


Fig. 1. Periodic structures with: (a) regular rectangular grids, and (b) arbitrarily skewed grids.

## II. IMPLEMENTATION OF THE PROPOSED METHOD

Here, three dimensional structures which are periodic in the  $x$ - and  $y$ -directions with skewed grids in the  $x$ -direction are considered. The oblique incident plane wave is launched along the angles  $\theta$  and  $\varphi$ . Hence, the PBC of any electromagnetic field component  $\Phi$  is expressed as:

$$\Phi(x+rT_x+s\Delta x, y+sT_y) = \Phi(x, y) \cdot e^{-j[k_x(rT_x+s\Delta x)+k_y sT_y]}, \quad (1)$$

where  $r$  and  $s$  are any integers,  $k_x$  and  $k_y$  are the components of wavenumber in the  $x$ - and  $y$ - directions respectively, which are calculated as:

$$\begin{aligned} k_x &= k \cdot \sin \theta \cdot \cos \varphi, \\ k_y &= k \cdot \sin \theta \cdot \sin \varphi, \end{aligned} \quad (2)$$

where  $k$  is the wavenumber of the excited plane wave in free space. It can be seen that the PBC along the  $y$ -direction is the same as that of the regular rectangular periodic structures, but it is more complex along the  $x$ -direction. In order to use the field transformation to remove the phase shift in the Maxwell's equations, a set of auxiliary variables is introduced as:

$$\begin{aligned} \mathbf{P}(x, y) &= \frac{\mathbf{E}(x, y)}{\eta_0} \cdot e^{j(k_x x + k_y y)}, \\ \mathbf{Q}(x, y) &= \mathbf{H}(x, y) \cdot e^{j(k_x x + k_y y)}, \end{aligned} \quad (3)$$

where  $\eta_0$  is the impedance of free space. By replacing  $\Phi$  in (1) with  $\mathbf{E}$  and  $\mathbf{H}$  respectively and substituting (3) into (1), we obtain:

$$\begin{aligned} \mathbf{P}(x+rT_x+s\Delta x, y+sT_y) &= \mathbf{P}(x, y), \\ \mathbf{Q}(x+rT_x+s\Delta x, y+sT_y) &= \mathbf{Q}(x, y). \end{aligned} \quad (4)$$

Obviously, it has been proved that the PBCs of the transformed fields  $\mathbf{P}$  and  $\mathbf{Q}$  possess the same forms as the case of normal incidence, without the phase shift. Therefore, it is confirmed that the previous work on wideband FDTD analysis to analyze regular rectangular periodic structures at oblique incidence can be extended to deal with skewed ones. In this paper, we choose to employ the split-FDTD method to develop the

implementation.

Considering a lossless anisotropic medium, by substituting (3) into Maxwell's equations, a set of transformed equations is obtained as:

$$j\omega \frac{\epsilon_{rx}}{c} P_x = \frac{\partial Q_z}{\partial y} - \frac{\partial Q_y}{\partial z} - j\omega \bar{k}_y Q_z + j\omega \bar{k}_z Q_y, \quad (5a)$$

$$j\omega \frac{\epsilon_{ry}}{c} P_y = \frac{\partial Q_x}{\partial z} - \frac{\partial Q_z}{\partial x} - j\omega \bar{k}_z Q_x + j\omega \bar{k}_x Q_z, \quad (5b)$$

$$j\omega \frac{\epsilon_{rz}}{c} P_z = \frac{\partial Q_y}{\partial x} - \frac{\partial Q_x}{\partial y} - j\omega \bar{k}_x Q_y + j\omega \bar{k}_y Q_x, \quad (5c)$$

$$j\omega \frac{\mu_{rx}}{c} Q_x = \frac{\partial P_y}{\partial z} - \frac{\partial P_z}{\partial y} - j\omega \bar{k}_z P_y + j\omega \bar{k}_y P_z, \quad (5d)$$

$$j\omega \frac{\mu_{ry}}{c} Q_y = \frac{\partial P_z}{\partial x} - \frac{\partial P_x}{\partial z} - j\omega \bar{k}_x P_z + j\omega \bar{k}_z P_x, \quad (5e)$$

$$j\omega \frac{\mu_{rz}}{c} Q_z = \frac{\partial P_x}{\partial y} - \frac{\partial P_y}{\partial x} - j\omega \bar{k}_y P_x + j\omega \bar{k}_x P_y, \quad (5f)$$

where

$$\bar{k}_x = \sin \theta \cdot \cos \varphi / c, \quad \bar{k}_y = \sin \theta \cdot \sin \varphi / c, \quad \bar{k}_z = 0, \quad (6)$$

and  $c$  is the speed of light. Although  $\bar{k}_z$  is zero, it is kept in (5) in order to maintain the symmetry and the cyclic feature of the equations. To conserve space, only (5c) is processed in detail to present the split method in the following. By defining a new variable  $P_{za}$ ,  $P_z$  is split into two parts as:

$$P_z = P_{za} + \frac{c}{\epsilon_{rz}} (\bar{k}_y Q_x - \bar{k}_x Q_y), \quad (7a)$$

where

$$j\omega \frac{\epsilon_{rz}}{c} P_{za} = \frac{\partial Q_y}{\partial x} - \frac{\partial Q_x}{\partial y}. \quad (7b)$$

Similarly, the split form of the other five components can be written conveniently. It can be seen that (7b) is exactly the ordinary formed FDTD formula, so that  $P_{za}$  can be obtained in the conventional iteration manner. With regard to the absorbing layers, the auxiliary differential equation (ADE) treatment [16] is utilized to implement the perfect matched layers (PML). By substituting  $Q_y$  and  $Q_x$  into (7a), and noting that  $\bar{k}_z = 0$ ,  $P_z$  can be obtained as:

$$P_z = \left(1 - \frac{c^2 \bar{k}_x^2}{\epsilon_{rz} \mu_{ry}} - \frac{c^2 \bar{k}_y^2}{\epsilon_{rz} \mu_{rx}}\right)^{-1} \left(P_{za} - \frac{c}{\epsilon_{rz}} \bar{k}_x Q_{ya} + \frac{c}{\epsilon_{rz}} \bar{k}_y Q_{xa}\right). \quad (8)$$

It should be noted that since the time step of  $P_z$  and  $P_{za}$  is  $n$ , that of  $Q_{ya}$  and  $Q_{xa}$  should be  $n$  as well, rather than  $n-1/2$ . Therefore, other than the leapfrog updates of the conventional FDTD, in each half-time-step, all the components need to be updated. Moreover, in order to retain the centered nature of the method, spatial averaging of  $Q_{ya}$  and  $Q_{xa}$  is also needed. Therefore, the discretization of (8) is written as:

$$P_z \Big|_{i,j,k}^n = \left[ 1 - \frac{c^2 \bar{k}_x^2}{\varepsilon_{rz} \mu_{ry}} - \frac{c^2 \bar{k}_y^2}{\varepsilon_{rz} \mu_{rx}} \right]^{-1} \cdot \left\{ P_{za} \Big|_{i,j,k}^n - \frac{c}{2\varepsilon_{rz}} \bar{k}_x (Q_{ya} \Big|_{i,j,k}^n + Q_{ya} \Big|_{i-1,j,k}^n) + \frac{c}{2\varepsilon_{rz}} \bar{k}_y (Q_{xa} \Big|_{i,j,k}^n + Q_{xa} \Big|_{i,j-1,k}^n) \right\}. \quad (9)$$

Similarly,  $Q_z$  is updated by:

$$Q_z \Big|_{i,j,k}^n = \left[ 1 - \frac{c^2 \bar{k}_x^2}{\mu_{rz} \varepsilon_{ry}} - \frac{c^2 \bar{k}_y^2}{\mu_{rz} \varepsilon_{rx}} \right]^{-1} \cdot \left\{ Q_{za} \Big|_{i,j,k}^n - \frac{c}{2\varepsilon_{rz}} \bar{k}_y (P_{xa} \Big|_{i,j,k}^n + P_{xa} \Big|_{i+1,j,k}^n) + \frac{c}{2\varepsilon_{rz}} \bar{k}_x (P_{ya} \Big|_{i,j,k}^n + P_{ya} \Big|_{i+1,j,k}^n) \right\}. \quad (10)$$

By substituting (9) and (10) into the counterpart formulas of (7a) respectively, the other four components can be updated as:

$$P_x \Big|_{i,j,k}^n = P_{xa} \Big|_{i,j,k}^n - \frac{c}{2\varepsilon_{rx}} \bar{k}_y (Q_z \Big|_{i,j,k}^n + Q_z \Big|_{i-1,j,k}^n), \quad (11a)$$

$$P_y \Big|_{i,j,k}^n = P_{ya} \Big|_{i,j,k}^n + \frac{c}{2\varepsilon_{ry}} \bar{k}_x (Q_z \Big|_{i,j,k}^n + Q_z \Big|_{i-1,j,k}^n), \quad (11b)$$

$$Q_x \Big|_{i,j,k}^n = Q_{xa} \Big|_{i,j,k}^n + \frac{c}{2\mu_{rx}} \bar{k}_y (P_z \Big|_{i,j,k}^n + P_z \Big|_{i+1,j,k}^n), \quad (11c)$$

$$Q_y \Big|_{i,j,k}^n = Q_{ya} \Big|_{i,j,k}^n - \frac{c}{2\mu_{ry}} \bar{k}_x (P_z \Big|_{i,j,k}^n + P_z \Big|_{i+1,j,k}^n). \quad (11d)$$

Hence, the updating equations have been fully presented. The stability condition of the split method for a square cell and  $\bar{k}_x = \bar{k}_y$  is [6]:

$$c\Delta t / \Delta s \leq \cos^2 \theta / \sqrt{2 + \cos^2 \theta}. \quad (12)$$

In terms of other cases, the rigorous stability condition is quite complicated [6], but the maximum allowed values along with  $\theta$  are not significantly discrepant from (12). Therefore, it can be seen that when the incident angle is close to grazing ( $\theta=90^\circ$ ), implicit methods such as those of [10] and [11] are more practical to be extended to the case of skewed grids.

When updating the aforementioned FDTD formulas, extra care of  $y$ -direction boundaries needs to be taken, compared with regular rectangular periodic structures. The schematic diagram of the FDTD grid arrangement for arbitrarily skewed periodic structures is shown in Fig. 2. Each unit cell ( $T_x \times T_y$ ) is meshed using  $N_x \times N_y$  grid cells ( $dx \times dy$ ), and  $N_x=5$ ,  $N_y=4$  are set here as an example.  $lx$  and  $\alpha$  are the skewed shift and angle respectively, of which the calculation relationship is:

$$lx = T_y / \tan \alpha. \quad (13)$$

The unit cell  $A$  in the center is the simulating object, while others surrounded by red lines are its neighboring unit cells. For any field  $\Psi$  on the boundaries in the  $x$ -direction, the PBC is the same as the conventional one which can be written as:

$$\begin{aligned} \Psi(i-1, j) &= \Psi(Nx, j) \quad \text{while } i=1, \\ \Psi(i+1, j) &= \Psi(1, j) \quad \text{while } i=Nx. \end{aligned} \quad (14)$$

For  $\Psi$  on the  $y$ -directional boundaries, two cases need to be discussed respectively:

1) *On the top boundary when  $\Psi(i, j+1)$  are needed:*

From (4) we can obtain:

$$\Psi(x, y) = \Psi(x + Tx - lx, y - T_y), \quad (15)$$

and its discretized form when  $j=Ny$  can be written as:

$$\Psi(i, j+1) = \Psi(i + Tx - lx, 1). \quad (16)$$

In Fig. 2, the fields  $\Psi(i, Ny+1)$  of the unit cell  $A$  are denoted by solid green triangles on the top boundary, while the fields  $\Psi(i+Tx-lx, 1)$  lying on the corresponding positions on the bottom boundary of  $A$  are indicated by the same marks. Since generally the skewed shift is not multiple integer of  $dx$ , the hollow green triangles are needed for interpolations. It should be noted that once the index of the hollow mark is larger than  $Nx$ , the cyclic shift is necessary to be utilized. Therefore, (16) can be rewritten as:

$$\begin{aligned} \Psi(i, Ny+1) &= \omega_2 \cdot \Psi(i + i_1, 1) + \omega_1 \cdot \Psi(i + i_2, 1) \\ i_1 &= \begin{cases} \left\lceil \frac{Tx - lx}{dx} \right\rceil & (\text{if } \left\lceil \frac{Tx - lx}{dx} \right\rceil \leq Nx) \\ \left\lceil \frac{Tx - lx}{dx} \right\rceil - Nx & (\text{if } \left\lceil \frac{Tx - lx}{dx} \right\rceil > Nx) \end{cases} \\ i_2 &= \begin{cases} i_1 + 1 & (\text{if } i_1 + 1 \leq Nx) \\ i_1 + 1 - Nx & (\text{if } i_1 + 1 > Nx) \end{cases} \\ \omega_1 &= \frac{Tx - lx}{dx} - \left\lceil \frac{Tx - lx}{dx} \right\rceil \\ \omega_2 &= 1 - \omega_1, \end{aligned} \quad (17)$$

where  $\lceil \cdot \rceil$  is the truncating function,  $\omega_1$  and  $\omega_2$  are the normalized distance between the solid mark and the hollow marks on its left and right hands respectively.

2) *On the bottom boundary when  $\Psi(i, j-1)$  are needed:* Similar to (16), the boundary condition for  $\Psi(i, j-1)$  when  $j=1$  is:

$$\Psi(i, j-1) = \Psi(i + lx, Ny). \quad (18)$$

Thus the fields  $\Psi(i, 0)$  of the unit cell  $A$  are denoted by solid blue circles on the bottom boundary in Fig. 2. Similar to (17), the PBC of  $\Psi(i, j-1)$  while  $j=1$  can be written as:

$$\Psi(i, 0) = \omega_2 \cdot \Psi(i + i_1, Ny) + \omega_1 \cdot \Psi(i + i_2, Ny)$$

$$i_1 = \begin{cases} \left\lceil \frac{lx}{dx} \right\rceil & (\text{if } \left\lceil \frac{lx}{dx} \right\rceil \leq Nx) \\ \left\lceil \frac{lx}{dx} \right\rceil - Nx & (\text{if } \left\lceil \frac{lx}{dx} \right\rceil > Nx) \end{cases}$$

$$i_2 = \begin{cases} i_1 + 1 & (\text{if } i_1 + 1 \leq Nx) \\ i_1 + 1 - Nx & (\text{if } i_1 + 1 > Nx) \end{cases}$$

$$\omega_1 = \frac{lx}{dx} - \left\lceil \frac{lx}{dx} \right\rceil$$

$$\omega_2 = 1 - \omega_1. \quad (19)$$

Therefore, by utilizing (14), (17) and (19), the fields on the boundaries for updating the FDTD formulas can be resolved. In the particular case when  $lx$  and  $T_x - lx$  are the integer multiples of  $dx$ , (17) and (19) are capable as well, with  $\omega_1=0$  and  $\omega_2=1$  respectively. It is worthwhile pointing out that the fields locating on the positions  $(i \pm 1/2, j \pm 1/2)$  are not necessary to be arranged specifically or marked in Fig. 2, since the criterion of their positions in the interpolation process is thoroughly dependent on the grid cell positions, i.e.,  $(i, j)$ .

It can be seen that the implementation of the proposed method to deal with general skewed periodic structures at oblique incidence is as simple and straightforward as the normal incident case. Owing to the confirmation of (4), the method is free of careful studies on the phase shift in individual boundary parts, which has to be taken in the dual plane wave method [13] and constant horizontal wavenumber method [14].

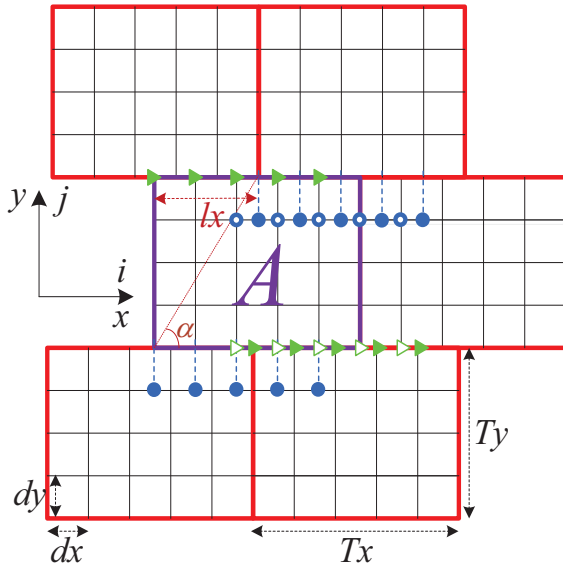


Fig. 2. Schematic diagram of the arbitrarily skewed FDTD grids.

### III. NUMERICAL RESULTS

To demonstrate the performance of our method, an example of a Jerusalem Cross FSS (JCFSS) between two anisotropic lossless media ( $\epsilon_{rx}=2.2$ ,  $\epsilon_{ry}=1.1$ ,  $\epsilon_{rz}=1.5$ ) is implemented, as shown in Fig. 3. The unit cell period is  $T_x=T_y=6$  mm, the thickness of the JCFSS is 0.625 mm, and the thickness of the substrate is 2 mm. The skewed angle is  $\alpha=60^\circ$ . The incident plane wave is propagating along the direction  $\theta=30^\circ$  and  $\varphi=50^\circ$ , and both the TM and TE cases are investigated. The structure is firstly simulated by our wideband method, using a sine modulated Gaussian pulse centered at 15 GHz and with 20 GHz bandwidth as the excitation. The grid cell size is  $\Delta x=\Delta y=\Delta z=0.125$  mm, and the time step is  $\Delta t=\Delta z/(5 \cdot c)$ . As a comparison, the example is also simulated by the dual plane wave method, which is repeated 41 times in the frequency range from 5 to 25 GHz by 0.5 GHz frequency step.

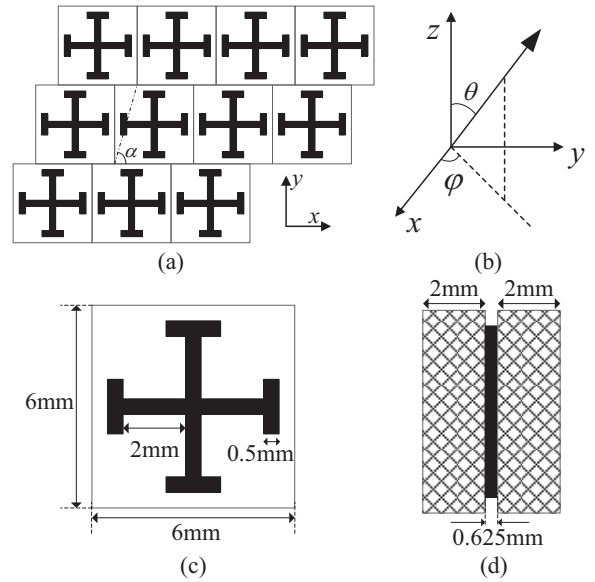


Fig. 3. Schematic diagram of the JCFSS: (a) top view of the skewed periodic JCFSS, (b) direction of the incident plane wave, (c) top view of one unit cell, and (d) side view of one unit cell.

The reflection coefficients of co- and cross-polarizations for both TM and TE cases are presented in Fig. 4. It can be noticed that good agreement between the results of dual plane wave method and results of our wideband method is obtained. However, it can be observed that some sharp peaks of the coefficients might be missed when using the method calculating on individual frequencies, while the wideband method possesses the capacity and advantage to present the details of the frequency response.

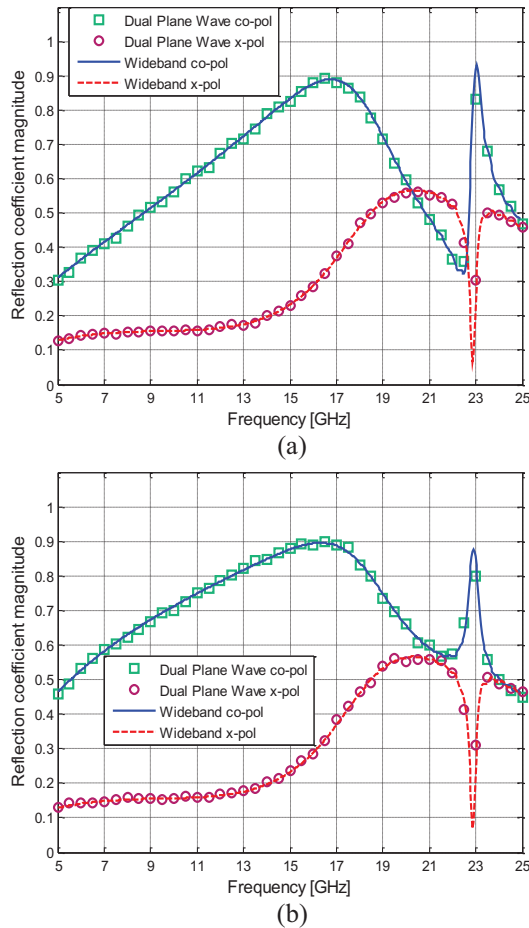


Fig. 4. Reflection coefficient co-polarization and cross polarization for JCFSS oblique incident plane wave ( $\theta=30^\circ$ ,  $\varphi=50^\circ$ ) with skewed angle  $\alpha=60^\circ$ : (a) TM case and (b) TE case.

#### IV. CONCLUSION

In conclusion, an efficient FDTD approach for the wideband analysis of arbitrarily skewed periodic structures at oblique incidence is introduced. By proving the field transformation technique to be valid in the skewed PBCs, the split-FDTD is extended to analyze periodic structures with skewed grids. The implementation avoids deliberate calculation of the phase shifts caused by the oblique incidence and the stagger of unit cells. Instead, it presents the PBC as simple as that in the normal incidence. And most significantly, our method realizes the wideband capability to analyze skewed periodic structures at oblique incidence, while the previous related FDTD work require multiple runs in terms of different frequencies. The validity and effectiveness of the method is verified by a numerical example, comparing with the results calculated by the dual plane wave method.

#### ACKNOWLEDGMENT

This work was supported by National Basic Research Program of China (973 Program) under Grant 2012CB315601.

#### REFERENCES

- [1] B. A. Munk, *Frequency Selective Surfaces: Theory and Design*, Wiley, 2000.
- [2] T. Wu, *Frequency Selective Surface and Grid Array*, Wiley, 1995.
- [3] R. Mittra, C. H. Chan, and T. Cwik, "Techniques for analyzing frequency selective surfaces - a review," *Proceedings of the IEEE*, vol. 76, no. 12, pp. 1593-1615, 1988.
- [4] Y. Rahmat-Samii and H. Mosallaei, "Electromagnetic band-gap structures: classification, characterization, and applications," in *Editor (Ed.) (Eds.): Book "Electromagnetic band-gap structures: classification, characterization, and applications," IET*, edn., pp. 560-564, 2001.
- [5] N. Amitay, V. Galindo, and C. P. Wu, *Theory and Analysis of Phased Array Antennas*, Wiley, 1972.
- [6] A. Taflov and S. C. Hagness, *Computational Electrodynamics*, Artech House, 2000.
- [7] P. Harms, R. Mittra, and W. Ko, "Implementation of the periodic boundary condition in the finite-difference time-domain algorithm for FSS structures," *Antennas and Propagation, IEEE Transactions on*, vol. 42, no. 9, pp. 1317-1324, 1994.
- [8] J. A. Roden, S. D. Gedney, M. P. Kesler, J. G. Maloney, and P. H. Harms, "Time-domain analysis of periodic structures at oblique incidence: orthogonal and nonorthogonal FDTD implementations," *Microwave Theory and Techniques, IEEE Transactions on*, vol. 46, no. 4, pp. 420-427, 1998.
- [9] J-B.Wang, B. Chen, and B-H. Zhou, "Improved split-field method for solving oblique incident wave on periodic structures," *Electronics Letters*, vol. 47, no. 16, pp. 898-900, 2011.
- [10] Z-Y. Cai, B. Chen, Q. Yin, and R. Xiong, "The WLP-FDTD method for periodic structures with oblique incident wave," *Antennas and Propagation, IEEE Transactions on*, vol. 59, no. 10, pp. 3780-3785, 2011.
- [11] J. Wang, B. Zhou, B. Chen, L. Shi, and C. Gao, "Weakly conditionally stable FDTD method for analysis of 3D periodic structures at oblique incidence," *Electronics Letters*, vol. 48, no. 7, pp. 369-371, 2012.
- [12] B. Liang, M. Bai, H. Ma, N. Ou, and J. Miao, "Wideband analysis of periodic structures at oblique incidence by material independent FDTD algorithm," *Antennas and Propagation, IEEE Transactions on*, vol. 62, no. 1, pp. 354-360,

2014.

[13] Z. Yun and M. F. Iskander, "Implementation of floquet boundary conditions in FDTD analysis of periodic phased array antennas with skewed grid," *Electromagnetics*, vol. 20, no. 5, pp. 445-452, 2000.

[14] K. ElMahgoub, F. Yang, A. Z. Elsherbeni, V. Demir, and J. Chen, "FDTD analysis of periodic structures with arbitrary skewed grid," *Antennas and Propagation, IEEE Transactions on*, vol. 58, no. 8, pp. 2649-2657, 2010.

[15] M. Veysoglu, R. Shin, and J. A. Kong, "A finite-difference time-domain analysis of wave scattering from periodic surfaces: oblique incidence case," *Journal of Electromagnetic Waves and Applications*, vol. 7, no. 12, pp. 1595-1607, 1993.

[16] O. Ramadan, "Auxiliary differential equation formulation: an efficient implementation of the perfectly matched layer," *Microwave and Wireless Components Letters, IEEE*, vol. 13, no. 2, pp. 69-71, 2003.



**Ming Bai** received the B.Sc. and Ph.D. degrees in Physics, from the University of Science and Technology of China (USTC), in 1996 and 2002, respectively.

From 2002 to 2006, he worked as a Postdoctoral Researcher in the Laboratory of Nanotechnology (LFSP), Spanish National Research Council (CSIC). In

2006, he joined School of Electronic and Information Engineering, Beihang University, as an Associate Professor and was promoted to Professor in 2015. His current research interests include computational electromagnetic and microwave imaging.



**Bin Liang** received the B.Sc. and Ph.D. degrees in Electronic and Information Engineering from Beihang University, Beijing, China, in 2008 and 2015, respectively.

From 2012 to 2014, he was a Visiting Research Student in School of Engineering and Digital Arts, University of Kent, UK. His research interests include computational electromagnetic, frequency selective surfaces, electromagnetic band-gap structures, and antennas.



**Hui Ma** received the B.Sc. and Ph.D. degrees in Electronic and Information Engineering from Beihang University, Beijing, China, in 2009 and 2015, respectively.

From 2012 to 2014, she was a Visiting Research Student in Electronic, Electrical and Computer Engineering Department, University of Birmingham, UK. Her research interests include antennas, microwave imaging and passive surface-space bi-static SAR.

# Modal Analysis of Frequency Selective Surface Containing Ring Loops

Mehran Shamaei Samani, Reza Sarraf Shirazi, and Gholamreza Moradi

Department of Electrical Engineering  
Amirkabir University of Technology, Tehran, Iran  
Mehranshamaey@aut.ac.ir, Sarraf@aut.ac.ir, Ghmoradi@aut.ac.ir

**Abstract** — Modal analysis of frequency selective surface (FSS) containing ring loops arranged periodically along any two skewed coordinates, will be calculated. In proposed modal analysis, a compatible set of orthonormal mode functions used for ring loops in addition to Floquet modes which are used in every infinite two dimensional arrays. This set of modes provides faster convergence in solving integral equation in accordance with this boundary condition problem. Calculations are compared with results of CST (Finite Integration Technique) and HFSS (Finite Element Method) full-wave simulators and they are in good agreement with each other.

**Index Terms** — Frequency Selective Surface (FSS), ring loop, Substrate Integrated Waveguide (SIW), TE and TM polarizations.

## I. INTRODUCTION

Frequency selective surface (FSS) as spatial filter [1-2], should have low insertion loss in passband and sharp roll-off rejection in out-of-band. However, these two characteristics are sufficient in filter designing, in spatial form of filters, stability of these characteristics about polarization and angle of incident is more important [3]. One of the significant parameters in this stability is symmetrical geometry. As circular loop is the most symmetrical object in all candidate elements in FSS designing, it is preferred to implement a stable FSS [4].

For the analytical calculation of electromagnetics problems such as boundary value conditions, modal analysis is the inseparable part of computations [5-6], so in the analysis of this paper, modal method is utilized to extract reflection coefficient.

Boundary value problem of open ended circular waveguide phased array, were solved generally by Amitay and Galindo [5]. They used the Ritz-Galerkin method to solve the integral equation.

For the case of ring loops or apertures, if the method similar to Amitay and Galindo is utilized, the convergence is so slowly [7]. To speed up the

convergence, in this paper, the fields of ring loop are expanded to a set of orthonormal mode functions which are compatible with geometry of ring loops and satisfy loop boundary conditions [7-8].

In this paper, thin perfectly conducting loops distributed periodically along any two skewed coordinates (nonorthogonal) coordinates is exposed with a plane wave of arbitrary polarization incident from any oblique angle like whatever seen in Fig. 1. The distance between loop elements should be less than  $\lambda/2$ . In the following parts of this paper, all the details of this method will be described and results are compared with simulations of CST and HFSS.

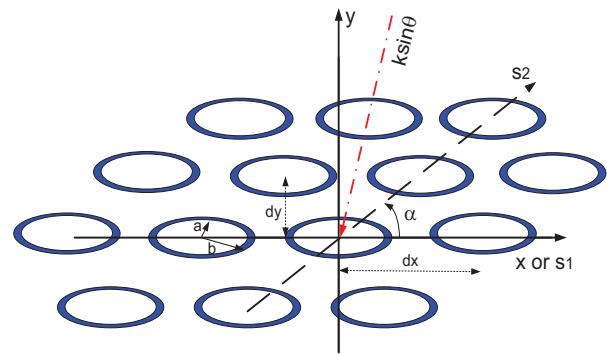


Fig. 1. Geometry of FSS with ring loops.

## II. THEORETICAL ANALYSIS

According to Fig. 1, array of ring loops which is distributed periodically along skewed coordinates  $s_1$  and  $s_2$ , is illuminated by a plane wave with propagation vector,  $\vec{k}$ . The angle between  $\vec{k}$  and the normal to the surface is  $\theta$  and between  $s_1$  and projection of  $\vec{k}$  is  $\phi$ .

Near the array of FSS, the electromagnetic fields must satisfy the periodicity condition of Floquet theorem. By employing this theorem, the scalar wave equation (the time dependence is eliminated) is in the form of [7]:

$$\psi_{pq} = e^{-j(U_{pq}x + V_{pq}y + W_{pq}z)}, \quad (1)$$

where

$$U_{pq} = k \sin \theta \cos \varphi + \frac{2\pi p}{dx}, \quad (2)$$

$$V_{pq} = k \sin \theta \sin \varphi + \frac{2\pi q}{dy} - \frac{2\pi p}{dx \tan \alpha}, \quad (3)$$

$$W_{pq} = \begin{cases} \sqrt{k^2 - T_{pq}^2} & \text{for } k^2 > T_{pq}^2 \\ -j\sqrt{T_{pq}^2 - k^2} & \text{for } k^2 < T_{pq}^2 \end{cases}, \quad (4)$$

which

$$T_{pq}^2 = U_{pq}^2 + V_{pq}^2,$$

$p$  and  $q$  are Floquet indices.  $W_{pq}$ , the modal propagation constants, is positive for propagating modes and negative imaginary for evanescent modes. The space between elements and the direction of  $k$ , determine the number of propagating modes. The electric field components transverse to the  $z$  axis (TE and TM mode functions), then can be expressed in terms of  $\psi$  as:

$$\bar{\Phi}_{pqTE} = \frac{1}{\sqrt{d_x d_y}} \left( \frac{V_{pq}}{T_{pq}} \hat{x} - \frac{U_{pq}}{T_{pq}} \hat{y} \right) \psi_{pq} \quad \text{TE modes}, \quad (5)$$

$$\bar{\Phi}_{pqTM} = \frac{1}{\sqrt{d_x d_y}} \left( \frac{U_{pq}}{T_{pq}} \hat{x} + \frac{V_{pq}}{T_{pq}} \hat{y} \right) \psi_{pq} \quad \text{TM modes}. \quad (6)$$

These fields are related to each other by modal impedance, as:

$$\eta_{pqTE} = \frac{k\eta_0}{W_{pq}}, \quad (7)$$

$$\eta_{pqTM} = \frac{W_{pq}\eta_0}{k}. \quad (8)$$

A plane wave with unit intensity electric field and in direction of  $(\theta, \varphi)$ , can be expressed as the sum of two E and H polarized plane waves. These plane waves, correspond to TE and TM Floquet modes with  $p, q=0$ . So we have for incident electric and magnetic fields:

$$\bar{E}^i = \sum_{r=1}^2 A_{00r} \bar{\Phi}_{00r}, \quad (9)$$

$$\bar{H}^i = \sum_{r=1}^2 \frac{A_{00r}}{\eta_{00r}} (\hat{z} \times \bar{\Phi}_{00r}), \quad (10)$$

In the above expressions,  $r$  designates TE and TM modes.  $A_{00r}$  is the magnitude of component. With  $R_{pqr}$  as the reflection coefficient, the scattered fields can be expressed as:

$$\bar{E}^s = \sum_p \sum_q \sum_{r=1}^2 R_{pqr} \bar{\Phi}_{pqr}, \quad (11)$$

$$\bar{H}^s = -\sum_p \sum_q \sum_{r=1}^2 \frac{R_{pqr}}{\eta_{pqr}} (\hat{z} \times \bar{\Phi}_{pqr}). \quad (12)$$

The unknown reflection coefficient,  $R_{pqr}$ , according to orthonormality of modes is:

$$R_{pqr} = \eta_{pqr} \iint_{\text{Loop}} \hat{z} \times \bar{H}^s \cdot \bar{\Phi}_{pqr}^* da, \quad (13)$$

$\bar{\Phi}_{pqr}^*$  is the complex conjugate of  $\bar{\Phi}_{pqr}$ . The boundary conditions then force that:

$$\bar{E}^i + \bar{E}^s = 0 \quad \text{over each loop}, \quad (14)$$

$$2\hat{z} \times (\bar{H}^i + \bar{H}^s) = \bar{K} \quad \text{over each loop}. \quad (15)$$

Substitution (9), (10) and (13) into (14) yields the integral equation:

$$\sum_{r=1}^2 A_{00r} \bar{\Phi}_{00r} = -\sum_p \sum_q \sum_{r=1}^2 \eta_{pqr} \bar{\Phi}_{pqr} \iint_{\text{Loop}} \hat{z} \times \bar{H}^s \cdot \bar{\Phi}_{pqr}^* da. \quad (16)$$

Here we replace the induced current,  $-\hat{z} \times \bar{H}^s$  with another set of orthonormal mode functions which are compatible to geometry of loops and satisfy boundary conditions, as:

$$-\hat{z} \times \bar{H}^s = \sum_m \sum_n \sum_{l=1}^2 (B_{mnl} \bar{\psi}_{mnl}) + B_{TEM} \bar{\psi}_{TEM}. \quad (17)$$

$l=1$  and  $l=2$  designate TE and TM mode respectively, then  $\bar{\psi}_{mnl}$  and  $\bar{\psi}_{TEM}$  for a ring loop can be expressed as [9]:

$$\bar{\psi}_{mn}^{TE} = \hat{\rho} \frac{n}{\rho} Z_n(k'_{cmn} \rho) \sin n\varphi \quad (18)$$

$$+ \hat{\phi} k'_{cmn} Z'_n(k'_{cmn} \rho) \cos n\varphi,$$

$$\bar{\psi}_{mn}^{TM} = \hat{\rho} k_{cmn} \bar{Z}'_n(k_{cmn} \rho) \sin n\varphi \quad (19)$$

$$+ \hat{\phi} \frac{n}{\rho} \bar{Z}_n(k_{cmn} \rho) \cos n\varphi,$$

$$\bar{\psi}_{TEM} = \frac{1}{\rho \ln b/a} [\hat{x} \cos \varphi + \hat{y} \sin \varphi], \quad (20)$$

which [10]:

$$Z_n = \frac{\sqrt{\pi \epsilon_n}}{2 \sqrt{\left( \frac{J_n(k'_{cmn} b)}{J_n(k'_{cmn} a)} \right)^2 (1 - (\frac{n}{a})^2) - (1 - (\frac{n}{b})^2)}}$$

$$\times (Y'_n(k'_{cmn} a) J_n(k'_{cmn} \rho) - J'_n(k'_{cmn} a) Y_n(k'_{cmn} \rho)),$$

$$\bar{Z}_n = \frac{\sqrt{\pi \epsilon_n}}{2 \sqrt{\left( \frac{J_n(k_{cmn} b)}{J_n(k_{cmn} a)} \right)^2 - 1}}$$

$$\times (Y_n(k_{cmn} a) J_n(k_{cmn} \rho) - J_n(k_{cmn} a) Y_n(k_{cmn} \rho)),$$

$k_{cmn}$  is the  $m$ th root of:

$$Y'_n(k'_c) J'_n(k'_c b/a) - J'_n(k'_c) Y'_n(k'_c b/a) = 0.$$

And  $k'_{cmn}$  is the  $m$ th root of:

$$Y_n(k_c) J_n(k_c b/a) - J_n(k_c) Y_n(k_c b/a) = 0.$$

If both sides of (16) multiplied by the complex conjugate of  $\bar{\psi}_{mnl}$  and  $\bar{\psi}_{TEM}$ , after that the products are integrated over the ring loop, the results are [7]:

$$\sum_{r=1}^2 A_{00r} C_{00r}^{*TEM} = -\sum_p \sum_q \sum_{r=1}^2 \eta_{pqr} C_{pqr}^{*TEM} \iint_{Loop} -\hat{z} \times \bar{H}^s \cdot \bar{\Phi}_{pqr}^* da, \quad (21)$$

$$\sum_{r=1}^2 A_{00r} C_{00r}^{*MNL} = -\sum_p \sum_q \sum_{r=1}^2 \eta_{pqr} C_{pqr}^{*MNL} \iint_{Loop} -\hat{z} \times \bar{H}^s \cdot \bar{\Phi}_{pqr}^* da, \quad (22)$$

where

$$C_{pqr}^{*MNL} = \iint_{Loop} \bar{\psi}_{MNL} \cdot \bar{\Phi}_{pqr}^* da, \quad (23)$$

$$C_{pqr}^{*TEM} = \iint_{Loop} \bar{\psi}_{TEM} \cdot \bar{\Phi}_{pqr}^* da. \quad (24)$$

The integral equation can be rewritten as:

$$[Z_{MNL}^{mnl}] [B_{mnl}] = [D_{mnl}]. \quad (25)$$

Which  $Z$  is a square matrix in which the row index is designated by  $M, N, L$  and the column index is designated by  $m, n, l$ . As there is no  $mn=00$  mode, the TEM mode is called  $00$  mode (Don't care  $l$ ) in matrix implementation. The matrix elements are given by:

$$[Z_{MNL}^{mnl}] = \sum_p \sum_q \sum_{r=1}^2 \eta_{pqr} C_{pqr}^{*MNL} C_{pqr}^{mnl}, \quad (26)$$

and

$$[D_{mnl}] = \sum_{r=1}^2 A_{00r} C_{00r}^{*mnl}. \quad (27)$$

$C_{pqr}^{mnl}$  is the coupling coefficient between modes in the both sides of interface and it can be seen as scalar products of these modes. Keep in mind that:

$r=l=1$  related to TE modes.

$r=l=2$  related to TM modes.

$mn=00$  related to TEM mode.

After a lot of mathematics calculations the close form of these integrals extract as bellow:

$$C_{pq1}^{mn1} = \langle \psi_{mn}^{TE} \cdot \varphi_{pq}^{TE} \rangle = \frac{k'_{cmn}}{2\sqrt{dxdy}} \left\{ \left(\frac{V}{T}\right)(X_1 + X_2) + \left(\frac{-U}{T}\right)(Y_1 + Y_2) \right\},$$

$$C_{pq2}^{mn1} = \langle \psi_{mn}^{TE} \cdot \varphi_{pq}^{TM} \rangle = \frac{k'_{cmn}}{2\sqrt{dxdy}} \left\{ \left(\frac{U}{T}\right)(X_1 + X_2) + \left(\frac{V}{T}\right)(Y_1 + Y_2) \right\},$$

$$C_{pq1}^{mn2} = \langle \psi_{mn}^{TM} \cdot \varphi_{pq}^{TE} \rangle = \frac{k'_{cmn}}{2\sqrt{dxdy}} \left\{ \left(\frac{V}{T}\right)(\bar{X}_1 + \bar{X}_2) + \left(\frac{-U}{T}\right)(\bar{Y}_1 + \bar{Y}_2) \right\},$$

$$C_{pq2}^{mn2} = \langle \psi_{mn}^{TM} \cdot \varphi_{pq}^{TM} \rangle = \frac{k'_{cmn}}{2\sqrt{dxdy}} \left\{ \left(\frac{U}{T}\right)(\bar{X}_1 + \bar{X}_2) + \left(\frac{V}{T}\right)(\bar{Y}_1 + \bar{Y}_2) \right\},$$

$$C_{pq1}^{TEM} = \langle \psi_{pq}^{TEM} \cdot \varphi_{pq}^{TE} \rangle = \frac{-2j\pi}{\ln(b/a)} \left( \frac{V}{T} \cos \varphi_r - \frac{U}{T} \sin \varphi_r \right) \{ J_1(Ta) - J_1(Tb) \},$$

$$C_{pq2}^{TEM} = \langle \psi_{pq}^{TEM} \cdot \varphi_{pq}^{TM} \rangle = \frac{-2j\pi}{\ln(b/a)} \left( \frac{U}{T} \cos \varphi_r + \frac{V}{T} \sin \varphi_r \right) \{ J_1(Ta) - J_1(Tb) \},$$

$$X_1 = \begin{cases} \varepsilon_{\frac{n+1}{2}} (-1)^{n+1/2} S_1 \frac{bB_{n+1,b} - aB_{n+1,a}}{T^2 - k'_{cmn}{}^2} & (n \text{ odd}) \\ -2j(-1)^{n/2} S_1 \frac{bB_{n+1,b} - aB_{n+1,a}}{T^2 - k'_{cmn}{}^2} & (n \text{ even}) \end{cases},$$

$$X_2 = \begin{cases} \varepsilon_{\frac{n-1}{2}} (-1)^{n-1/2} S_2 \frac{bB_{n-1,b} - aB_{n-1,a}}{T^2 - k'_{cmn}{}^2} & (n \text{ odd}) \\ -2j(-1)^{n-2/2} S_2 \frac{bB_{n-1,b} - aB_{n-1,a}}{T^2 - k'_{cmn}{}^2} & (n \text{ even}) \end{cases},$$

$$Y_1 = \begin{cases} \varepsilon_{\frac{n+1}{2}} (-1)^{n+1/2} C_1 \frac{bB_{n+1,b} - aB_{n+1,a}}{T^2 - k'_{cmn}{}^2} & (n \text{ odd}) \\ 2j(-1)^{n/2} C_1 \frac{bB_{n+1,b} - aB_{n+1,a}}{T^2 - k'_{cmn}{}^2} & (n \text{ even}) \end{cases},$$

$$Y_2 = \begin{cases} -\varepsilon_{\frac{n-1}{2}} (-1)^{n-1/2} C_2 \frac{bB_{n-1,b} - aB_{n-1,a}}{T^2 - k'_{cmn}{}^2} & (n \text{ odd}) \\ -2j(-1)^{n-2/2} C_2 \frac{bB_{n-1,b} - aB_{n-1,a}}{T^2 - k'_{cmn}{}^2} & (n \text{ even}) \end{cases},$$

$$\bar{X}_1 = \begin{cases} -\varepsilon_{\frac{n+1}{2}} (-1)^{n+1/2} S_1 \frac{b\bar{B}_{n+1,b} - a\bar{B}_{n+1,a}}{T^2 - k'_{cmn}{}^2} & (n \text{ odd}) \\ 2j(-1)^{n/2} S_1 \frac{b\bar{B}_{n+1,b} - a\bar{B}_{n+1,a}}{T^2 - k'_{cmn}{}^2} & (n \text{ even}) \end{cases},$$

$$\bar{X}_2 = \begin{cases} \varepsilon_{\frac{n-1}{2}} (-1)^{n-1/2} S_2 \frac{b\bar{B}_{n-1,b} - a\bar{B}_{n-1,a}}{T^2 - k'_{cmn}{}^2} & (n \text{ odd}) \\ -2j(-1)^{n-2/2} S_2 \frac{b\bar{B}_{n-1,b} - a\bar{B}_{n-1,a}}{T^2 - k'_{cmn}{}^2} & (n \text{ even}) \end{cases},$$

$$\bar{Y}_1 = \begin{cases} -\varepsilon_{\frac{n+1}{2}} (-1)^{n+1/2} C_1 \frac{b\bar{B}_{n+1,b} - a\bar{B}_{n+1,a}}{T^2 - k'_{cmn}{}^2} & (n \text{ odd}) \\ -2j(-1)^{n/2} C_1 \frac{b\bar{B}_{n+1,b} - a\bar{B}_{n+1,a}}{T^2 - k'_{cmn}{}^2} & (n \text{ even}) \end{cases},$$

$$\bar{Y}_2 = \begin{cases} -\varepsilon_{\frac{n-1}{2}} (-1)^{n-1/2} C_2 \frac{b\bar{B}_{n-1,b} - a\bar{B}_{n-1,a}}{T^2 - k'_{cmn}{}^2} & (n \text{ odd}) \\ -2j(-1)^{n-2/2} C_2 \frac{b\bar{B}_{n-1,b} - a\bar{B}_{n-1,a}}{T^2 - k'_{cmn}{}^2} & (n \text{ even}) \end{cases},$$

$$B_{n\pm 1, r_i} = TJ_{n+2}(Tr_i) Z_{n\pm 1}(k'_{cmn} r_i) - k'_{cmn} J_{n\pm 1}(Tr_i) Z_{n+2}(k'_{cmn} r_i) \quad (r_i = a, b),$$

$$\begin{aligned} \bar{B}_{n\pm 1, r_i} &= T J_{n+2}(Tr_i) \bar{Z}_{n\pm 1}(k_{cnn} r_i) \\ &\quad - k_{cnn} J_{n\pm 1}(Tr_i) \bar{Z}_{n+2}(k_{cnn} r_i) \quad (r_i = a, b), \\ S_1 &= \pi \sin((n+1)\varphi_T), \\ S_2 &= \pi \sin((n-1)\varphi_T), \\ C_1 &= \pi \cos((n+1)\varphi_T), \\ C_2 &= \pi \cos((n-1)\varphi_T), \\ \varphi_T &= \tan^{-1}\left(\frac{V}{T}\right). \end{aligned}$$

To calculate the reflection coefficient  $R_{pqr}$ , first, the unknown coefficient  $B_{mnl}$  and  $B_{TEM}$  should be evaluated from (25) and then these values substituted in (17). The number of modes for each region should be chosen carefully which only the significant modes are assigned [7].

### III. RESULTS

According to the formulation achieved in the previous section, and for the case of geometry of Fig. 1, and for all Floquet modes which  $T_{pq}$  (transverse wave number) in them are less than 10 times the  $k$  (wave number) and for 12 lowest modes for circular loop, the reflection coefficient, is calculated. Increasing the number of modes cause to obtain more accurate response in the expense of times (Because the output of integral equation is a multiterminal network and there are a lot of nested loop in it, therefore it grows rapidly). For a new geometrical parameters and frequency band, sometimes it is time consuming procedure to find the optimized number of modes (often up to 9 and less than 14). But by determining the optimized number, for a wide range of parameters and frequency bands in the vicinity of that case, it can be ok.

The geometrical parameters of a sample FSS array are described in Table 1.

Table 1: Geometrical parameters for FSS array

Parameter	Value	Parameter	Value
$a$	5 (mm)	$b$	6 (mm)
$dx$	15 (mm)	$dy$	15 (mm)
$\alpha$	90°		

The results are plotted in Fig. 2, for normal incidence (TE or TM plane wave) in compare with CST and HFSS simulators. In Fig. 3, the reflection coefficient for some  $\theta$  and TE polarization is plotted. Also in Fig. 4, it is repeated for TM polarization. As it is clear in both polarizations, by increasing  $\theta$  the resonant frequency reduced somewhat.

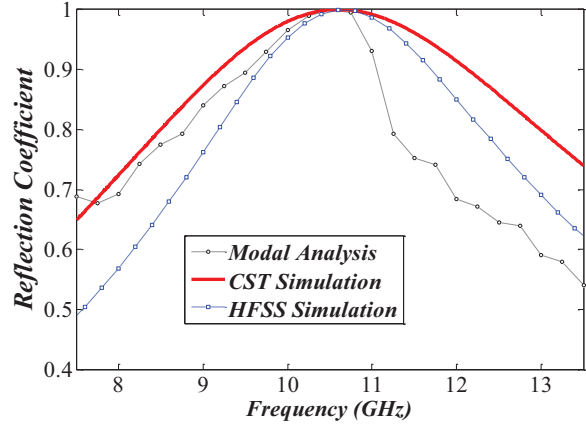


Fig. 2. Comparison of reflection coefficient between modal analysis, CST and HFSS simulation.

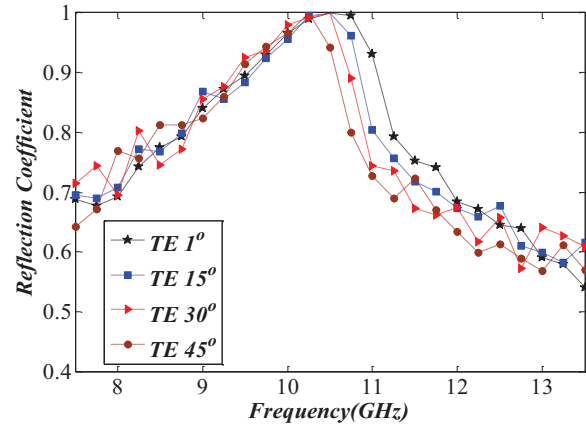


Fig. 3. Reflection coefficient for some angles of incidence and TE polarization.

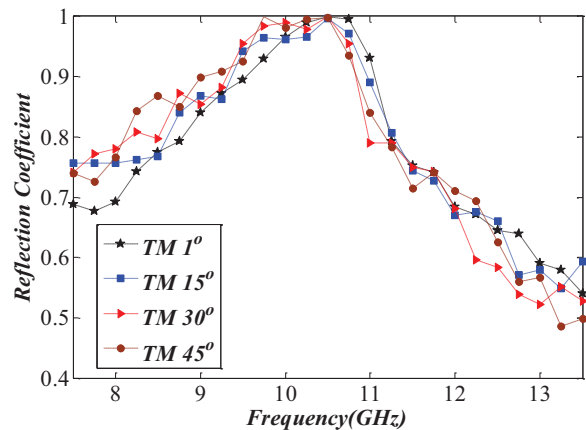


Fig. 4. Reflection coefficient for some angles of incidence and TM polarization.

#### IV. CONCLUSION

Modal analysis of a FSS containing ring loops is formulated and calculated. For this geometry, a set of orthonormal mode functions compatible with circular loop were defined to replace the induced current. This replacement and setting an optimized number of modes can cause to faster convergence than a simple integral equation with just Floquet modes.

The results were compared with CST and HFSS simulators and relatively good agreement was achieved. Also, as the ring element has the best geometrical symmetry, the frequency response for proposed FSS has stable characteristics about incident polarization and angle up to 45°.

#### REFERENCES

- [1] B. A. Munk, *Frequency Selective Surfaces: Theory and Design*, John Wiley & Sons, New York, 2000.
- [2] R. Mitra, C. H. Chan, and T. Cwik, "Techniques for analyzing frequency selective surfaces—a review," *Proceedings of the IEEE*, vol. 76, no. 12, Dec. 1988.
- [3] J. Shaker and L. Shafai, "Removing the angular sensitivity of FSS structures using novel double-layer structures," *IEEE Microw. Guided Wave Lett.*, vol. 5, no. 10, pp. 324-325, Oct. 1995.
- [4] E. A. Parker and S. M. A. Hamdy, "Rings as elements for frequency selective surfaces," *Electronics Letters*, 1981.
- [5] N. Amitay and V. Galindo, "The analysis of circular waveguide phased array," *Bell Syst. Tech. J.*, vol. 47, pp. 1903-1932, Nov. 1968.
- [6] G. V. Borgiotti, "Modal analysis of periodic planar phased arrays of apertures," *Proceedings of the IEEE*, vol. 56, no. 11, Nov. 1968.
- [7] C. C. Chen, "Scattering by a two-dimensional periodic array of conducting plates," *IEEE Trans. Antennas Propag.*, vol. 18, no. 5, pp. 660-665, Sep. 1970.
- [8] C. C. Chen, "Transmission through a conducting screen perforated periodically with apertures," *IEEE Trans. Microw. Theory Tech.*, vol. 18, no. 9, pp. 627-632, Sep. 1970.
- [9] N. Amitay and V. Galindo, "On the scalar product of certain circular and Cartesian wave functions,"

*IEEE Trans. Microw. Theory and Tech.*, vol. 16, no. 4, pp. 265-266, Apr. 1968.

- [10] N. Marcuvitz, *Waveguide Handbook*, first edition, McGraw-Hill, New York, 1951.



**Mehran Shamaei** was born in 1984 and received the B.S. and M.S. degrees from the Amirkabir University of Technology (Tehran Polytechnic), Tehran, Iran, in 2008 and 2010, respectively, all in Electrical Engineering. He is currently working toward the Ph.D. degree at same university. His research interests include frequency selective surfaces and reflect array antennas.



**Reza Sarraf Shirazi** was born in Yazd, Iran in 1958. He received the Ph.D. degrees in Electrical Engineering from Amirkabir University of Technology, Tehran, Iran in 2006. His main research interests are numerical Electromagnetics and radio wave propagation. He is currently an Assistant Professor with the Electrical Engineering Department, Amirkabir University of Technology. He has published several papers in the refereed journals and international conferences.



**Gholamreza Moradi** was born in Shahriar, Iran in 1966. He received the Ph.D. degree in Electrical Engineering from Amirkabir University of Technology, Tehran, Iran in 2002. His main research interests are numerical Electromagnetics, antennas, active microwave and mm-wave circuits and systems. He is currently an Associate Professor with the Electrical Engineering Department, Amirkabir University of Technology. He has published several papers in the refereed journals and international conferences.

# Multi-Band Frequency Selective Surface Design Based on Idea of Clusters in Cellular Communication Systems

Mehran Shamaei Samani, Reza Sarraf Shirazi, and Gholamreza Moradi

Department of Electrical Engineering  
Amirkabir University of Technology, Tehran, Iran  
Mehranshamaey@aut.ac.ir, Sarraf@aut.ac.ir, Ghmoradi@aut.ac.ir

**Abstract** — A frequency selective surface which can provide up to 4 passbands will be proposed. The passbands are nearly independent so it simplifies the design procedure. The base of the design is according to frequency reuse in cellular communications which there are  $N$  different frequencies in one cluster. The array cells in this FSS are hexagons and the resonators on top and bottom of each cell are aperture loops. As the elements and cells are in the most geometrical symmetry, stability about polarization and angle of incidence is in the good state. As some examples, a dual-band, a triple-band and a quad-band FSS are simulated with CST software. The results are in good agreement with theoretical calculations.

**Index Terms** — Aperture loop, cluster size, dual-band FSS, frequency selective surface (FSS), quad-band FSS, triple-band FSS.

## I. INTRODUCTION

In many communicational systems we need to design frequency selective surfaces with more than one passband [1] such as dual-band, triple-band [1]-[2] and even quad-band [3] structures. In these multiband FSSs, it is hard to design the whole structure entirely and it is valuable to have a procedure which passbands can be designed independently and separately in it [4], after that whole structure is constructed by adding these independent designs [1].

To have the most stable frequency response for a bandpass FSS, the best choice is circular aperture, for its geometrical symmetry [5]. Also, to select the array cells, a good choice is hexagon because it is nearly similar to a circle and compatible with aperture loop and it can cover surface perfectly. By using hexagonal array cells, a honeycomb structure is raised which can be related to cellular communications. Keep in mind that in those systems, for frequency reuse, it is routine that the centre frequencies are selected deferent from each other and some clusters are constructed [6]. In the next section, a short introduction of this concept is proposed; however, one of the possible cases is the

cluster size of 4. The configuration of cells in this cluster size is shown in Fig. 1.

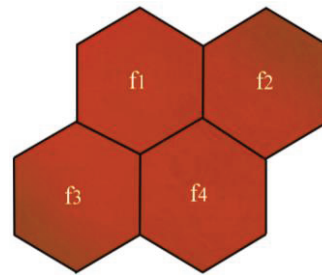


Fig. 1. Cluster size of 4.

If the resonant frequency of circular aperture available in each cluster is selected according to Fig. 2, a multiband FSS with four passbands can be implemented. If two or three passbands are needed, three or two apertures can be selected the same, respectively. So by this configuration, a FSS with 2, 3 or 4 passbands is designed. Modularity of passbands cause to simplify multiband designing, so preliminary design is simple to do. Then final optimization will be completed by some tuning of the geometrical parameters.

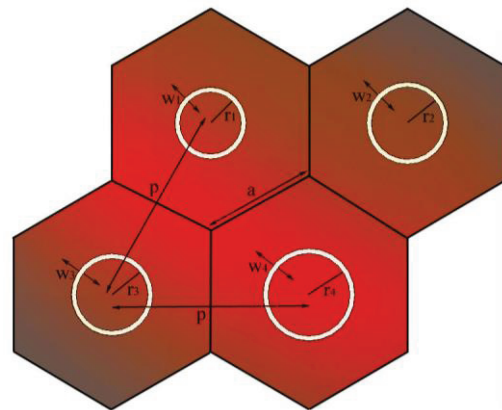


Fig. 2. Geometry of a multiband FSS.

## II. DESIGN

The resonant frequency of a circular aperture can be estimated by the approximate equation in (1), which was only suitable for the calculating the resonant frequency of conventional aperture type FSS [7]:

$$f_r = \frac{c}{\sqrt{\epsilon_{eff}}} \frac{1.2}{2\pi(r + w/2)}, \quad (1)$$

$c$  is speed of light in free space.  $\epsilon_{eff}$  for thin substrate, can be calculated from equation (2) [8]:

$$\epsilon_{eff} = \epsilon_r + (1 - \epsilon_r)e^{-Nx}. \quad (2)$$

$N$  is an exponential factor, this parameter varies for different cell shapes, here, it is 2.2,  $x$  is:

$$x = \frac{10t}{\lambda_0}, \quad (3)$$

where  $\lambda_0$  is free space wavelength and  $t$  is thickness of substrate.

Which  $c$  is the speed of light in free space,  $r$  is the inner radius and  $w$  is the width of aperture. For the design of multiband FSS, the centre frequency of each band is independently designed with a circular resonator with  $f_r$  according to equation (1). This aperture exists on top and bottom of substrate. There are some coupling effects that vary a little resonant frequency that in the final tuning frequency response can be optimized.

In cellular communication, cluster size,  $N$ , is selected according to how many frequencies are needed. This number is equal to (4) [6]:

$$N = i^2 + j^2 + ij. \quad (4)$$

Here  $i$  and  $j$  are positive integers or zero and  $i \geq j$ . According to Fig. 3,  $i$  and  $j$  are shift parameters, means move  $i$  cells from centre of a reference cell along any of the sides of hexagons, turn anticlockwise by  $60^\circ$  and then move  $j$  cells along this direction, leads to the same frequency as the reference [6]. Any value of  $N$  given by this relationship produce clusters which cover the whole surface with  $N$  independent  $f_r$ . Some examples of different  $N$  are shown in Fig. 4.

In cellular system  $N=7$  is the preferable number to design. In our purpose for multiband FSS,  $N=4$  is sufficient and good choice.

For FSS with rectangular cells periodicity is along two perpendicular axes but for a FSS with honeycomb structure elements arranged periodically along coordinates that enclose the  $60^\circ$  angle [9]. To prevent making grating lobes, the distance between elements along two coordinates should be smaller than  $\lambda/2$  [10].

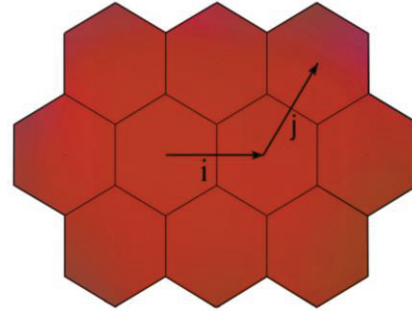


Fig. 3. Geometry of a multi-band FSS.

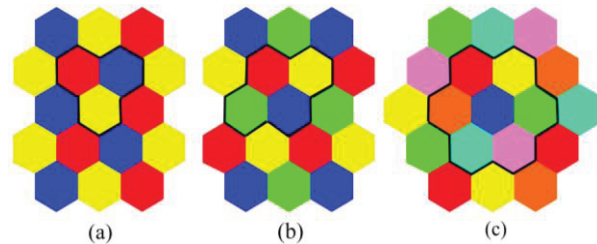


Fig. 4. Some cluster sizes: (a)  $N=3$ , (b)  $N=4$ , and (c)  $N=7$ .

## III. SIMULATED RESULTS

In the previous section it is shown that 2, 3 or 4 passbands with the proposed FSS can be achieved. In this section, three examples proposed for dual-band, triple-band and quad-band FSS.

### A. Design for dual-band FSS

According to the notes and relationship mentioned in the previous section, and for the geometry of Fig. 2, the geometrical parameters of a dual-band FSS are described in Table 1. As it is mentioned in the previous section to achieve two passbands, two resonators should be selected similar. The dielectric constant and height for substrate is 2.65 and 1.5 mm.

Table 1: Geometrical parameters for dual-band FSS

Parameter	Value (mm)	Parameter	Value (mm)
$r_1$	3	$w_2$	0.55
$r_2$	3.25	$w_3$	0.55
$r_3$	3.25	$w_4$	0.44
$r_4$	3	$a$	9.5
$w_1$	0.44	$p$	16.45

According to  $r_i$  and  $w_i$  ( $i=1,4$ ) and equation (1), the resonant frequencies can be listed as Table 2.

Table 2: Calculated resonant frequencies for dual-band FSS

Resonant Frequency	Value (GHz)
$f_1$	11.06
$f_2$	12.11

The transmission and reflection coefficient of simulated FSS is shown in Fig. 5. There are two passbands in frequencies which are calculated with equation (1).

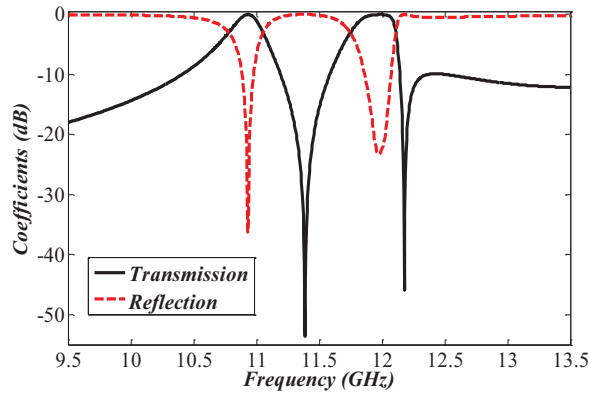


Fig. 5. Transmission and reflection coefficient for dual-band FSS.

### B. Design for triple-band FSS

The geometrical parameters of a triple-band FSS are described in Table 3. In addition, dielectric constant and height for substrate is fixed in all three examples. Again, two resonators are selected the same.

Table 3: Geometrical parameters for triple-band FSS

Parameter	Value (mm)	Parameter	Value (mm)
$r_1$	2.7	$w_2$	0.44
$r_2$	3.15	$w_3$	0.44
$r_3$	3.15	$w_4$	0.44
$r_4$	3.6	$a$	10
$w_1$	0.44	$p$	17.3

Again with these new  $r_i$  and  $w_i$ , three resonant frequencies are calculated according to Table 4.

Table 4: Calculated resonant frequencies for triple-band FSS

Resonant Frequency	Value (GHz)
$f_1$	10.21
$f_2$	11.57
$f_3$	13.35

The transmission and reflection coefficient of simulated triple-band FSS is shown in Fig. 6. As it is clear from this figure, three passbands which are obtained from simulation are compatible with calculated ones.

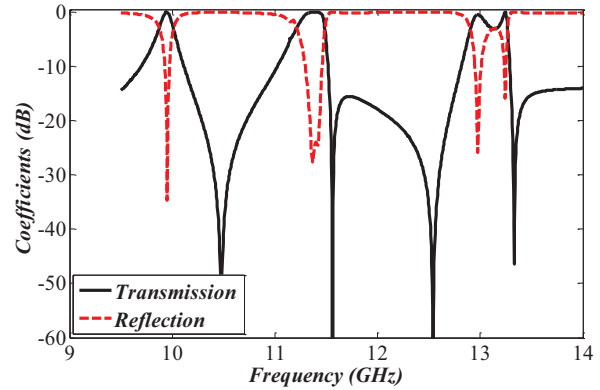


Fig. 6. Transmission and reflection coefficient for triple-band FSS.

### C. Design for quad-band FSS

The geometrical parameters for a quad-band FSS are listed in Table 5.

Table 5: Geometrical parameters for quad-band FSS

Parameter	Value (mm)	Parameter	Value (mm)
$r_1$	2.7	$w_2$	0.49
$r_2$	3.0	$w_3$	0.5
$r_3$	3.3	$w_4$	0.44
$r_4$	3.6	$a$	10
$w_1$	0.4	$p$	17.32

For this new configuration, four resonant frequencies are calculated with equation (1). Table 6 shows these resonances.

Table 6: Calculated resonant frequencies for quad-band FSS

Resonant Frequency	Value (GHz)
$f_1$	10.21
$f_2$	10.98
$f_3$	12.01
$f_4$	13.45

In Fig. 7, the transmission and reflection coefficient of simulated FSS is represented. Four separate passbands are obtained in this figure, which except for third resonance, the others are in good agreement with calculations.

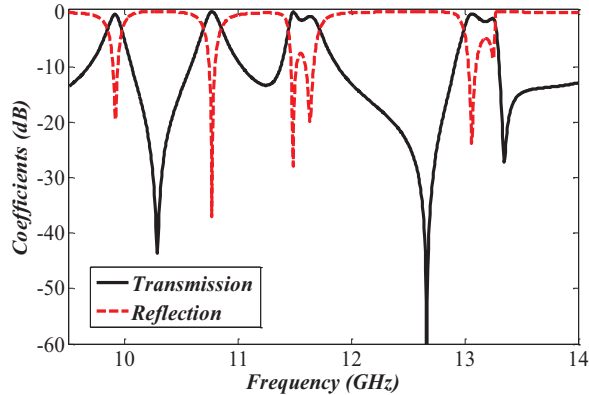


Fig. 7. Transmission and reflection coefficient for quad-band FSS.

#### IV. CONCLUSION

Multiband FSS based on aperture loop and hexagonal cells was proposed, which can produce up to four passbands. The transmission bands are designed separately and independently, so the design procedure can be simple to do. Three examples, dual-band, triple-band and quad-band FSS, were simulated to show how this passbands can be achieved.

#### REFERENCES

- [1] G. Q. Lou, et. al., "Triband frequency selective surface with periodic cell perturbation," *IEEE Microw. and Wireless Components Lett.*, vol. 17, no. 6, Jun. 2007.
- [2] J. Huang, T. K. Wu, and S. W. Lee, "Tri-band frequency selective surface with circular ring elements," *IEEE Trans. Antennas Propag.*, vol. 42, no. 2, Feb. 1994.
- [3] T. K. Wu, "Four-band frequency selective surface with double square loop patch elements," *IEEE Trans. Antennas Propag.*, vol. 42, no. 12, Feb. 1994.
- [4] G. Q. Luo, W. Hong, H. J. Tang, J. X. Chen, and L. L. Sun, "Triband frequency selective surface with periodic cell perturbation," *IEEE Microw. Wireless Compon. Lett.*, vol. 17, no. 6, Jun. 2007.
- [5] E. A. Parker and S. M. A. Hamdy, "Rings as elements for frequency selective surfaces," *Electronics Letters*, vol. 17, no. 17, Aug. 1981.
- [6] J. D. Parsons, *The Mobile Radio Propagation Channel*, 2<sup>nd</sup> edition, John Wiley and Sons, New York, 2000.
- [7] G. Q. Luo, W. Hong, Q. H. Lai, K. Wu, and L. L. Sun, "Design and experimental verification of compact frequency selective surface with quasi elliptic bandpass response," *IEEE Trans. Microw. Theory and Tech.*, vol. 55, no. 12, Dec. 2007.
- [8] F. Costa, A. Monorchia, and G. Manara, "An equivalent circuit model of frequency selective

surfaces embedded within dielectric layers," *Antennas and Propagation Society International Symposium (APSURSI)*, Jun. 2009.

- [9] C. C. Chen, "Scattering by a two-dimensional periodic array of conducting plates," *IEEE Trans. Antennas Propag.*, vol. 18, no. 5, pp. 660-665, Sep. 1970.
- [10] R. Mitra, C. H. Chan, and T. Cwik, "Techniques for analyzing frequency selective surfaces - a review," *Proceedings of the IEEE*, vol. 76, no. 12, Dec. 1988.



**Mehran Shamaei** was born in 1984 and received the B.S. and M.S. degrees from the Amirkabir University of Technology (Tehran Polytechnic), Tehran, Iran, in 2008 and 2010, respectively, all in Electrical Engineering. He is currently working toward the Ph.D.

degree at the same university. His research interests include frequency selective surfaces and reflect array antennas.



**Reza Sarraf Shirazi** was born in Yazd, Iran in 1958. He received the Ph.D. degrees in Electrical Engineering from Amirkabir University of Technology (Tehran Polytechnic), Tehran, Iran in 2006. His main research interests are numerical Electromagnetics and

radio wave propagation. He is currently an Assistant Professor with the Electrical Engineering Department, Amirkabir University of Technology. He has published several papers in the refereed journals and international conferences.



**Gholamreza Moradi** was born in Shahriar, Iran in 1966. He received the Ph.D. degree in Electrical Engineering from Amirkabir University of Technology (Tehran Polytechnic), Tehran, Iran in 2002. His main research interests are numerical

Electromagnetics, antennas, active microwave and mm-wave circuits and systems. He is currently an Associate Professor with the Electrical Engineering Department, Amirkabir University of Technology. He has published several papers in the refereed journals and international conferences.

# Design Investigation of an X-Band SIW H-Plane Band Pass Filter with Improved Stop Band Using Neural Network Optimization

Zahra S. Tabatabaeian and Mohammad H. Neshati

Department of Electrical Engineering  
 Ferdowsi University of Mashhad, 91779-48974, Mashhad, Iran  
 ztaba14@gmail.com, neshat@um.ac.ir

**Abstract** — In this paper, an X-band H-plane band pass filter based on substrate integrated waveguide (SIW) technology is introduced. Back propagation neural network (BPNN) method is applied to optimize parameters of the proposed filter. The stop band of the proposed filter is improved by cascading the H-plane filter with a low pass filter designed and implemented using defected ground structure (DGS). A prototype of the proposed filter is made and experimental results are presented and also compared with those obtained by simulation. Measured reflection coefficient and transmission coefficient in pass band are better than -20 dB and -3.7 dB respectively. Measured results agree well with those obtained by simulation.

**Index Terms** – Band pass filter, neural network, Substrate Integrated Waveguide (SIW).

## I. INTRODUCTION

Microwave filters using rectangular metallic waveguides have been widely used in microwave communication systems. In recent years, a new kind of microwave transmission structure named substrate integrated waveguide (SIW) [1] has been introduced. SIW structures have similar propagation characteristics as the conventional metallic rectangular waveguide. They offer all advantages of rectangular waveguide and planar structures such as low insertion loss, high quality factor and easily integration with planar structures [1]. Moreover, they are low profile and their fabrication cost is low, especially in a production line. Based on the SIW technology, many passive and active devices such as filters, couplers [2], antennas [3] and mixers [4] have been proposed and successfully realized and tested.

Simulation process for SIW structure often requires a relative long time due to existence of via arrays, which needs to be meshed, leading to increasing the complexity of calculation. In turn, an optimization procedure is required to improve design and implementation of microwave components.

In this paper, a microwave H-plane filter is designed, optimized and numerically investigated. Using back

propagation neural network (BPNN) method, an optimization process is applied to obtain filter parameters. To improve stop band response of the filter, a low pass filter using defected ground structure (DGS) is added to the proposed filter. The designed filter is numerically studied using high frequency structure simulator (HFSS).

## II. THE H-PLANE FILTER DESIGN

The top view of the proposed filter and its geometrical parameters are shown in Fig. 1. It consists of seven cascaded rectangular cavities. The via holes have a diameter of  $d$  and the distance between two adjacent vias is denoted by  $S$ . The proposed filter is symmetric along  $AA'$  line in such a way that  $W_i=W_{n+1-i}$  and  $l_i=l_{n-i}$ . TLY031 is used as the substrate with  $\epsilon_r=2.2$  and  $h=0.787$  mm. The desired pass band is considered between  $f_1=9.5$  GHz and  $f_2=10.5$  GHz.

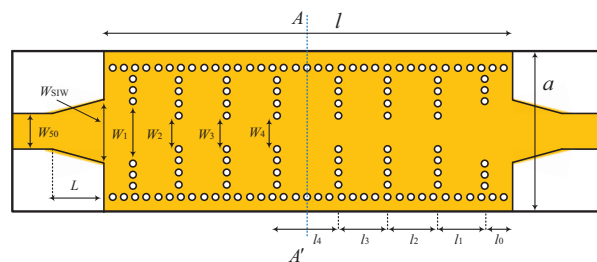


Fig. 1. The proposed H-plane filter structure.

At first, the parameters of the proposed filter are designed based on conventional rectangular waveguide formula, and then, they are adjusted for SIW structures using equivalent width formula. The fractional bandwidth of the proposed filter is defined by Equation (1) [5]:

$$FB_{\lambda} = \frac{\lambda_{g1} - \lambda_{g2}}{\lambda_{go}}, \quad (1)$$

in which

$$\lambda_{go} = \frac{\lambda_{g1} + \lambda_{g2}}{2}, \quad (2)$$

$$\lambda_{gi} = \frac{c}{f_i \sqrt{1 - (f_c/f_i)^2}} \frac{1}{\sqrt{\epsilon_r}} \quad i=1,2, \quad (3)$$

$$f_c = \frac{c}{2a_{RW}}, \quad (4)$$

$c$  and  $a_{RW}$  are light velocity in free space and the equivalent rectangular waveguide width respectively. Then, from the following equations, impedance invert values of the conventional rectangular waveguide is evaluated [5]:

$$\frac{K_{o1}}{Z_o} = \sqrt{\frac{\pi FB_\lambda}{2g_o g_1}}, \quad (5)$$

$$\frac{K_{i,i+1}}{Z_o} = \frac{\pi FB_\lambda}{2} \sqrt{\frac{1}{g_i g_{i+1}}} \quad i=1,2,\dots,n-1, \quad (6)$$

$$\frac{K_{n,n+1}}{Z_o} = \sqrt{\frac{\pi FB_\lambda}{2g_n g_{n+1}}}, \quad (7)$$

where  $g_o, g_1, g_2, \dots, g_{n+1}$  are normalized elements of seventh order Chebyshev with 0.01 dB ripple. The susceptance values of symmetrical windows can be enhanced as follows:

$$\frac{X_{i,i+1}}{Z_o} = \frac{K_{i,i+1}/Z_o}{1 - (K_{i,i+1}/Z_o)^2}. \quad (8)$$

In return, width  $W_{RWi}$  ( $i=1, 2, \dots, n+1$ ) of symmetrical window can be obtained by Equations (9) and (10) [5]:

$$\frac{X}{Z_o} = \frac{a_{RW}}{\lambda_{go}} \tan^2 \left\{ \frac{\pi W_{RWi}}{2a_{RW}} \left[ 1 + \frac{1}{6} \left( \frac{\pi W_{RWi}}{\lambda_o} \right)^2 \right] \right\}, \quad \frac{W_{RWi}}{a_{RW}} \ll 1, \quad (9)$$

$$\frac{X}{Z_o} = \frac{a_{RW}}{\lambda_{go}} \cot^2 \left\{ \frac{\pi W'_{RWi}}{2a_{RW}} \left[ 1 + \frac{2}{3} \left( \frac{\pi W'_{RWi}}{\lambda_o} \right)^2 \right] \right\}, \quad \frac{W'_{RWi}}{a_{RW}} \gg 1, \quad (10)$$

in which

$$W'_{RWi} = \frac{a_{RW} - W_{RWi}}{2}, \quad (11)$$

$$\lambda_o = \frac{c}{\sqrt{f_1 f_2}}. \quad (12)$$

Finally,  $l_{iRW}$  can be obtained using Equation (13) [5]:

$$l_{RWi} = \frac{\lambda_{go}}{2\pi} \theta_i, \quad (13)$$

$$\theta_i = \pi - \frac{1}{2} \left[ \tan^{-1} \left( \frac{2X_{i-1,i}}{Z_o} \right) + \tan^{-1} \left( \frac{2X_{i,i+1}}{Z_o} \right) \right]. \quad (14)$$

The parameters  $W_i, l_i$  and  $a$  of SIW structure can be obtained from  $W_{RWi}, l_{RWi}$  and  $a_{RW}$ , using the following equation [6]:

$$W_{RW} = \frac{W_{SIW}}{\sqrt{1 + \left( \frac{2W_{SIW} - d}{S} \right) \left( \frac{d}{W_{SIW} - d} \right)^2 - \frac{4W_{SIW}}{5S^4} \left( \frac{d^2}{W_{SIW} - d} \right)^3}}.$$

### III. NEURAL NETWORK OPTIMIZATION

Back propagation neural network (BPNN) is generally used in function approximation. In fact, BPNN is a non-linearity artificial neural network and it has been proved that any continuous function in enclosed interval can be approached by a BPNN with a hidden layer. A BPNN model is shown in Fig. 2.

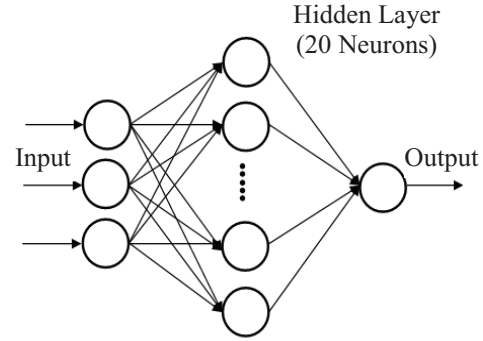


Fig. 2. Back propagation neural network model.

#### A. Back propagation algorithm

A back propagation (BP) network has to be trained. Input vectors and the corresponding target vectors are used to train a network until it could approximate the required function. BPNN use a gradient descent algorithm, in which the network weights are moved along the negative of the gradient of the performance function. Properly trained back propagation networks tend to give reasonable answers when presented with inputs that they have never seen.

#### B. Levenberg-Marquardt back propagation

The trainlm training function is chosen to train the network in this paper. It is a network training function that updates weight and bias values according to Levenberg-Marquardt optimization. Trainlm is often the fastest back propagation algorithm in the toolbox, and is highly recommended as a first choice supervised algorithm; although, it does require more memory than the other algorithms [7].

### IV. OPTIMIZATION PROCEDURE

The basic parameters of the filter are shown in Fig. 1.  $W_{SIW}$  is chosen from 5 mm to 9 mm,  $L$  is varied from 6 mm to 12 mm and  $W_{50}$  is selected from 1.854 mm to 2.854 mm.  $W_{SIW}, L$  and  $W_{50}$  are chosen to be the input of the neural network and the maximum of  $S_{11}$  in the pass band is considered to be the output of the optimization process. The neural network has 20 neurons in its hidden layer and the training function is chosen trainlm. Table 1 summarizes few training data and their reported  $S_{11}$  which are obtained using HFSS. Testing data are summarized in Table 2. The testing data show that the

BPNN output data and  $S_{11}$  results obtained from HFSS agree well with each other.

After training the neural network, the optimum values of the inputs in which maximum  $S_{11}$  in the pass band and  $l_i$  can be obtained by means of Equations (15) and (16) [8]. Distance between different defect parts is uniform and designated by  $l$ :

$$l_i = \frac{N_3}{N_i} l_3 \quad i = 1, 2, 3, \quad (15)$$

$$N_i = \sqrt[4]{C}. \quad (16)$$

$C$  is constant. By increasing  $C$ , return loss in pass band will be increased [8]. In this paper,  $C$  and  $l_3$  are chosen 3.3 and 2.2 mm, respectively. So,  $l_1=1$  mm and  $l_2=1.8$  mm are calculated. Geometrical parameters of the DGS filter are summarized in Table 4.

Table 1: Training data for the optimization procedure

$W_{SIW}$ (mm)	$L$ (mm)	$W_{50}$ (mm)	$S_{11}$ (dB)
5	10	2.354	-8.81
7	12	2.354	-10.46
9	8	2.354	-11.20
7	8	2.604	-22.10
7	10	2.104	-15.63
7	8	2.104	-14.39
9	10	2.104	-14.64
7	8	2.854	-17.65

Table 2: Testing data for the optimization procedure

$W_{SIW}$ (mm)	$L$ (mm)	$W_{50}$ (mm)	$S_{11}$ (dB) (BPNN)	$S_{11}$ (dB) (HFSS)
8.1	7.5	2.8	-20.01	-19.83
5.2	7.6	2.4	-12.73	-12.84
6.4	8.6	2.6	-19.58	-19.28
7.8	11.2	2	-12.70	-13.03
7.3	7.1	2.5	-18.22	-18.38
7.5	7.9	1.9	-10.64	-10.47
7.6	9	2.3	-16.13	-16.15

Table 3: The geometrical parameters of the proposed filter

Parameter	Value (mm)	Parameter	Value (mm)
$a$	20.67	$l_0$	8.03
$l$	90.0	$l_1$	9.54
$d$	1.0	$l_2$	10.79
$W_1$	10.48	$l_3$	11.08
$W_2$	7.66	$l_4$	11.12
$W_3$	6.86	$h$	0.787
$W_4$	6.7	$S$	1.5

### V. RESULTS AND DISCUSSIONS

Simulated  $S$ -parameters of the designed filter using the optimized parameters versus frequency are shown in Fig. 3 (a) and Fig. 3 (b). The optimum value of  $S_{11}$  is -24.90 dB, which agrees well with the result obtained using HFSS which is -24.37 dB. It can be seen that the stop band of the filter is very small; especially the second harmonic of the input is suppressed only -3 dB. In order to improve the stop band characteristic of the proposed filter, two low pass filters are cascaded, one at the input port and the other at the output.

#### A. Low pass DGS filter

A defected ground structure (DGS) low pass filter is

chosen to improve the stop band response of the proposed filter. Figure 4 shows the DGS structure of the filter. In this structure  $g=0.3$  mm,  $v_2=1.2$  mm,  $v_1=0.7$  mm and  $l_i$  can be obtained by means of Equations (15) and (16) [8]. Distance between different defect parts is uniform and designated by  $l$ :

#### B. Simulation results of the DGS filter

Simulated  $S$ -parameters of the designed DGS filter are shown in Fig. 5. It can be seen that maximum insertion loss in pass band is 3.48 dB, while between 16 GHz to 20 GHz stop band attenuation is at least 40 dB.

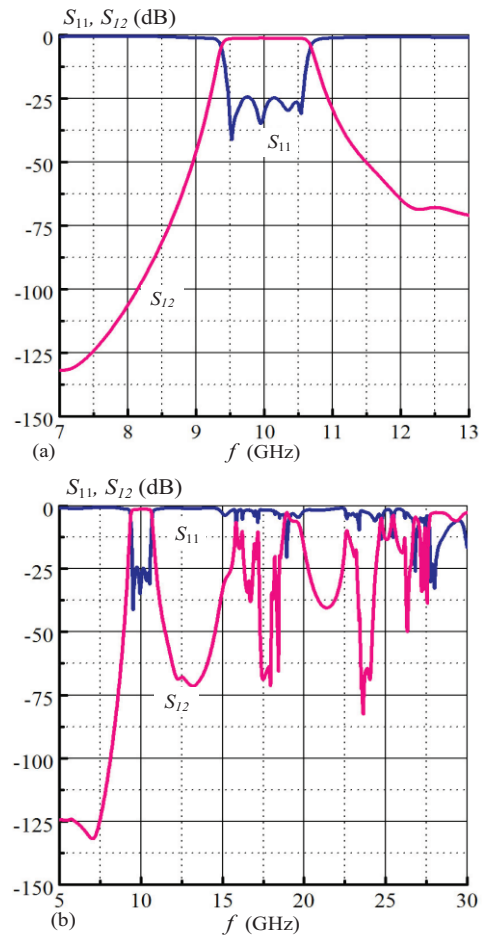


Fig. 3. Simulated  $S$ -parameters of the proposed filter using optimized parameters for two frequency ranges: (a) narrowband and (b) wideband.

Table 4: Geometrical parameters of the DGS structure

Parameter	Value (mm)
$l_1$	1
$l_2$	1.8
$l_3$	2.2
$v_1$	0.7
$v_2$	1.2
$g$	0.3
$l$	1.2

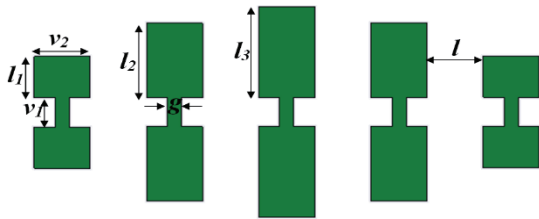


Fig. 4. DGS structure for the proposed filter.

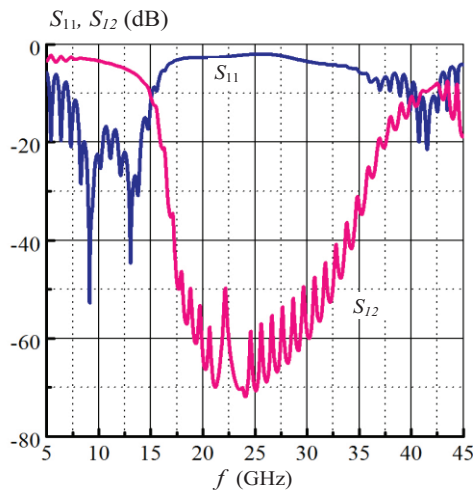


Fig. 5. Simulated  $S$ -parameters of the proposed DGS structure.

**C. Simulation results of the filter with DGS**

The designed filters are cascaded with each other. The final filter structure and its simulated frequency response are shown in Fig. 6 and Fig. 7 respectively. It can be seen that the applied DGS low pass filter suppress the undesired harmonics and the stop band of the filter response is highly improved. It can be seen that a very wide stop band bandwidth, with at least 20 dB attenuation is obtained by the proposed filter. However, passband insertion loss is increased by a little compared to that of the filter without DGS. The obtained results show that simulated  $S_{11}$  and insertion loss are better than -23 dB and 3 dB in pass band respectively, while stop band attenuation is at least 20 dB. The simulated detailed performance of the proposed filter with optimized

parameters including DGS filter are listed in Table 5. Also, simulated characteristics of a few recently published research are also summarized in this table for comparison.

**D. Measured results**

To evaluate the designed procedure of the proposed filter, a prototype of the proposed filter is fabricated using TLY031 substrate with electrical characteristics including:  $\epsilon_r=2.2$ ,  $h=0.787$  mm and tan loss of 0.009. The photo of the fabricated filter is shown in Fig. 8.  $S$ -parameters of the filter are measured using HP 8510 network analyzer. The measured results are shown in Figs. 9 (a) and 9 (b), including the simulation results for comparison. It can be seen that the obtained  $S_{11}$  is better than -20 dB in pass band. Also, insertion loss of the filter is better than 3.7 dB in pass band and the attenuations of the filter is better than 19 dB in stop band. Moreover, a very good agreement is obtained between measured and simulated results.

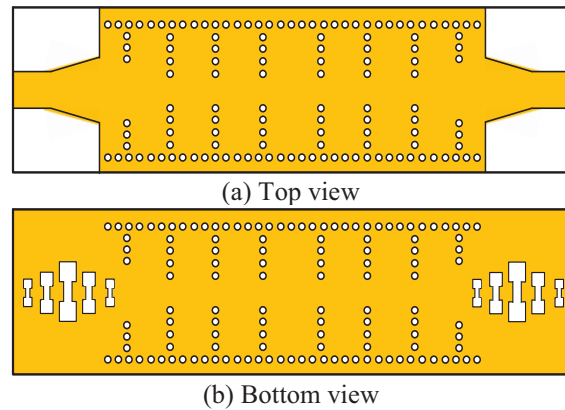


Fig. 6. Structure of the proposed filter with DGS.

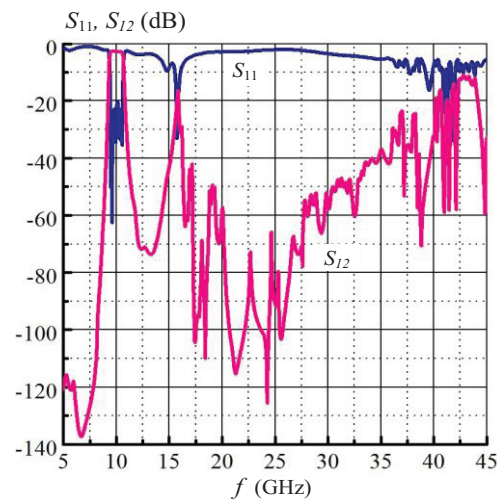


Fig. 7. Simulated  $S$ -parameters of the proposed filter with DGS.

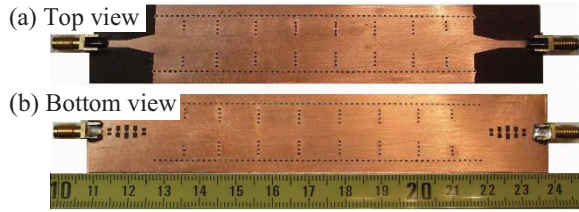


Fig. 8. The photo of the fabricated filter.

Table 5: Comparison of the simulated performance of the proposed filter with recently published ones

Filter	FBW (%)	S <sub>11</sub> (dB)	S <sub>21</sub> (dB)	End of the Stopband (GHz)
[9]	5.8	<-22	-1.7	16.7
[10]	7.6	<-14	-1.3	14
[11]	8	<-27	-2	25
[12]	5	<-12.5	-4.3	20.2
[13]	18.7	<-20	-2.3	12.2
[14]	4	<-10	-3.8	12.6
[15]	4.9	<-8	-1	18.2
[16]	4.9	<-17.6	-2.6	13.8
This paper	13	<-23.6	-3	40.6

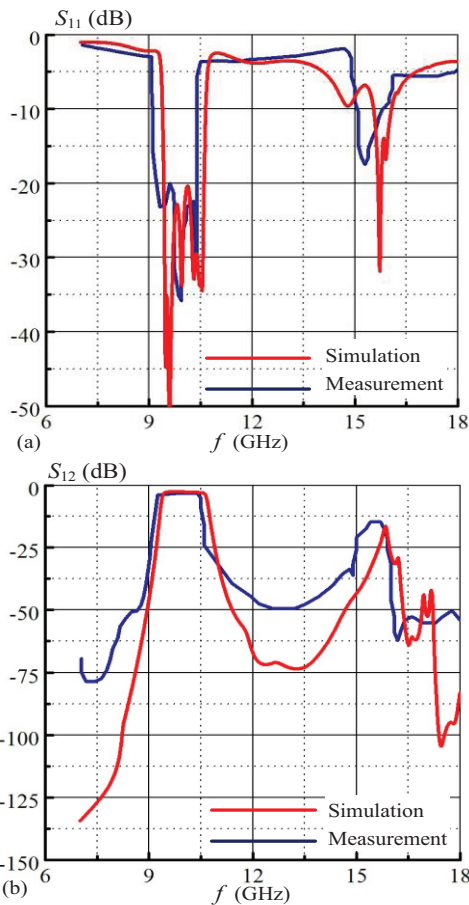


Fig. 9. Simulation and measurement results of the fabricated filter: (a) S<sub>11</sub>, and (b) S<sub>12</sub> in a narrowband region.

### VI. CONCLUSION

An X-band H-plane filter cascaded with a DGS structure is designed based on neural network and numerically investigated using HFSS in this paper. Back propagation neural network is applied to optimize the parameters of the proposed filter. Results show that, measured reflection coefficient and transmission coefficient are -20 dB and -3.7 dB respectively. In addition, a very good agreement is obtained between measured results and those obtained by simulation. Moreover, it is concluded that neural network is very useful for optimizing microwave devices.

### REFERENCES

- [1] D. Deslandes and K. Wu, "Integrated microstrip and rectangular waveguide in planar form," *IEEE Microw. Wireless Compon. Lett.*, vol. 11, no. 2, pp. 68-70, Feb. 2001.
- [2] D. F. Guan, Z. P. Qian, Y. S. Zhang, and Y. Cai, "A hybrid SIW and GCPW guided-wave structure coupler," *IEEE Microw. Wireless Compon. Lett.*, vol. 24, iss. 8, pp. 518-520, 2014.
- [3] H. Dashti, M. Shahabadi, and M. H. Neshati, "SIW cavity-backed slot antennas with improved gain," *21<sup>st</sup> Iranian Conference on Electrical Engineering*, pp. 1-4, 2013.
- [4] F. F. He, K. Wu, W. Hong, L. Han, and X. P. Chen, "Low-cost 60-GHz smart antenna receiver subsystem based on substrate integrated waveguide technology," *IEEE Transactions on Microwave Theory and Techniques*, vol. 60, iss. 4, pp. 1156-1165, 2012.
- [5] X. Zou, C. Tong, and D. Yu, "Design of an X-band symmetrical window bandpass filter based on substrate integrated waveguide," *Cross Strait Quad-Regional Radio Science and Wireless Technology Conference*, pp. 571-574, 2011.
- [6] M. Salehi and E. Mehrshahi, "A closed-form formula for dispersion characteristics of fundamental SIW mode," *IEEE Microwave and Wireless Components Letters*, vol. 21, pp. 4-6, 2011.
- [7] *Fecit R&D Center of Science and Technology Products, Neural Network Theory and Matlab Implementation*, Beijing: Publishing House of Electronics Industry, 2005.
- [8] P. Vagner and M. Kasal, "Design of microstrip lowpass filter using DGS," *Radio Elektronika, 17<sup>th</sup> International Conference*, pp. 1-4, 2007.
- [9] J. D. Martinez, S. Sirci, M. Taroncher, and V. E. Boria, "Compact CPW-fed combline filter in substrate integrated waveguide technology," *IEEE Microwave and Wireless Components Letters*, vol. 22, pp. 7-9, 2012.
- [10] L. S. Wu, Y. X. Guo, J. F. Mao, and W. Y. Yin, "Design of a substrate integrated waveguide balun filter based on three-port coupled-resonator circuit

model," *IEEE Microwave and Wireless Components Letters*, vol. 21, pp. 252-254, 2011.

- [11] Y. Fei, L. Rui-zhu, and Y. Hong-xi, "Canonical ridged SIW filters in LTCC," *IEEE International Conference on Microwave Technology & Computational Electromagnetics*, pp. 190-192, 2011.
- [12] G. S. Huang and C. H. Chen, "Non uniformly folded waveguide resonators and their filter applications," *IEEE Microwave and Wireless Components Letters*, vol. 20, pp. 136-138, 2010.
- [13] P. Hong and H. Jin, "Half mode substrate integrated waveguide bandpass filter using cross-coupling," *International Conference on Computational Problem-Solving*, pp. 196-198, 2012.
- [14] F. T. Ladani, S. Jam, and R. Safian, "A novel X-band bandpass filter using substrate integrated waveguide resonators," *IEEE Asia-Pacific Conference on Applied Electromagnetics*, pp. 1-5, 2010.
- [15] E. Mehrshahi, M. Salehi, and R. Rezaiesarlak, "Substrate integrated waveguide filters with stopband performance improvement," *International Conference on Microwave and Millimeter Wave Technology*, pp. 2018-2020, 2010.
- [16] L. S. Wu, X. L. Zhou, and W. Y. Yin, "A novel multilayer partial H-plane filter implemented with folded substrate integrated waveguide," *IEEE Microwave and Wireless Components Letters*, vol. 19, pp. 494-496, 2009.



**Zahra Sadat Tabatabaeian** was born in Mashhad, Iran on May 7, 1988. She received her B.Sc. and M.Sc. degrees in Electrical Engineering from Ferdowsi University of Mashhad, Iran in 2010 and 2012 respectively, and now she is currently working toward her Ph.D.

degree in Electrical Engineering at Ferdowsi University of Mashhad. Her research interests include microwave passive circuit design and meta-materials.



**Mohammad H. Neshati** was born in Yazd, Iran. He received his B.Sc. in Electrical Engineering from Isfahan University of Technology, Isfahan, Iran; M.Sc. degree from Amir-Kabir University of Technology, Tehran, Iran and Ph.D. from the University of Manchester (UMIST),

England in 2000. Since 2006 he has been with the Department of Electrical Engineering of Ferdowsi University of Mashhad Iran, where he is Associate Professor. His current research includes electromagnetic, antenna theory and design, microwave active and passive circuit design.

# A Circular Slot UWB Antenna with Independently Tunable Quad-Band Filtering Characteristics

Yingsong Li<sup>1</sup>, Wen Zhang<sup>2</sup>, and Wenhua Yu<sup>1</sup>

<sup>1</sup> College of Information and Communications Engineering  
Harbin Engineering University, Harbin 150001, China  
liyingsong@ieee.org, liyingsong@hrbeu.edu.cn

<sup>2</sup> Huawei Technologies Co., Ltd.  
Shanghai, China

<sup>3</sup> 2COMU, Inc.  
4031 University Drive, Suite 100, Fairfax, VA 22030, USA  
wenyu@2comu.com

**Abstract** — An effective design method is proposed to develop an excellent performed quad-band filtering UWB antenna. A spiral-shaped stub (SSS), two T-shaped stubs (TSSs) and an arc-shaped slot (ASS) are utilized to realize the proposed quad-band filtering characteristics. The independently tunable band-notched characteristics are carried out by adjusting the dimensions of SSS, TSS and ASS respectively. The proposed quad-band filtering UWB antenna is fabricated and measured for validation. The simulated and measured results show that this antenna can provide a wide bandwidth covering 3.1-10.6 GHz with four band notched characteristics and omnidirectional radiation patterns in its H-plane, which render it suitable for indoor UWB communication applications.

**Index Terms** — Notch band, quad-band notch characteristics, stub, UWB antenna.

## I. INTRODUCTION

Since the Federal Communication Commission allocated the 3.1-10.6 GHz band for commercial ultra-wideband (UWB) communication systems, many research efforts have been put into UWB communication technology in both industry and academy [1]. As one of the key components of the UWB system, designing of UWB antennas has been widely studied to achieve wide impedance matching, stable radiation patterns and small size for various portable UWB systems [2-7]. However, some existing narrowband systems over the allocated UWB frequency band have been extensively studied and widely used, such as 3.3-3.7 GHz WiMAX band, 3.9-4.2 GHz C-band, 5.15-5.825 GHz WLAN band, the downlink of X-band satellite communication system operating at 7.25-7.75 GHz and ITU band operating at

8.025-8.4 GHz. As a result, these existing narrowband systems may give potential interferences to the UWB system. In order to eliminate or reduce the unwanted interferences from mentioned narrowband systems above, a great number of UWB antennas with single or dual band notched characteristics have been designed and their performances have been well investigated in the previously arts [8-15]. Most of these UWB antennas have only single or two notch bands, which limit their applications when more than two narrowband interferences happen simultaneously. Recently, several UWB antennas with triple or quadruple band notched have been designed and their performance has been experimentally verified [16-21]. However, most of these band notches are realized by etching various slots on the radiating patch or ground plane, which may leak extra electromagnetic waves. In addition, parasitic strips, open circuit stubs and stepped impedance resonator [22-29] are also employed to develop multiple notch band UWB antennas. Although several band-notched UWB antennas have been designed with triple or four notch bands, they have complex structures which include holes and multilayered substrates. Additionally, some of these four band-notched UWB antennas are large in size, which limit their utilization. Owing to the limits of the space in the modern portable terminals, it is a real challenge to design a compact UWB antenna with multiple band-notched characteristics.

For these reasons, an effective design method is proposed to develop an excellent quad-band filtering UWB antenna. The proposed antenna is designed on the basis of a wide slot UWB antenna with a ring shaped radiating patch. A spiral-shaped stub (SSS), two T-shaped stubs (TSSs) and an arc-shaped slot (ASS) are employed to develop quad-band filtering bands operating at 3.5 GHz,

4.1 GHz, 5.5 GHz and 7.8 GHz to filter out the potential narrowband interferences from WiMAX, C-band, WLAN and X-band. To utilize the limited space, the T-shaped stubs are inserted into the ring shaped radiating patch with an isolation element. By optimizing the dimensions and position of the SSS, TSSs and ASS, four designated band notches are achieved to prevent the interferences from the aforementioned narrowband systems. The proposed antenna is fabricated and measured to verify the design effectiveness with respect to its frequency characteristics, including impedance bandwidth, tunable notch band, radiation patterns and gain.

## II. ANTENNA DESIGN

The configuration of the proposed quad-band filtering UWB antenna is demonstrated in Fig. 1. The proposed antenna is printed on a substrate whose relative permittivity, loss tangent and thickness are 2.65, 0.002, and 1.6 mm, respectively. For this antenna, it consists of a wide slot with circular shaped that is etched on the CPW ground plane, a circular ring-shaped radiating patch, an SSS, two TSSs, an ASS, an isolation element between the upper TSS and the lower TSS, and a CPW ground plane together with a 50-Ohm CPW feed structure. The 50-Ohm CPW feed structure is comprised of a CPW-fed transmission line whose width is  $W1=3.6$  mm, and a gap  $g$  with a width of 0.2 mm. In this design, the upper TSS is used to generate the lowest notch band operating at 3.5 GHz band, while the 3.9-4.2 GHz C-band is given by the lower TSS. The SSS is employed to provide a notch operating at 5.5 GHz WLAN band and the ASS is designed to prevent the potential interferences from the ITU band or X-band around 8 GHz. The proposed antenna has been investigated and optimized by the HFSS. The center frequencies of these notch bands can be tuned by adjusting the dimensions of the SSS, TSSs and ASS to render the proposed notches suitable to filter out the aforementioned narrowband interferences. The antenna is well optimized and the optimal structure parameters are listed as follows:  $L=32$  mm,  $W=24$  mm,  $L1=5.9$  mm,  $L2=7$  mm,  $L3=3.7$  mm,  $L4=4.6$  mm,  $L5=1.9$  mm,  $L6=2.3$  mm,  $L7=2.8$  mm,  $L8=4.2$  mm,  $L9=1.1$  mm,  $W1=3.6$  mm,  $R=11.8$  mm,  $r1=6.7$  mm,  $r2=5$  mm,  $r3=12.5$  mm,  $r4=12.3$  mm,  $g=0.2$  mm,  $g1=0.5$  mm,  $g2=0.3$  mm,  $g3=0.2$  mm,  $d1=0.8$  mm,  $d2=0.8$  mm,  $d3=0.6$  mm,  $d4=0.4$  mm,  $d5=2.1$  mm,  $d6=0.4$  mm,  $s=0.2$  mm, and  $\Theta=29^\circ$ .

The design procedure of the proposed quad-band filtering UWB antenna is summarized as follows. Firstly, a circular wide slot UWB antenna is designed to cover a wide UWB band ranging from 3.1 GHz to 10.6 GHz. Next, the SSS, ASS and TSSs are integrated into the circular wide slot UWB antenna step by step to reject the designated four narrowband bands. Each band-notch

structure will be integrated into the UWB antenna to fine-tune the dimensions. Finally, all four band-notched elements and the UWB antenna are put together and optimized for desired performance. In this design, each band-notch structure, namely ASS, SSS, upper TSS and lower TSS, is responsible for creating four frequency filtering bands. Here, total resonance length of each notch band is mainly determined by the lengths of the band-notch structures. The center frequency of each band-notch is approximately given by using the following formulas:

$$f_{notch} = \frac{c}{2L_{ASS(or\ TSSs\ or\ SSS)}\sqrt{\epsilon_{eff}}}, \quad (1)$$

$$\epsilon_{eff} = \frac{\epsilon_r + 1}{2}, \quad (2)$$

where  $L_{ASS(or\ TSSs\ or\ SSS)}$  is the total resonance length of each band-notch structure,  $\epsilon_r$  is the relative permittivity,  $\epsilon_{eff}$  is the effective dielectric constant and  $c$  is the speed of light. At the beginning, the initial lengths of the ASS, SSS and TSSs are theoretically calculated based on the above formulas and then a simulation solver HFSS is utilized to get the optimal dimensions to tune the desired center frequencies of the notches.

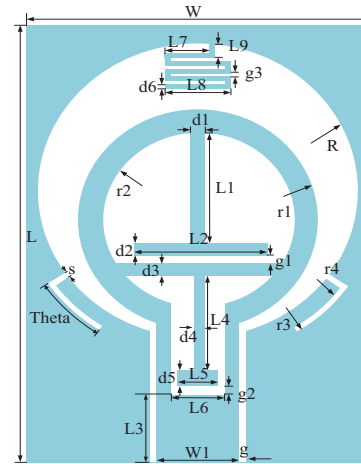


Fig. 1. Geometry of the proposed antenna.

## III. PERFORMANCE OF THE PROPOSED ANTENNA

In this section, parameters  $L1$ ,  $L4$ ,  $L8$  and  $\Theta$  are selected to investigate the independently tunable band-notched characteristics. Figure 2 (a) shows the effects of  $L1$  on the impedance matching of the proposed quad-band filtering UWB antenna. It can be seen that the center frequency of the lowest notch band moves to the low frequency with an increase of  $L1$ . When  $L1$  increases from 5.8 mm to 6.2 mm, the center frequencies of the lowest notch band move from 3.6 GHz to 3.0 GHz. This is attributed to the prolonged resonance length of

upper TSS and the coupling between the upper TSS and the isolation element.

Figure 2 (b) depicts effects of L4 on the band-notched function. It is found that the center frequency of the 4.2 GHz notch band shifts toward low frequency when L4 increase from 4.1 mm to 5.1 mm, which is caused by the increased resonance length of lower TSS. Additionally, the upper and lower TSS can affect both the lowest notch band and 4.2 GHz notch band because they interact with each other through the isolation element. Figure 2 (c) gives the effects of the parameter L8 on the notch band characteristics. It is observed that the center frequency of 5.5 GHz notch band shifts from 5.7 GHz to 5.2 GHz as L8 increasing from 3.9 mm to 4.5 mm. Additionally, the center frequencies of the other notch bands remain constant. The expended L8 not only increases the resonance of the SSS but also enhances the coupling between the SSS and the circular slot. Thus, the notch moves from high frequency to low frequency with a reducing notch bandwidth. Figure 2 (d) demonstrates the effects of Theta on the tunable notch band characteristics. We note that the center frequency of the highest notch band shifts toward lower frequency with an increment of Theta. With an increase of Theta ranging from 27° to 30°, the resonance length of the ASS is prolonged, and hence, the center frequency of the highest notch band corresponding to the quarter wavelength resonance moves to low frequency. From the discussions above, we can conclude that the center frequencies of these proposed notch bands are tunable by adjusting the dimensions of the ASS, TSSs and SSS. The lowest band-notch is generated by the upper TSS, while the 4.2 GHz band-notch is produced by the lower TSS. The 5.5 GHz WLAN band-notch is realized by using an SSS inserted inside of the circular wide slot and the highest band-notch is implemented by the ASS that is embedded in the CPW ground plane.

In order to further understand the principle of the proposed antenna, the surface current distributions are investigated by the HFSS and the simulated results are shown in Fig. 3. Figure 3 (a) shows the surface current distribution at 3.5 GHz notch band. It is found that the current distribution mainly flows along the upper T-shaped stub. However, the upper T-shaped stub has some effects on the lower T-shaped stub via the isolation element inserted in the circular ring radiating patch. As for the 4.2 GHz band-notch, the surface current mainly focuses on the lower T-shaped stub, which can determine its center frequency, and the result is shown in Fig. 3 (b). When the band-notch appears at 5.5 GHz, the surface current concentrates on the spiral shaped stub and its effect is shown in Fig. 3 (c). In this case, the current on the CPW ground plane, T-shaped stubs and the arc-shaped slot are small. Thus, the spiral shaped stubs mainly affect the band-notch characteristics of the 5.5 GHz WLAN band. As for the 7.8 GHz notch band, it can be

observed that the strong current distribution flows along the arc-shaped slot.

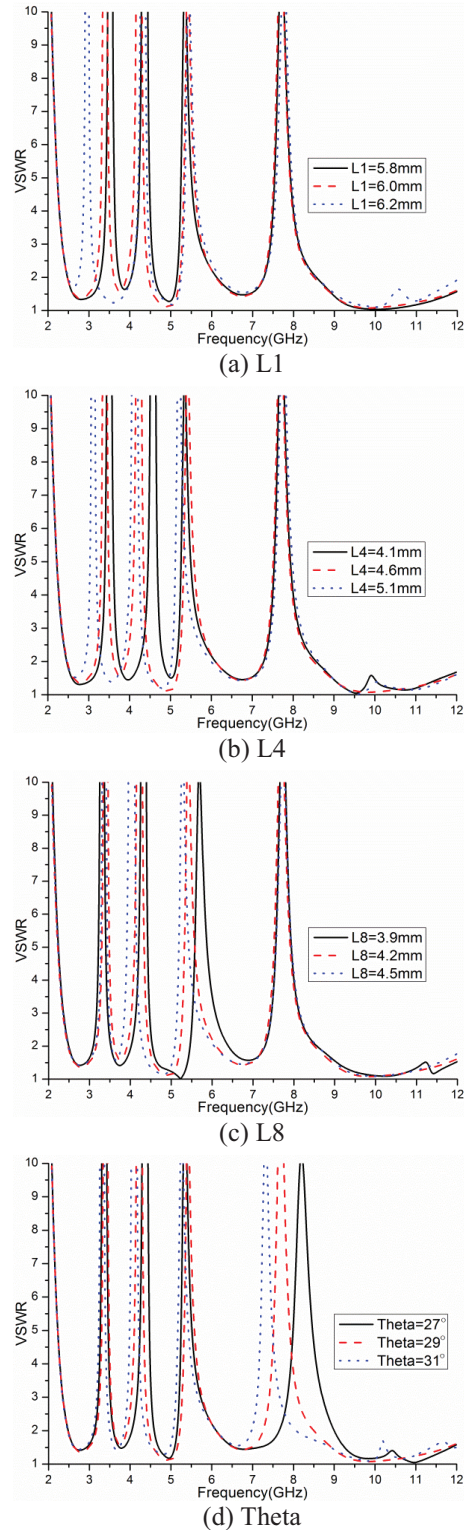


Fig. 2. Parameter effects on the band-notched characteristics of the proposed antenna.

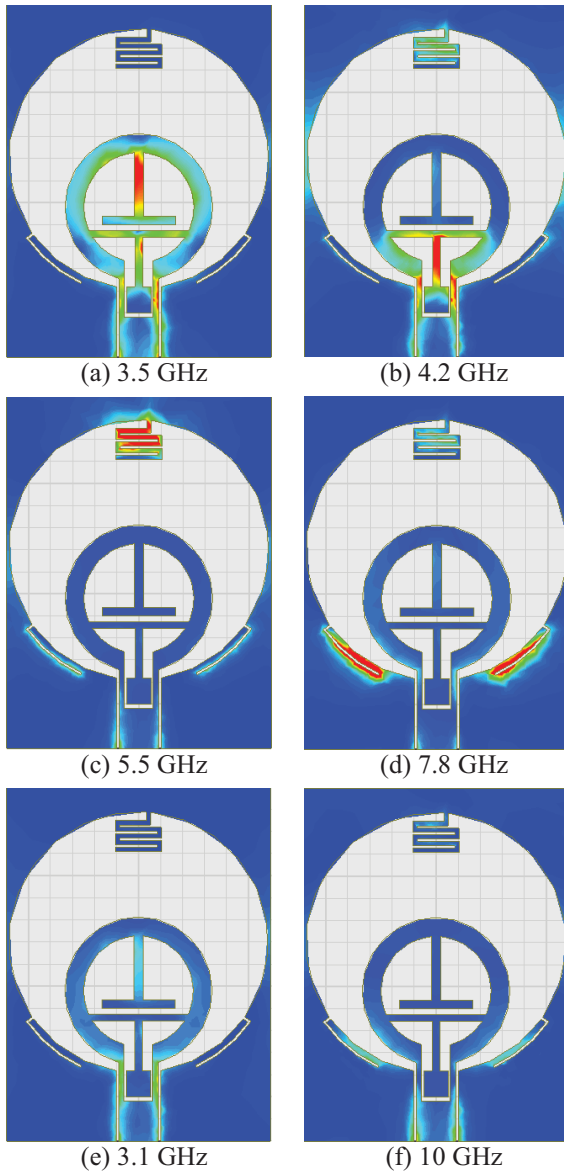


Fig. 3. Current distribution of the proposed antenna.

From the current distributions, we can see that the current distributions mainly concentrate on the corresponding band-notch structures, and hence, affect the band-notch characteristics that have been verified in Fig. 2. Thus, we can say that the energy cannot effectively radiate at the above designated notch bands, and hence, four notch bands are formed to prevent the potential narrowband interferences from the mentioned narrowband systems. At the operating bands such as 3.1 GHz and 10 GHz, the surface currents distribute on the CPW-fed structures and the circular wide-slot, while the current on the arc-shaped slot, T-shaped stubs and spiral shaped stub are weak; which indicates that the existence of band-notch structures has little effects on the UWB antenna at pass-band frequencies.

#### IV. RESULTS AND DISCUSSIONS

In order to verify the performance of the quad-band filtering UWB antenna, the proposed antenna has been optimized, fabricated and measured in an anechoic chamber. The prototype of the fabricated antenna is shown in Fig. 4. The measured impedance characteristics of the fabricated antenna in comparison with the optimized curve are shown in Fig. 5, which is obtained by using Agilent N5224A vector network analyzer. It can be seen that the proposed antenna covers the entire UWB bandwidth except for the designated four notch bands, which aim to suppress the potential interferences from 3.5 GHz WiMAX band, 4.2 GHz C-band, 5.5 GHz WLAN band and 8 GHz X-band. Also, the measured VSWR agrees well with the simulated one, which helps validate the results from the HFSS. The arc-shaped slot, T-shaped stubs and spiral shaped stub function as filters, which produce non-resonance characteristics in the corresponding notch bands. The deficiencies between the measured and simulated VSWRs are attributed to the fabrication tolerance and manual welding inaccuracies.



Fig. 4. Fabricated antenna.

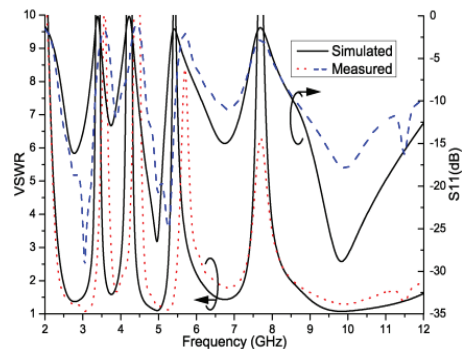


Fig. 5. Measured VSWR and  $S_{11}$  of the antenna.

The radiation patterns of the proposed quad-band-notched UWB antenna are measured at 3.1 GHz, 3.9 GHz, 5.0 GHz, 6.5 GHz and 9.0 GHz, which are shown in Fig. 6. It is found that nearly omnidirectional radiation patterns are obtained in the H-plane, while a figure of 8-like radiation patterns is achieved. Though the fabricated antenna can provide omnidirectional radiation patterns

that are suitable for UWB applications, the radiation patterns are distorted in the E-plane at high frequencies, which is caused by the leaky electromagnetic waves given by the designed band-notch structures. The measured gains versus the frequency are obtained by comparing the proposed quad-band-notched UWB antenna to that of a standard horn antenna in an anechoic chamber and the measured results are shown in Fig. 7. It is clearly shown that there is a significant gain reduction at the notch bands, which drop quickly to -5.2 dBi at WiMAX band, -3.8 dBi at 4.2 GHz C-band, -2.9 dBi at WLAN band and -2.2 dBi at X-band. Additionally, the proposed antenna has a stable gain in the entire UWB operating band out of the designed four notch bands. From the discussions above, we can see that the proposed UWB antenna can provide good quadruple frequency rejection characteristic and nearly omnidirectional radiation patterns. The radiation efficiencies of the proposed antenna at the entire UWB operation band are above 84%, while the radiation efficiencies are 25%, 29%, 40% and 48% at the notches for WiMAX band, C-band, WLAN band and X-band, respectively.

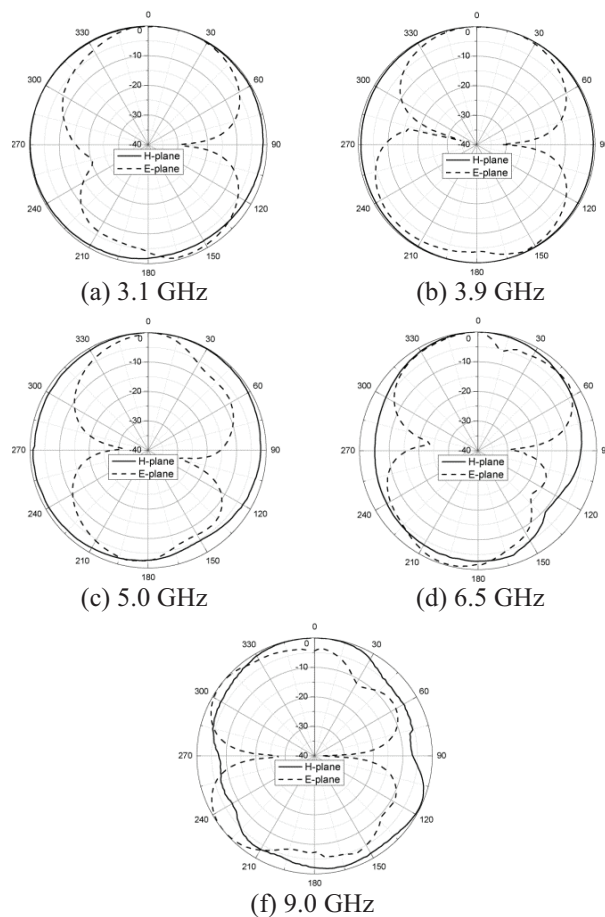


Fig. 6. Radiation patterns of the proposed antenna.

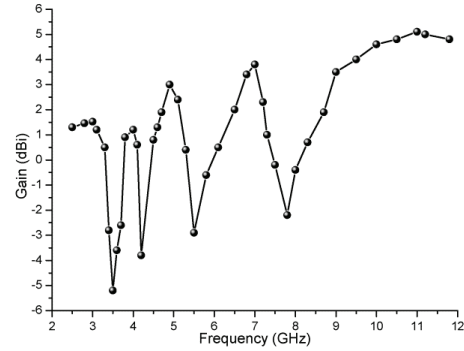


Fig. 7. Gains of the proposed antenna.

## V. CONCLUSION

A CPW-fed quad-band-notched UWB antenna with independently tunable band-notch characteristics has been proposed to solve the interference problem and its performance has been verified both numerically and experimentally. The quad-band-notched characteristics are realized by using slot and stub technologies, namely, an arc-shaped slot, a spiral shaped stub and two T-shaped stubs. The independent tunable band-notch characteristics, current distribution, radiation patterns and gains have been studied and discussed in detail. The numerical and experimental results demonstrated that the proposed antenna had a wide bandwidth, quad-band-notch characteristics, stable omnidirectional radiation patterns and appropriate gains, indicating that the antenna is a good candidate for band-notch UWB communication applications.

## ACKNOWLEDGMENT

This work was supported in part by a grant from National Natural Science Foundation of China (No. 51209055), Pre-Research Fund of the 12<sup>th</sup> Five-Year Plan (No. 4010403020102), the Science and Technology Innovative Talents Foundation of Harbin (2013RFXXJ083) and Fundamental Research Funds for the Central Universities (No. HEUCFD1433, HEUCF1508).

## REFERENCES

- [1] M. G. Di Benedetto, T. Kaiser, A. F. Molish, I. Oppermann, C. Politano, and D. Porcino, "UWB communications systems: a comprehensive overview," *EURASIP Signal Processing and Communications*, Hindawi, 2006.
- [2] J. Liang, C. C. Chiau, X. Chen, and C. G. Parini, "Study of a printed circular disc monopole antenna for UWB systems," *IEEE Transactions on Antennas and Propagation*, vol. 53, no. 11, pp. 3500-3504, 2005.
- [3] E. S. Angelopoulos, A. Z. Angelopoulos, D. I. Kaklamani, A. A. Alexandridis, F. Lazarakis, and

- K. Dangakis, "Circular and elliptical CPW-fed slot and microstrip-fed antennas for ultrawideband applications," *IEEE Antennas and Wireless Propagation Letters*, vol. 5, pp. 294-297, 2006.
- [4] R. Azim, M. T. Islam, and N. Misran, "Compact tapered-shape slot antenna for UWB applications," *IEEE Antennas and Wireless Propagation Letters*, vol. 10, pp. 1190-1193, 2011.
- [5] R. Azim, M. T. Islam, N. Misran, S. W. Cheung, and Y. Yamada, "Planar UWB antenna with multi-slotted ground plane," *Microwave and Optical Technology Letters*, vol. 53, no. 5, pp. 966-968, 2011.
- [6] M. Koohetani and M. Golpour, "Compact rectangular slot antenna with a novel coplanar waveguide fed diamond patch for ultra wideband applications," *Microwave and Optical Technology Letters*, vol. 52, no. 2, pp. 331-334, 2010.
- [7] S. Singhal, T. Goel, and A. K. Singh, "Inner tapered tree-shaped fractal antenna for UWB applications," *Microwave and Optical Technology Letters*, vol. 57, no. 3, pp. 559-567, 2015.
- [8] Y. S. Li, X. D. Yang, C. Y. Liu, and T. Jiang, "Compact CPW-fed ultra-wideband antenna with dual band-notched characteristics," *Electronics Letters*, vol. 46, no. 14, pp. 967-968, 2010.
- [9] Q-X. Chu and Y-Y. Yang, "A compact ultrawideband antenna with 3.4/5.5 GHz dual band-notched characteristics," *IEEE Transactions on Antennas and Propagation*, vol. 56, no. 12, pp. 3637-3644, 2008.
- [10] S. Tripathi, A. Mohan, and S. Yadav, "A compact UWB antenna with dual 3.5/5.5 GHz band-notched characteristics," *Microwave and Optical Technology Letters*, vol. 57, no. 3, pp. 551-556, 2015.
- [11] J. Xu, D-Y. Shen, G-T. Wang, X-H. Zhang, X-P. Zhang, and K. Wu, "A small UWB antenna with dual band-notched characteristics," *International Journal of Antennas and Propagation*, vol. 2012, pp. 1-7, 2012.
- [12] M. Mehranpour, J. Nourinia, Ch. Ghobadi, and M. Ojaroudi, "Small square monopole antenna with inverted T-shaped notch in the ground plane for UWB application," *IEEE Antennas and Wireless Propagation Letters*, vol. 8, pp. 728-731, 2009.
- [13] N. Ojaroudi, M. Ojaroudi, and H. Ebarhimian, "Band-notched UWB microstrip slot antenna with enhanced bandwidth by using a pair of C-shaped slots," *Microwave and Optical Technology Letters*, vol. 54, no. 2, pp. 515-518, 2012.
- [14] N. Ojaroudi, M. Ojaroudi, and N. Ghadimi, "Dual band-notched small monopole antenna with novel W-shaped conductor backed-plane and novel T-shaped slot for UWB applications," *IET Microwaves, Antennas & Propagation*, vol. 7, no. 11, pp. 8-14, 2013.
- [15] D. H. Lee, H. Y. Yang, and Y. K. Cho, "Tapered slot antenna with band-notched function for ultrawideband radios," *IEEE Antennas and Wireless Propagation Letters*, vol. 11, pp. 682-685, 2012.
- [16] T. D. Nguyen, D. H. Lee, and H. C. Park, "Very compact printed triple band-notched UWB antenna with quarter-wavelength slots," *IEEE Antennas and Wireless Propagation Letters*, vol. 11, pp. 411-414, 2012.
- [17] C. C. Lin, P. Jin, and R. W. Ziolkowski, "Single, dual and tri-band-notched ultrawideband (UWB) antennas using capacitively loaded loop (CLL) resonators," *IEEE Transactions on Antennas and Propagation*, vol. 60, no. 1, pp. 102-109, 2011.
- [18] M. T. Islam, R. Azim, and A. T. Mobashsher, "Triple band-notched planar UWB antenna using parasitic strips," *Progress In Electromagnetics Research*, vol. 129, pp. 161-179, 2012.
- [19] Z. H. Wu, F. Wei, X-W. Shi, and W-T. Li, "A compact quad band-notched UWB monopole antenna loaded one lateral I-shaped slot," *Progress In Electromagnetics Research*, vol. 139, pp. 303-315, 2013.
- [20] J. Xu, D. Shen, J. Zheng, X. Zhang, and K. Wu, "A novel miniaturized UWB antenna with four band-notches," *Microwave and Optical Technology Letters*, vol. 55, no. 6, pp. 1202-1206, 2013.
- [21] M. T. Islam, R. Azim, and A. T. Mobashsher, "Triple band-notched planar UWB antenna using parasitic strips," *Progress In Electromagnetics Research*, vol. 129, pp. 161-179, 2012.
- [22] Y. Li, W. Li, and Q. Ye, "A CPW-fed circular wide-slot UWB antenna with dual-notch bands by combining slot and parasitic element techniques," *Microwave and Optical Technology Letters*, vol. 56, no. 5, pp. 1240-1244, 2014.
- [23] Y. Li, W. Li, and W. Yu, "A switchable UWB slot antenna using SIS-HSIR and SIS-SIR for multi-mode wireless communications applications," *Applied Computational Electromagnetics Society Journal*, vol. 27, no. 4, pp. 340-351, 2012.
- [24] X. Qing and Z. N. Chen, "Compact monopole-like slot antenna and band-notched design for ultrawideband applications," *Radio Science*, vol. 44, no. 2, pp. 1-13, 2009.
- [25] M. Ojaroudi, G. Ghanbari, N. Ojaroudi, and C. Ghobadi, "Small square monopole antenna for UWB applications with variable frequency band-notch function," *IEEE Antennas and Wireless Propagation Letters*, vol. 8, pp. 1061-1064, 2009.
- [26] Y. Li, W. Li, and R. Mittra, "Miniaturized CPW-fed UWB antenna with dual frequency rejection bands using stepped impedance stub and arc-shaped parasitic element," *Microwave and Optical Technology Letters*, vol. 56, no. 4, pp. 783-787,

- 2014.
- [27] S. J. Wu, C. H. Kang, K. H. Chen, and J. H. Tarng, "Study of an ultrawideband monopole antenna with a band-notched open-looped resonator," *IEEE Transactions on Antennas and Propagation*, vol. 58, no. 6, pp. 1890-1897, 2010.
- [28] J. R. Kelly, P. S. Hall, and P. Gardner, "Band-notched UWB antenna incorporating a microstrip open-loop resonator," *IEEE Transactions on Antennas and Propagation*, vol. 59, no. 8, pp. 3045-3048, 2011.
- [29] Y. Liu, Z. Chen, and S. Gong, "Triple band-notched aperture UWB antenna using hollow-cross-loop resonator," *Electronics Letters*, vol. 50, no. 10, pp. 728-730, 2014.

# Dual Band Bandpass Filter Using Multilayer Structure

S. Majidifar<sup>1</sup> and S-V. Makki<sup>2</sup>

<sup>1</sup> Department of Electrical Engineering  
Kermanshah University of Technology, Kermanshah, Iran  
s.majidi@kut.ac.ir

<sup>2</sup> Department of Electrical Engineering  
Razi University, Kermanshah, Iran  
v.makki@razi.ac.ir

**Abstract** — In this paper, a new method to design a dual band bandpass filter (BPF) is presented. This method is based on a simple principle: different substrates (dielectric constants) will result different resonant frequencies for a resonator. The basic structure of this method is studied and then a planar band pass resonator is designed to utilize in this structure. Response of the proposed dual layer filter is tuned using resonator shifting and resonator scaling. In addition to improve the filter response, resonator shifting improves the filter size. The final structure is designed, fabricated and measured and simulation results are in good agreement with measured values. The central frequencies of this dual band BPF are  $f_1=3.85$  GHz and  $f_2=5.3$  GHz and a deep transition zero at 4.57 GHz, guarantees isolation between passbands.

**Index Terms** — Coupling, dual band, effective dielectric constant, multilayer structure.

## I. INTRODUCTION

With the rapid development of modern wireless technologies, multi-service communication systems have become a widespread tendency. The dual-wideband bandpass filter (BPF) is an important requirement of these systems. In order to meet these requirements, various approaches were applied to design different kinds of the dual band BPFs. Parallel connect of two single-band BPFs as an important method in dual-band BPFs design (method 1) was presented in [1], [2]. This method requires a complex design process and large circuit size. In [1], the authors have presented a multilayer dual-band BPF in a low-temperature co-fired ceramic (LTCC) substrate for ultra-wideband applications. This bandpass filter consists of two wideband bandpass filters and matching circuits. A class of the wideband dual band BPFs with controllable response was proposed in [2]. In this approach, two multi-mode resonators (MMRs) with short-circuited

stubs have been parallel connected to form the basic structure of the proposed dual-band BPF.

One of the direct design methods of the dual-band BPFs (method 2) formed by inserting a bandstop filtering response in between a wide passband to divide it into two passbands [3], [4]. A dual-band filter consists of a bandstop filter and a wideband bandpass filter in a cascade connection, was proposed in [3]. In this structure, the bandstop filter has been implemented using a coupled-serial-shunted line, while the wideband bandpass filter was constructed using a serial-shunted line configuration. In [4], a dual-wideband BPF was presented, which is divided into two parts: the wideband passband filter and the narrowband stopband filter. Both filters have been designed with conventional synthesis methods, under the assumption that the common connecting lines serve as J- and K-inverters simultaneously. In this approach, tuning is still needed after combining the BPF and BSF. Another type of dual-band BPFs was formed by applying the fundamental-order and its higher order resonances to build up various dual-band BPFs (method 3), as discussed in [5]. A dual-band response was obtained via a large perturbation in a single resonator and second-order dual-mode dual-band filters were realized by a new cascading principle in [5]. Coupling coefficients between the two resonators in both bands of this filter is controlled independently, but the band control in this approach is difficult compared to the mentioned methods. On the other hand, odd/even-mode methods (method 4) were applied to form a different coupling path for each passbands of a dual band BPF, as discussed in [6-9]. A microstrip dual-band BPF using a single quadruple-mode resonator (QMR) has been proposed in [6]. According to the even/odd-mode method, two pairs of symmetrical resonant modes are shown in this structure. In [7], the authors have presented a tri-stubs loaded multimode resonator (TSLMR) for designing dual-band BPFs. The TSLMR produces four splitting modes. A pair of even/odd modes is used to

form the first passband, while another pair produces the second passband. This descriptive method cannot be used in the complex structures. The configuration of a multi band BPF can be based on either multilayer [10-12] or single layer [13]. In [10], a compact dual-layered quad-band (DLQB) BPF was presented to provide four passbands at the desired frequencies. The designed filter was fabricated on two FR4 boards. This proposed DLQB-BPF consists of two L-shaped resonators on the top layer and two coupled SIRs on the second layer. The bottom of the second layer is the ground plane. Based on open-loop resonators (OLRs), an independently tunable dual-band (ITDB) BPF was presented in [11]. The top layer of the proposed ITDB BPF is composed of transmission feed lines and OLRs in a SIR structure. The bottom layer is constructed by OLRs in an asymmetrical SIR with a defect-grounded structure. A multilayer dual-band BPF embedded in a low temperature co-fired ceramics (LTCC) has been presented in [12].

Some of the novel dual-band BPFs have proposed having a compact size, high selectivity and high isolation [14-16]. Many of the recent researches have focused on tunable or reconfigurable BPFs for applications in the multi-band communication systems [17-20]. Authors in [17] have presented a novel multilayer dual-band filter using two dual-mode cross-slotted patch resonators. In this work, the operating frequency and bandwidth in each passband can be individually controlled and the design procedure based on the coupling matrix has been presented. A novel approach to the design of tunable dual-band BPF was presented in [18]. The proposed filter structure offers two tunable passbands, as well as a fixed first passband and controllable second passband. In this filter, the first passband center frequency has a tunable range of 34.14% from 0.85 to 1.2 GHz, and second passband center frequency has a tunable range of 41.81% from 1.40 to 2.14 GHz. A new varactor-tuned microstrip dual-band BPF has been investigated in [19]. In this approach, by employing the dual coupling paths, the two passbands can then be fully controlled and designed independently. In addition, for the electronic tuning, three varactors are loaded on the open-ends of each resonator. There is an increasing interest in utilizing the high-temperature superconducting (HTS) structures in dual band BPFs design. In [20], a miniaturized high-temperature superconducting dual-band bandpass filters (DBPFs) using stub loaded meander line resonators has been proposed. In this approach, the center frequencies of the bands can be independently controlled. The bandwidths of the DBPF can be flexibly adjusted using a capacitance-loaded microstrip line between the resonators.

In this paper, a dual band BPF is presented using a simple principle: different dielectric constant results in different resonant frequencies. This condition creates using multilayer configuration. To verify the validity of

the proposed method, a dual-band BPF prototype is designed, fabricated, and measured. Compactness, simple design process and tunable passbands are realized by this method.

## II. BASIC STRUCTURE

Figure 1 shows the basic structure of the dual band BPF. This structure is composed of two equal bandpass resonators (R1 and R2), which are coupled together. The first resonator is placed on a substrate with the relative dielectric constant of  $\epsilon_r$  and thickness of  $2H$  and the top layer of this resonator is free space. The second resonator is surrounded by two substrates with the relative dielectric constant of  $\epsilon_r$ .

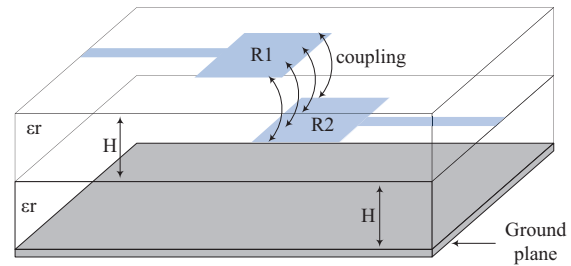


Fig. 1. Proposed structure of the dual band BPF.

According to equations (1, 2) the effective dielectric constant of the R2 is greater than R1, therefore the resonant frequency of them are different.

For  $w/h \leq 1$ :

$$\epsilon_{re} = \frac{\epsilon_r + 1}{2} + \frac{\epsilon_r - 1}{2} \left\{ [1 + 12 \frac{h}{w}]^{-0.5} + 0.04 [1 - \frac{w}{h}]^2 \right\}$$

$$z_c = \frac{\eta}{2\pi \sqrt{\epsilon_{re}}} \ln \left[ 8 \frac{h}{w} + 0.25 \frac{w}{h} \right]. \quad (1)$$

For  $w/h \geq 1$ :

$$\epsilon_{re} = \frac{\epsilon_r + 1}{2} + \frac{\epsilon_r - 1}{2} [1 + 12 \frac{h}{w}]^{-0.5}$$

$$z_c = \frac{\eta}{\sqrt{\epsilon_{re}}} \left\{ \frac{w}{h} + 1.393 + 0.677 \ln \left[ \frac{w}{h} + 1.444 \right] \right\}^{-1}. \quad (2)$$

## III. FILTER DESIGN

In order to design a dual band BPF using proposed structure, a band pass resonator must be designed and utilized in proposed structure. Figure 2 shows the layout and simulation results of a H-shape resonator which is designed on the RT/DUROID 5880 with  $\epsilon_r=2.2$ , thickness of 15 mil. and loss tangent of 0.0009.

The dimensions of this resonator are as follows:  $a=0.24$  mm,  $b=3.92$ ,  $c=3.2$  mm,  $d=9.15$ ,  $e=0.24$ ,  $g=0.71$  mm,  $h=7$  mm,  $i=3$  mm,  $n=0.95$  mm,  $m=1.17$  mm. As it is shown in Fig. 2 (b), the resonant frequency of the H-shape resonator is 5.14 GHz and return loss in the passband is 29.8 dB.

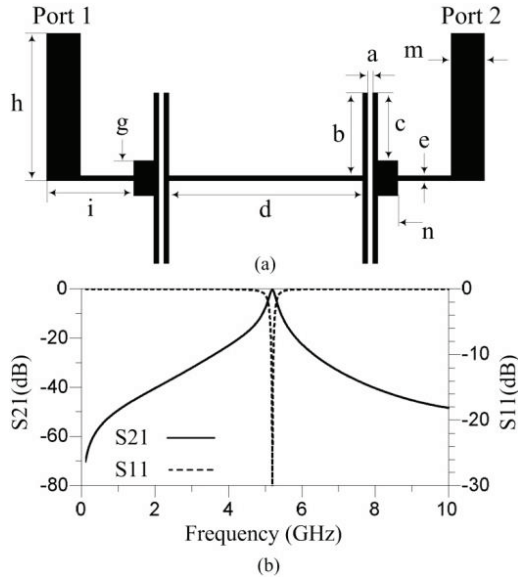


Fig. 2. Proposed H-shape resonator: (a) layout and (b) simulation results.

The basic structure using H-shaped resonator is shown in Fig. 3 (a). A comparison between simulation results of the H-shape resonator and basic dual-layer BPF is shown in Fig. 3 (b). The RT/DUROID 5880 is used as the substrate of the layers.

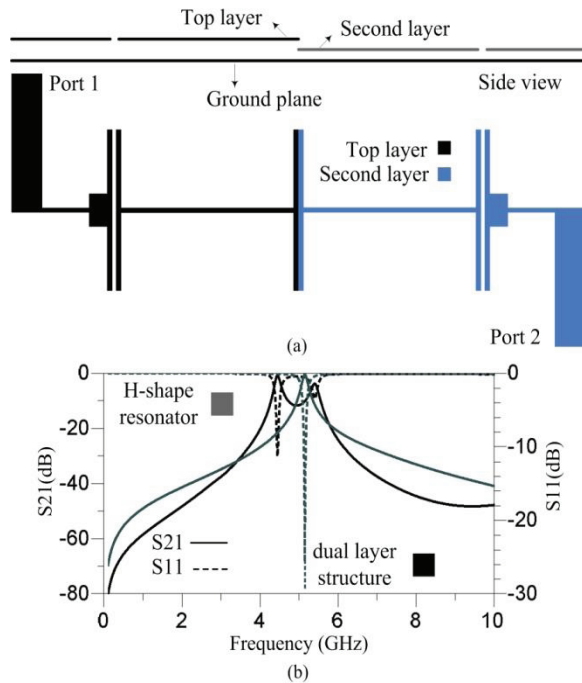


Fig. 3. Dual-layer proposed structure using H-shape resonator: (a) layout and (b) simulation results in comparison with the H-shape resonator response.

As shown in the Fig. 3 (b), two passbands are created in 4.44 GHz and 5.4 GHz by the resonators on the second layer and top layer of the dual layer structure. According to the equation (1), the effective permittivity of the top layer is 1.71 and for the second layer the effective permittivity is 2.2 (for a line with  $w=0.24$  mm). The effective permittivity of the single layer H-shape resonator for a line with  $w=0.24$  mm is 1.74, which has a value between 1.71 and 2.2; therefore, passbands of the dual-layer BPF have created in sides of the H-shape resonator passband. It is evident from Fig. 3 (b) that, passbands performance and isolation between them are not optimized. The passbands frequencies are tuned using resonator scaling and shifting them toward each other. Resonator shifting impresses two passbands frequencies simultaneously and decreases them because the coupling between resonators is increased. Figure 4 (a) and Fig. 4 (b) show the layout and simulation results of the resonator shifting in proposed dual layer structure.

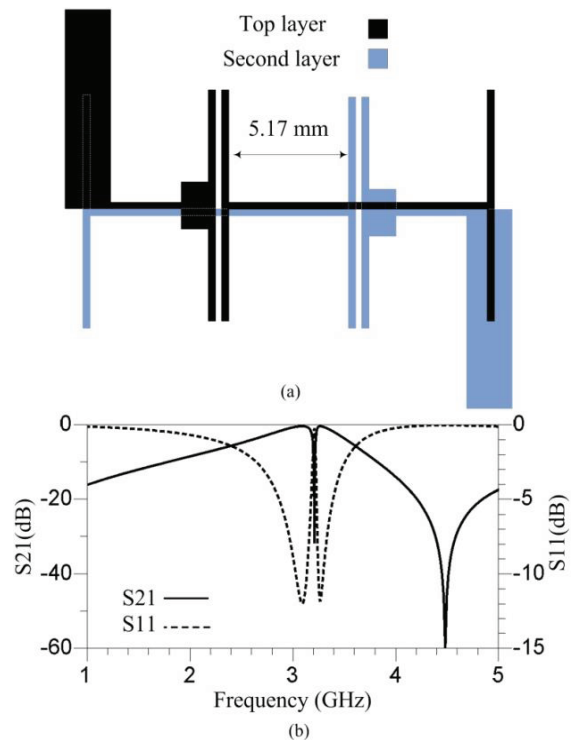


Fig. 4. Resonator shifting in proposed dual layer structure: (a) layout and (b) simulation results.

As it is shown in Fig. 4, resonator shifting in addition to increasing the isolation between bands, reduces the dimension of the filter. But the passbands frequencies are closed together.

In order to improve the response of the proposed dual layer structure, resonator scaling is used. Figure 5 (a) shows the layout of the proposed dual band BPF.

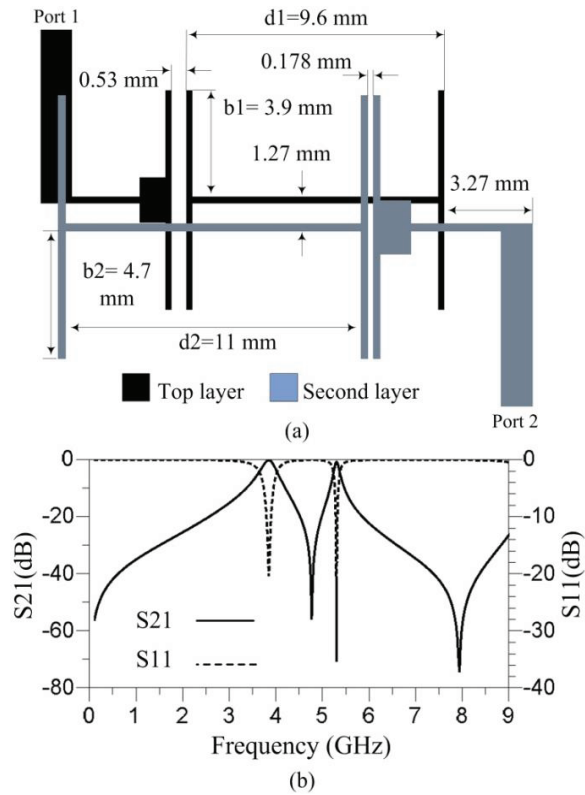


Fig. 5. Proposed dual band BPF: (a) layout and (b) simulation results.

Figure 5 (a) shows the dimension of the proposed filter. The important things about the filter layout are as follows:

- The end of the H-shape resonator in the second layer is coupled with the 50  $\Omega$  input line in the top layer.
- Central transition lines in top and second resonator are parallel and have a weak coupling.
- In order to improve the passband performance, coupling distance of the top resonator is increased to 0.53 mm because the substrate thickness has been increased.
- In order to band tuning, the dimensions of the second resonator are scaled with the rate of 1.2.

Filter design was done in 3 steps:

1. Creation of different resonant frequencies for two equal resonators through creating different dielectric constants for them (as it is shown in Fig. 3).
2. Minimizing the filter size and increasing the isolation between bands through overlapping the resonators in top and second layer (as it is shown in Fig. 4).
3. Tuning the passbands using resonator scaling (as it is shown in Fig. 5). If the dimension of the top resonator increase/decrease, the second passband

shifts to the lower/higher frequencies, and if the dimensions of the second resonator increase/decrease, the first passband shifts to the lower/higher frequencies.

Between the dimensions of the filter, b1, b2, d1, d2 have the most effect on the filter response. Figure 6 shows the filter response as a function of b1, b2, d1, d2.

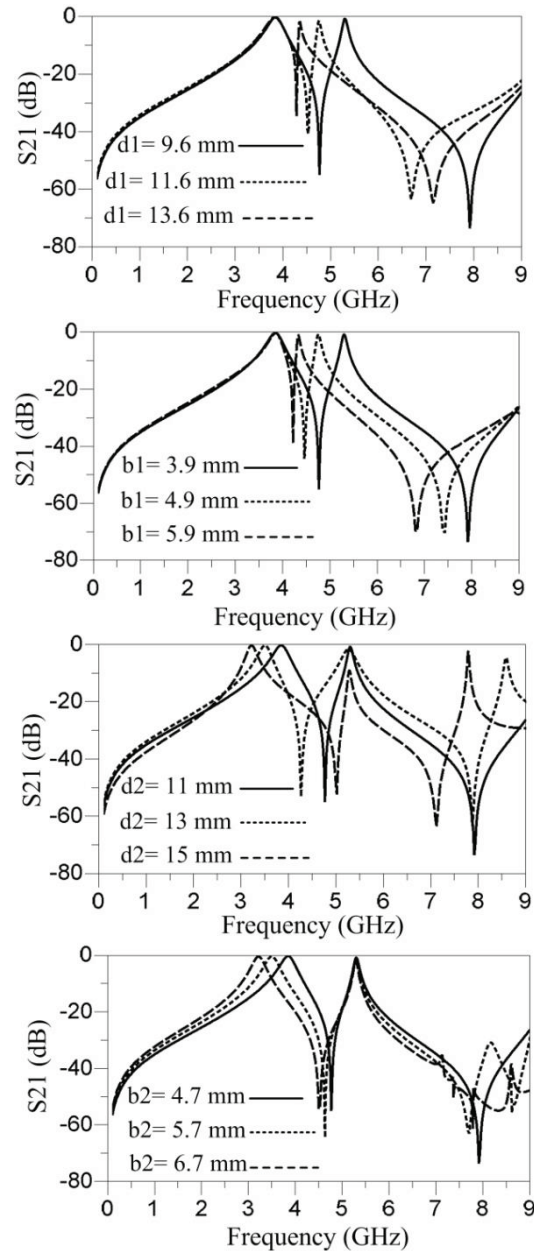


Fig. 6. Filter response as a function of b1, b2, d1, d2.

Figure 7 depicts the fabrication pictures and simulation/fabrication results of the proposed dual band BPF. The top/bottom of the top layer and the second layer are shown in Fig. 7 (a) and Fig. 7 (b), respectively.

The bottom of the top layer is not metalized but the bottom of the second one is metalized, as the ground plane.

Circles on four sides of the resonators in both layers have created simultaneously. These circles have perforated at the top and bottom layers and with overlaying these holes, the correct distance between the resonators is realized.

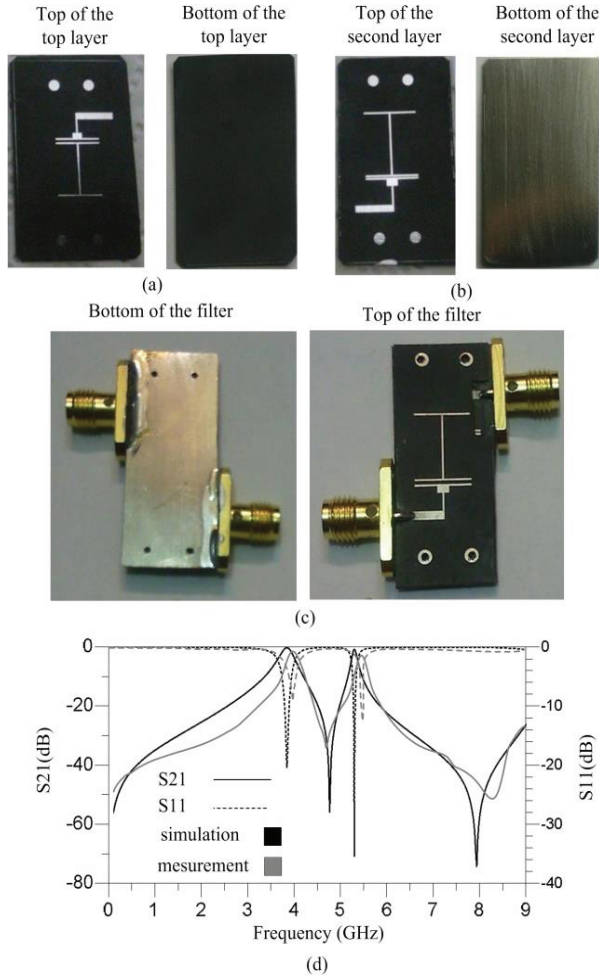


Fig. 7. Proposed dual band BPF: (a) fabrication picture of the top layer, (b) fabrication picture of the second layer, (c) fabrication picture of the filter, and (d) simulation/fabrication results.

#### IV. RESULT DISCUSSION

The proposed dual-band BPF fabricated on the RT/Duroid 5880 substrate. As illustrated in Fig. 6, the simulated central frequencies are 3.85 and 5.3 GHz with fractional bandwidths of 4.7 and 2.2%, respectively. A deep transmission zero between the two bands was located at 4.75 GHz, resulting in high isolation with an attenuation level of more than 58 dB. The return losses

of the first and second bands (at the central frequencies) are 21 dB & 36 dB and insertion losses of them are 0.68 dB & 0.23 dB. Table 1 compares the proposed design method with those are mentioned.

Table 1: Comparison between design methods

Methods	Advantages	Disadvantages
Proposed	Compactness-simple design process-tunable passbands	Difficult fabrication
Method 1	Simple passband control	Complex design process-large circuit size
Method 2	Compact size-good isolation	Complex design process-difficult tuning
Method 3	Simple structure	Difficult passband control
Method 4	Tunable passbands	Complex design process

#### V. CONCLUSION

In a novel dual band bandpass filter presented using a simple dual-layer method. At the top layer, designed H-shape resonator was placed and the scaled H-shape resonator was used on the second layer. Due to differences in the effective dielectric constant of the resonators, the resonant frequencies of them are different. Tuning of the passbands performances are possible using resonator scaling and shifting them toward each other. The central frequencies of this dual band BPF are  $f_1=3.85$  GHz and  $f_2=5.3$  GHz.

#### REFERENCES

- [1] S. Oshima, K. Wada, R. Murata, and Y. Shimakata, "Multilayer dualband bandpass filter in low-temperature co-fired ceramic substrate for ultra-wideband applications," *IEEE Trans. Microw. Theory Techn.*, vol. 58, no. 3, pp. 614-623, Mar. 2010.
- [2] R. Zhang and L. Zhu, "Synthesis and design of wideband dual-band bandpass filters with controllable in-band ripple factor and dual-band isolation," *IEEE Trans. Microw. Theory Techn.*, vol. 61, no. 5, pp. 1820-1828, 2013.
- [3] L-C. Tsai and C-W. Hsue, "Dual-band bandpass filters using equallength coupled-serial-shunted lines and transform technique," *IEEE Trans. Microw. Theory Techn.*, vol. 52, no. 4, pp. 1111-1117, Apr. 2004.
- [4] A-S. Liu, T-Y. Huang, and R-B. Wu, "A dual wideband filter design using frequency mapping and stepped-impedance resonators," *IEEE Trans. Microw. Theory Techn.*, vol. 56, no. 12, pp. 2921-

- 2929, Dec. 2008.
- [5] S. Fu, B. Wu, J. Chen, S-J. Sun, and C-H. Liang, "Novel second order dual-mode dual-band filters using capacitance loaded square loop resonator," *IEEE Trans. Microw. Theory Techn.*, vol. 60, no. 3, pp. 477-483, Mar. 2012.
- [6] J. Xu, W. Wu, and C. Miao, "Compact and sharp skirts microstrip dual-mode dual-band bandpass filter using a single quadruple-mode resonator (QMR)," *IEEE Trans. Microw. Theory Techn.*, vol. 61, no. 3, pp. 1104-1113, 2013.
- [7] Y. Peng, L. Zhang, and Y. Leng, "A dual-mode dual-band bandpass filter using a tri-stubs loaded multimode resonator (TSLMR)," *J. of Electromagn. Waves and Appl.*, vol. 28, no. 16, pp. 2067-2073, 2014.
- [8] S. Yang, L. Lin, J. Chen, K. Deng, and C. H. Liang, "Design of compact dual-band bandpass filter using dual-mode stepped-impedance stub resonators," *Electronics Letters*, vol. 50 no. 8 pp. 611-613, 2014.
- [9] L. Lin, S. J. Sun, B. Wu, and C. H. Liang, "Dual-band bandpass filter with wide upper stopband using quad-mode stepped impedance stub-loaded resonator," *Electronics Letters*, vol. 50 no. 16, pp. 1145-1146, 2014.
- [10] R. M. Weng and P. Y. Hsiao, "Double-layered quad-band bandpass filter for multi-band wireless systems," *J. of Electromagn. Waves and Appl.*, vol. 23, pp. 2153-2161, 2009.
- [11] H. Y. Chang, R. M. Weng, and Y. F. Kuo, "An independently tunable dualband bandpass filter using open-loop resonators," *J. of Electromagn. Waves and Appl.*, vol. 29, no. 1, pp. 1-13, 2015.
- [12] A. M. Elelimy and A. M. El-Tager, "Dual-band BPF embedded in multilayer low temperature co-fired ceramics (LTCC) for WiMAX applications," *Engineering and Technology (ICET), 2014 International Conference on*, Cairo, Apr. 19-20, 2014.
- [13] Y-T. Kuo and C. Y. Chang, "Analytical design of two-mode dualband filters using E-shaped resonators," *IEEE Trans. Microw. Theory Techn.*, vol. 60, no. 2, pp. 250-260, Feb. 2012.
- [14] D. Li, Y. Zhang, K. Xu, K. Song, and L. W. Li, "Compact dual-wideband bandpass filter with good selectivity using side coupled  $\lambda/4$  shorted SIR," *J. of Electromagn. Waves and Appl.*, vol. 29, no. 1, pp. 69-79, 2015.
- [15] L. Wang and B. R. Guan, "A novel high selectivity dual-band band-pass filter with inductive source-load coupling," *J. of Electromagn. Waves and Appl.*, vol. 26, no. 13, pp. 1734-1740, 2012.
- [16] J. Xu, C. Miao, and W. Wu, "A compact and high isolation dual mode dual-band bandpass filter with tunable transmission zeros," *J. of Electromagn. Waves and Appl.*, vol. 26, nos. 17-18, pp. 2390-2397, 2012.
- [17] G. Q. Zhang, J. X. Chen, J. Shi, H. Tang, H. Chu, and Z. H. Bao, "Design of multilayer balun filter with independently controllable dual passbands," *IEEE Microwave and Wireless Components Letters*, vol. 25, no. 1, 2015.
- [18] G. Chaudhary, Y. Jeong, and J. Lim, "Harmonic suppressed dual-band bandpass filters with tunable passbands," *IEEE Trans. Microw. Theory Techn.*, vol. 60, no. 7, 2012.
- [19] C. F. Chen, "A compact reconfigurable microstrip dual-band filter using varactor-tuned stub-loaded stepped impedance resonators," *IEEE Microwave and Wireless Components Letters*, vol. 23, no. 1, 2013.
- [20] N. Sekiya and S. Sugiyama, "Design of miniaturized HTS dual-band bandpass filters using stub loaded meander line resonators and their applications to tri-band bandpass filters," *IEEE Transaction on Applied Superconductivity*, vol. 25, no. 3, 2015.



chipless RFID and microstrip sensors.



2008.

# Nonlinear Analysis of Active Aperture Coupled Reflectarray Antenna Containing Varactor Diode

I. Aryanian, A. Abdipour, and G. Moradi

Department of Electrical Engineering  
Amirkabir University of Technology, Tehran, 15914, Iran  
iman\_aryanian@aut.ac.ir, abdipour@aut.ac.ir, ghmoradi@aut.ac.ir

**Abstract** — Radiation pattern of reflectarray antenna can be controlled using varactor diode in the antenna structure, but may cause nonlinear response. Thus, it is needed to design active reflectarray antenna considering nonlinear behavior of the unit cell. However, in the past papers, active element of varactor tuned reflectarray antenna is assumed linear, while in this paper, nonlinear analysis of active reflectarray antenna is explained and an active aperture coupled reflectarray unit cell containing two varactor diodes is analyzed. Harmonic balance method is used in analyzing active unit cell using nonlinear model of the diode. Therefore, this paper shows the significance of nonlinear analysis of active reflectarray antenna, and also the effect of nonlinear element in radiation pattern is presented. By the explained method, the impact of nonlinearities on performance of reflectarrays can be investigated. Furthermore, any active reflectarray cell having active device by any nonlinear model can be used in the analysis, and the impact of parameters of the model can be studied.

**Index Terms** — Active antenna, beam forming, nonlinear analysis, reflectarray antenna, steerable antenna.

## I. INTRODUCTION

A microstrip reflectarray antenna is a low profile planar reflector that consists of microstrip patch arrays printed on a dielectric substrate which its surface is illuminated by a feed antenna. Each element of the array is designed to produce required reflection phase shift to form a desired pattern. The phase can be controlled by active element which gives the capability of controlling the pattern [1,2]. Different methods are used to add reconfigurability to reflectarray antenna, using microstrip elements with an integrated electronic control, like MEMs-based structures [3], varactor loaded patches [4,5], PIN diodes [6] or liquid crystal based structures [7]. Varactor tuned reflectarray elements may be able to control phase of the unit cell

continuously over a 360 degrees range.

Harmonic balance analysis of nonlinearly loaded antennas is reported in the past papers [8,9] but it is not explained for reflectarray antenna. Nonlinear analysis of active reflectarray antenna is essential when radiated power of the antenna is such that active elements behave nonlinear. In this paper, it is shown that power distribution on the antenna surface may cause some active elements of antenna to behave nonlinear. In these cases, unit cell of active reflectarray antenna should be analyzed in a two-step process to consider nonlinear behavior of active element. First, passive radiation part should be simulated by full wave analysis method to obtain parameters of the passive part. For this purpose, unit cell of the antenna is simulated assuming infinite array and the active element is replaced by a two port network. Also, two spatial ports are considered for each polarization of incident plane wave which are modelled as Floquet port. Next, obtained scattering parameters are used in nonlinear analysis of the unit cell. This process is carried out in this paper for an active unit cell in the centre frequency of 5.4 GHz where the unit cell has two varactor diodes. Nonlinear results are used in designing a sample reflectarray antenna.

## II. UNIT CELL CONFIGURATION

Aperture coupled microstrip antenna have been used for single or dual linear polarization reflectarrays [10,11]. In this structure, each cell consists of a microstrip line coupled to the radiating patch on the opposite side of the substrate via an aperture in the ground plane as shown in Fig. 1. The unit cell contains two varactor diodes as shown in Fig. 1. Parameters of the unit cell are borrowed from [4] to compare its test results by this paper where relative dielectric constant for 1 mil substrate is 3.4, and for line substrate is 2.2. The patch is separated from the ground plane and slot by a 3-mm thick foam with a relative dielectric constant of 1.11. Other parameters of the unit cell are given in Table 1. Unit cell is designed for the center frequency of 5.4 GHz.

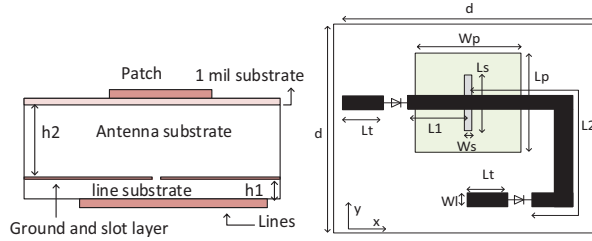


Fig. 1. Antenna unit cell schematic.

Table 1: Unit cell parameters

Parameter	Value	Parameter	Value
$L_p$	19.5 mm	$W_p$	15.5 mm
$h_1$	0.5 mm	$L_s$	15.4 mm
$W_s$	0.76 mm	$W_l$	1.5 mm
$h_2$	3 mm	$d$	35 mm
$L_2$	16.1 mm	$L_1$	6 mm
$L_t$	7.8 mm		

### III. UNIT CELL MODELING

To simulate the unit cell assuming infinite array, active elements are replaced by two port networks. The unit cell is modelled as a six port network as shown in Fig. 2, in which ports 5 and 6 are spatial ports modeled as Floquet port, and ports 1 to 4 are located in the transmission line. After modeling the linear part of the unit cell, active elements are added to the analysis by nonlinear two port networks as shown in Fig. 2.

Parameters of the varactor diodes used in this work are given in Table 2, and nonlinear diode model is shown in

Fig. 3, which has one nonlinear capacitance and one nonlinear current source.  $C_p$  and  $L_p$  are parasitic capacitance and inductance of the model. Also,  $R_s$  is series ohmic resistance,  $C_j(v)$  is the nonlinear junction capacitance, and  $R_j(v)$  is the nonlinear junction impedance of the model.

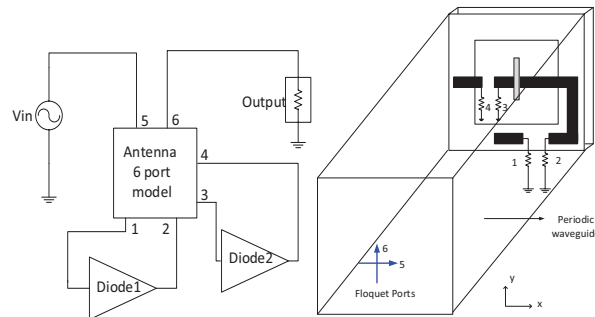


Fig. 2. Six port modelling of the unit cell.

Table 2: Diode parameters

Symbol	Quantity	Value
$I_s$	Saturation current	100 (pA)
$N$	Ideal factor	2
$V_t$	Thermal voltage	26 (mV)
$C_{j0}$	Junction capacitance	1.7 (pF)
$M$	Grading coefficient	0.9
$v_j$	Junction potential	1.2
$F_c$	Forward-bias depletion capacitance coefficient	0.5
$L_p$	Parasitic inductance	0.4 (nH)
$C_p$	Parasitic capacitance	0.1 (pF)
$R_s$	Ohmic resistance	0.9 (Ohm)

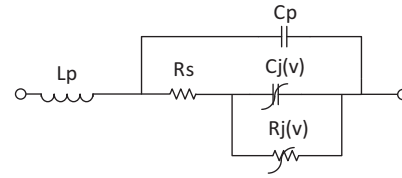


Fig. 3. Nonlinear model of the diode.

Current source of the model is given as [12]:

$$I_d = \begin{cases} I_s (e^{v_d/NV_t} - 1), & v_d \geq -10NV_t \\ I_s (e^{-10} - 1) + \frac{I_s}{NV_t} e^{-10} (v_d + 10NV_t), & v_d < -10NV_t \end{cases} \quad (1)$$

As well, electric charge is expressed as:

$$Q_j = \begin{cases} \frac{V_j C_{j0}}{1-M} \left( 1 - \left( 1 - \frac{v_d}{V_j} \right)^{1-M} \right), & v_d \leq F_c V_j \\ \frac{C_{j0}}{(1-F_c)^M} \left[ v_d + \frac{M}{V_j (1-F_c)} \left( \frac{v_d^2}{2} - V_j F_c v_d \right) \right], & v_d > F_c V_j \end{cases} \quad (1)$$

Besides, capacitance of the model is obtained as:

$$C_j = \begin{cases} C_{j0} \left( 1 - \frac{v_d}{V_j} \right)^{-M}, & v_d \leq F_c V_j \\ \frac{C_{j0}}{(1-F_c)^M} \left[ 1 + \frac{M}{V_j (1-F_c)} (v_d - V_j F_c) \right], & v_d > F_c V_j \end{cases}, \quad (2)$$

where  $v_d$  is voltage of diode,  $C_{j0}$ ,  $M$ ,  $N$ ,  $F_c$ ,  $V_j$ ,  $I_s$  are parameters of the diode model and  $V_t$  is 26 mV.

### IV. NONLINEAR ANALYSIS

The nonlinear analysis of the unit cell is performed using harmonic balance method [13]. Hence, the unit cell is divided into nonlinear and linear networks as shown in

Fig. 4.

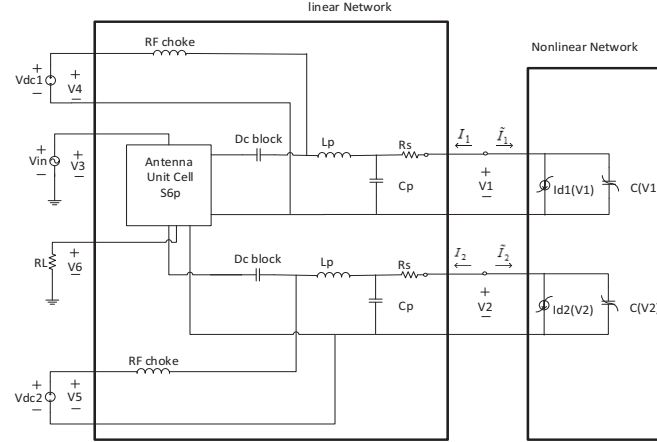


Fig. 4. Dividing the unit cell to nonlinear and linear networks.

The nonlinear network is composed of nonlinear capacitances and nonlinear current sources and the linear network consists of parasitic elements and lumped elements of the unit cell, and also 6-port network of the unit cell obtained in the previous section. Our aim is to find voltages of  $V_1$  and  $V_2$  of

Fig. 4, to have  $I_1 + \tilde{I}_1 = 0$ , and  $I_2 + \tilde{I}_2 = 0$ .

#### A. Currents of the linear part

Current of the linear subcircuit can be expressed as:

$$\begin{bmatrix} I_1 \\ I_2 \\ \vdots \\ I_6 \end{bmatrix} = \begin{bmatrix} Y_{11} & Y_{12} & \dots & Y_{16} \\ Y_{21} & Y_{22} & \dots & Y_{26} \\ \vdots & \vdots & \vdots & \vdots \\ Y_{61} & Y_{62} & \dots & Y_{66} \end{bmatrix} \begin{bmatrix} V_1 \\ V_2 \\ \vdots \\ V_6 \end{bmatrix}. \quad (3)$$

Partitioning the Y matrix in (4) gives an expression for I, the vector of currents of linear part in ports 1 and 2:

$$I = \begin{bmatrix} I_1 \\ I_2 \end{bmatrix} = \begin{bmatrix} Y_{11} & Y_{12} \\ Y_{21} & Y_{22} \end{bmatrix} \begin{bmatrix} V_1 \\ V_2 \end{bmatrix} + \begin{bmatrix} Y_{13} & Y_{14} & Y_{15} \\ Y_{23} & Y_{24} & Y_{25} \end{bmatrix} \begin{bmatrix} V_3 \\ V_4 \\ V_5 \end{bmatrix} = Y_L \cdot V + Y_S \cdot V_S. \quad (4)$$

$I_S = Y_S V_S$  represents a set of current sources in parallel with the first and second ports; which transforms the input and output port excitations into this set of current sources.

#### B. Currents of the nonlinear part

Fourier transforming the charge waveform at each port gives the charge vectors for the capacitors at each port:

$$F\{q_1(t)\} \rightarrow Q_1, \quad F\{q_2(t)\} \rightarrow Q_2, \quad (5)$$

and the charge vector, Q, is:

$$Q = \begin{bmatrix} Q_1 \\ Q_2 \end{bmatrix}. \quad (6)$$

The nonlinear-capacitor current is the time derivative of the charge waveform. Taking the time derivative corresponds to multiplying by  $j\omega$  in the frequency domain, so:

$$i_c(t) = \frac{dq(t)}{dt} \leftrightarrow jk\omega_p Q \quad k=0,1,\dots,K \quad (7)$$

$$\Rightarrow I_c = j\Omega Q,$$

where  $\Omega$  is a diagonal matrix with 2 cycles of  $0, \omega_0, \dots, k\omega_0$  along the main diagonal where  $k=3$  is the number of harmonics determined.

Fourier transforming from nonlinear current vector in time domain gives the nonlinear current vector in frequency domain:

$$F\{i_{d1}(t)\} \rightarrow I_{d1}, \quad F\{i_{d2}(t)\} \rightarrow I_{d2}. \quad (8)$$

Therefore, vector of nonlinear current sources in ports 1 and 2,  $I_G$  is:

$$I_G = \begin{bmatrix} I_{d1} \\ I_{d2} \end{bmatrix}. \quad (9)$$

So, nonlinear current vector of ports 1 and 2 is  $\tilde{I} = I_G + I_C$ .

Calculating the admittance parameters of linear network of

Fig. 4, which is a  $6 \times 6$  matrix obtained using ADS simulation, the following harmonic balance equation is obtained [13]:

$$F(v) = I_s + Y_L \cdot V + j\Omega Q + I_G = 0. \quad (10)$$

In this equation,  $y_{m,n} = \text{diag}(y_{m,n}(k\omega_c))$ , and V is the vector of nonlinear voltages of the nonlinear ports. Harmonic balance equation can be solved with different methods, among which the Newton-Raphson [13] technique is the most common technique and is used in this paper. Newton-Raphson technique is an

iterative method involving calculation of Jacobian matrix, which contains derivatives of all components of the vector  $F(v)$ , with respect to the components of  $V$ .

To obtain  $S_{11}$  parameter which shows the reflection from the unit cell in the same polarization with the incident field, LSSP simulation is used in ADS simulation. The LSSP simulation (Large-Signal S-Parameter Simulation) in the simulation-LSSP palette of ADS software, computes S-parameters for nonlinear circuits such as those that employ power amplifiers and mixers. In the latter case, S-parameters can be computed across frequencies, that is, from the RF input to the IF output. LSSP simulation is based on the harmonic balance simulation and uses harmonic balance techniques.

The port which the reflection coefficient should be calculated from it in the written harmonic balance code by MATLAB software, is considered as the input port. Then, voltage and current at this port is evaluated by running harmonic balance code.

In the next step, voltage of the input port  $V_{in}$  is obtained and input impedance from this port is calculated as:

$$Z_{in}(\omega_0) = \frac{V_{in}(\omega_0)}{I_{in}(\omega_0)}. \quad (11)$$

Now  $S_{11}$  is evaluated by:

$$S_{11}(\omega_0) = \frac{Z_{in}(\omega_0) - Z_0}{Z_{in}(\omega_0) + Z_0}. \quad (12)$$

Phase and amplitude of the  $S_{11}$  shows the reflected signal from the unit cell in the same polarization with the incident field. Considering nonlinear diode model and harmonic balance analysis, amplitude response and phase shift of the reflected signal from the cell for different power levels are obtained as shown in Fig. 5 and

Fig. 6, in which nonlinear result of harmonic balance analysis is verified by ADS simulation.

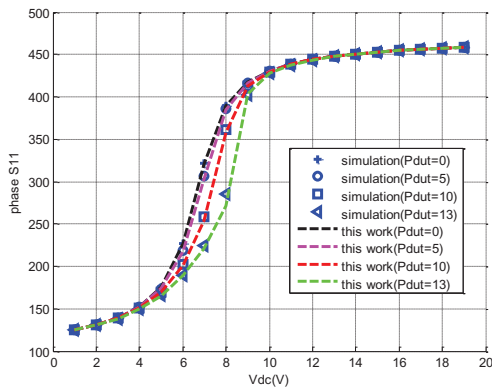


Fig. 5. Phase response of the active unit cell by nonlinear analysis.

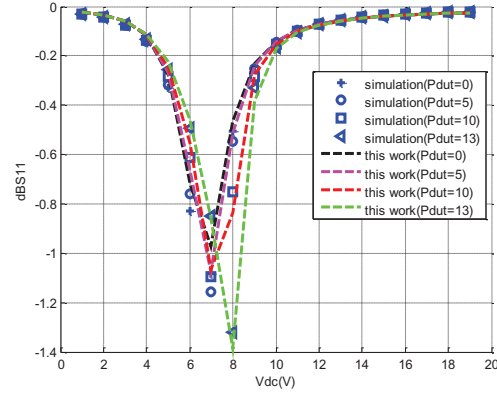


Fig. 6. Amplitude response of the active unit cell by nonlinear analysis.

Simulation results show that reflection phase and amplitude depend on the incident power. As the power increases, rectification and harmonics of the fundamental frequency starts to appear. This causes the reflection phase curves to be different from the ones obtained at a low power and the losses to increase. For high power levels, nonlinear behavior such as rectification occurs in the positive excursion of the RF signal when the reverse bias voltage is set to low values because of diode conduction. This rectification affects the reflection coefficient as can be seen in

Fig. 6. Besides, Fig. 5 shows that reflection phase is different from that of linear analysis. The maximum error of reflection phase in Fig. 5 is about 120 degrees which occurs in bias voltage of 8 (V), which shows that nonlinear phenomenon cannot be neglected. The unit cell is fabricated and tested in [4] and measurement results show this nonlinear behavior but nonlinear analysis is not performed in [4]. Test results of [4] are close to the results of this paper. However, because the parameters of the diode model is not specified in [4], the selected parameters for the varactor diode in this paper is different, and this leads to different cell response.

## V. SAMPLE ACTIVE REFLECTARRAY DESIGN

To simulate the active antenna, a 31.5 cm × 31.5 cm antenna is designed using the explained unit cell by focal length of 39 cm in the frequency of 5.4 GHz. Assuming center of reflectarray as center of Cartesian coordinates, feed antenna is placed in (0, 0, 39 cm). First step to design the antenna is to find required phase shift of each cell to have a focused beam in a desired direction. Considering our antenna has N reflecting elements that are illuminated by a feed located at the focal point of the antenna, the excitation terms are proportional to the magnitude and phase of the electric

field at the  $n$ th patch. The feed has a certain angular taper over the antenna surface which can be included in the pattern analysis by multiplying the relative complex excitation term by a raised cosine factor [14], that can be adjusted to match the pattern of the actual feed by choosing the proper  $q$ , which is the exponent of the feed pattern function represented by  $\cos^q \theta$  and is determined from the taper factor at the edges of the reflectarray, which is about -10 dB for a focused beam [14]. The angular taper of the feed can be modelled as  $\frac{e^{-jkR_n}}{R_n} \cos^q \theta_n$ . Consequently, by multiplying the complex excitation term by the compensating phase and amplitude factor  $A_n e^{-jk\psi_n}$  resulted from each element, the complex reflected field from each element can be expressed in the form:

$$A_n \frac{\cos^q \theta_n}{|R_n|} e^{-j(kR_n - \psi_n)}, \quad (13)$$

in which  $\psi_n$  is the compensation phase of the  $n$ th element and  $(R_n)$  is the distance between the feed phase center and the  $n$ th element phase center. The required phase shift at each element to produce a collimated beam in a given direction is [14]:

$$\psi_n = k_0(R_n - (x_n \cos \phi_b + y_n \sin \phi_b) \sin \theta_b), \quad (14)$$

where  $\theta_b, \phi_b$  shows the beam direction,  $k_0$  is the free space propagation constant, and  $(x_n, y_n)$  is the coordinates of element  $n$ .

Gain of the antenna can be computed using the input power of the feed horn  $P_F$ , according to:

$$G(\theta, \varphi) = \frac{4\pi r^2}{2\eta_0 P_F} |E(\theta, \varphi)|^2, \quad (15)$$

where  $\eta_0$  is the intrinsic impedance of the free space and  $|E(\theta, \varphi)|$  is the amplitude of the far electric field. Hence, far electric field should be calculated to obtain gain of the antenna which is explained in [14].

If nonlinear behavior of unit cell is not considered, the errors in the amplitude and phase of the reflected signal from each cell may reduce the gain. Antenna directivity with and without considering the nonlinear effect of active elements is shown in Fig. 8 and Fig. 9. In Fig. 8, feed power is so that some cells are in nonlinear region. Power distribution of the antenna for this scenario is shown in Fig. 7. In this case, considering amplitude and phase nonlinear behavior of the unit cell shown in Fig. 5 and

Fig. 6, nonlinear analysis shows degradation in gain which cannot be assessed by linear analysis. In another scenario in Fig. 9, feed power is so that all cells are in linear region, where linear and nonlinear simulations have the same result. So, when feed power

is below 0 dBm, it is not necessary to consider the nonlinear effects. However, to assess the pattern of the active reflectarray antenna correctly, for all feed power, the nonlinear behavior of active element should be considered.

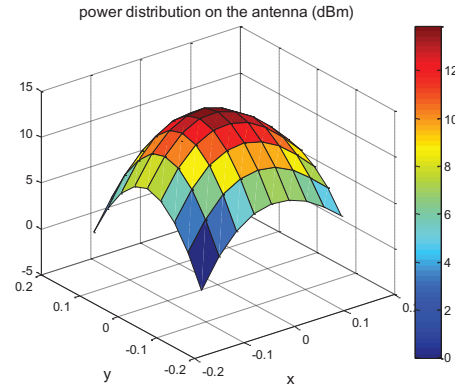


Fig. 7. Supposed power on the antenna surface.

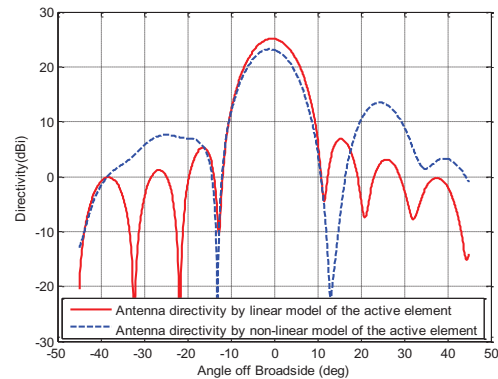


Fig. 8. Antenna directivity with and without considering the nonlinear effect of active elements when feed power is so that some cells are in nonlinear region.

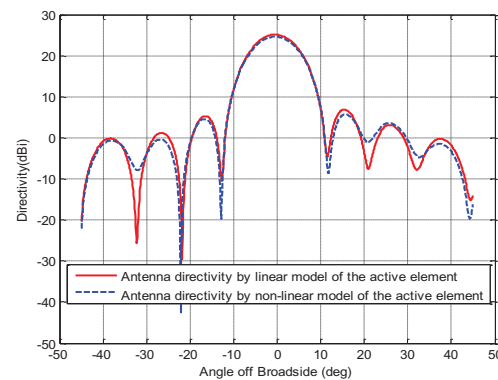


Fig. 9. Antenna directivity with and without considering the nonlinear effect of active elements when feed power is so that all cells are in linear region.

## VI. CONCLUSION

Active reflectarray antenna containing varactor diode has been analysed considering nonlinear performance of the active element. The unit cell has been divided into two linear and nonlinear parts. Scattering parameters of the linear part is obtained using HFSS software and used in the harmonic balance analysis. A sample active reflectarray antenna has been designed which shows the error in predicting the pattern of the antenna with linear modeling of the active element.

## REFERENCES

- [1] T. Makdissy, R. Gillard, E. Fourn, E. Girard, and H. Legay, "Phase-shifting cell for dual linearly polarized reflectarrays with reconfigurable potentialities," 2013.
- [2] F. Venneri, S. Costanzo, and G. Di Massa, "Design and validation of a reconfigurable single varactor-tuned reflectarray," *Antennas and Propagation, IEEE Transactions on*, vol. 61, pp. 635-645, 2013.
- [3] O. Bayraktar, O. A. Civi, and T. Akin, "Beam switching reflectarray monolithically integrated with RF MEMS switches," *Antennas and Propagation, IEEE Transactions on*, vol. 60, pp. 854-862, 2012.
- [4] M. Riel and J. Laurin, "Design of an electronically beam scanning reflectarray using aperture-coupled elements," *Antennas and Propagation, IEEE Transactions on*, vol. 55, pp. 1260-1266, 2007.
- [5] F. Venneri, S. Costanzo, and G. Di Massa, "Reconfigurable aperture-coupled reflectarray element tuned by single varactor diode," *Electronics Letters*, vol. 48, pp. 68-69, 2012.
- [6] B. D. Nguyen, K. T. Pham, V.-S. Tran, L. Mai, N. Yonemoto, A. Kohmura, et al., "Electronically tunable reflectarray element based on C-patch coupled to delay line," *Electronics Letters*, vol. 50, pp. 1114-1116, 2014.
- [7] G. Perez-Palomino, R. Florencio, J. A. Encinar, M. Barba, R. Dickie, R. Cahill, et al., "Accurate and efficient modeling to calculate the voltage dependence of liquid crystal based reflectarray cells," 2014.
- [8] K.-C. Lee and T.-N. Lin, "Application of neural networks to analyses of nonlinearly loaded antenna arrays including mutual coupling effects," *Antennas and Propagation, IEEE Transactions on*, vol. 53, pp. 1126-1132, 2005.
- [9] D. Liao, "Scattering and imaging of nonlinearly loaded antenna structures in half-space environments," in *SPIE Defense, Security, and Sensing*, pp. 87140I-87140I-10, 2013.
- [10] M. Bialkowski and H. Song, "Dual linearly polarized reflectarray using aperture coupled microstrip patches," in *Antennas and Propagation Society International Symposium, 2001, IEEE*, pp. 486-489, 2001.
- [11] F. Venneri, S. Costanzo, G. Di Massa, and G. Amendola, "Aperture-coupled reflectarrays with enhanced bandwidth features," *Journal of Electromagnetic Waves and Applications*, vol. 22, pp. 1527-1537, 2008.
- [12] P. Antognetti, G. Massobrio, and G. Massobrio, *Semiconductor Device Modeling with SPICE*, McGraw-Hill, Inc., 1993.
- [13] S. A. Maas, *Nonlinear Microwave and RF Circuits*, Artech House, 2003.
- [14] J. Huang, *Reflectarray Antenna*, Wiley Online Library, 2008.



**Iman Aryanian** was born in Iran in 1986. He obtained his B.Sc. in Electrical Engineering from Amirkabir University of Technology, Tehran, Iran in 2008, and the M.Sc. from Amirkabir University of Technology, Tehran, Iran in 2010. He is currently working toward his Ph.D. program. His research interests are in the areas of reflectarray antenna, computational electromagnetic, semiconductor RF modeling, electromagnetic theory, and computational electromagnetics.



**Abdolali Abdipour** was born in Alashtar, Iran, in 1966. He received his B.Sc. degree in Electrical Engineering from Tehran University, Tehran, Iran, in 1989, his M.Sc. degree in Electronics from Limoges University, Limoges, France, in 1992, and his Ph.D. degree in Electronic Engineering from Paris XI University, Paris, France, in 1996. He is currently a Professor with the Electrical Engineering Department, Amirkabir University of Technology (Tehran Polytechnic), Tehran, Iran. He has authored 5 books and has authored or co-authored over 290 papers in refereed journals and local and international conferences. His research areas include wireless communication systems (RF technology and transceivers), RF/microwave/millimeter-wave/THz circuit and system design, electromagnetic (EM) modeling of active devices and circuits, high-frequency electronics (signal and noise), nonlinear modeling, and analysis of microwave devices and circuits.



**Gholamreza Moradi** was born in Shahriar, Iran in 1966. He received his B.Sc. in Electrical Communication Engineering from Tehran University, Tehran, Iran in 1989, and the M.Sc. in the same field from Iran University of Science and Technology in 1993. Then he received his Ph.D. degree in Electrical Engineering

from Tehran Polytechnic University, Tehran, Iran in 2002. His research areas include applied and numerical Electromagnetics, Microwave measurement and antenna. He has published more than fifty journal papers and has authored/co-authored five books in his major. He is currently an Associate Professor with the Electrical Engineering Department, Amirkabir University of Technology (Tehran Polytechnic), Tehran, Iran.

# Design and Fabrication of Aperture Coupled Microstrip Increased Bandwidth Antenna

Mohsen Jafari Chashmi<sup>1</sup>, Hadi Ghobadi<sup>2</sup>, and Mahdi Oliaei<sup>2</sup>

<sup>1</sup> Department of Electrical and Computer Engineering  
Shahid Beheshti University (SBU), Tehran, Iran  
ch.mohsen@gmail.com

<sup>2</sup> Department of Electrical and Computer Engineering  
Khaje Nasir Toosi University of Technology (KNTU), Tehran, Iran  
hadi63@ee.kntu.ac.ir, m.oliaei90@ee.kntu.ac.ir

**Abstract** — This paper presents aperture coupled microstrip antenna with three resonants. The antenna bandwidth has been enhanced due to clip in the patch edges and varies the current distribution well in order to create the third resonant. There is a compromise between radiation characteristics and the antenna bandwidth. These two factors have been optimized in designed and fabricated samples. E-plane and H-plane patterns indicate the appropriate propagation pattern of antenna is between 1.3 to 2.3 GHz frequency band, which clarifies achieved bandwidth more than 53% by using certain method in the novel one radiating element. Of course, there is bandwidth enhancement up to this limit by utilization of multiple radiating elements.

**Index Terms** — Aperture coupled microstrip antenna, bandwidth enhancement, coupling, resonant frequency, slot.

## I. INTRODUCTION

The microstrip antennas have many applications due to their planar structures and mechanical formations, but they suffer from narrow bandwidth. Many procedures have been done for bandwidth enhancing and different methods proposed; although these methods decrease the performance of antenna propagation [1]. Conventional methods for increasing bandwidth of these antennas are categorized in three general groups: bandwidth enhancement by feeding network, variation in patch's physical structure and material connected with feeding network and patch. Many types of microstrip antennas such as rectangular, circular, semi-circular and triangular patches have been investigated with mathematics concepts in [2]. The basis of current structure design has been adopted from aperture coupled microstrip antenna which introduced by Pozar [3].

The general purpose of this paper is enhancement of

aperture coupled microstrip antenna bandwidth as possible as it can; consequently, the radiation characteristics of an end-fire antenna have been observed here.

Fundamental discussion of current paper is achieving three resonants in the antenna by employing one radiating element which it is contrary with other two resonants aperture coupled microstrip multiple radiating element antennas.

As a result, optimum energy coupling methods have been considered for a patch [4]-[9]. One H form slot has been created which it is responsible for controlling the coupling energy on patch. Also, slot structure size increasing cause to create a degree of freedom for bandwidth enhancement.

With variation on patch structure by cutting both sides (clipping dimensions from edges in addition to patch length and width), it is possible to add degree of freedom for controlling  $S_{11}$  antenna parameter. Nevertheless, the current distribution form in the patch changes, which this cause to multiple controlling in antenna bandwidth; consequently, the bandwidth enhancement is achieved more than 53%. Certainly, it is necessary to draw attention to this point that multiple radiating elements aperture coupled antennas have bandwidth enhancement up to this limit [10] and many procedures have been done in this field [11]. Next section presents aperture coupled microstrip antenna design and its important parameters, then simulation results are obtained in HFSS software, finally the fabrication results have been demonstrated for verification of design procedure.

## II. ANTENNA STRUCTURE AND ITS DESIGN PRINCIPLES

Side view of designed physical structure of aperture coupled microstrip antenna has been illustrated in Fig. 1. The center frequency of this L-band aperture antenna is

1.7 GHz. In this type of antenna, the radiating element is the upper metal patch. The energy is coupled from feeding network through the aperture which is located on metal plate under the upper patch. Therefore, the effective coupling parameters are antenna feeding network, slot and patch dimensions. Indeed, the degree of freedom for broadbanding of aperture coupled microstrip antenna is its feeding network which it consists of a probe or microstrip line that it causes bandwidth enhancement about 5% to more than 15% [12], [13].

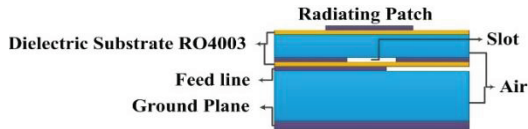


Fig. 1. Side view of aperture coupled microstrip antenna.

So, fundamental cases engaged with the bandwidth and radiation characteristics of microstrip antennas can be studied as below:

**A. Dimensions and dielectric characteristics of upper section**

It is obvious that antenna radiation performance and its bandwidth become so well as increase the upper dielectric layer thickness and decrease its relative permittivity coefficient [14], whereas coupling factor will be decreased. RO4003 substrate type is used with dielectric constant  $\epsilon_r=3.38$  and thickness of 1.52 mm and its lower air layer thickness is equal to 12 mm.

Employing simple calculations [15], the  $\epsilon_{eff}$  of this combined structure (RO4003 with dielectric constant  $\epsilon_r=3.38$  and air with  $\epsilon_r=1$ ) is calculated which it is less than using microstrip dielectric absolutely. The air layer role is creating one degree of freedom for antenna bandwidth enhancement.

**B. Dimensions and dielectric characteristics of lower section**

In spite of energy coupling which performs from this line, increasing in dielectric constant and its thickness reduction is a reason for coupling improvement [16].

Also, the microstrip material type of RO4003 with dielectric constant  $\epsilon_r=3.38$  and thickness of 1.52 mm for this dielectric. Thickness of each microstrip antenna layer has been shown in Fig. 2.



Fig. 2. Distances and thicknesses of antenna layers in mm.

**C. Dimensions and characteristics of feeding network and slot**

Obviously, the feeding network has a direct relation with its characteristic impedance. If the impedance matching meets its requirements, the  $S_{11}$  and antenna bandwidth parameters will be improved. The feeding network alignment must be vertical on slot without any deviations for improving coupled energy [16]. It is important to notice that the feeding network length effects on bandwidth, too.

In other side, the slot dimensions have direct effect on coupling and antenna radiation characteristics. Its structure is in H form and vertical on feeding network alignment as mentioned above. The effect of slot dimensions on  $S_{11}$  parameter is inevitable as presented in simulation.

Slot and feeding network have been placed in two sides of RO4003 microstrip line and physical structure and its dimensions have been shown in Fig. 3.

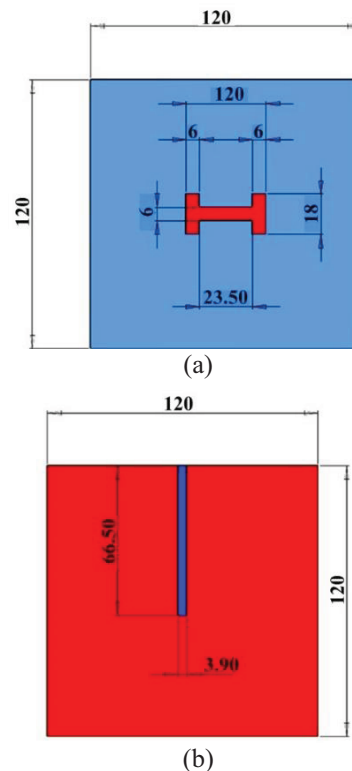


Fig. 3. (a) Feeding network and (b) slot (dimensions in mm).

**D. Dimensions and characteristics of patch (radiation element)**

Patch dimensions have direct relation with resonant frequency and bandwidth of antenna. The antenna bandwidth has been enhanced intensely due to clip in the patch edges and varies the current distribution well in order to create the third resonant. This operates

notwithstanding transformation linear into circular polarization by adjusting of exact dimensions and sufficient energy coupling of slot. In the next section, clipped patch effect has been presented by HFSS software.

The patch is placed in structure's center for optimum coupling [4] and its characteristics and dimensions have been illustrated in Fig. 4.

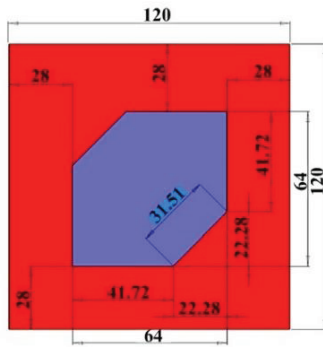


Fig. 4. Patch characteristics and dimensions (in mm).

### III. SIMULATION AND FABRICATION RESULTS

There is a compromise between radiation characteristics and the antenna bandwidth. As mentioned previously, many parameters related to optimizing coupling are in contrary with increasing bandwidth. The three resonant frequencies effect on upper (due to patch), lower (due to slot) and mid (due to feeding network) band frequency of  $S_{11}$  parameter, respectively. Of course, all of these resonants influence each other. The simulation design has been done in HFSS software. Schematic (Fig. 5) and results of aperture coupled antenna presented in the following.

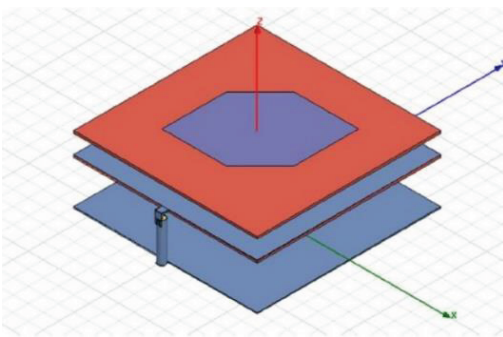


Fig. 5. Illustration of aperture coupled microstrip antenna.

#### A. Return loss and VSWR diagram

The  $S_{11}$  diagram has been presented with and without using clipped patch in order to investigate its effect on antenna bandwidth. The VSWR and return loss

diagrams have been illustrated in Figs. 6 and 7, correspondingly.

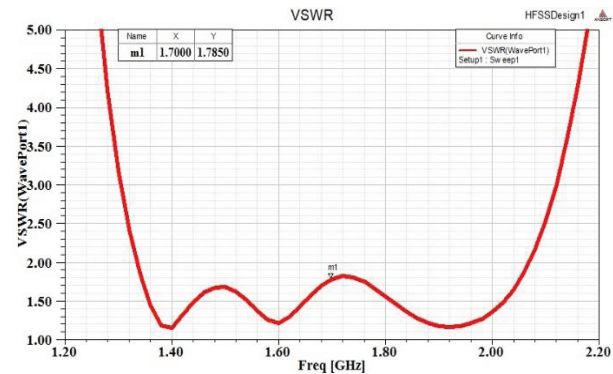


Fig. 6. VSWR diagram of the antenna.

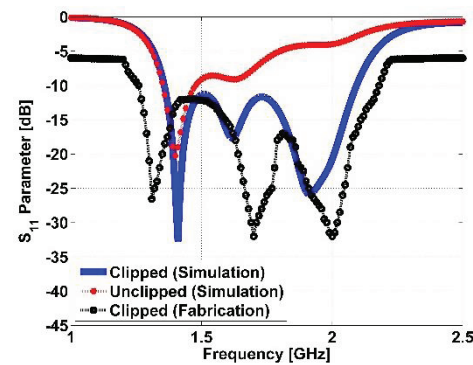


Fig. 7. Power reflection coefficient diagram of the antenna.

#### B. Gain diagram

The gain of a conventional rectangular patch is in order of 6 or 7 dB. As shown in Fig. 8, aperture coupled antenna gain has been reached to 9 dB by employing mentioned methods.

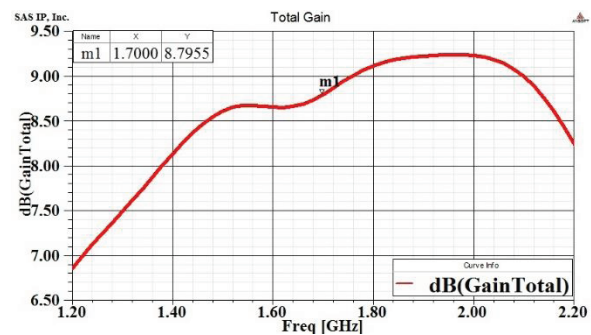


Fig. 8. Gain diagram versus frequency of the antenna.

#### C. Axial ratio diagram

The axial ratio parameter is defined for elliptical or circular polarization. The axial ratio is the ratio of the

magnitudes of the major and minor axis defined by the electric field vector. The axial ratio in the proximity of center frequency (1.7 GHz) shows that there is (quasi) circular polarization in this band (Fig. 9).

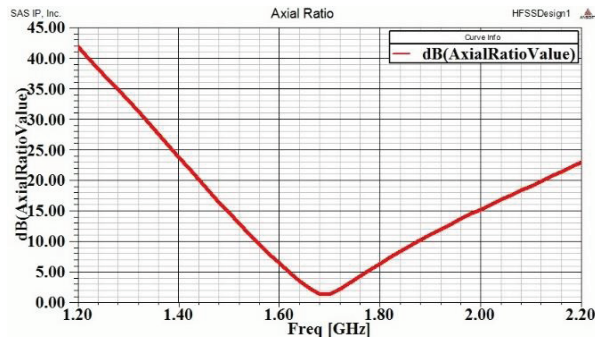


Fig. 9. Axial ratio (AR) diagram versus frequency of the antenna.

The aperture coupled microstrip prototype has been shown in Fig. 10. The fabrication results are categorized in two groups as mentioned in the following. The fabricated  $S_{11}$  parameter of this antenna illustrated in Fig. 7 with its simulated one. It is important to notice which the return loss result of aperture coupled microstrip antenna fabrication complies with its simulation result, appropriately.

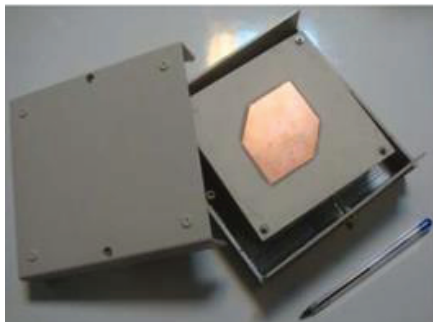


Fig. 10. Prototype of the antenna.

**D. Radiation patterns**

Figures 11 and 12 show the simulated and fabricated results of the antenna for six frequency values of the band, respectively. The simulations and experiments show that increase of clipping number on patch edges hasn't a sensitive effect on bandwidth enhancement; therefore, it's not mandatory to increase these numbers.

The Fig. 11 (a) is in accordance with the Fig. 12 (a) and (b); Fig. 11 (b) with the Fig. 12 (c) and (d); Fig. 11 (c) with the Fig. 12 (e) and (f); Fig. 11 (d) with the Fig. 12 (g) and (h); Fig. 11 (e) with the Fig. 12 (i) and (j); Fig. 11 (f) with the Fig. 12 (k) and (l). A brief look at these pictures, it can be seen that the both simulated and fabricated results are in very good accordance each other.

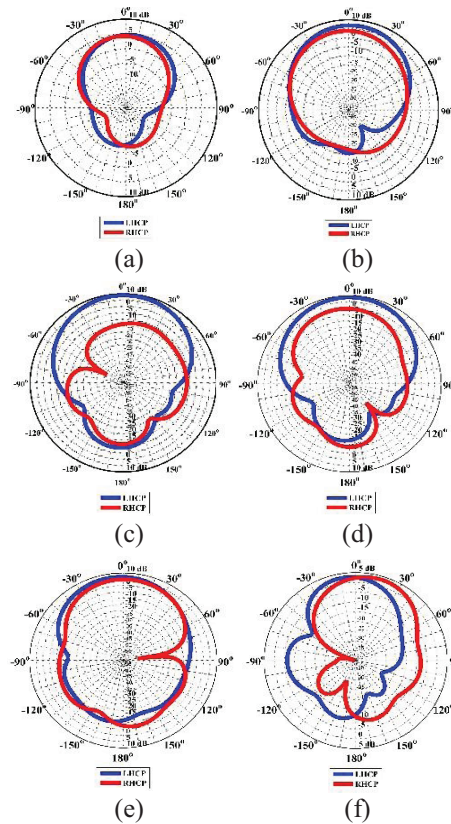
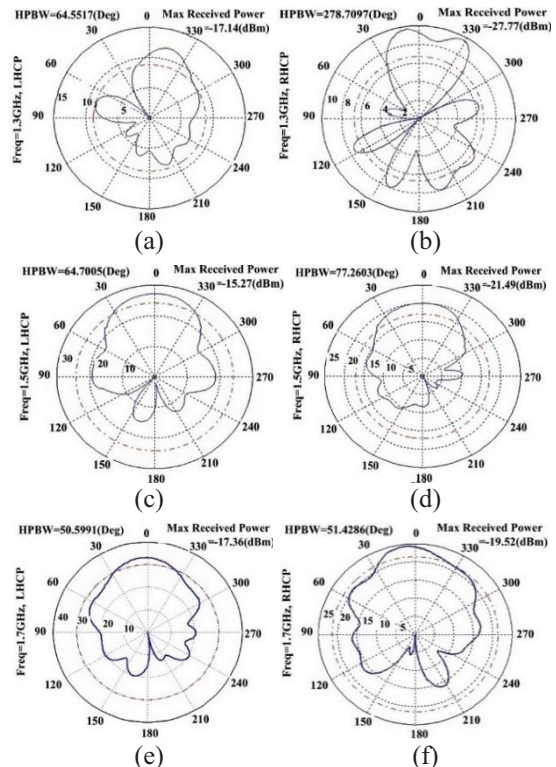


Fig. 11. Simulated radiation pattern results at: (a) 1.3 GHz, (b) 1.5 GHz, (c) 1.7 GHz, (d) 1.8 GHz, (e) 2.1 GHz, and (f) 2.3 GHz.



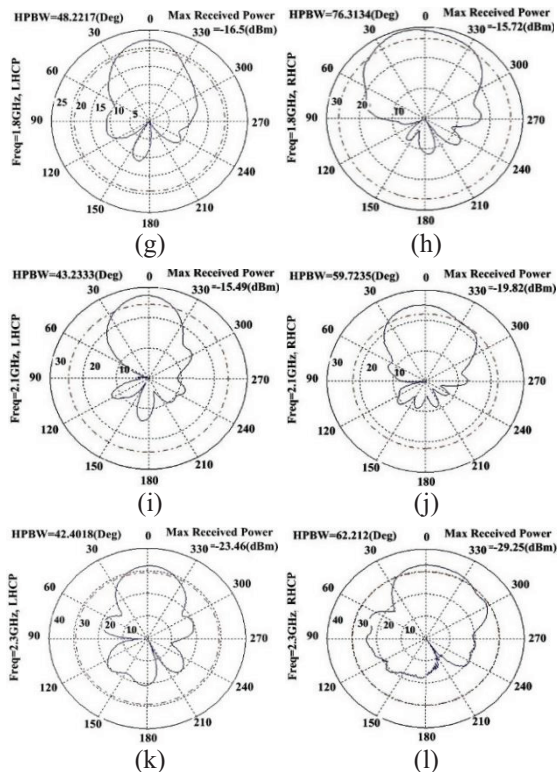


Fig. 12. Normalized measured radiation pattern results at six frequencies of Fig. 11; left column: LHCP, right column: RHCP.

#### IV. CONCLUSION

This paper presented aperture coupled microstrip antenna with three resonants. The antenna bandwidth enhanced due to clip in the patch edges and varied the current distribution well in order to create the third resonant. There was a compromise between radiation characteristics and the antenna bandwidth. These two factors were optimized in designed and fabricated samples. E-plane and H-plane patterns indicated the appropriate propagation pattern of antenna was between 1.3 to 2.3 GHz frequency band, which clarified bandwidth more than 53% was achieved by using certain method in the novel one radiating element. Of course, there was bandwidth enhancement up to this limit by utilization of multiple radiating elements.

#### REFERENCES

- [1] D. M. Pozar, "A review of aperture coupled microstrip antennas: history, operation, development, and applications," *Electrical and Computer Engineering University of Massachusetts at Amherst*, MA 01003, May 1996.
- [2] R. Garg and A. Ittipiboon, *Microstrip Antenna Design Handbook*, Artech House, 2001.
- [3] D. M. Pozar, "Microstrip antenna aperture-coupled

to a microstrip-line," *Electronics Lett.*, vol. 21, no. 2, pp. 49-50, Jan. 1985.

- [4] D. M. Pozar and S. D. Targonski, "Improved coupling for aperture coupled microstrip antennas," *Electronics Lett.*, vol. 27, no. 13, pp. 1129-1131, June 1991.
- [5] V. Rathi, G. Kumar, and K. P. Ray, "Improved coupling for aperture coupled microstrip antennas," *IEEE Trans. Antennas Propagat.*, vol. 44, pp. 1196-1198, Aug. 1996.
- [6] K. L. Wong, *Compact and Broadband Microstrip Antennas*, John Wiley & Sons, Ed. 1, ISBN: 0-471-41717-3, 2002.
- [7] K. M. Luk, K. F. Lee, and H. W. Lai, "Development of wideband L-probe coupled patch antenna," *Applied Computational Electromagnetics Society (ACES) Journal*, vol. 22, no. 1, pp. 88-96, Mar. 2007.
- [8] J. S. Meiguni, M. Kamyab, and A. Hosseinbeig, "Spherical aperture-coupled antennas with parasitic element," *Applied Computational Electromagnetics Society (ACES) Journal*, vol. 27, no. 12, pp. 999-1006, 2012.
- [9] M. M. Bilgic and K. Yegin, "High gain, wideband aperture coupled microstrip antenna design based on gain-bandwidth product analysis," *Applied Computational Electromagnetics Society (ACES) Journal*, vol. 29, no. 8, pp. 639-646, Aug. 2014.
- [10] S. D. Targonski, R. B. Waterhouse, and D. M. Pozar, "Design of wide-band aperture-stacked patch microstrip antennas," *IEEE Transactions on Antennas and Propagation*, vol. 46, no. 9, Sep. 1998.
- [11] N. Herscovici, B. Tomasic, J. Ginn, and T. Donisi, "A wide-band single-layer aperture-coupled microstrip antenna," *3<sup>rd</sup> European Conference on Antennas and Propagation (EuCAP)*, pp. 2357-2360, 2009.
- [12] J. F. Zurcher, "The SSFIP: a global concept for high performance broadband planar antennas," *Electronics Letters*, vol. 24, pp. 1433-1435, Nov. 1988.
- [13] F. Croq and A. Papiernik, "Large bandwidth aperture coupled microstrip antenna," *Electronics Letters*, vol. 26, pp. 1293-1294, Aug. 1990.
- [14] C. A. Balanis, *Antenna Theory Analysis and Design*, John Wiley & Sons Inc. Publication, Chapter 14, New Jersey, 2005.
- [15] E. O. Hammerstad and O. Jensen, "Accurate models for microstrip computer-aided design," *Digest IEEE MIT-S Internat. Microwave Symposium*, pp. 407-409, 1980.
- [16] S. Chakraborty, T. Chakraborty, B. Gupta, and D. R. Poddar, "Transmission line model of dual patch aperture coupled microstrip antenna," *Proc. URSI General*, 2005.



**Mohsen Jafari Chashmi** was born in Gonbad-e-kavoos, Iran, on March 21, 1983. He received the B.S. and M.S. degrees in Electrical and Communication Engineering from Shiraz University (SHU), Shiraz, Iran and Shahid Beheshti University (SBU), Tehran, Iran in 2006 and

2013, respectively.

His current research interests are about microwave passive devices, microwave waveguide components (polarizer, OMT), microstrip & reflector & UWB antennas and antenna broad-banding method.



**Hadi Ghobadi** was born in Arak, Iran, on September 18, 1984. He received the B.S. and M.S. (from Khaje Nasir Toosi University of Technology-KNTU) degrees in Electrical and Computer Science Engineering in 2006 and 2013, respectively.

His current research interests are about microwave active devices, microstrip antenna and waveguide filter fields.



**Mahdi Oliaei** was born in Dubai, UAE, in 1988. He received his B.Sc. and M.Sc. degrees in Electrical and Electronic Engineering from Iran University of Science and Technology (IUST), and Electrical and Computer Science Engineering from Khaje Nasir Toosi University of Technology

(KNTU), Tehran, Iran, in 2011 and 2013, correspondingly.

His current research interest are about millimeter and sub-millimeter (THz) wave antennas, photonics, plasmonics, and quantum fields. His previous research interests include electromagnetic compatibility (EMC), metamaterials, microwave devices, radar systems and networking.

He also has served as Reviewer for two ISI Journals and one conference, so far: IET Microwaves, Antennas & Propagation (MAP), The Applied Computational Electromagnetics Society (ACES), and European Conference on Antennas & Propagation (EuCAP).

He is currently working on Radar, (Anti) Jamming and Satellite Telecommunications at industries.

# Full-Wave Fast Solver for Circuit Devices Modeling

Yuteng Zheng, Yanwen Zhao, Zaiping Nie, and Qiangming Cai

Department of Electrical Engineering  
University of Electronic Science and Technology of China, Chengdu, 611731, China  
zhengyuteng413@gmail.com, ywzhao@uestc.edu.cn

**Abstract** — The analysis of complex circuit components with electrically small size is an important problem for radio frequency circuit modeling. In this paper, we present a fast solver which is based on low-frequency stable integral equation and accelerated with the multilevel accelerated Cartesian expansion algorithm (MLACEA). MLACE algorithm is usually based on electric field integral equation which suffers from low-frequency breakdown problems. To keep the algorithm stable, the augmented electric field integral equation (AEFIE) is used in our solver. Regarding the truncation order of the expansion, the efficiency and accuracy of MLACEA are investigated. By adjusting the truncation order, we can keep the algorithm in good performance. Numerical examples show the efficiency and the capability of the proposed method.

**Index Terms** — Fast algorithm, low-frequency problem, method of moments.

## I. INTRODUCTION

The electric field integral equation (EFIE) solved by the method of moments (MoM) [4] is widely used in practical RF and microwave circuit modeling and design [6]. Due to the increasing integration density, the electromagnetic (EM) analysis of circuit problems become more challenging. Furthermore, the manufacturing technique of three-dimensional (3D) passives RF components [1], logic cells [2] and system in package (SIP) techniques [3] have received considerable amount of attention recently. By utilizing these techniques, the 2D planar structures are changed into 3D multilayer stereoscopic and even curved structures. Because of the increasing complexity, the scale of numerical problem for EM modeling is dramatically increased.

For 3D circuit modeling, the following two problems need to be concerned. One is the high computational complexity of MoM. To reduce the complexity and accelerated the simulation speed, many kinds of fast algorithms have been studied. The algorithms based on fast Fourier transforms (FFT) are widely used for quasi-planar structures. Suppose the scale of a problem is  $N$ . Then numerical complexity of

the matrix vector production (MVP) and memory consumption can be reduced from  $O(N^2)$  to  $O(N \log N)$  [5,6]. However, FFT methods require a projection between the original mesh and the uniform grid, so it is difficult to balance the workload for multiscale problems. The oct-tree based fast algorithms, such as the low-frequency multilevel fast multipole algorithm (LF-MLFMA) [7] and the multilevel accelerated Cartesian expansion algorithm (MLACEA) [8,9], have lower numerical complexity. Even for 3D structures the MVP time and memory consumptions of these two methods have  $O(N)$  complexity. LF-MLFMA has been successfully applied on low-frequency EM modeling such as [7,10], while the implementation of MLACEA on low-frequency EM modeling is seldom reported.

The other problem need to be concerned is the low-frequency breakdown problem of EFIE, which restricts the fast algorithm to handle low-frequency EM problems. The low-frequency breakdown problem of EFIE occurs when the discretization is so fine that the mesh size is much smaller than the wavelength [11]. In this situation, the condition number of the matrix increases, and the convergence of iterative method is getting worse. The low-frequency breakdown problem often influenced the accuracy of circuit device modeling. Loop-tree decomposition [12] is usually employed to remedy the low-frequency breakdown problem, and many fast solvers base on this method have been developed [6,7]. However, searching for loop basis functions is difficult for multiple connected surfaces, especially in 3D case. Recently some low-frequency stable EFIE methods were developed, such as the augmented electric field integral equations (AEFIE) [10], the current and charge integral equations (CCIE) [13], the separated potential integral equations (SPIE) [14], and surface integral equations using constraint-based Helmholtz decompositions [16,17]. They all remedy the low-frequency breakdown problem successfully.

In this paper, we used AEFIE to remedy the low-frequency breakdown problem. Compared with other integral equations, the operator in AEFIE is simpler. This advantage not only results in simplicity of programming

but also in less memory and time consumption of the fast algorithm. However, the AEFIE still suffers from the low-frequency inaccuracy problem in extremely low-frequency, but this inaccuracy problem can be eliminated with perturbation method [15]. The paper is organized as follows. The AEFIE and its MoM solution are reviewed in Section II. Then, in order to remedy the low-frequency breakdown problem of EFIE and to keep the matrix equation in good condition, the AEFIE is used as the basic formula of the MLACEA algorithm. Particularly, the truncation order of MLACEA is analyzed to figure out its influence on the efficiency and the accuracy. At last, several large unknown targets have been simulated to show the capability of the proposed method.

## II. THEORY

### A. Augmented electric field integral equation

Consider a perfect electric conducting (PEC) surface  $S$  placed in free space is excited by a incident field  $\mathbf{E}^{inc}$ . The mixed potential integral equation in terms of the induced current  $\mathbf{J}(\mathbf{r})$  on the PEC surface  $S$  can be achieved by using the tangential boundary condition of electric field, given as:

$$\begin{cases} \mathbf{n} \times \mathbf{E}^{inc}(\mathbf{r}) = \mathbf{n} \times [\mathbf{j}\omega\mathbf{A}(\mathbf{r}) + \nabla\Phi(\mathbf{r})] \\ \mathbf{A}(\mathbf{r}) = \mu \int_S dS' \mathbf{J}(\mathbf{r}') G(\mathbf{r}, \mathbf{r}') \\ \Phi(\mathbf{r}) = \mathbf{j}\eta k^{-1} \int_S dS' \nabla' \cdot \mathbf{J}(\mathbf{r}') G(\mathbf{r}, \mathbf{r}') \end{cases} \quad (1)$$

In the above equations,  $G(\mathbf{r}, \mathbf{r}')$  is the scalar Green's function in free space:

$$G(\mathbf{r}, \mathbf{r}') = \frac{e^{-jkR}}{4\pi R}, \quad (2)$$

where  $R = |\mathbf{r} - \mathbf{r}'|$  represents the distance between the source point  $\mathbf{r}'$  and the field point  $\mathbf{r}$ .  $\eta = \sqrt{\mu_0/\epsilon_0}$  denotes the wave impedance,  $k = \omega\sqrt{\epsilon_0\mu_0}$  denotes the wave number of free space and  $\mathbf{n}$  is the unit outer normal to surface  $S$ . This integral equation suffers from the low-frequency breakdown problem, because of the different frequency dependence of vector potential and scalar potential in the low-frequency region [11]. In order to separate the vector and scalar potential and remove the frequency dependence, the current continuity equation given as:

$$\nabla \cdot \mathbf{J}(\mathbf{r}) = -\mathbf{j}\omega\rho(\mathbf{r}), \quad (3)$$

is added. It works as a constraint for the charge and the current. To get the discretized form of the equations, the surface current  $\mathbf{J}(\mathbf{r})$  is expanded over a set of RWG basis functions as:

$$\mathbf{f}_n(\mathbf{r}) = \begin{cases} (\mathbf{r} - \mathbf{r}_n^+) / (2A_n^+), & \mathbf{r} \in T_n^+ \\ -(\mathbf{r} - \mathbf{r}_n^-) / (2A_n^-), & \mathbf{r} \in T_n^- \end{cases} \quad (4)$$

The charge is expanded as pulse functions:

$$h_n(\mathbf{r}) = 1/A_n, \quad \mathbf{r} \in T_n, \quad (5)$$

where  $A_i$  is the area of triangle  $T_i$ . Then EFIE is tested by RWG basis functions  $\mathbf{f}_m(\mathbf{r})$ , and the current continuity equation is tested by  $h_m(\mathbf{r})$ . Matrix equations can be finally written as:

$$\mathbf{B} \cdot \mathbf{j}k\mathbf{I} + \mathbf{D}^T \cdot \mathbf{P} \cdot \mathbf{c}\rho = \eta^{-1}\mathbf{b}, \quad (6a)$$

$$\mathbf{D} \cdot \mathbf{j}k\mathbf{I} + \tilde{\mathbf{I}} \cdot ck^2\rho = \mathbf{0}. \quad (6b)$$

The elements of sub matrices are defined as:

$$b(m) = \int_{S_m} dS \mathbf{f}_m(\mathbf{r}) \cdot \mathbf{E}^{inc}(\mathbf{r}), \quad (7)$$

$$B(m, n) = \int_{S_m} dS \mathbf{f}_m(\mathbf{r}) \cdot \int_{S_n} dS' \mathbf{f}_n(\mathbf{r}') G(\mathbf{r}, \mathbf{r}'), \quad (8)$$

$$P(m, n) = \int_{T_m} dS h_m(\mathbf{r}) \int_{T_n} dS' h_n(\mathbf{r}') G(\mathbf{r}, \mathbf{r}'), \quad (9)$$

$$D(m, n) = \frac{1}{A_n} \int_{T_m} dS h_m(\mathbf{r}) \nabla \cdot \mathbf{f}_n(\mathbf{r}), \quad (10)$$

where  $S_n = T_n^+ \cup T_n^-$ .  $\mathbf{I}$  and  $\rho$  denote the coefficients of current and charge unknowns.  $\tilde{\mathbf{I}}$  is the identity matrix.  $c$  is the light speed in free space. In this matrix equation, the vector potential and scalar potential are balanced. After using a proper frequency scaling [10], the low-frequency breakdown can be remedied.

### B. Implementation of MLACEA

In this section, MLACEA is applied on the AEFIE for acceleration. Similar to MLFMA, the basis functions are divided into groups of small cubes using the oct-tree structure. Based on whether two boxes are within one box interval, the interaction between the basis functions and the testing functions inside any two boxes is classified as the near-field interaction or the far-field interaction.

To calculate the far-field interaction with MLACEA, the scalar Green's function is expanded with the Cartesian tensor expansion which is given as:

$$\psi(\mathbf{r} - \mathbf{r}') = \sum_{q=0}^{\infty} \frac{(-1)^q}{q!} \mathbf{r}'^{(q)} \cdot \mathbf{q} \cdot \nabla^{(q)} \psi(\mathbf{r}), \quad (11)$$

where  $\nabla^{(q)}$  is  $q$ -fold grid operator of  $\mathbf{r}$  and  $\mathbf{A}^{(p+q)} \cdot \mathbf{q} \cdot \mathbf{B}^{(q)}$  represents  $q$ -fold tensor contraction between tensors  $\mathbf{A}^{(p+q)}$  and  $\mathbf{B}^{(q)}$ . Then this expansion is applied on the Green's function. As an example, the scalar Green's function is expanded with two-level accelerated Cartesian expansion algorithm in the following derivation. For far-field group interaction, the scalar Green's function  $G(\mathbf{r}, \mathbf{r}')$  is expanded using (11) twice, both in the center of source group  $\mathbf{r}_\alpha^c$  and the center of field group  $\mathbf{r}_\alpha^c$  as:

$$G(\mathbf{r}, \mathbf{r}') \approx \sum_{q=0}^Q \frac{1}{q!} (\mathbf{r} - \mathbf{r}_\alpha^c)^{(q)} \cdot \mathbf{q} \cdot \sum_{p=0}^Q \nabla^{(p+q)} G(\mathbf{r}_\alpha^c, \mathbf{r}_\alpha^c) \cdot \mathbf{p} \cdot \left[ \frac{(-1)^p}{p!} (\mathbf{r}' - \mathbf{r}_\alpha^c)^{(p)} \right], \quad (12)$$

where  $Q$  is the truncation order.

Then we can apply this expansion in MoM. When we solve the MoM linear equations using an iterative method, the matrix vector product (MVP) is a very time consuming part. To reduce the MVP time, fast algorithm is applied. The matrices in (6b) are calculated directly because they are highly sparse matrix. While MLACEA is applied on the matrices in (6a) to speed up the calculation. After the expansion using (12), the storage for far-field interaction matrix is no more needed, and the calculation of:

$$\mathbf{V} = \mathbf{B} \cdot \mathbf{jkI} + \mathbf{D}^T \cdot \mathbf{P} \cdot \mathbf{c}\rho, \quad (13)$$

can be represented by MLACEA approximately, given as:

$$\mathbf{V} \approx \mathbf{B}_{near} \cdot \mathbf{jkI} + \mathbf{D}^T \cdot \mathbf{P}_{near} \cdot \mathbf{c}\rho + \mathbf{jkV}_A^{far} + \mathbf{cV}_\phi^{far}, \quad (14)$$

where  $\mathbf{B}_{near}$  and  $\mathbf{P}_{near}$  represent the near-field interactions corresponding to vector and scalar potentials respectively. They are computed and stored using conventional MoM.  $\mathbf{V}_A^{far}$  and  $\mathbf{V}_\phi^{far}$  are far-field interactions of vector potential and scalar potential. Corresponding to any testing function  $\mathbf{f}_m(\mathbf{r})$  or  $h_n(\mathbf{r})$ , we denote the contributions from charge and current in far-field groups as  $V_A^{far}(m)$  or  $V_\phi^{far}(m)$ . They can be represented into two level MLACEA form as:

$$V_A^{far}(m) = \sum_{q=0}^Q \mathbf{F}_m^{A,-}(q, \mathbf{r}_\alpha^c) \cdot \mathbf{q} \cdot \quad (15a)$$

$$\sum_{p=0}^Q \sum_{\alpha' \in \mathbf{G}_\alpha^{far}} \mathbf{T}(q+p; \mathbf{r}_\alpha^c, \mathbf{r}_{\alpha'}^c) \cdot \mathbf{p} \cdot \mathbf{S}_{\alpha'}^A(p, \mathbf{r}_{\alpha'}^c),$$

$$V_\phi^{far}(m) = \sum_{q=0}^Q \mathbf{F}_m^{\phi,-}(q, \mathbf{r}_\alpha^c) \cdot \mathbf{q} \cdot \quad (15b)$$

$$\sum_{p=0}^Q \sum_{\alpha' \in \mathbf{G}_\alpha^{far}} \mathbf{T}(q+p; \mathbf{r}_\alpha^c, \mathbf{r}_{\alpha'}^c) \cdot \mathbf{p} \cdot \mathbf{S}_{\alpha'}^\phi(p, \mathbf{r}_{\alpha'}^c),$$

where  $\mathbf{G}_\alpha^{far}$  denotes the set of far-field groups related to the group  $\alpha$ . In MLACEA, the tensors formed by aggregating the source points inside a group are called multipole expansions. The corresponding current and charge multipole expansions are given as:

$$\mathbf{S}_{\alpha'}^A(p, \mathbf{r}_{\alpha'}^c) = \sum_{n \in \mathbf{G}_{\alpha'}^{self}} I_n \mathbf{F}_n^{A,+}(p, \mathbf{r}_{\alpha'}^c), \quad (16a)$$

and

$$\mathbf{S}_{\alpha'}^\phi(p, \mathbf{r}_{\alpha'}^c) = \sum_{n \in \mathbf{G}_{\alpha'}^{self}} \rho_n \mathbf{F}_n^{\phi,+}(p, \mathbf{r}_{\alpha'}^c), \quad (16b)$$

where  $\mathbf{G}_{\alpha'}^{self}$  represents the set of current and charge basis functions in the group  $\alpha'$ .  $\mathbf{F}_n^{A,+}$  and  $\mathbf{F}_n^{\phi,+}$  are aggregation factors corresponding to each basis function, called multipole factors. The multipole factors of currents and charges in (16) are given as:

$$\mathbf{F}_n^{A,+}(p, \mathbf{r}_{\alpha'}^c) = \frac{(-1)^p}{p!} \int_{S_n} dS' (\mathbf{r}' - \mathbf{r}_{\alpha'}^c)^{(p)} \mathbf{f}_n(\mathbf{r}'), \quad (17a)$$

and

$$\mathbf{F}_n^{\phi,+}(p, \mathbf{r}_{\alpha'}^c) = \frac{(-1)^p}{p!} \int_{T_n} dS' (\mathbf{r}' - \mathbf{r}_{\alpha'}^c)^{(p)} h_n(\mathbf{r}'). \quad (17a)$$

The integration regions of the two integrals above are different. One is on a basis function, and the other is on a triangle patch. The interaction from source group to field group is connected by the translation operator:

$$\mathbf{T}(p; \mathbf{r}_\alpha^c, \mathbf{r}_{\alpha'}^c) = \nabla^{(p)} G(\mathbf{r}_\alpha^c, \mathbf{r}_{\alpha'}^c). \quad (18)$$

It is applied on the multipole expansion and transforms them into the local expansion  $\mathbf{R}_\alpha(q, \mathbf{r}_\alpha^c)$  in field region. Then the local expansion will be contracted with the local factors to achieve  $V_A^{far}(m)$  and  $V_\phi^{far}(m)$ . The local factors in (15) are:

$$\mathbf{F}_m^{A,-}(p, \mathbf{r}_\alpha^c) = \frac{1}{p!} \int_{S_m} dS (\mathbf{r} - \mathbf{r}_\alpha^c)^{(p)} \mathbf{f}_m(\mathbf{r}), \quad (19a)$$

$$\mathbf{F}_m^{\phi,-}(p, \mathbf{r}_\alpha^c) = \frac{1}{p!} \int_{S_m} dS (\mathbf{r} - \mathbf{r}_\alpha^c)^{(p)} \nabla \cdot \mathbf{f}_m(\mathbf{r}). \quad (19b)$$

Similarly the multilevel form use a translation operator between the parent level and the child level recursively. With multilevel recursion, higher efficiency can be achieved. Here, (15a) which corresponds to the vector potential is used as an example to show the derivation of the multilevel algorithm. It is written in a new form as:

$$V_A^{far}(m) = \sum_{p=0}^Q \mathbf{F}_m^{A,-}(p, \mathbf{r}_{\alpha_l}^c) \cdot \mathbf{p} \cdot \left[ \mathbf{R}_{\alpha_l}^l(p, \mathbf{r}_{\alpha_l}^c) + \sum_{p=0}^Q \sum_{\alpha'_l \in \mathbf{G}_{\alpha_l}^{rel}} \mathbf{T}(q+p; \mathbf{r}_{\alpha_l}^c, \mathbf{r}_{\alpha'_l}^c) \cdot \mathbf{p} \cdot \mathbf{S}_{\alpha'_l}^A(p, \mathbf{r}_{\alpha'_l}^c) \right], \quad (20)$$

where  $\mathbf{R}_{\alpha_l}^l(q, \mathbf{r}_{\alpha_l}^c)$  is the local expansion of  $\alpha_l$  on the  $l$ th level.  $\mathbf{G}_{\alpha_l}^{rel}$  indicates the set of the distant relative groups. The term  $\alpha_{l-1}$  indicates the parent group of  $\alpha_l$ , and the distant relative groups can be defined as the groups on the  $l$ th level who are not only in the far-field region of  $\alpha_l$  but also inside the near-field region of  $\alpha_{l-1}$ . On each level, the local expansion is given as:

$$\begin{aligned} \mathbf{R}_{\alpha_l}^l(p, \mathbf{r}_{\alpha_l}^c) &= \sum_{q=p}^Q \frac{1}{(q-p)!} \mathbf{R}_{\alpha_{l-1}}^{l-1}(q, \mathbf{r}_{\alpha_{l-1}}^c) \\ &\quad \cdot (q-p) \cdot (\mathbf{r}_{\alpha_l}^c - \mathbf{r}_{\alpha_{l-1}}^c)^{(q-p)} \\ &\quad + \sum_{p=0}^Q \sum_{\alpha'_l \in \mathbf{G}_{\alpha_l}^{rel}} \mathbf{T}(q+p; \mathbf{r}_{\alpha_l}^c, \mathbf{r}_{\alpha'_l}^c) \cdot \mathbf{p} \cdot \mathbf{S}_{\alpha'_l}^A(p, \mathbf{r}_{\alpha'_l}^c), \end{aligned} \quad (21)$$

where  $\mathbf{r}_{\alpha_l}^c$  and  $\mathbf{r}_{\alpha_{l-1}}^c$  are the centroids of the child groups and the parent group respectively. The first part on the

right hand side of this equation does not need to be calculated when this equation is applied on the highest level. Similarly, the multipole-to-multipole translation is expressed with:

$$\mathbf{S}_{\alpha'}^{l-1}(p, \mathbf{r}_{\alpha'}^c) = \sum_{\alpha'_i \in \mathbf{G}_{\alpha'}^{\text{son}}} \sum_{q=p}^Q \frac{1}{(q-p)!} \mathbf{S}_{\alpha'_i}^l(q, \mathbf{r}_{\alpha'_i}^c) (\mathbf{r}_{\alpha'}^c - \mathbf{r}_{\alpha'_i}^c)^{(q-p)}, \quad (22)$$

where  $\mathbf{G}_{\alpha'}^{\text{son}}$  indicates the child groups of  $\alpha'_i$ . This equation is applied on the aggregation of child groups. Recursively using (21) and (22), the algorithm can be easily applied to multilevel form.

### III. NUMERICAL RESULTS

All numerical computations have been performed on a 64-bit PC using Intel core-i5 CPU with 3.0 GHz clock speed. The generalized minimum residual (GMRES) which restarts every 30 iterations was used as solver of linear equation.

The computational complexity of proposed method is analyzed in the first example. A PEC cube with a side length of 10 mm is calculated at 300 MHz. The target is divided into 1200 triangular patches, and the induced current is then expanded with 1800 RWG basis functions. By connecting each pair of the adjacent midpoints of the three edges in a triangular patch, this triangle is divided into the four small triangular patches with one-half of the original edge length. This refinement is done recursively to obtain five different discretization schemes. They are named from coarse to fine by the letters A to F. The group size is optimized to keep the average number of unknowns around 30 approximately in each group on the bottom level. The truncation order of Cartesian expansion is set as 2. The CPU times for calculating the near-field matrix and the matrix vector product are both shown in Fig. 1. The black solid line, a linear function in terms of the number of unknowns  $N$ , is shown as a reference. According to this solid line, it is easy to find out that the memory consumption, the CPU time for the near-field matrix calculation and the MVP are all  $O(N)$ .

The error convergence of MLACEA when calculating the finest mesh F is discussed. The mesh contains 1228800 triangle patches and 1843200 RWG basis functions. For the Cartesian expansion the truncation order  $Q$  impacts the accuracy of the algorithm. To balance the efficiency and accuracy, the truncation order should be carefully selected. Although the numerical precision has been tested in previous work by calculating the relative error of the scalar potential, here we evaluate the relative error of the impedance matrix so that the error induced by the transformation from potential to impedance matrix elements can be included. The relative error defined as:

$$O(\mathbf{Z}) = \frac{\|\delta \mathbf{V}\|_2}{\|\mathbf{V}\|_2} = \frac{\|V_{ACE}(\mathbf{Z}, \mathbf{I}) - \mathbf{Z}_{MoM} \cdot \mathbf{I}\|_2}{\|\mathbf{Z}_{MoM} \cdot \mathbf{I}\|_2}, \quad (23)$$

is used to measure the truncation error of the algorithm quantitatively. By a given vector  $\mathbf{I}$ ,  $\mathbf{Z}_{MoM} \cdot \mathbf{I}$  is calculated by direct multiplication.  $V_{ACE}(\mathbf{Z}, \mathbf{I})$  is achieved by MLACEA. In Table 1, as truncation order increases, the time consumption of MVP grows exponentially, while the relative error only decreases slowly. After the trade-off between efficiency and accuracy, two orders expansion is used in the following example for better numerical performances. With the help of the preconditioner in [10], the residual error can be converged to less than  $10^{-4}$  within 110 iterations. The details on the convergence history of five cases are shown in Fig. 2. The bi-static RCS results of first five cases, shown in Fig. 3, are in good agreement.

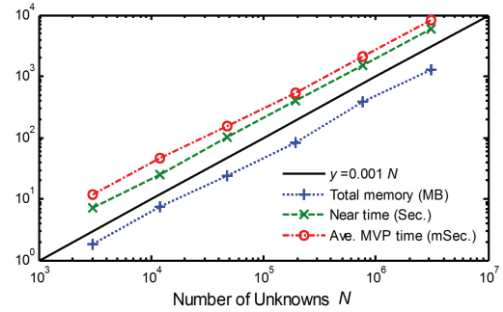


Fig. 1. The computational complexity of time and memory for the proposed method.

Table 1: Relative error convergence and normalized time consumption

Truncation Order	Normalized Time	Relative Error $O(B)$	Relative Error $O(P)$
0	1	$1.92 \times 10^{-1}$	$1.08 \times 10^{-1}$
1	2	$3.98 \times 10^{-2}$	$2.13 \times 10^{-2}$
2	5	$9.76 \times 10^{-3}$	$5.71 \times 10^{-3}$
3	16	$2.98 \times 10^{-3}$	$1.76 \times 10^{-3}$
4	44	$1.06 \times 10^{-3}$	$5.36 \times 10^{-4}$

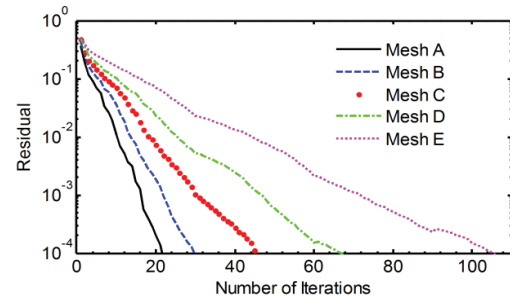


Fig. 2. History of iteration for different mesh densities.

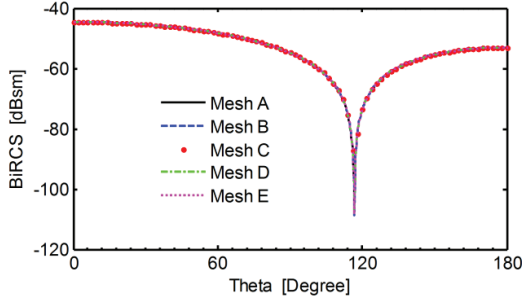


Fig. 3. The bi-static RCS results for different mesh densities.

In the second example, a 3D micro-coil inductors has been modeled to test the capability of the algorithm. The design of the inductor is referred from [1], with the length of  $275 \mu\text{m}$ , the width of  $75 \mu\text{m}$ , the height of  $100 \mu\text{m}$ , the inner diameter of  $50 \mu\text{m}$ , and the total length of about  $5.25 \text{ mm}$ . Because the low-frequency breakdown problem is more serious compared with lossy media, the inductor is set as a PEC to investigate the performance of our solver. The inductor model is divided into 6776 triangles. Based on these triangles, 8862 current unknowns and 6776 charge unknowns are formed. Port 1 is excited with delta gap voltage source as shown in Fig. 4. To verify the accuracy of the solution, the inductance is extracted by the three methods, namely: EFIE, AEFIE and AEFIE combined with MLACEA. They are compared through a wide frequency band from 500 MHz to 25 GHz. The structure is divided into 5 levels oct-tree to keep the average number of unknowns in each group within 20 RWG basis functions. The truncation order is set as two to cut down the time consumption. EFIE is solved by LU decomposition for its bad condition number of matrix in the low-frequency. AEFIE is solved by GMRES both with and without the acceleration of MLACEA. The comparison of consumption in computation from Table 2 proves that AEFIE combined with MLACEA is much more efficient than the direct MoM solver. The results of inductance obtained by AEFIE combined with MLACEA have the same the accuracy as the traditional MoM throughout the whole bandwidth. On the other hand, EFIE can't provide the correct inductance results in the low-frequency band from 500 MHz to 8 GHz due to the low-frequency breakdown of the solutions.

Next, six discretizations of a spiral inductor are generated and named as A to F, from coarse to fine. Mesh A has 6147 inner edges. While F has 285 909 edges, which is 44 times larger than A. The total size of the inductor is  $1.2 \times 10^{-3} \lambda$  at 3 GHz. Figure 5 shows the extracted inductance for all the cases. The inductance converges to 2.348 nH as the mesh density increases. It

agrees well with the result from the MoM. With the limit of computer memory, mesh A is calculated using the MoM and the inductance is 2.329 nH. The surface current distribution on the densest mesh F is presented in Fig. 6 with color bar in dB scale. The computational costs of mesh E and F are summarized in Table 3 in detail. By keeping the average number of unknowns in each finest box around 20, the fast solver consumed very little time in near-field matrix calculation. All cases can converge to  $10^{-4}$  quickly and show good stability.

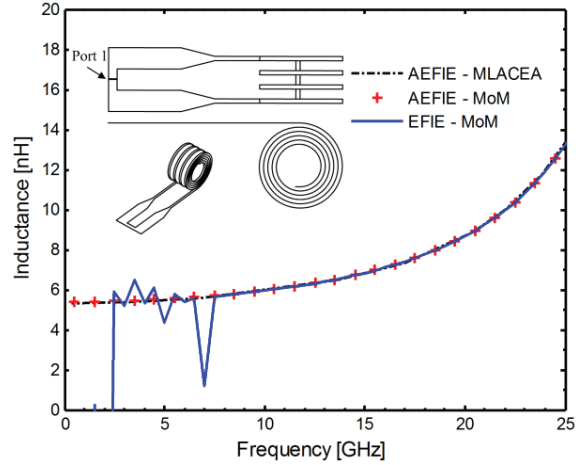


Fig. 4. The inductor model and the inductance calculated by EFIE-MoM, AEFIE-MoM and AEFIE-MoM with MLACEA acceleration.

Table 2: Average memory and time consumption of one frequency point using AEFIE

	MoM	MLACEA
Total memory (MB)	1960	59
Near field calculation time (s)	160	3.8
Number of iterations	48	49
Time per iteration (s)	1.05	0.12
Total time (s)	210	10

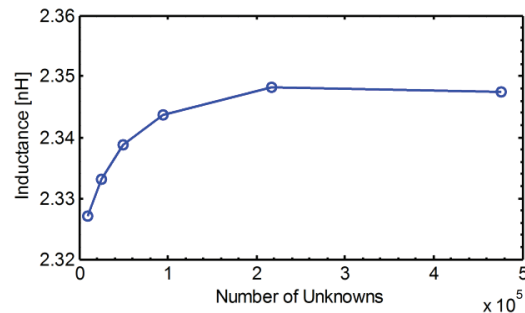


Fig. 5. The inductance calculated by meshes in different densities.

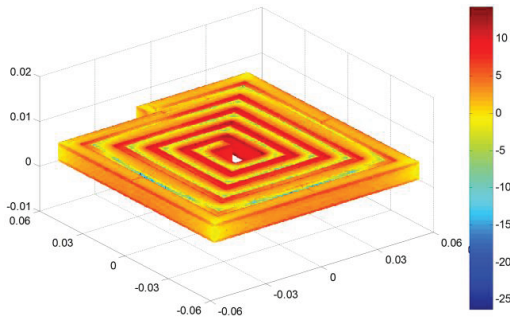


Fig. 6. The current distribution of inductor model: mesh F, unit in mm.

Table 3: Memory and time consumption of different mesh density

	Mesh E	Mesh F
Number of total unknowns	217 270	476 515
Total memory (MB)	813	1 239
Near field calculation time (s)	146	233
Number of iterations	149	188
Time per iteration (s)	1.23	2.59
Total iteration time (s)	184	502
Total time (s)	334	747

#### IV. CONCLUSION

A fast numerical algorithm, AEFIE combined with MLACEA, has been presented in this paper to model the circuit devices with electrically small and complex structures. The condition number of the impedance matrix is greatly improved by AEFIE. Because of this MLACEA shows a good stability for the low-frequency problems with large number of unknowns. With the optimization of the truncation order, the efficiency as well as the accuracy of the solver has been ensured. Its ability to cut down the memory cost and CPU time consumption can be put to use. Some work are under going to eliminate the low-frequency inaccuracy problem of AEFIE, in order to achieve a stable solver for more wide frequency band.

#### ACKNOWLEDGMENT

The authors thank the Natural Science Foundation of China under Grant No. 61371050, No. 61231001 and the National Ministerial Foundation.

#### REFERENCES

- [1] M. S. Mohamed Ali, B. Bycraft, C. Schlosser, B. Assadsangabi, and K. Takahata, "An out-of-plane spiral-coil inductor formed using locally controlled bimorph actuation," *Micro. Nano Lett.*, vol. 6, pp. 1016-1018, Dec. 2011.
- [2] S. J. Kim, J. J. Lee, H. J. Kang, J. B. Choi, Y-S. Yu, Y. Takahashi, and D. G. Hasko, "One electron-based smallest flexible logic cell," *Appl. Phys. Lett.*, vol. 101, 183101, 2012.
- [3] S. F. Al-Sarawi, D. Abbott, and P. D. Franzone, "A review of 3D packaging technology," *IEEE Trans. CPMT*, vol. 21, pp. 2-14, Jan. 1998.
- [4] R. F. Harrington, *Field Computation by Moment Methods*, IEEE Press, New York, 1993.
- [5] S. M. See and J-F. Lee, "A fast IE-FFT algorithm for solving PEC scattering problems," *IEEE Trans. Magn.*, vol. 41, pp. 1476-1479, May 2005.
- [6] V. I. Okhmatovski, J. Morsey, and A. C. Cangellaris, "Loop-tree implementation of the adaptive integral method (AIM) for numerically-stable, broadband, fast electromagnetic modeling," *IEEE Trans. Antennas Propagat.*, vol. 52, pp. 2130-2140, Aug. 2004.
- [7] J. S. Zhao and W. C. Chew. "Applying LF-MLFMA to solve complex PEC structures," *Micro. Opt. Technol. Lett.*, vol. 28, pp. 155-160, Feb. 2001.
- [8] B. Shanker and H. Huang, "Accelerated Cartesian expansions - a fast method for computing of potential of the form  $r - v$  for all real  $v$ ," *J. Comput. Phys.*, vol. 226, pp. 732-753, Jan. 2007.
- [9] M. Vikram, H. Huang, B. Shanker, and T. Van, "A novel wideband FMM for fast integral equation solution of multiscale problems in electromagnetics," *IEEE Trans. Antennas Propag.*, vol. 57, pp. 2094-2104, July 2009.
- [10] Z. G. Qian and W. C. Chew, "Fast full-wave surface integral equation solver for multiscale structure modeling," *IEEE Trans. Antennas Propag.*, vol. 57, pp. 3594-3601, Nov. 2009.
- [11] Z. G. Qian and W. C. Chew, "A quantitative study on the low-frequency breakdown of EFIE," *Micro. Opt. Technol. Lett.*, vol. 50, pp. 1159-1162, May 2008.
- [12] J. S. Zhao and W. C. Chew, "Integral equation solution of Maxwell's equations from zero frequency to microwave frequencies," *IEEE Trans. Antennas Propagat.*, vol. 48, pp. 1635-1645, Oct. 2000.
- [13] M. Taskinen and P. Ylä-Oijala, "Current and charge integral equation formulation," *IEEE Trans. Antennas Propagat.*, vol. 54, pp. 58-67, Jan. 2006.
- [14] D. Gope, A. R. Ruehli, and V. Jandhyala, "Solving low-frequency EM-CKT problems using the PEEC method," *IEEE Trans. Adv. Packag.*, vol. 30, pp. 313-320, May 2007.
- [15] Z. G. Qian and W. C. Chew, "Enhanced A-EFIE with perturbation method," *IEEE Trans. Antennas Propag.*, vol. 58, pp. 3256-3264, Dec. 2010
- [16] J. Cheng and R. J. Adams, "Electric field-based surface integral constraints for Helmholtz decompositions of the current on a conductor,"

*IEEE Trans. Antennas Propag.*, vol. 61, pp. 4632-4640, Sep. 2013.

- [17] N. Hendijani, J. Cheng, and R. J. Adams, "Combined field integral equation using a constraint-based Helmholtz decomposition," *IEEE Trans. Antennas Propag.*, vol. 62, pp. 1500-1503, Mar. 2014.



**Yuteng Zheng** was born in Lanzhou, China, in 1988. He received the B.S. degree in Electromagnetics and Microwave Technology from the University of Electronic Science and Technology of China, Chengdu, in 2010, where he is currently working toward his Ph.D. degree. His research interests include numerical methods in computational electromagnetics, especially integral equation based methods and fast algorithms.



**Yanwen Zhao** was born in Sichuan Province of China, March 23, 1965. He received the M.S. degree in Geophysical Exploration from the University of Chang Jiang in 1994, and the Ph.D. degree in Electrical Engineering from the University of Electrical and Science Technology of China (UESTC). He is currently a Professor of Electrical Engineering in UESTC. Zhao is a Senior Member of the Chinese Institute of Electronics. His research interests include computational electromagnetics, fields and waves in inhomogeneous media and inverse

scattering. He has received the second prize of the National Award for Science and Technology Progress.



**Zaiping Nie** was born in Xi'an, China, in 1946. He received the B.S. degree in Radio Engineering and the M.S. degree in Electro-magnetic Field and Microwave Technology from the Chengdu Institute of Radio Engineering (now UESTC: University of Electronic Science and Technology of China), Chengdu, P. R. China, in 1968 and 1981, respectively. From 1987 to 1989, he was a Visiting Scholar with the Electromagnetics Laboratory, University of Illinois, Urbana. Currently, he is a Professor with the Department of Microwave Engineering, UESTC. Nie is a Fellow of IEEE. He has published more than 300 journal papers. His research interests include antenna theory and techniques, fields and waves in inhomogeneous media, computational electromagnetics, electromagnetic scattering and inverse scattering, new techniques for antenna in mobile communications, and transient electromagnetic theory and applications.



**Qiangming Cai** was born in Sichuan Province of China, on December 12, 1987. He received the B.S. degree in Physics from the Sichuan Normal University, China, in 2011, and is currently working toward the Ph.D. degree in the University of Electrical and Science Technology of China (UESTC). His research interests include numerical methods in electromagnetics with focus on fast solution of frequency domain integral equation.

## Firefly Algorithm for Failure Correction of Linear Array of Dipole Antennas in Presence of Ground Plane with Mutual Coupling Effects

R. Muralidharan<sup>1</sup>, A. Vallavaraj<sup>1</sup>, and G. K. Mahanti<sup>2</sup>

<sup>1</sup> Department of Electrical and Computer Engineering  
Caledonian College of Engineering, Sultanate of Oman  
muralidharan@caledonian.edu.om, vallavaraj@caledonian.edu.om

<sup>2</sup> Department of Electronics and Communication Engineering  
National Institute of Technology, Durgapur, 713209, India  
gautammahanti@yahoo.com

**Abstract** — In this paper, firefly algorithm is utilized for the correction of radiation pattern of a linear antenna array of parallel half-wavelength dipole antennas spaced uniformly when defected completely with more than one dipole element. Mutual coupling between the antennas along has been considered along with the effect of distance between the antenna array and the ground plane on the radiation pattern. Adjustments are done in the values of the excitation voltage of the remaining non-defective elements through evolutionary algorithm such that the parameters, namely, side lobe level and maximum reflection coefficient ( $S_{11}$ ) in dB of the corrected pattern are calculated and efforts are taken to make it closer to the original pattern values. This certainly avoids replacing of defective elements. The element pattern of individual elements in the array has been assumed omnidirectional in the plane considered. Examples are shown to produce the response of the proposed approach using evolutionary algorithm for three element failures out of twenty elements in the array with the effect on various distances between the antenna array and ground plane. Even though, the method is utilized here for a linear dipole antenna array, it can be applied for other antenna array configurations also.

**Index Terms** — Antenna array, failure correction, mutual coupling, reflection coefficient, side lobe level.

### I. INTRODUCTION

High directivity is one of the major advantages of equally spaced linear antenna array [1,7] over individual elements, when it is excited uniformly. But, this will well result in production of relatively higher side lobe level (SLL), which in a radiation pattern refers to the ratio of the amplitude of the peak of main lobe to that of peak of the side lobe in decibels. The level of the side lobe level will worsen, in case of failure of even two or three

elements in an antenna array, and specifically in analog beam forming; it will lead to the replacement of the elements resulting in time consumption. The scenario will be different in digital beam forming, as there is no need to replace the defective elements. Instead, the current or voltage excitations of the remaining unaffected elements can be modified in such a way that the resulting radiation pattern closely matches with the expected pattern. Literature survey has revealed that this alternative of replacement proved quite applicable in various field of operations like radar, satellite and in military applications. There is no single method or a combination of methods that has been evolved as the best one, which can produce a radiation pattern that exactly matches with the desired one.

Literature survey reports many array failure correction techniques in the past [2-6]. Array failure correction using genetic algorithm has been described in the article [2,3]. Array failure correction with a digitally beamformed array is discussed in [4]. Failure correction method of array in general is presented in [5]. Simulated annealing technique [6] is applied to optimize the performance of arrays with failed elements.

An exhaustive study of the mutual coupling that exists in antenna arrays has been discussed by researchers dealing with various applications of antenna arrays [7-11]. In this paper, firefly algorithm [12,13] is used in recovering the damaged pattern with expected side lobe level and reflection coefficient ( $S_{11}$ ) in dB respectively.

Instead of using isotropic antennas for testing, here, the real antennas with mutual coupling has been considered for various distances between the ground plane and the array. The reason for optimizing reflection coefficient ( $S_{11}$ ) in dB is to have a better match between antenna and its feeding network. When the antenna is considered a faulty one, the voltage across it is assumed

as zero, but the current flowing through it is not zero because of induced current due to mutual coupling or in other words, it will act as a parasitic radiator.

## II. THEORY

The free space far-field pattern  $FAR(\phi)$  in azimuth plane (x-y plane) for a linear array [1] of parallel half-wavelength dipole antennas equally spaced at a distance  $d$  apart along the x-axis shown in Fig. 1, is given by Equation (1):

$$FAR(\phi) = \left[ \sum_{n=1}^N I_n e^{j(n-1)kd \cos \phi} \right] \times EP(\phi), \quad (1)$$

where  $n$ =element number,  $N$ =total number of element,  $j$ =imaginary quantity,  $d$ =inter element spacing,  $k=2\pi/\lambda$ =wave number,  $\lambda$ =wavelength,  $\phi$ =azimuth angle of the far-field point measured from x-axis (0 to 180 degree),  $I_n$ =complex excitation current of  $n$ -th element, obtained from  $[I]_{N \times 1} = [Z]^{-1} N \times N [V]_{N \times 1}$ , being  $[Z]$  the impedance matrix (size  $N \times N$ ) and  $[V]$  the voltage matrix (size  $N \times 1$ ) of the elements (obviously  $V_n=0$  for faulty element).

The expressions related to self-impedances  $Z_{nn}$  and mutual impedances  $Z_{nm}$  in the impedance matrix  $Z$  are taken from [7] and applied assuming the dipoles to be very thin and sinusoidal current distribution in every dipole, the former being calculated specifically with Tai's formula [7].

All the elements are fed with constant excitation phase of zero degree. The element pattern of each and every dipole element in the array has been assumed omnidirectional in the plane considered, i.e.,  $EP(\phi)=1$ .

A sum pattern is generated in the broadside direction for the currents  $I_n$  that are calculated from the input voltage excitations and the mutual coupling impedance matrix.

If the active impedance is real, every dipole will be radiating effectively, but since,

$$V_n = Z_{nn} I_n + \sum_{m \neq n} Z_{nm} I_m, \quad (2)$$

where  $Z_{nn}$  is the self-impedance of dipole  $n$  and  $Z_{nm}$  is the mutual impedance between dipoles  $n$  and  $m$ , the active impedance ( $Z_n^A = V_n / I_n$ ) becomes:

$$Z_n^A = Z_{nn} + \sum_{m \neq n} Z_{nm} (I_m / I_n). \quad (3)$$

When a ground plane is placed at a distance  $h$  behind the array, and parallel to  $x$ - $z$  plane, the image principles [7] are applied to calculate the self and mutual impedances of the elements and to calculate the new impedance matrix of the antenna array.

In the impedance matrix, self-impedance  $Z_{nn}$  is replaced by  $(Z_{nn} - Z_{nn}^*)$  and mutual impedance  $Z_{nm}$  is replaced by  $(Z_{nm} - Z_{nm}^*)$ , where  $Z_{nm}^*$  is the mutual impedance between the  $n$ th dipole and its image, and  $Z_{mm}^*$  is the mutual impedance between the  $n$ th dipole and

the image of the  $m$ th dipole.

The expression for the element factor is also obtained from [7].

The far-field pattern (in  $\phi$ -domain) in the horizontal plane in the above case is given by equation (4):

$$FAR(\phi) = \sum_{n=1}^N [\sin(kh \sin \phi)] I_n e^{j(n-1)kd \cos \phi}, \quad (4)$$

where  $h$  is distance between ground plane and array and the bracketed term in above equation is the element factor.

Considering that the characteristic impedance  $Z_0$  of the feeding network is  $50 \Omega$ , the reflection coefficient ( $S_{11}$ ) in dB at the input of  $n$ -th dipole antenna [1] is given by:

$$S_{11}^n = 20 \log_{10} \left[ \frac{|Z_n^A - Z_0|}{|Z_n^A + Z_0|} \right]. \quad (5)$$

Finally, the maximum reflection coefficient ( $S_{11}^m$ ) among all elements is derived. A low value of  $S_{11}^m$  ensures that the impedance matching condition holds good for all the elements of the array. The active impedance of failed element is assumed zero.

The problem is now to find the set of new excitation voltage amplitude of the elements excluding the failed elements using firefly algorithm that will minimize the chosen fitness function and at the same time correct the damaged pattern.

For obtaining the optimized (original) radiation pattern without any failures, the following cost function  $F1$  is used:

$$F1 = k1(SLL_o - SLL_d)^2 H(T1). \quad (6)$$

For obtaining the failure corrected pattern,

$$F2 = k1(SLL_o - SLL_d)^2 H(T1) + \quad (7)$$

$$k2(S_{11}^{mo} - S_{11}^{md})H(T2),$$

is used, where  $T1 = (SLL_o - SLL_d)$  and  $T2 = (S_{11}^{mo} - S_{11}^{md})$ .  $H(T1)$  and  $H(T2)$  denotes the Heaviside step functions, which can be expressed as follows:

$$H(Ti) = \begin{cases} 0, & \text{if } Ti < 0 \\ 1, & \text{if } Ti \geq 0 \end{cases}, \quad (8)$$

for  $i=1$  and 2.

In Equations (6) and (7),  $SLL_o$  is the obtained side lobe level and  $SLL_d$  is the desired side lobe level in dB,  $S_{11}^{mo}$  denotes the maximum obtained reflection coefficient in dB and  $S_{11}^{md}$  denotes the desired maximum reflection coefficient in dB,  $k1$  and  $k2$  are weighting coefficients to control each of the terms of Equations (6) and (7). The desired side lobe level is set to -20 dB and maximum reflection coefficient ( $S_{11}$ ) is set to be -15 dB. In this correction process, the values of the controlling weights are made equal to unity.

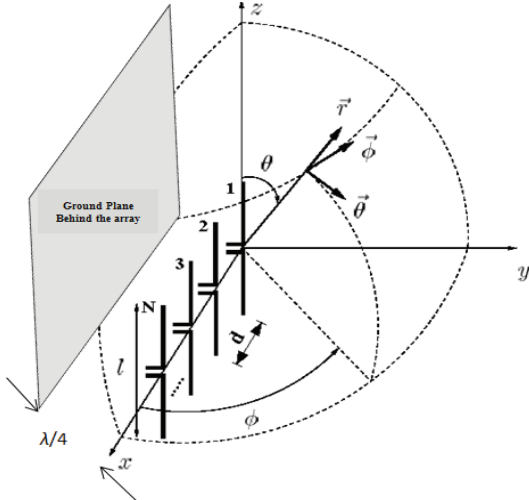


Fig. 1. A uniformly spaced linear array of parallel dipole antennas with ground plane placed at a distance  $\lambda/4$  behind the array.

### III. FIREFLY ALGORITHM

The firefly algorithm was developed by the author Yang and it was based on the unique flash characteristic features of fireflies [12,13], which uses flash as the signal to attract other fireflies. The algorithm is described as follows.

#### A. Initial positions

The fireflies are initially positioned in the  $w$ -dimensional space as described below:

$$v_m = (v_{m1}, v_{m2}, \dots, v_{mw}), \quad (9)$$

for  $m=1, 2, \dots, N$ .

#### B. Brightness of fireflies

For a minimization problem with function  $f(v_m)$ , the value of the brightness ( $I_m$ ) of each firefly at any generation is calculated and is:

$$I_m \propto 1/f(v_m). \quad (10)$$

#### C. Global best

The fireflies are positioned in a hierarchy depending on the value of their intensity or brightness at that particular generation. For a given population, the position of the firefly with a value of maximum brightness is treated to be current global best ( $gbest$ ) and its brightness is treated as best fitness value at that generation [12-13].

#### D. Updation of locations

The remaining fireflies are made to move towards the brighter firefly ( $gbest$ ) and their locations for the next iteration in the algorithm are updated based on their

attraction towards the brighter firefly. The movement of firefly  $m$  towards brighter firefly  $n$  is summarized by:

$$v_m = v_m + \beta_0 e^{-\gamma r_{mn}^2} (v_n - v_m) + \alpha \epsilon_m, \quad (11)$$

where the product of  $\beta_0$  and  $e^{-\gamma r_{mn}^2}$  in Equation (11) denotes the attractiveness between the two fireflies  $m$  and  $n$ .  $\gamma$  refers to the light absorption coefficient in a given medium.  $r_{mn}$  is the Cartesian distance between the two fireflies  $m$  and  $n$  at  $v_m$  and  $v_n$ , and is obtained from the following Equation (12).

$$r_{mn} = \|v_m - v_n\| = \sqrt{\sum_{j=1}^w (v_{m,j} - v_{n,j})^2}. \quad (12)$$

Firefly algorithm disallows the motion of the brightest firefly to any other direction at current generation. In this juncture, the algorithm allows remaining fireflies other than the brightest one to modify their locations based on Equation (11) and saves the brightest firefly's location. Proceeding in this way, the global best ( $gbest$ ) solution is updated regularly in the corresponding successive iterations of the algorithm.  $\beta_0$  is the value of the attractiveness at  $r=0$  and  $\alpha \epsilon_m$  is for introducing randomization where  $\alpha$  is the randomization parameter and  $\epsilon_m$  is a vector of random numbers drawn from a Gaussian distribution or uniform distribution [12,13]. Repeat from steps (B) to (D) till the current iteration reaches specified number of iterations and the algorithm gives the location of the most brightest firefly ( $gbest$ ) as the overall solution of the population. The value of brightness of that brightest firefly ( $gbest$ ) is treated as the global fitness value of the objective function.

The following Table 1 shows the firefly algorithm settings.

Table 1: Firefly algorithm settings

Parameters	Value
Number of flies	20
Randomness	0.25
Minimum value of $\beta$	0.2
Absorption coefficient	1
Choice of initial population	Random
Maximum number of iterations	200

### IV. SIMULATED RESULTS

A firefly (FF) optimized linear array of 20 parallel dipole antennas of length  $\lambda/2$  and radius  $0.005\lambda$ , spaced uniformly with  $\lambda/2$  distance apart along  $x$ -axis has been taken for consideration to produce a radiation pattern in azimuth plane ( $x$ - $y$  plane). The array is optimized for a side lobe level of -20 dB and maximum reflection coefficient ( $S_{11}$ ) in dB of -15 dB using FF algorithm with

various distances of  $h$  (distance between ground plane and array) at  $0.10\lambda$ ,  $0.15\lambda$ ,  $0.20\lambda$  and  $0.25\lambda$ . As for any evolutionary algorithm dealing with minimization problems, the lower the value of global fitness suggests the maximum fitness of the array to the desired specifications. Three elements namely, 5, 7 and 15<sup>th</sup> are considered to be failed elements and their amplitudes (voltages) are made equal to zero for obtaining the damaged pattern. The above elements are chosen randomly for test purpose.

The FF algorithm is utilized here for recovering the radiation pattern closer to the original pattern for all the various distances used above. The algorithm minimizes the stated objective function and finally produces the voltage excitations of the remaining defective elements that will be used to obtain the radiation pattern with expected parameters. Or in other words, the values of obtained side lobe level and reflection coefficient ( $S_{11}$ ) in dB are made approachable to the expected one. The terms used in connection to side lobe level and reflection coefficient ( $S_{11}$ ) in dB fitness in equations (6) and (7) are made equal to zero when their corresponding values are lower when compared with expected values by multiplying Heaviside step function. Program is written in Matlab. Figure 2 shows corrected voltage distribution for various distances of array from ground plane with three element failures.

Table 2 shows the value of the voltage amplitude distribution of the 20 elements in the array with three failures at 5, 7 and 15<sup>th</sup> positions with the effect of ground plane. The values of the original, damaged and corrected radiation pattern's SLL can be found from Table 3, which shows that the parameters reached the expected value. These values are obtained from the radiation pattern shown in Fig. 3 to Fig. 6.

As seen from Table 4, the maximum reflection coefficient ( $S_{11}$ ) in dB for corrected pattern is better than

the damaged pattern and it is proved for various distances between the ground plane and the array. Also, it can be found that the maximum absolute value of active impedance of the elements in the corrected pattern increases as the distance between the ground plane and array increases. For a distance of  $0.1\lambda$ , the maximum absolute active impedance was found to be 67.09 ohms, and for a distance of  $0.25\lambda$  it was found to be 134.64 ohms, which shows that the absolute value of maximum active impedance increases when the distance between array and ground plane increases. It becomes obvious from the Table 4 that the algorithm was effective in improving the cost function parameters to a good agreement between the damaged and corrected patterns.

A plot of fitness value with number of iterations in Fig. 7 shows that as the distance between the ground plane and antenna array increases, the fitness value converges but relatively at a higher value when compared to the ones with the least distances.

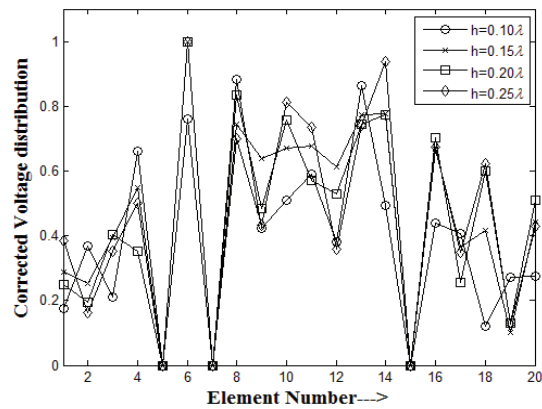


Fig. 2. Corrected voltage distribution with three element failures at 5, 7 and 15<sup>th</sup> positions with various distances of array from ground plane.

Table 2: Obtained voltage distribution for corrected pattern with 3 failures using firefly algorithm

Distance of Antenna Array from the Ground Plane	Voltage Distribution of 20 Elements for Corrected Pattern with 3 Failures at 5, 7 and 15 <sup>th</sup> Positions						
$h=0.10\lambda$	0.1741	0.3690	0.2092	0.6594	0.0000	0.7613	0.0000
	0.8825	0.4245	0.5089	0.5900	0.3809	0.8650	0.4936
	0.0000	0.4392	0.4060	0.1197	0.2715	0.2751	
$h=0.15\lambda$	0.2880	0.2532	0.3950	0.5495	0.0000	1.0000	0.0000
	0.7452	0.6395	0.6697	0.6758	0.6119	0.7749	0.7758
	0.0000	0.6675	0.3639	0.4159	0.1028	0.4424	
$h=0.20\lambda$	0.2507	0.1938	0.4042	0.3512	0.0000	1.0000	0.0000
	0.8336	0.4849	0.7574	0.5711	0.5299	0.7456	0.7720
	0.0000	0.7020	0.2546	0.5995	0.1292	0.5113	
$h=0.25\lambda$	0.3836	0.1632	0.3506	0.4996	0.0000	1.0000	0.0000
	0.6992	0.4335	0.8129	0.7345	0.3590	0.7405	0.9363
	0.0000	0.6751	0.3486	0.6214	0.1265	0.4297	

Table 3: Value of side lobe level in dB for original, damaged and corrected patterns with 3 failures using firefly algorithm

Distance h	Patterns	SLL (dB)
Ground plane with $h=0.10\lambda$	Original	-20.12
	Damaged	-14.78
	Corrected	-20.04
Ground plane with $h=0.15\lambda$	Original	-20.49
	Damaged	-16.12
	Corrected	-20.00
Ground plane with $h=0.20\lambda$	Original	-20.42
	Damaged	-16.27
	Corrected	-20.00
Ground plane with $h=0.25\lambda$	Original	-20.29
	Damaged	-16.19
	Corrected	-20.66

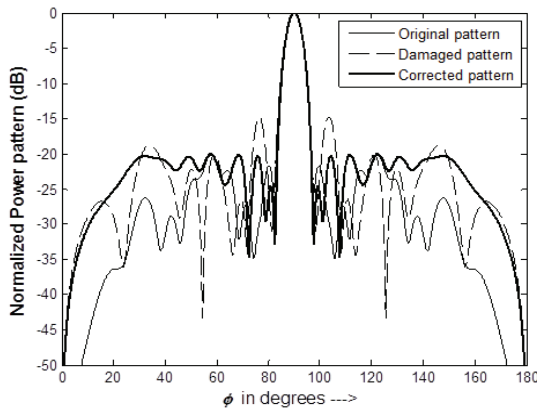


Fig. 3. Original (no failures), damaged and corrected normalized power pattern with three element failures at 5, 7 and 15<sup>th</sup> positions with a distance of  $h=0.10\lambda$  from ground plane.

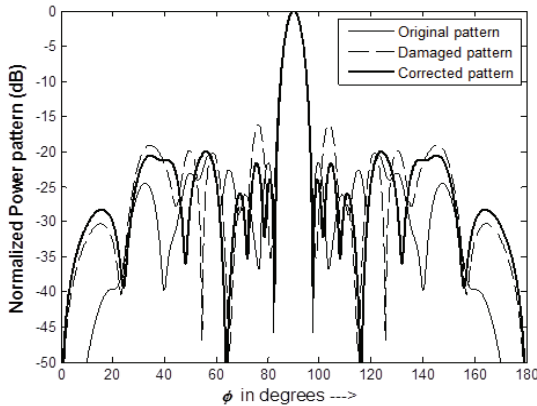


Fig. 4. Original (no failures), damaged and corrected normalized power pattern with three element failures at 5, 7 and 15<sup>th</sup> positions with a distance of  $h=0.15\lambda$  from ground plane.

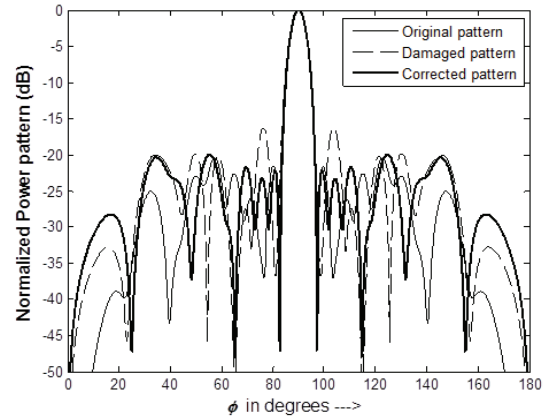


Fig. 5. Original (no failures), damaged and corrected normalized power pattern with three element failures at 5, 7 and 15<sup>th</sup> positions with a distance of  $h=0.20\lambda$  from ground plane.

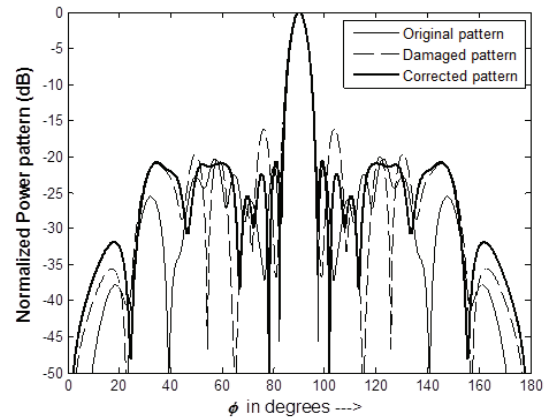


Fig. 6. Original (no failures), damaged and corrected normalized power pattern with three element failures at 5, 7 and 15<sup>th</sup> positions with a distance of  $h=0.25\lambda$  from ground plane.

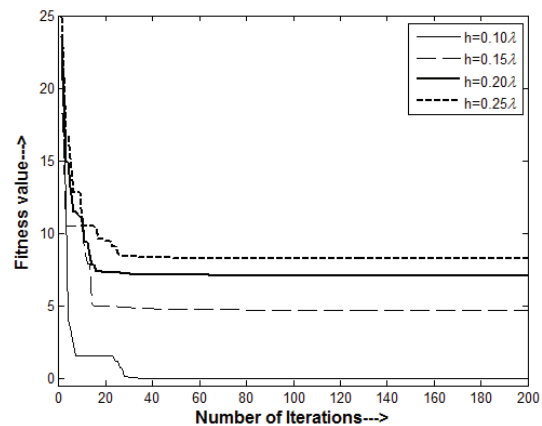


Fig. 7. Fitness value versus number of iterations.

In order to get a global magnitude that can tell how well is the agreement between the original and corrected patterns in relation with the original and damaged patterns, the following equation (13) is used. If  $NPPO$  being original normalized power pattern,  $NPPC$  being corrected normalized power pattern and  $NPPD$  being damaged normalized power pattern, the root mean square error  $Err$  is given by:

$$Err = \sqrt{\frac{\int_0^\pi (NPPO(\varnothing) - NPPC(\varnothing))^2 d\varnothing}{\int_0^\pi (NPPD(\varnothing) - NPPC(\varnothing))^2 d\varnothing}} \quad (13)$$

The root mean square error has been found to be 2.0624 (when  $h=0.10\lambda$ ), 1.5439 (when  $h=0.15\lambda$ ), 1.3210 (when  $h=0.20\lambda$ ) and 1.1810 (when  $h=0.25\lambda$ ).

Table 4. Maximum reflection coefficient ( $S_{11}$ ) in dB and maximum absolute value of active impedance for the original (without failures), damaged and corrected pattern with 3 failures

Distance of Antenna Array from Ground Plane	Maximum Absolute Value of Active Impedance (ohms)			Maximum Reflection Coefficient ( $S_{11}$ ) in dB		
	Original Pattern	Damaged Pattern	Corrected Pattern	Original Pattern	Damaged Pattern	Corrected Pattern
$h=0.10\lambda$	64.77	67.57	67.09	-17.81	-16.51	-16.71
$h=0.15\lambda$	88.56	97.53	94.01	-11.11	-09.84	-10.30
$h=0.20\lambda$	107.20	124.58	117.06	-8.78	-7.39	-7.93
$h=0.25\lambda$	119.62	147.97	134.64	-7.73	-6.11	-6.78

## V. CONCLUSIONS

This paper presents a technique based on firefly algorithm optimization for failure correction of three elements out of 20 element linear array of parallel half-wave length dipole antennas in presence of ground plane with fixed side lobe level and maximum reflection coefficient ( $S_{11}$ ) in dB. Instead of isotropic radiators, realistic antennas with mutual coupling are used in the simulations. The paper also takes care of matching between antenna and the feed network by minimizing maximum reflection coefficient ( $S_{11}$ ) in dB. Results have been simulated for the original, damaged and corrected patterns and they depicted that the corrected radiation pattern approached the expected pattern in a span of 200 iterations to an acceptable level of the parameters like SLL and reflection coefficient ( $S_{11}$ ) in dB; or in other words, they clearly show a very good level of improvement of corrected pattern when compared with damaged one. To extend this research work, importance can be given to fine tuning of setting of parameters like attractiveness parameter, absorption coefficient, etc. for firefly algorithm. This work can also be extended with a modification in the cost function, different number of failures, varying dynamic range ratio, change in number of elements considered, various steering angles and for other array configurations.

## REFERENCES

- [1] C. A. Balanis, *Antenna Theory: Analysis and Design*, 2<sup>nd</sup> ed., Singapore: John Wiley and Sons (Asia), 2003.
- [2] B-K. Yeo and Y. Lu, "Array failure correction with a genetic algorithm," *IEEE Transactions on Antennas and Propagation*, vol. 47, no. 5, pp. 823-828, May 1999.
- [3] J. A. Rodriguez, F. Ares, E. Moreno, and G. Franceschetti, "Genetic algorithm procedure for linear array failure correction," *Electronics Letters*, vol. 36, no. 3, Feb. 2000.
- [4] R. J. Mailloux, "Array failure correction with a digitally beamformed array," *IEEE Trans. on Antennas Propag.*, vol. 44, pp. 1542-1550, Dec. 1996.
- [5] H. Steyskal and R. J. Mailloux, "Generalization of an array failure correction method," *In: Proc. IEE-Microwave Antennas Propag.*, pp. 332-336, 1998.
- [6] J. A. Rodriguez and F. Ares, "Optimization of the performance of arrays with failed elements using the simulated annealing technique," *J. Electromagn. Waves Appl.*, vol. 12, pp. 1625-1637, 1998.
- [7] R. S. Elliott, *Antenna Theory and Design*, New York, USA: Prentice-Hall, 1981.
- [8] N. Pathak, B. Basu, and G. K. Mahanti, "Combination of inverse fast fourier transform and modified particle swarm optimization for synthesis of thinned mutually coupled linear array of parallel half-wave length dipole antennas," *Progress In Electromagnetics Research M, PIER M*, vol. 16, pp. 105-115, 2011.
- [9] J. A. Rodriguez, F. Ares, E. Moreno, and G. Franceschetti, "Design of efficient, easily feed matched array antennas by joint optimization of excitations and element geometry: a pencil beam example," *Electronics Letters*, vol. 34, no. 13,

- 1998.
- [10] J. H. Lee and Y. L. Chen, "Performance analysis of antenna array beamformers with mutual coupling effects," *Progress In Electromagnetics Research B*, vol. 33, pp. 291-315, 2011.
- [11] M. Thevenot, C. Menudier, A. El Sayed Ahmad, Z. El Nashef, F. Fezai, Y. Abdallah, E. Arnaud, F. Torres, and T. Monediere, "Synthesis of antenna arrays and parasitic antenna arrays with mutual couplings," *International Journal of Antennas and Propagation*, vol. 2012, 22 pages, 2012.
- [12] X. S. Yang, "Firefly algorithm, stochastic test functions and design optimization," *International Journal of Bio-Inspired Computation*, vol. 2, no. 2, pp. 78-84, 2010.
- [13] B. Basu and G. K. Mahanti, "Fire fly and artificial bees colony algorithm for synthesis of scanned and broadside linear array antenna," *Progress In Electromagnetics Research B*, vol. 32, pp. 169-190, 2011.



**R. Muralidharan** obtained his B.E. in Electronics & Communication Eng. from Madras University, India, M.E. in Applied Electronics from Anna University, India and his Ph.D. from National Institute of Technology, Durgapur, India.

He has more than 13 years of teaching experience in subjects related to Electronics and Communication Engineering. Presently, he is working as Senior Lecturer, Department of Electrical and Computer Engineering, Caledonian College of Engineering, Oman. His research area is array antenna failure correction with evolutionary algorithms.



**Athinarayanan Vallavaraj** was born in India in 1965. He received his B.E. degree in Electronics & Communication Engineering in 1987, M.E. degree in Microwave & Optical Engineering in 1993, both from Madurai Kamaraj University, India, and the Ph.D. in

Communications Systems in 2008 from the Glasgow Caledonian University, UK.

From 1987 to 1999, Vallavaraj was employed at Mepco Schlenk Engineering College, India. In 1999, he joined the Caledonian College of Engineering, Oman. He has more than two decades of teaching and research experience in India and Oman. Currently he is the Associate Dean – Undergraduate Studies at Caledonian College of Engineering, Oman.

His research activity includes peak power problems in multicarrier modulation systems, wireless communication systems and signal processing. He has co-authored a number of technical books published by McGraw Hill International, Singapore and Tata McGraw Hill Publishing Company, New Delhi. He has also published several research papers in the international conferences and journals.

Vallavaraj is a Senior Member of the Institute of Electrical and Electronics Engineers, Senior Member of the IEEE Signal Processing Society, the IEEE Communications Society, and the IEEE Vehicular Technology Society. He is also a Life Member of Indian Society for Technical Education and a Member of Oman Society of Engineers.



**G. K. Mahanti** was born in the year of 1967 in West Bengal, India. He obtained his B.E. in Electronics & Communication Eng. from NIT, Durgapur, India, M.E. in Electronics System and Communication from NIT, Rourkela, India and Ph.D. (Eng.)

from IIT, Kharagpur, India. He has more than 20 years of teaching and research experience. Presently he is working as a Professor, Department of Electronics and Communication Engineering, National Institute of Technology, Durgapur, India. He is a Senior Member of IEEE, USA.

He has produced seven Ph.D. students. He has published approximately 85 papers in journals and in national and international conferences. He was the Reviewer of many international journals like Electronics Letter, IEEE Antennas and Wireless Propagation Letter, Progress in Electromagnetics Research, International Journal of Adaptive Control & Signal Processing and many conferences. He was also the Program Committee Member of many national and international conferences. His biography is listed in Marqui's Who is Who in the world. His research area is array antenna synthesis, evolutionary algorithms & Electromagnetics.

# Lattice Boltzmann Model for Simulation of Avalanche Formation and Streamer Discharge in Breakdown of Gaseous Dielectrics

Nan Wang<sup>1,2</sup> and Qingquan Lei<sup>1</sup>

<sup>1</sup> College of Electrical & Electronic Engineering  
Harbin University of Science Technology, Harbin 150080, P.R. China  
51949083@qq.com, lei\_qingquan@sina.com

<sup>2</sup> School of Mathematical Science  
Heilongjiang University, Harbin 150080, P.R. China

**Abstract** — Gas discharges play a central role in the electrical breakdown of matter, both in nature and technology. Therefore, accurate modeling and simulation of streamers in gaseous discharge processes are of particular interest. This study presents the formulation of computationally efficient models of the charge density and electric field produced by the lattice Boltzmann method. The propagation of double-headed streamers is described in 1-cm plane-to-plane geometry in pure nitrogen at atmospheric pressure by 1.5D and 2D models. The lattice Boltzmann method was successfully applied to the simulation of streamer discharges. Therefore, this scheme is a potential way of simulating gaseous discharge problems.

**Index Terms** — Lattice Boltzmann method, numerical simulation, streamer discharge.

## I. INTRODUCTION

The discharge phenomena in gaseous dielectrics have high practical importance. Knowledge of the discharge characteristics in gaseous dielectrics is important in solving several practical problems that arise in insulation systems. Completely revealing the mechanism of streamer discharges based on existing experiment strategies is impossible, and many important microcosmic physical quantities remain undetermined. Thus, numerical simulation has become an important method in advancing the development of gas discharge theory. Different models have been developed to study streamer propagation. However, a high-accuracy algorithm is required for the streamer discharge distribution of particles in large changes in space. Kunhardt and Min introduced the finite difference and finite element methods, respectively, to solve this model. Kunhardt presented results from a self-consistent, 2D numerical simulation of streamer formation and propagation in non-attaching (N<sub>2</sub>) and attaching (N<sub>2</sub>-SF<sub>6</sub> mixture) gases using a one-moment

fluid model [1]. Min proposed the use of an adaptive mesh generation as a method of streamer simulation. A higher resolution and more efficient grid distribution with fewer grids can be obtained through adaptive mesh generation [2]. However, this method generally requires the Poisson and Boltzmann equations to be solved in each step, which make calculations complex and computer programs generally difficult to complete.

Describing charge density, electric-field distribution, temperature, and other physical quantities has been a major problem in simulating the streamer discharge development process by computer technology. 2D flux-corrected transport techniques are well-known and popular methods for the numerical calculation of streamer propagation. These methods allow for the numerical solution of transport equations under strongly space-charge-dominated conditions such as those that occur at the head of propagating streamers. Medvedev recently applied the lattice Boltzmann model (LBM) to simulate the electric breakdown in liquids and investigated pre-breakdown hydrodynamic flows and initial stages of the electric breakdown in dielectric liquids. These three models (the purely thermal, bubble, and combined models) were used to describe the expansion of streamer channels [3]. Kupershtokh developed an efficient lattice Boltzmann equation (LBE) model to simulate different electrohydrodynamic (EHD) phenomena. This model includes fluid dynamics, electric-charge transport through advection and conduction currents, and action of electric forces upon space charges in liquids [4]. The current study applies the LBE model for the numerical simulation of avalanche and streamers.

## II. MODEL FORMULATION

### A. Lattice Boltzmann model

The kinetic nature of LBM introduces three important features that distinguish it from other numerical methods. First, the convection operator (or

streaming process) of the LBM in phase space (or velocity space) is linear. This feature is borrowed from kinetic theory and contrasts with nonlinear convection terms in other approaches that use macroscopic representations. Simple convection combined with a relaxation process (or collision operator) allows the recovery of nonlinear macroscopic advection through multi-scale expansions. Second, incompressible Navier–Stokes (NS) equations can be obtained in the nearly incompressible limit of the LBM. The pressure in the LBM is calculated using an equation of state. By contrast, pressure satisfies a Poisson equation with velocity strains that act as sources in the direct numerical simulation of incompressible NS equations. Solving this equation for pressure often produces numerical difficulties that require special treatment such as iteration or relaxation. Third, the LBM utilizes a minimal set of velocities in phase space. The phase space is a complete functional space in traditional kinetic theory with the Maxwell–Boltzmann equilibrium distribution. The averaging process involves information from the entire velocity phase space. Given that only one or two speeds and a few moving directions are used in LBM, the transformation that relates to the microscopic distribution function and macroscopic quantities is simplified, which consists of simple arithmetic calculations.

The LBE can be obtained from either discrete velocity models or the Boltzmann kinetic equation, and deriving macroscopic NS equations from the LBE can be performed in several ways. This study uses an LBM model that begins from a discrete kinetic equation for the particle distribution function, which is commonly used [5-7]. Thus,

$$f_i(\mathbf{x} + e_i \Delta t, t + \Delta t) - f_i(\mathbf{x}, t) = \Omega_i(f_i(\mathbf{x}, t)), \quad (1)$$

where  $f_i$  is the particle velocity distribution function along the  $i$ -th direction,  $\Delta t$  is the time increment,  $e_i$  is the lattice direction velocity, and  $\Omega_i(f_i(\mathbf{x}, t))$  is the collision operator that represents the change rate for  $f_i$  that results from collision:

$$\rho = \sum_i f_i \quad \rho \mathbf{u} = \sum_i f_i e_i, \quad (2)$$

where  $\rho$  is the density, and  $\mathbf{u}$  is the particle velocity.

This study uses the Bhatnagar–Gross–Krook (BGK) approximation as follows:

$$\Omega_i(f_i(\mathbf{x}, t)) = -(f_i - f_i^{eq}) / \tau, \quad (3)$$

where  $\tau$  is a single relaxation time parameter. In the BGK model, relaxation time  $\tau$  governs transport coefficients such as viscosity, heat conductivity, and diffusivity, and is expressed as:

$$\tau = 3\nu \frac{\Delta t}{\Delta x^2} + 0.5, \quad (4)$$

where  $\nu$  is the kinematics viscosity of fluid,  $\Delta x$  is the lattice length, and  $f_i^{eq}$  in Equation (3) is the equilibrium distribution function. The equilibrium distribution

function can be analytically obtained [8]:

$$f_i^{eq} = \omega_i \rho \left( 1 + \frac{e_i \cdot \mathbf{u}}{c_s^2} + \frac{(e_i \cdot \mathbf{u})^2}{2c_s^4} - \frac{\mathbf{u}^2}{2c_s^2} \right). \quad (5)$$

At this point, we consider the following 2D model with nine velocities:

$$e_i = \begin{cases} (0, 0), & i=0 \\ \left( \cos\left(\frac{(i-1)\pi}{2}\right), \sin\left(\frac{(i-1)\pi}{2}\right) \right), & i=1, 2, 3, 4 \\ \left( \cos\left(\frac{(i-5)\pi}{2} + \frac{\pi}{4}\right), \sin\left(\frac{(i-5)\pi}{2} + \frac{\pi}{4}\right) \right), & i=5, 6, 7, 8 \end{cases} \quad (6)$$

The direction of  $e_i$  is shown in Fig. 1 for the nine-velocity model.

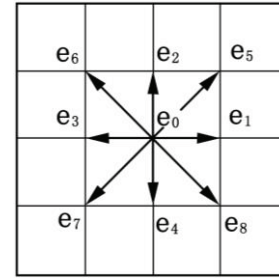


Fig. 1. Lattice velocities for the 2D model.

In Equation (5),  $\omega_i$  is the weight coefficient,  $\omega_0 = 4/9$ ,  $\omega_1 = \omega_2 = \omega_3 = \omega_4 = 4/9$ ,  $\omega_5 = \omega_6 = \omega_7 = \omega_8 = 1/36$ , and  $c_s$  is the sound speed expressed as:

$$c_s = \sqrt{RT} = 1/\sqrt{3}. \quad (7)$$

This study uses the lattice Boltzmann method to solve equations for the concentrations of electric charge carriers. We considered a new gravity model in the lattice Boltzmann method for charged particle transport forced by an electric field. When a body force is included in the Boltzmann equation, expressing force in terms of its gravitational potential ( $-\rho \nabla \phi$ ) is common. If this approach is considered and the density variation produced by the body force is negligible, the Boltzmann equation that incorporates the body force can be expressed in the same form as in the absence of gravity but with an altered pressure ( $p \rightarrow p + \rho \phi$ ). If a gravitational force  $\mathbf{F}$  acts, then a change in momentum  $\Delta p = \mathbf{F}$  at every time step occurs. This condition was incorporated into a model of equilibrium distribution [9,10]. Thus,

$$\Omega_i(f_i(\mathbf{x}, t)) = -(f_i - f_i^{eq}) / \tau + \Delta t F_i, \quad (8)$$

where

$$F_i = \omega_i \left( 1 - \frac{1}{2\tau} \right) \frac{e_i \cdot \mathbf{F}}{c_s^2}. \quad (9)$$

## B. LBM model for avalanche

A key problem encountered in the breakdown

simulation is the establishment of the electron avalanche. A numerical simulation of an electron avalanche generally adopts the random Monte Carlo algorithm. However, the form of an electron avalanche and contact between the breakdown field strength and process cannot be reflected properly with this method. This study presents a simulation of the signal development of an electron avalanche using a transport model based on Boltzmann equations.

The electron avalanche formation process was described to simulate this breakdown, and the number of electrons can be expressed using the following equation:

$$n = \alpha dx, \quad (10)$$

where  $n$  is the number of newly generated electrons produced by collision,  $\alpha$  is the ionization coefficient, and  $dx$  is the distance of an electron avalanche. We assume that the  $n_0$  electron at the negative electrode causes an electron avalanche breakdown by impact ionization under the action of the breakdown strength. Thus,

$$n = n_0 \exp \int_0^x \alpha dx. \quad (11)$$

This study uses a 2D nine-velocity D2Q9 model to describe the breakdown evolution process [9,11]. Positive ions and electrons were mainly considered to describe the initial electron avalanche formation process:

$$n = n_e = \rho_e, \quad n_p = \rho_p, \quad (12)$$

$$\rho_e = \sum_i f_{e_i}, \quad \rho_p = \sum_i f_{p_i}. \quad (13)$$

The expression for the charge density distribution function is as follows:

$$f_i(x+e_i\Delta t, t+\Delta t) = (\alpha_i - \eta_i) f_i(x, t) + \frac{f_i^{eq}(\rho_e + \rho_p, u) - f_i(x, t)}{\tau}, \quad (14)$$

where  $e_i$  is the direction vector of the electron. In the following 2D nine-velocity D2Q9 model:

$$e_i = \begin{bmatrix} 0 & 1 & 0 & -1 & 0 & 1 & -1 & -1 & 1 \\ 0 & 0 & 1 & 0 & -1 & 1 & 1 & -1 & -1 \end{bmatrix}, \quad (15)$$

$\alpha_i$  is the impact ionization coefficient, which is related to the electric field and particle mobility velocity. Electron and positive ion velocities can be written as the electron and positive ion mobilities that multiply the electric field, respectively.

The discharge process is transient, so the Poisson equation and particle transport equation should be solved at each step. For a given charge distribution, the electric field can be calculated by the charge intensity. The impact ionization coefficient and particle velocity can then be calculated by the local field. Furthermore, next-step charge distribution can be calculated by previous step parameters.

### C. Simulation for streamer discharges

For streamer simulations in nitrogen at atmospheric pressure, the following standard drift-diffusion equations were used for electrons, positive ions, and anion, which were coupled to the Poisson equation:

$$\begin{cases} \frac{\partial n_e}{\partial t} + \nabla \cdot (v_e n_e) = \nabla^2 (D n_e) + (\alpha - \eta) n_e + |v_e| + s \\ \frac{\partial n_p}{\partial t} + \nabla \cdot (v_p n_p) = \alpha n_e + |v_e| + s \\ \frac{\partial n_n}{\partial t} + \nabla \cdot (v_n n_n) = \eta n_e + |v_e| \\ \nabla \cdot (\varepsilon \nabla U) = -e(n_p - n_n - n_e) \\ E = -\nabla U \end{cases}, \quad (16)$$

where  $n_e$  and  $n_p$  are electron and positive ion densities, respectively,  $n_n$  is the anion density,  $v_i = u_i E$  is the drift velocity of electrons,  $E$  is the electric field, and  $u_i$  is the electron mobility.  $D$  is the electron diffusion coefficient, and  $\alpha$  represents the impact ionization coefficient.  $U$  is the electric potential,  $s$  is the photoionization,  $\varepsilon$  is the permittivity of free space, and  $e$  is the electron charge [12, 13].

Considering the photoionization process in a numerical simulation is important. The photoionization model developed by Zhelezniak was introduced into the numerical simulation of streamer discharge in atmospheric air [14,15]. Given the non-locality of radiative transfer, the photoionization model involves describing radiative relations between all points of the plasma. Thus, calculating the photoionization model is complex. A model derived by Zheleznyak is an example of photoionization in air, where the photoionization rate at the point of observation  $\mathbf{r}$  because of source points of emitting photoionizing UV photons at  $\mathbf{r}'$  is as follows:

$$S = \iiint_D \frac{I(\mathbf{r}') f(R)}{4\pi R^2} dD, \quad (17)$$

where  $R = |\mathbf{r} - \mathbf{r}'|$ . The photon production in this model is assumed to be proportional to the ionization production rate  $S_i$ , and  $I(\mathbf{r})$  is given by the following:

$$I(\mathbf{r}) = \xi \frac{n_u(\mathbf{r}')}{\tau_u} = \frac{p_q}{p + p_q} \xi \frac{v_u}{v_i} S_i(\mathbf{r}), \quad (18)$$

where  $\xi$  is the photoionization efficiency,  $n_u(\mathbf{r})$  is the density of  $\mathbf{u}$ , the ratio  $p_q/(p+p_q)$  is a quenching factor,  $\tau_u$  is the lifetime of the excited state  $\mathbf{u}$  that accounts for the effects of spontaneous emission and quenching,  $v_u$  is the electron impact excitation frequency for level  $\mathbf{u}$ , and  $S_i = v_i n_e$  (where  $n_e$  is the electron number density and  $v_i$  is the ionization frequency). The function  $f(R)$  in Equation (17) is defined in two studies [16-18].

The distribution function and charge density were used in the present study to describe photoionization. In a traditional LBM model,  $\Omega_i$  is required to satisfy the conservation of the total mass and total momentum at each lattice as follows:

$$\sum_i \Omega_i = 0, \quad \sum_i \Omega_i e_i = 0. \quad (19)$$

The sum of all collision operators  $\Omega_i$  in our model is equal to photoionization:

$$\sum_i \Omega_i = S, \quad \sum_i \Omega_i e_i = S \mathbf{u}. \quad (20)$$

If only the physics in long wavelengths and low-frequency limits are important, the lattice spacing  $\Delta x$  and time increment  $\Delta t$  in Equation (1) can be regarded as small parameters of the same order  $\varepsilon$ . Through a Taylor expansion in time and space, the following continuum form of the kinetic equation accurate to the second order in  $\varepsilon$  can be obtained:

$$\frac{\partial f_i}{\partial t} + e_i \cdot \nabla f_i + \varepsilon \left( \frac{1}{2} e_i^2 \cdot \nabla^2 f_i + e_i \cdot \nabla \frac{\partial f_i}{\partial t} + \frac{1}{2} \frac{\partial^2 f_i}{\partial t^2} \right) = \frac{\Omega_i}{\varepsilon}. \quad (21)$$

The Chapman–Enskog expansion can be employed to derive the macroscopic hydrodynamic equation, which is essentially a formal multi-scaling expansion:

$$\begin{cases} \frac{\partial}{\partial t} = \varepsilon \frac{\partial}{\partial t_1} + \varepsilon^2 \frac{\partial}{\partial t_2} \\ \frac{\partial}{\partial x} = \varepsilon \frac{\partial}{\partial x_1} \end{cases}. \quad (22)$$

The Equation (22) assumes that the diffusion time scale  $t_2$  is much slower than the convection time scale  $t_1$ . The one-particle distribution function  $f_i$  can similarly be expanded formally on the local equilibrium distribution function  $f_i^{eq}$  and photoionization distribution function  $f_i^{seq}$ :

$$f_i = f_i^{eq} + f_i^{seq} + \varepsilon (f_i^{neq}). \quad (23)$$

At this point,  $f_i^{eq}$  depends on the local macroscopic variables ( $\rho$  and  $\rho \mathbf{u}$ ) and should satisfy the following constraints:

$$\sum_i f_i^{eq} = \rho, \quad \sum_i f_i^{eq} e_i = \rho \mathbf{u}. \quad (24)$$

$f_i^{seq}$  depends on the local macroscopic variables ( $S$  and  $S \mathbf{u}$ ) and should satisfy the following constraints:

$$\sum_i f_i^{seq} = S, \quad \sum_i f_i^{seq} e_i = S \mathbf{u}. \quad (25)$$

Thus,

$$f_i^{neq} = f_i^{(1)} + \varepsilon f_i^{(2)} + O(\varepsilon^2), \quad (26)$$

is the non-equilibrium distribution function, which has the following constraints:

$$\sum_i f_i^{(k)} = 0, \quad \sum_i f_i^{(k)} e_i = 0, \quad (27)$$

for both  $k = 1$  and  $k = 2$ . When  $f_i$  is inserted into the collision operator  $\Omega_i$ , the Taylor expansion provides the following:

$$\Omega_i = \Omega_i(f_i^{eq}) + \Omega_i(f_i^{seq}) + O(\varepsilon^3). \quad (28)$$

From Equation (21), we note that when  $\varepsilon \rightarrow 0$ , then  $\Omega_i(f_i^{eq}) = 0$ ,  $\Omega_i(f_i^{seq}) = S$ . This condition leads to the following linearized collision operator:

$$\frac{\Omega_i}{\varepsilon} = \frac{M_{ij}}{\varepsilon} (f_i - f_i^{eq} - f_i^{seq}), \quad (29)$$

where

$$M_{ij} = \frac{\partial \Omega_i(f_i^{eq})}{\partial f_j}, \quad (30)$$

is the collision matrix that determines the scattering rate between directions  $i$  and  $j$ . For a given lattice,  $M_{ij}$  only depends on the angle between directions  $i$  and  $j$ , and has a limited set of values. For mass and momentum conservation collision,  $M_{ij}$  satisfies the following constraints [19]:

$$\sum_i M_{ij} = 0, \quad \sum_i M_{ij} e_i = 0. \quad (31)$$

If we further assume that the local particle distribution relaxes to an equilibrium state at a single rate:

$$M_{ij} = -\frac{1}{\tau} \delta_{ij}, \quad (32)$$

we then arrive at the lattice BGK (LBGK) collision term [20]:

$$\frac{\Omega_i}{\varepsilon} = \frac{1}{\tau} (f_i^{seq} - f_i^{neq}) = \frac{1}{\tau} f_i^{seq} - \frac{1}{\varepsilon \tau} (f_i^{(1)} + f_i^{(2)}), \quad (33)$$

and the LBGK equation:

$$f_i(\mathbf{x} + e_i \Delta t, t + \Delta t) - f_i(\mathbf{x}, t) = -\frac{f_i - f_i^{eq} - f_i^{seq}}{\tau}. \quad (34)$$

Photoionization is described at this point by the equilibrium distribution function from an LBGK model:

$$f_i^{seq} = E_i(S, \mathbf{u}) = \omega_i S \left( 1 + \frac{e_i \cdot \mathbf{u}}{c_s^2} + \frac{(e_i \cdot \mathbf{u})^2}{2c_s^4} - \frac{u^2}{2c_s^2} \right). \quad (35)$$

Finally, the LBM equation for streamer discharge simulation is written as follows:

$$f_i(\mathbf{x} + e_i \Delta t, t + \Delta t) - f_i(\mathbf{x}, t) = -\frac{f_i - f_i^{eq} - f_i^{seq}}{\tau} + \Delta t F_i. \quad (36)$$

## D. Numerical algorithm processes

The solution procedure can be illustrated by the following numerical algorithms:

- Initial equilibrium distribution function  $f_i(\mathbf{x}, 0)$ ;
- Poisson's equation and algorithm for the electric field force and photoionization are solved;
- Continuity equations are computed as follows:

$$f_i'(\mathbf{x}, t) = f_i(\mathbf{x}, t) + \frac{f_i - f_i^{eq} - f_i^{seq}}{\tau} + \Delta t F_i; \quad (37)$$

- Migration for location is executed as follows:

$$f_i(\mathbf{x} + e_i \Delta t, t + \Delta t) = f_i'(\mathbf{x}, t); \quad (38)$$

- Macroscopic quantities are computed as follows:

$$\rho(\mathbf{x}, t + \Delta t) = \sum_{i=1} f_i(\mathbf{x}, t + \Delta t), \quad (39)$$

$$\rho \mathbf{u}(\mathbf{x}, t + \Delta t) = \sum_{i=1} f_i e_i(\mathbf{x}, t + \Delta t); \quad (40)$$

(f) If  $t + \Delta t < t_{\text{final}}$ , then step (b) is repeated.

### III. NUMERICAL RESULTS

#### A. Numerical results of an electron avalanche

This section first investigates the physical quantity of electron density, which depicts the process of an electron avalanche. The computational domain is  $256 \times 256$ , and the characteristic is  $L = 256$ ,  $\Delta x = 1$ . The electric breakdown of gas that occurs in a uniform electric field is directed vertically. We used periodic boundary conditions at the sides of the computation area and solid walls at the top and bottom. Charge injection from the tip results in the formation of an electron avalanche. As the conductive channel reaches the second electrode, the channel stage of the electric breakdown begins. Simulation results are shown in Fig. 2.

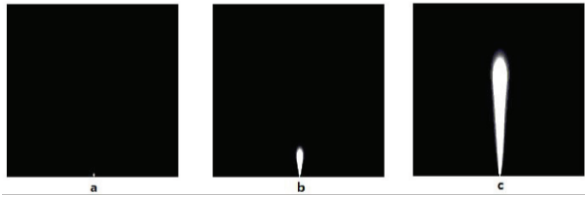


Fig. 2. Growth of an electron avalanche channel. Time at: (a)  $t = 10$ , (b)  $t = 200$ , and (c)  $t = 1000$ . The white color corresponds to the electron density.

Figure 3 shows an initial electron avalanche in the ionization chamber, which was obtained from a study [21]. The shape of the electron avalanche has a rough vertebral shape. Comparing Figs. 2 and 3 shows a remarkable similarity in the shape of the electron avalanche. Therefore, the result of using an LBE simulation is valid. The numerical simulation method is feasible at least for describing the shape of an electron avalanche.

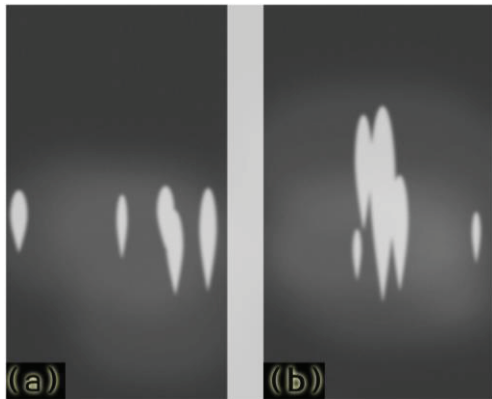


Fig. 3. Initial electron avalanche in the ionization chamber is shown.  $P = 270$  (133 Pa),  $E = 10.5$  kV/cm.

#### B. Propagation of a 1.5D model for streamer discharges

The following section attempts to demonstrate the efficiency of using an LBM model for the two examples selected among classic streamer simulation test cases. First, a 1.5D model was used. The numerical solutions of these equations have been limited to simple situations for a long time, in which the streamer was assumed to be confined inside a cylinder with a constant radius. Inside the cylinder, the charged particle density was assumed to be confined inside a cylinder with a constant radius and constant along the radial direction. The space and time evolution of charged particles can only be calculated in one dimension (along the direction of propagation) under these conditions, and the electric field was obtained using the so-called disc method. If only a 1D approach is necessary to calculate the space and time variations of charged particle densities, noting that the electric field has to be calculated in two dimensions is important. This approach is recognized in 1.5D model studies, and was popular during the early stages of streamer simulation. At present, this approach is mainly used to rapidly check the accuracy of different numerical models. Thus, the 1.5D model was used in the subsequent sections for the said purpose. Second, the complete 2D propagation of a double-headed streamer under a homogeneous electric field was investigated. These results allow us to check the efficiency of the LBM in different scenarios and demonstrate strong improvements compared with other models. Calculations were made using the 1.5D approximation defined in the previous section, and the propagation of a double-headed streamer was calculated by an LBM Q1D3 model. The propagation of a double-headed streamer was considered in plane-to-plane geometry in pure nitrogen at atmospheric pressure [22]. The cathode is located at  $x = 1$  and the anode is located at  $x = 0$ . The applied voltage is equal to 52 kV. A 0.05 cm discharge radius was selected. The initial distribution of electrons and ions has the following Gaussian shape:

$$n_e(x, 0) = n_p(x, 0) = n_b + n_0 \left( \exp\left(-\frac{(x-x_0)^2}{\sigma_x}\right) \right), \quad (41)$$

with  $\sigma_x = 0.027$  cm,  $x_0 = 0.5$  cm,  $n_0 = 10^{14}$  cm<sup>3</sup>, and  $n_b = 10^8$  cm<sup>3</sup>. Two streamers start to propagate toward the opposite electrodes in this case.

Figures 4 and 5 reveal the space variation of the net charge density and electric field during double-headed streamer propagation. Figure 4 shows the comparison of charge densities at four different time points ( $t = 0.5, 1.5, 2.5, 3$  ns) during streamer head propagation. Figure 5 shows the comparison of the electric field at four different time points ( $t = 0.5, 1.5, 2.5, 3$  ns) during streamer head propagation. After 2.5 ns of propagation, the propagation distance of the anode-directed streamer

is 1.8 cm, whereas that of the cathode-directed streamer is 2.8 cm. The velocity of the anode-directed streamer is  $0.8 \times 10^8$  cm/s to  $1.8 \times 10^8$  cm/s, whereas that of the cathode-directed streamer is  $0.4 \times 10^8$  cm/s to  $1.0 \times 10^8$  cm/s. Two regions have large charge densities on the head of the double-headed streamer. These results are similar to the findings of a previous study [23].

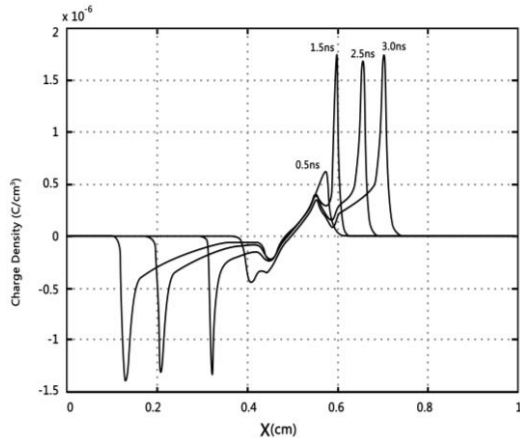


Fig. 4. Double-headed streamer front propagation and charge density at different time points ( $t = 0.5, 1.5, 2.5, 3$  ns) are shown.

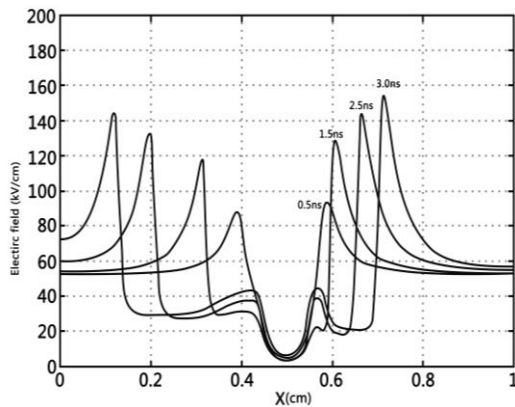


Fig. 5. Double-headed streamer front propagation and electric field at different time points ( $t = 0.5, 1.5, 2.5, 3$  ns) are shown.

### C. Propagation of 2D double-headed streamer

Calculations in this section were performed using the 2D approximation defined in the previous section, and the propagation of a double-headed streamer was calculated using the LBM Q2D9 model. The size of the computational domain is  $1.4 \times 0.125$  cm<sup>2</sup>. The center of the Gaussian distribution is located in the middle of the simulation domain at  $x_0 = 0.7$  cm. The applied voltage is equal to 52 kV. Figure 6 shows a cross-sectional

view of the charge density distributions and electric field at  $t = 3.0$  ns, which was obtained using the Q2D9 LBM model. This cross-sectional view represents an example of the 2D views of the simulation results. The streamer propagation under homogeneous electric fields validates the effectiveness of the LBM model compared with other computational models [24,25].

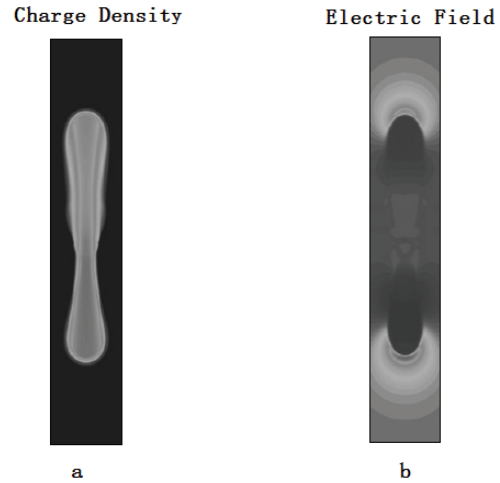


Fig. 6. Propagation of a double-headed streamer in a 2D domain and a cross-sectional view of distributions of the: (a) charge density and (b) electric field at  $t = 3.0$  ns.

## IV. DISCUSSION AND CONCLUSION

This study attempted to simulate the gaseous discharge process using an LBM model. The LBM model has been developed into an alternative and promising scheme for different types of numerical simulations in recent years. Unlike other numerical schemes, the lattice Boltzmann method was based on microscopic models and mesoscopic kinetic equations. This scheme can be particularly successful in fluid flow applications and numerical simulations of EHD problems. This study is only an experimental application of the LBM, which was applied to break down gaseous dielectric problems. We have also compared the LBM streamer model with other results obtained using different numerical techniques to solve transport equations for charged particles. The efficiency of the LBM was supported by similar results. Several issues remained unsolved in this model, such as the use of simple photoionization. In addition, the LBM model has several unique advantages on the complex boundary problem and porous material issues. Combined with the theory of discharge gas systems and characteristic advantage of this model, several gas discharge conditions at the complex boundary were examined. This study can be an important reference for solving several practical problems in the future.

### ACKNOWLEDGMENT

This research was supported by the Major Research Plan of the National Natural Science Foundation of China (2012CB723308), and the Science Technology Research Program of the Heilongjiang Educational Committee (12541611).

### REFERENCES

- [1] C. Wu and E. Kunhardt, "Formation and propagation of streamers in  $N_2$  and  $N_2$ - $SF_6$  mixtures," *Physical Review A*, vol. 37, no. 11, pp. 4396-4406, Jun. 1988.
- [2] G. E. Georghiou, et. al., "Numerical modelling of atmospheric pressure gas discharges leading to plasma production," *Journal of Physics D Applied Physics*, vol. 38, no. 20, pp. 303-328, Sep. 2005.
- [3] D. A. Medvedev, "Lattice Boltzmann model for simulation of the electric breakdown in liquids," *Procedia Computer Science I*, vol. 1, no. 1, pp. 811-818, Apr. 2010.
- [4] A. L. Kupershtokh, "Lattice Boltzmann equation method in electrohydrodynamic problems," *Journal of Electrostatics*, vol. 64, no. 7-9, pp. 581-585, Nov. 2006.
- [5] H. Huang, L. Wang, and X-Y. Lu, "Evaluation of three lattice Boltzmann models for multiphase flows in porous media," *Computers and Mathematics with Applications*, vol. 61, no. 12, pp. 3606-3617, 2011.
- [6] Y. L. He and Y. Wang, *Lattice Boltzmann Method Theory and Application*, Science Press, China, 2009.
- [7] S. Chen and G. D. Doolen, "Lattice Boltzmann method for fluid flows," *Annu. Rev. Fluid Mech.*, vol. 30, no. 5, pp. 329-364, Aug. 1998.
- [8] Y. Qian and D. d'Humieres, "Lattice BGK models for Navier-Stokes equation," *Europhys*, vol. 17, no. 6, pp. 479-484, Jan. 1992.
- [9] Z. Li. Guo and C. G. Zheng, *Theory and Application of Lattice Boltzmann Method*, Science Press, China, 2009.
- [10] J. M. Buick and C. A. Greated, "Gravity in a lattice Boltzmann model," *Physical Review E*, vol. 61, no. 5, pp. 5307-5320, May 2000.
- [11] N. Wang, Q. Lei, and X. Wang, "Lattice Boltzmann model for simulation of the electric charge flow and calculation of electrorheology," *International Journal of Digital Content Technology and its Applications*, vol. 6, no. 17, pp. 135-143, Sep. 2012.
- [12] L. B. Loeb and J. M. Meek, "The mechanism of spark discharge in air at atmospheric pressure," *J. Appl. Phys*, vol. 11, no. 6, pp. 438-47, Nov. 1940.
- [13] A. J. Davies and C. S. Davies, "Computer simulation of rapidly developing gaseous discharges," *PROC. IEE.*, vol. 118, no. 6, pp. 816-823, 1971.
- [14] M. B. Zheleznyak, A. K. Mnatsakanian, S. V. Sizykh, "Photoionization of nitrogen and oxygen mixtures by radiation from gas discharge," *High Temperature*, vol. 20, no. 3, pp. 357-362, 1982.
- [15] J. Roger-Riba, P. Casals-Torrens, and R. Bosch, "Defects identification in XLPE medium-voltage cables by applying multivariate methods," *DYNA*, vol. 89, no. 6, pp. 633-641, 2014.
- [16] G. W. Penney and G. T. Hummert, "Photoionization measurements in air oxygen and nitrogen," *Journal of Applied Physics*, vol. 41, no. 2, pp. 572-577, Aug. 1970.
- [17] A Bourdon, et. al., "Efficient models for photoionization produced by non-thermal gas discharges in air based on radiative transfer and the Helmholtz equations," *Plasma Sources Science and Technology*, vol. 16, no. 3, pp. 656-678, Aug. 2007.
- [18] W. J. Yao and S. P. Chen, "Elastic-plastic analytical solutions of deformation of uplift belled pile," *Tehnicki Vjesnik-Technical Gazette*, vol. 21, no. 6, pp. 1201-1211, Dec. 2014.
- [19] R. Benzi, S. Succi, M. Vergassola, "The lattice Boltzmann equation theory and applications," *Phys. Rep.*, vol. 222, no. 3, pp. 145-97, 1992.
- [20] P. L. Bhatnagar, E. P. Gross, and M. Krook, "A model for collision processes in gases: small amplitude processes in charged and neutral one component system," *Phys. Rev.*, vol. 94, no. 3, pp. 511-525, Jan. 1955.
- [21] Y. Zhang, *High Voltage and Insulation Technology*, China Power Press, Beijing, 2002.
- [22] A. Boretti and S. Jiang, "Development of a two stroke direct injection jet ignition compressed natural gas engine," *Journal of Power Technologies*, vol. 94, no. 3, pp. 145-152, Mar. 2014.
- [23] D. Bessieres, J. Paillol, A. Bourdon, and P. Segur, "A new one-dimensional moving mesh method applied to the simulation of streamer discharges," *Journal of Physics D: Applied Physics*, vol. 40, no. 21, pp. 6559-6570, Apr. 2007.
- [24] C. Zhuang and R. Zeng, "Discountinuous Galerkin method for short air gap discharge simulations and its applications," *High Voltage Engineering*, vol. 39, no. 4, pp. 970-978, Apr. 2013.
- [25] Y. Zhang and R. Zeng, X-C. Yang, and B. Zhang, "Study on photoionization produced by discharge in atmospheric air by numerical method," *Proceedings of the CSEE*, vol. 29, no. 4, pp. 110-116, Feb. 2009.



**Nan Wang** (1984.5-), male, native place: Harbin in China, Ph.D. Student of the Harbin University of Science Technology, working in the School of Mathematical Science of Heilongjiang University. Research focus: lattice Boltzmann and high-voltage insulation.



**Qingquan Lei** (1938.7-), male, native place: Sichuan Province in China, Academician of the Engineering Academy, and Professor of the Harbin University of Science Technology. Research focus: high voltage and insulation techniques.